Structures électromagnétiques à bandes interdites pour des applications de filtre

Heba Badr El Din Badr El-Din El-Shaarawi

THÈSE

En vue de l'obtention du

DOCTORAT DE L'UNIVERSITÉ DE TOULOUSE

DÉLIVRÉ PAR *Université Paul Sabatier*

Discipline ou spécialité :

Micro-ondes, Electro-magnétisme,Opto-électronique

Présentée et soutenue par *Heba Badr El-Din Abdo El-Shaarawy*

Le *17 Décembre 2009*

Titre : *Structures électromagnétiques à bandes interdites pour des applications de filtre*

JURY

Roberto SORRENTINO, Professeur, Université de Perugia, Italie.
Eric RIUS, Professeur, Université de Brest, France.
Pierre BLONDY, Professeur, Université de Limoges, France.
Jean Louis CAZAUX, Ingénieur,Thales Alenia Space, France.
Eric KERHERVE, Professeur, Institut Polytechnique de Bordeaux, France.
Hervé AUBERT, Professeur, Institut National Polytechnique, France.
Robert PLANA, Professeur, Université Paul Sabatier, France.
Fabio COCCETTI, Ingénieur, NovaMEMS, France.

Ecole doctorale : *GEET*
Unité de recherche : *LAAS-CNRS*

Directeurs de Thèse : *Pr. Robert PLANA, Pr. Essam HASHISH, Pr. Mostafa EL-SAID, Dr. Fabio COCCETTI*
Rapporteurs: *Pr. Roberto SORRENTINO, Pr. Eric RIUS*

LIST OF CONTENTS

CHAPTER THREE

STUDY OF THE ELECTROMAGNETIC BANDGAP (EBG) AND DEFECTED GROUND STRUCTURE PHENOMENA

CHAPTER FOUR

NOVEL RECONFIGURABLE DEFECTED GROUND STRUCTURE RESONATOR FOR MULTI-STOPBAND FILTER ON COPLANAR WAVEGUIDE TECHNOLOGY

CHAPTER FIVE

ALTERNATIVE APPLICATIONS OF BANDGAP STRUCTURES IN THE MICROWAVE RANGE

LIST OF TABLES

LIST OF FIGURES

LIST OF ABBREVIATIONS

AMC	Artificial magnetic conductor
BPF	Bandpass filter
BST	Barium strontium titane
CB-CWG	Conductor-backed coplanar waveguide
CPW	Coplanar waveguide
CTCPW	Cross-tie coplanar waveguide
CTOCPW	Cross-tie-overlay coplanar waveguide
DGS	Defected ground structure
EBG	Electromagnetic bandagap
EM	Electromagnetic
FDTD	Finite difference time domain
FM	Ferromagnetic
HMIC	Hybrid microwave integrated circuits
LAAS	Laboratory of analysis and architecture of systems
LPF	Low pass filter
MEMS	Microelectromechanical system
MIS	Metal-insulator-semiconductor
MMIC	Monolythic microwave integrated circuits
NFC	Near field communication
PBG	Photonic bandagap
PCB	Printed circuit board
RFID	Radio frequency identification
SCML	Schotky contact microstrip line
SWF	Slow-wave factor
TEM	Transverse electromagnetic
UC-PBG	Uniplanar compact photonic bandgap structure
VNA	Vector network analyzer
VPDGS	Vertically periodic defected ground structure
VVC	Voltage controlled variable capacitor diode

LIST OF SYMBOLS

f	frequency
ω	angular frequency
f_o	central frequency
f_c	cutoff frequency
L	inductance
C	capacitance
R	resistance
ε_r	relative dielectric constant of the material
ε_{eff}	effective dielectric constant
h	substrate height
$tan\ (\delta)$	loss tangent of the substrate
Z_o	characteristic impedance
λ_o	wavelength in free space
λ_g	wavelength in the guided medium
E	electric field
H	magnetic field
μ	permeability of the medium
c	velocity of light in free space
P	polarisation
n	medium refractive index
$\bar{n}$	aveage refractive index
k	wave number

ACKNOWLEDGEMENTS

The first to thank for giving me the power to do this job is GOD. I have always believed that you have given me enough strength to face any difficulty, but that is not only what you have offered me, you have given me happiness and joy while doing my job through the people surrounding me, helping and supporting me whenever and wherever I needed.

I thank Prof. Robert Plana for allowing me the chance to be one of his students in the group. In addition to his help with respect to all needed equipments, material and software, he has guided me towards better ideas and projects that are closer to the industrial life.

I would also like to thank my Egyptian supervisors, Prof. Essam Hashish and Prof. Mostafa El-Said. You are both like parents to me since my undergraduate studies. I have never imagined myself writing the last page in this thesis, while you have always foreseen that from the day of my graduation. Your belief in me has always been a great support.

Dr. Fabio Coccetti, most probably, I am the most stubborn, annoying and hard to tutor student you have ever worked with. I will not thank you only for your help, but also for your friendship. You have always been available, understanding and easy to talk to.

I would also like to take the chance to thank Prof. Hervé Aubert and Dr. Daniela Dragomirescu. Although you are not my supervisors, you are always there for me whenever I need any help. Even when it is hard for me to express myself in French, you have always had the time to wait and listen.

Ahmed, my colleague, my friend, and all my family, it has been a very long time together now, ten years ago as young undergraduates who hardly understood what they were doing, till Ph.D. students acting like grownups. It has been hard on both of us, but I would like you to know that without you I would have never achieved one single step. Thank you for always being there for me, thank you for being my husband.

Nour, although you are so young, you are always kind and understanding. Watching you playing and hearing your giggles with your father are the main sources of joy in my heart.

To Mam and Dad, for all my life, I have wanted you to be proud of me, not because you are difficult to please, but because you have always been my role models. You have been great parents; I wish I can be as half as good as you are with me.

To my sister, Bassant, you have always been a second mam. When I was young, I hated it, but now, I understand that you have always cared. You will always be my best friend.

Finally, I thank all my friends in France and in Egypt. If I mention the name of every one of you, I will not have enough space, neither for your names nor for the amount of thanks need me to express. Everyone of you have been so special in the way he is, and in the way he acted, but overall, you have all succeeded in being supporting and loving friends whether you are in the neighboring office or in a far away country. I am really lucky to have you all.

ABSTRACT

The increasing development of wireless applications turns out to new requirements for transceiver architectures that have to feature excellent microwave performances (linearity, spurious rejection, noise figure and bandwidth) and enhanced integration density that is achieved through the miniaturization of the modules as well as the introduction of multi standard functionalities. All these requirements translate to the need of filter circuits as miniaturized as possible and featuring the highest performance in term of insertion loss and rejection.

Since the late 1980's, electromagnetic bandgap (EBG) structures and defected ground structures (DGS) have attracted the interest of many researchers, due to their interesting properties in terms of size miniaturization, suppression of surface waves and arbitrary stopbands. Since then, they have been used in many applications like lowpass filters, bandpass filters, antennas, waveguides and others. Based on the interesting features proposed by EBG and DGSs, the main aim of this thesis is to achieve miniaturized reconfigurable filters that may serve in wireless communication systems.

EBG structures are periodic structures which allow the propagation of electromagnetic waves in certain frequency bands and forbid them in other bands known as the "bandgap". The first step taken towards achieving the goal is to study the state of the art of bandgaps structures, their advantages, disadvantages, applications, and the most important achievements using such structures. Also, a one-dimensional multi-layer periodic structure is studied with two different analytical techniques, the Coupled-Wave Theory and the Bloch-Wave Formalism. Due to the many design parameters of EBG structures, and the difficulty in their modeling, DGS attracted the interest of many researchers as they have the main advantages proposed by EBG structures but by using only one or two cells, in addition, they are easier to model. So the next step in this thesis is to study the different modeling techniques of DGSs. The dumbbell shape DGS is modeled using the parallel *LC*, parallel *RLC*, the π-equivalent circuit and others where a comparison between the different models is presented and a conclusion of which is the best suitable to be used in more complex designs. Using the developed models, low-pass

filters of order three are designed and simulated on microstrip transmission line and coplanar waveguide technologies.

After developing a good understanding of the DGSs, a novel reconfigurable DGS resonator, for multi-stopband filter on CPW, is presented, in the frequency range from 0-11 GHz. First, the complete structure of the resonator and where the reconfigurability elements are put are explained. The structure has three different switches on each side of the CPW ground planes, giving four different configurations. As a first design step, these switches are modeled as ideal ones, i.e. open and short circuits. In each configuration, the structure has been modeled using the parallel *RLC* circuit, fabricated and measured, where all results show good agreement. The resonator is then implemented using PIN diodes as the reconfigurability element. The measurement results with the measurement setup are illustrated in the thesis.

Finally, the last step of this study is to use the DGS in the implementation of the bandpass filters. Two applications of the DGSs are presented. First, a compact inductively coupled BPF using the DGS unit cell operating at 5 GHz is implemented. Then to validate this theory, another filter of the same type of order two at the same frequency is designed. Then, a reconfigurable bandpass filter using this structure is proposed. Using a MEMS switch, the structure would convert from a single resonance structure at 5 GHz to a multi resonance structure at 2.8 and 8 GHz.

The second application is the enhancement of the ring resonator filter. Ring resonator based filters are featuring attractive behavior but they are suffering from two kinds of drawbacks that limit their implementation in real applications. The first one is their large size due to the two tuning stubs, while the second deals with the existence of higher order modes which limit the out-of-band rejection. Both issues degrade the whole system performance and need to be assessed to find solutions to overcome these drawbacks. This thesis aims to propose some solutions to reduce the size and increase the rejection of the stopband of the ring resonator filter, while keeping its overall performances with respect to its wide bandwidth, sharp rejection and low insertion-loss. In order to do so, two different design approaches are considered. The first is at the filter layout level, through a space saving redesign of the tuning stubs, while the second is at the wave propagation level, through the exploitation of DGS properties.

Finally, for future work, the implementation of these structures on silicon substrates using MEMS switches and ferroelectric materials is proposed to achieve overall better performance and easy tuning.

CHAPTER ONE

INTRODUCTION

1.1. Motivation of the Thesis

Nowadays, the rapid development of communication systems is turning into wireless ubiquity; which means that everyone expects to reach whatever he wants, whenever he wants and wherever he wants. By this way, mobile systems, or in other words, the mobile handset is required to do many applications following different standards using different technologies. Fig.1.1 illustrates a complete view of the different applications that should be achieved at the same time and its corresponding enabling technology.

Fig. 1.1. Different mobile applications and their enabling technologies [1].

From Fig. 1.1, it is clear that the mobile handset should serve many applications starting from the MP3s, NFC (Near Field Communication), mobile TV

to radio and media player. Each application has its enabling technology, for example NFC is achieved by RFID (Radio Frequency Identification) and location presence is achieved by the GPS and so on. That means that we have a crowded frequency spectrum to operate on as shown in Fig. 1.2. The frequency spectrum starts at 800 MHz by the GSM low band frequency and ends by 6 GHz for the IEE802.11a for the Wi-Fi application.

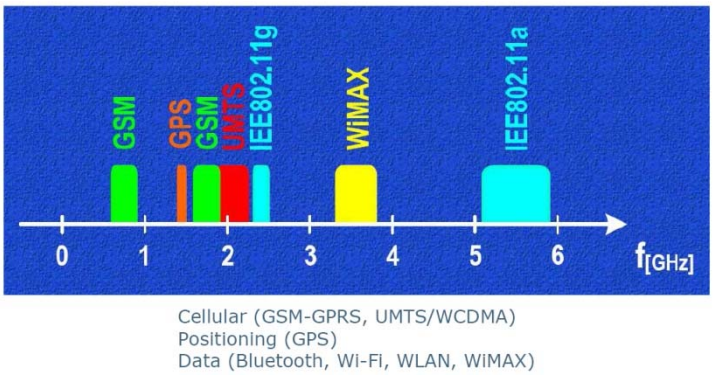

Fig. 1.2. The different bands along the frequency spectrum from 0 to 6 GHz [2].

Based on the applications needed from the mobile handset, we may summarize the requirements needed in a handset for these applications to come true as [3]:

- The mobile should operate at a wide frequency range starting from 0.8 to 6 GHz; and it should allow multi-band operation.
- The handset should allow multi-standard (e.g., Bluetooth + GSM +Wi-Fi) with different data rates (10k-2Gpbs).
- Minimal interference (selectivity is mandatory) as more than one application is present along the same frequency band.
- Easy adaptation to new standards which allows short-time-to market.
- More functionality/services, as it is not just a phone, but a multi-media system (video, camera, e-commerce, electronic postcards, wireless amusement park).
- Increased battery life and reduced power consumption per function.
- Compact size, light weight and low profile.
- Low Cost.

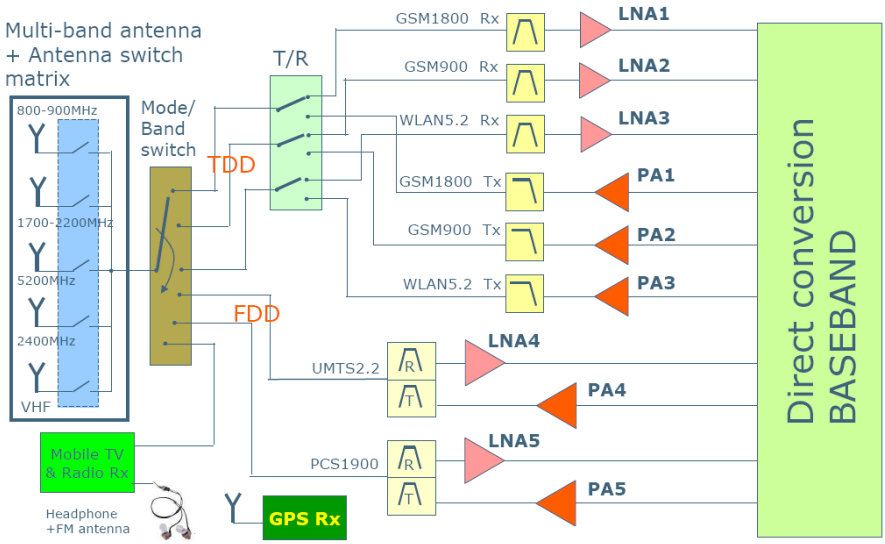

Fig. 1.3. Basic architecture of a mobile handset [1].

Fig. 1.3 shows the architecture of the handset for all applications to take place. This architecture consists of a great number of passive and active devices with about 5~10% of them active at a time. At the same time these components take about 80% of the PCB space and 70% of the cost. So in order to achieve the reduction in size needed and minimize the cost, these extra filters and amplifiers should be miniaturized or removed. To reduce the size and the count of the components, reconfigurability should be used. In this case the architecture will be reduced to the one shown in Fig. 1.4.

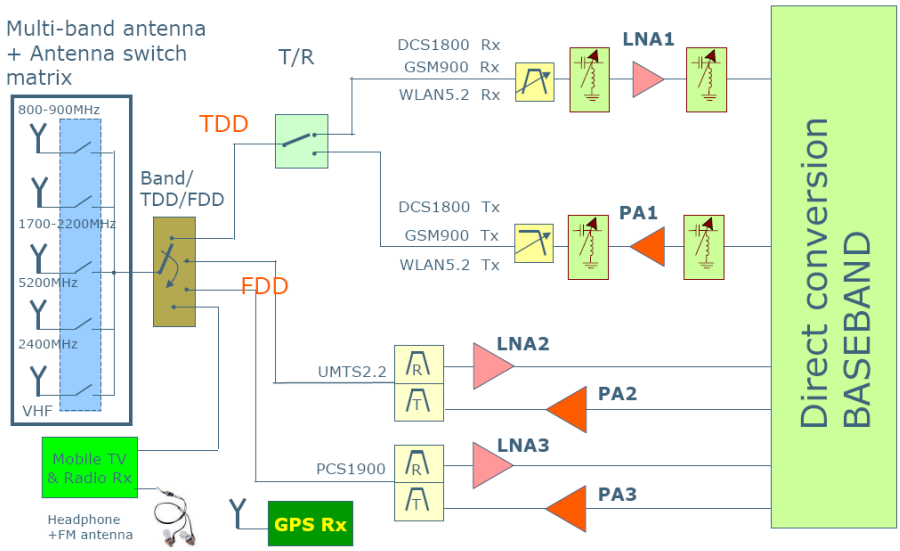

Fig. 1.4. Reduced architecture of the handset [1].

The advantages of miniaturization and reconfigurability are:

- Lower component count.
- Smaller size and/or cost.
- Easy adaptation to upcoming standards.

On the other hand, it has the following disadvantages:

- Tunable components present lower performance parameters than fixed devices.
- Requires additional control circuitry.
- Additional calibration effort (e.g. to be performed over voltage and temperature).
- Increasing difficulty in the design process.

The reconfigurable reduced architecture of the mobile handset imposes the implementation of miniaturized reconfigurable bandpass filters along the frequency band from 0.8 to 6 GHz. The aim of this thesis is to reach miniaturized and reconfigurable tunable filters over the previously mentioned spectrum with good characteristics.

In the following section of this chapter, we will explain why we have chosen electromagnetic bandgap (EBG) and defected ground structures (DGS) to achieve our goal, then a more illustrative presentation of the different work and development of bandgap structures will be presented in Chapter Two.

1.2. Introduction to Electromagnetic Bandgap (EBG) Structures and Defected Ground Structures (DGS)

Electromagnetic bandgap (EBG) structures are periodic structures that initially evolved in the optical domain by the name of photonic bandgap (PBG) structures in the late 1980's [4], [5]. EBG structures may be implemented in different ways; either by etching gaps in the metal of the ground plane [6], or the signal line [7], or by drilling periodic holes in the dielectric [8].

These periodic structures have very interesting features which make them very promising candidates to a number of applications [9]. EBG structures allow the propagation of electromagnetic waves in certain frequency bands and forbid them in

other bands known as bandgap. This first property is used in many applications for the suppression of higher order harmonics and undesirable passbands.

The second feature of these structures is that they increase the effective inductance and capacitance of the line, supporting slow-wave propagation. Consequently, all passive and active components that are implemented using EBG have a miniaturized size compared to conventional components. Many articles reported more than 40% reduction in size [9].

On the other hand, contradicting all slow-wave technologies, EBG structures do not suffer from excess losses in the passbands; on the contrary, such structures might give better insertion and return loss values due to their ability to suppress surface waves. Surface waves are caused by the multiple reflections of electromagnetic waves between the ground plane and the air-dielectric interface. They are the source of two basic problems in many systems. First problem is the leakage of energy through leaky waves and end-fire radiation. The second problem is the spurious coupling between circuit components and antenna elements. These problems cause an overall reduction in the system efficiency, limit the bandwidth, and limit the applicable frequency range of microstrip systems [9].

Finally, we may summarize the advantages of EBG structures into seven main points:

1. Easy fabrication.
2. Low cost.
3. Compatibility with standard circuit technologies.
4. Ability of these structures to introduce distinctive stopbands
5. Slow-wave effect which is very important for size reduction.
6. Low attenuation in the passband.
7. Suppression of surface waves.

Although EBG structures have been used by many researchers in a wide variety of applications whether filters, antennas, amplifiers, waveguides and others, they have one basic disadvantage which is the difficulty in its modeling due to the too many parameters that should be considered, such as the lattice period, shape, size and location. This disadvantage helped in the evolution of defected ground structures (DGS). A DGS unit cell is a defect in the ground plane of a physical transmission line be it microstrip, coplanar waveguide or whatever structure where a reference

ground plane conductor exists. Such defects have all the advantages of the EBG structures except that only one or two cells are needed instead of a periodic structure to produce the same performance. The advantage in DGS over EBG structures makes them easy to model, and therefore, to involve in more complicated structures and applications.

Nowadays, new EBG structures and DGSs are being exploited everyday to reach maximum miniaturization and minimum losses. Also the trend towards a reconfigurable EBG and DGS has started a couple of years ago, showing promising results. For all these reasons, we have chosen EBG and DGS to achieve our targets.

1.3. Achievements and Organization of the Thesis

In this section, we will show the flow and the organization of this thesis. The thesis consists of six chapters. The first chapter is a short introductory chapter that focuses on three basic points. First, in Section 1.1, we explain the motivation of the thesis. We illustrate the need for miniaturized and reconfigurable lowpass and bandpass filters in the frequency range from 0.8 MHz to 6 GHz to fulfill the demands of the proposed reduced mobile handset configuration illustrated. Second, in Section 1.2, the reasons for choosing EBG and DGS technologies for achieving our goal are explained pointing out the advantages and disadvantages of each. Finally, in Section 1.3, we show our flow in studying our technique to achieve the goal.

Chapter Two is devoted to the state of the art of the work previously presented in EBG and DGS. We first give a brief introduction of the definition of bandgap structures in Section 2.1, and then we move to the historical background of the bandgap structures in Section 2.2. In this section, a comparison between the bandgap structures and previous technologies that introduce slow-wave effect for the miniaturization of the structure is provided, and how the bandgap structures developed from the optical domain to the micro-wave and millimeter wave domain providing interesting features for a number of applications. In Section 2.3, we focus on the most important work published in the EBG and the evolution of DGSs in the year 2000. Finally, Section 2.4 presents the ideas given in Chapter Two in a brief conclusion.

In Chapter Three, we explore the different techniques for studying the EBG and DGS pointing out the advantages and disadvantages of each. In Section 3.2 we study

the periodic structure using two different analytical techniques, the Coupled-Wave Theory and the Bloch-Wave Formalism. For both techniques, we study a simple multilayer structure periodic in one direction. Both techniques show that periodic structures produce a stopband where propagation is forbidden known as the "bandgap". From the shown complexity of studying and modeling of EBG structures, we changed our attention to DGSs. Section 3.3 is totally devoted to studying the dumbbell shaped DGS unit cell. First, in Section 3.3.1, the frequency characteristics of the cell and how each physical dimension affects the response of the structure are studied. In Section 3.3.2, the different modeling techniques and the parameter extraction of each are discussed. We have explored the parallel *LC*-circuit, parallel *RLC*-circuit, π-equivalent circuit and others, and then a conclusion illustrating which circuit is more suitable in representing the DGS is presented. In Section 3.3.3, these models are used in the implementation of higher order low-pass filters on microstrip line and coplanar waveguide technologies.

In Chapter Four, our novel reconfigurable DGS resonator for the implementation of a multi-stopband filter on coplanar waveguide technology is presented. We start with the structure description in Section 4.2. In Section 4.3, the response of the resonator is studied in each configuration; followed by modeling the structure using cascaded parallel *RLC*-equivalent circuit. Finally, design equations using the slot-line design equations are given. Section 4.4 is devoted for the measurement results of the structure using PIN diodes illustrating the measurement setup and the biasing technique.

In Chapter Five, two basic applications based on the aforementioned DGS are proposed. First, a DGS based inductively coupled resonator bandpass filter is introduced in Section 5.2. In Section 5.2.2, the conventional inductively coupled resonator, its design procedure and advantages over capacitively coupled resonator are presented. In Section 5.2.3, a defect is introduced in the middle of the inductively coupled resonator. Using this technique, first and second order filters have been implemented giving all design procedures and advantages. In Section 5.2.4, a reconfigurable defect is introduced in the middle of the resonator which converts the structure from a single resonance circuit to a multiband structure. In Section 5.3, the second application which is the miniaturization of ring resonator filter using DGS is given. We use three types of DGSs, the circle, squares and uniplanar photonic

bandgap (UC-PBG) structures, providing a comparison between the three different filters.

The conclusion and the perspectives of this thesis are summarized in Chapter Six. Section 6.1 gives a summary to all the work presented in this thesis. In Section 6.2, the foreseen future work and perspectives are presented. As a matter of fact, our future plans have two main endeavors. First, in section 6.2.1, the fabrication of the introduced DGS on silicon substrates using MEMS switches is proposed. The advantage behind that is that the MEMS switch provides better performance with respect to power consumption, linearity and above all insertion loss. Second, in Section 6.2.3, we introduce the advantages of fabricating DGSs by using Ferroelectric materials, and the steps needed towards that.

References of Chapter One

[1] AMICOM, “European R&D achievements in RF MEMS and RF-Microsystems”, *Workshop Europ. Microw. Week (EuMW)*, October 2007.

[2] Rofougaran, “Next generation software defined radios”, *Workshop IEEE Int. Microw. Symp. (IMS)*, June 2006.

[3] M. Brandolini and F. Svelto, “Reconfigurable Si RF Receiver Front-Ends for Multi-Standard Radios”, *Workshop IEEE Int. Microw. Symp. (IMS)*, June 2007.

[4] A. Yariv and P. Yeh, Optical Waves in Crystals, Wiley & Sons, 1984.

[5] E. Yablonovitch, “Inhibited spontaneous emission in solid state physics and electronics,” *Phys. Rev. Lett.*, Vol. 58, No. 20, pp. 2059-2062, 1987.

[6] V. Radisic, Y. Qian, R. Coccioli, and T. Itoh, “Novel 2-D photonic bandgap Structures for microstrip lines,” *IEEE Microw. Guided Wave Lett.*, Vol. 8, No. 2, pp. 69-71, Feb. 1998.

[7] B. Lin, Q. Zheng and N. Yuan, “A novel planar PBG structure for size reduction,” *IEEE Microw. Wireless Comp. Lett.*, Vol.16, No. 5, pp. 269–271, May 2006.

[8] Y. Qian, V. Radisic, and T. Itoh, “Simulation and experiment of photonic bandgap structures for microstrip circuits,” *Proceedings of Asia Pacific Microw. Conf. (APMC)*, Hong Kong, China, pp. 585–588, 1997.

[9] F. R. Yang, K. P. Ma, Y. Qian, and T. Itoh, “A uniplanar compact photonic-band gap (UC-PBG) structure and its applications for microwave circuits,” *IEEE Trans. Microw. Theory Tech.*, Vol. 47, No. 8, pp. 1509–1514, Aug. 1999.

CHAPTER TWO

STATE OF THE ART OF BANDGAP STRUCTURES

2.1. Introduction

Photonic bandgap (PBG) structures are periodic structures in which optical waves are forbidden in certain frequency bands. Due to the analogy between electromagnetic wave propagation in multidimensional periodic structures and electron wave propagation in crystals, PBG structures find applications in both optics and microwave regime. Although one- and two-dimensional periodic structures have long been investigated in the microwave community, new concepts and ideas recently developed in the optics regime [1], [2] have sparked new interest in the microwave area. Among the new ideas, the most attractive to microwave engineers is the ability to forbid electromagnetic wave propagation in either all or selected directions. Extensive investigations have been conducted to translate and apply these new concepts to the microwave and millimeter-wave domain [3]-[5] and several applications at microwave frequencies have been developed, including antenna substrates [6]-[8], resonant cavities, and filters [9].

Planar electromagnetic bandgap (EBG) structures consist of a uniformly distributed periodic metallic pattern on one side of a dielectric slab. They exhibit some interesting features such as distinctive passband and stopband, slow-wave effects, low attenuation in the passband, and suppression of surface waves when serving as the ground plane of planar microstrip circuits. Moreover, EBG structures can also be used to realize a perfectly magnetic conducting (PMC) surface, which finds applications in designing a TEM waveguide and a low profile cavity backed slot antenna [10].

The organization of this chapter is as follows; Section 2.2 gives the historical background of bandgap structures. First, a comparison between previous

technologies and that of bandgap structures is presented then we pass to the work which presents the basic building blocks in the development of bandgap structures. Section 2.3 is devoted to the previous work presented in bandgap structures. First, the progress of EBG structures is considered in Section 2.3.1, then the evolution of defected ground structure (DGS) is given in Section 2.3.2. Finally, Section 2.4 is devoted for the conclusion.

2.2. Historical Background

In this section, a brief summary about the history, progress and development of the electromagnetic bandgap structures and the evolution of defected ground structures (DGS) is presented. In the first part of this section, we show a comparison between the EBG structures versus other technologies and why they have become the interest of thousands of researchers since its invention in 1989. In the second part of this section, the main building blocks in the progress of EBG structures and how it has proved itself for various types of applications since then are given.

2.2.1. EBG versus Other Technologies

Reducing circuit dimensions in both hybrid and monolithic microwave integrated circuits (HMICs, MMICs) is important from the cost and reliability point of view. Passive devices, especially those designed using distributed transmission lines, occupy most space. Slow-wave propagation has been investigated as a method to reduce the transmission line length for a given phase. Fig. 2.1 lists a few representative works of slow-wave transmission lines from the past 30 years. The unit for the vertical axis is dB/λ_g, where λ_g is the guided wavelength. This is a reasonable choice of unit for a fair comparison of losses associated with various slow-wave lines, since all known methods for enhancing the slow-wave factor (SWF), also known as the normalized phase constant (β/k_o), lead to an increasing attenuation constant.

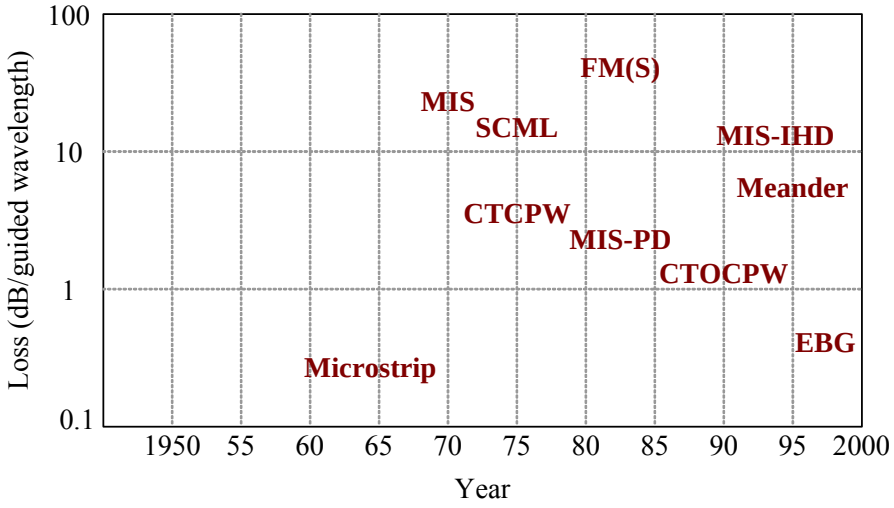

Fig. 2.1. Losses of slow-wave lines [11].

Slow-wave transmission lines such as the metal-insulator-semiconductor (MIS) microstrip, ferromagnetic (FM) microstrip, ferromagnetic semiconductor (FMS) microstrip, or Schottky-contact microstrip line (SCML) configurations were extensively investigated several years ago. These slow-wave lines, which incorporate layered substrates, show losses near 10 dB/λ_g. However, these uniform guiding structures have greatly improved the SWF. Some modified structures use inhomogeneous doping (MIS-IHD), or periodically doped structures (MIS-PD) for MIS coplanar waveguides to reduce the attenuation and enhance the SWF, thus extending the slow-wave propagation frequency range. Several periodic structures such as the cross-tie coplanar waveguides (CTCPW), cross-tie-overlay coplanar waveguide (CTOCPW) and meander microstrip have been proposed to enhance the performance of the slow-wave transmission line. These improved slow-wave transmission lines have losses between 1-10 dB/λ_g. Notice that improved slow-wave transmission lines employ complicated fabrication process and still have high insertion losses.

Microstrip that incorporates an electromagnetic bandgap structure (EBG) and experience periodic perturbations from the substrate, ground plane or the transmission line itself has recently shown great potential for a great variety of applications in microwave electronics and antenna development. These EBG structures exhibit a significant increase in the SWF without increase in losses for a microstrip on an electromagnetic bandgap (EBG) ground plane. As shown in Fig.

2.1, the microstrip on an EBG configuration further reduces the loss, representing a breakthrough of the 1 dB/λ_g barrier after decades of effort to improve the slow-wave lines.

2.2.2. Progress and Development of EBG Structures

The progress of EBG structures, since their invention in the 1987 in the optical domain, has not followed a series pattern of development; on the contrary, it followed parallel enhancement and improvement through the innovation of different structures and patterns. Each structure proved to have certain advantages making it suitable for specific applications. This overview is focused on the most famous structures and their applications.

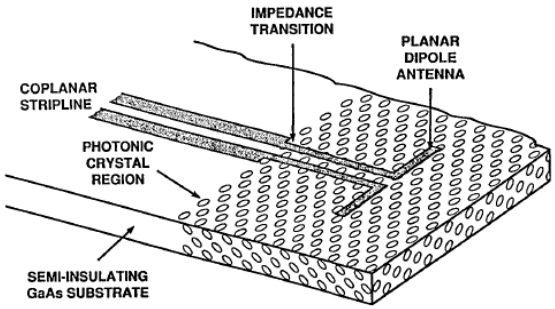

Fig. 2.2. The proposed planar dipole antenna lying over the photonic-crystal region of a semi-insulating GaAs substrate [6].

Since the invention of PBG structures in 1989, they were totally designed for optical applications till the publication of a paper by Brown et al., proposing the building of a planar antenna on photonic crystal substrate in 1993 [6]. This paper was a break through as it transferred the idea of PBG structures from the optical domain to the microwave and millimeter wave bands. It stated the advantages of using EBG in three main applications which were (1) planar antennas, (2) delay lines, and (3) nonreciprocal devices. It also stated that each of these applications falls into the general class of signal propagation and control. The photonic crystal is well suited for this class of applications because of the absence of propagation in the bandgap and because of the nature of the dispersion curves at frequencies above and below the bandgap. Fig. 2.2 shows the proposed dipole antenna on the PBG structure.

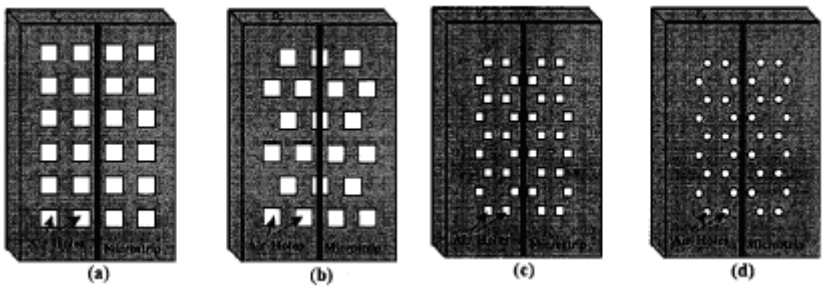

Fig. 2.3. Several EBG structures for microstrip circuits: (a) Square-lattice, square-hole, (b) Triangular-lattice, square-hole, (c) Honeycomb-lattice, square-hole, (d) Honeycomb-lattice, circular-hole [5].

In 1997, Qian, Radistic and Itoh produced a paper which is still considered one of the literature items in the PBG structures [5]. They reported the first comprehensive investigation of synthesized dielectric materials which possess distinctive stopbands for microstrip lines. They performed the first full-wave, comprehensive study of a category of EBG structures which are suitable for microstrip-based circuits and antennas. Four types of these EBG structures had been simulated using FDTD. Fig. 2.3 shows the four types of EBG structures. The EBG holes were drilled through the dielectric substrate, and a conductive tape was applied in the ground plane of the microstrip line.

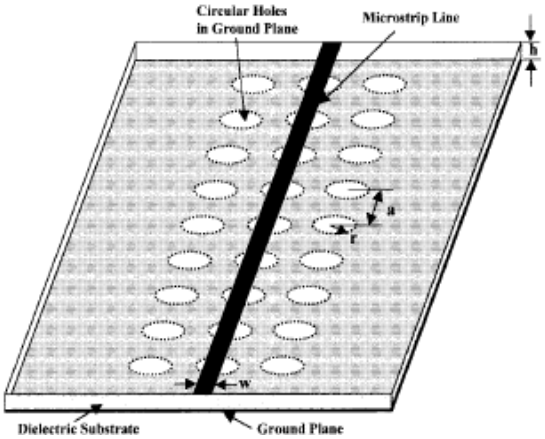

Fig. 2.4. Three-dimensional view of a proposed EBG structure. The square lattice circles are etched in the ground plane of a microstrip line [12].

In February, 1998, the same group, Radisic et al. proposed a two-dimensional (2-D) EBG structure for microstrip lines [12], in which a periodic 2-D pattern consisting of circles was etched in the ground plane of microstrip line. The main advantage of this structure is that no drilling through the substrate was required. Three EBG circuits were fabricated with different circle radii to determine the optimum dimensions. Fig. 2.4 shows the proposed (2-D) EBG structure. The paper provided no analysis for the proposed structure as all the responses were fabricated and measured.

Providing the attractive characteristics of EBG structures and ease of fabrication, many passive and active microwave and millimeter-wave devices have been developed to suppress the harmonics and realize the compact physical dimensions of circuits. Several efforts have been made to realize such devices on various EBG circuits, e.g., a power amplifier with EBG circuits [13], [14], the PBG structure for slow-wave circuits [15], and realization of a magnetic wall in waveguide [16], [17]; their experimental results are sufficient to show the validity of EBG circuit applications. However, in the late 1990's, a lot of researchers recognized that it is difficult to use EBG structures for the design of the microwave or millimeter-wave components due to the difficulties of the modeling. There are too many design parameters, which have an effect on the bandgap property, such as the number of lattice, lattice shapes, lattice spacing, and relative volume fraction. All these modeling problems were the cause of the emergence of the defected ground structures (DGS) [18], [19].

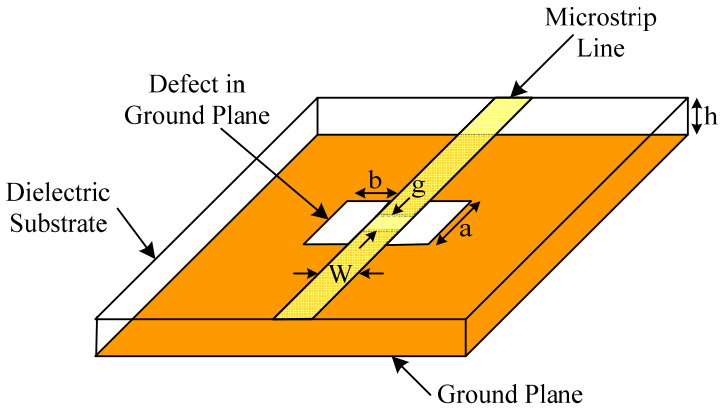

Fig. 2.5 The etched lattice shape of the proposed DGS cell.

Fig. 2.5 shows the etched lattice shape of the proposed DGS section, which is located on the backside metallic ground plane. The proposed DGS unit section can provide cutoff frequencies and attenuation pole in some frequency without any periodic array of DGSs, which facilitated the modeling of the structure.

The advantage of these DGS unit cells is that they are easier to model, and consequently, to use in more complex structures. Different techniques have been invented to model these DGS like parallel *RLC* resonators, or π-sections which all give a simple and good representation for the behavior of these structures [18]-[21].

In the following section, an overview of the most important works that have been done in the domain of electromagnetic bandgap and defected ground structures from the time of their invention till now is given.

2.3. Overview of the Most Important EBG and DGS Works

The overview given here is divided in two parts. The first part deals with the advancements in the electromagnetic bandgap structures, while the second deals with that of defected ground structures. In this section, we will try to present the most inspiring work in this domain, in addition to the latest advancements and developments.

2.3.1. Electromagnetic Bandgap (EBG) Structures

In this section, we will focus on the development of EBG structures, in particular planar EBG structures due to their ease in fabrication and compatibility with Monolithic Integrated Circuit (MIC) and Monolithic Microwave Integrated Circuits (MMIC) technologies. Actually, due to these reasons, most of the development of the EBG structures is on the planar structures to work with microstrip transmission lines and coplanar waveguides.

After the paper published by Radisic et al. in February, 1998 [12], in 1999 two break through papers with two different well-known EBG structures have been studied, the first is the Uniplanar Compact- Photonic Bandgap (UC-PBG) Structure published by Itoh et al. in [17], [21]-[24] and the grounded metallic plates (mushroom) structure published by Yablonovitch et al. in [25].

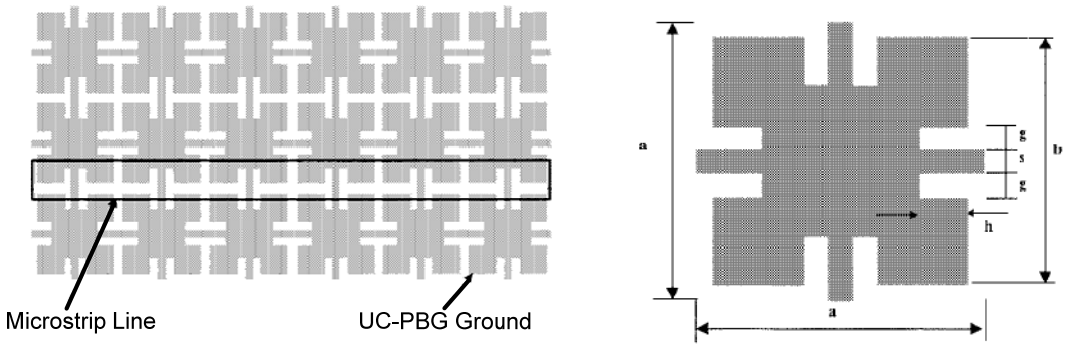

(a) (b)

Fig. 2.6. (a) Schematic of UC-PBG metallic pattern on a dielectric slab. (b) Unit cell of the UC-PBG structure [21].

The UC-PBG structure is a 2-D photonic band gap (PBG) structure for microwave integrated circuits. This structure is a two-dimensional square lattice with each element consisting of a metal pad and four connecting branches as shown in Fig. 2.6 (a) and (b).

Due to the slow-wave effect generated by this unique structure, the period of the PBG lattice is only 0.1 λ_o at the cutoff frequency, resulting in the most compact PBG lattice ever achieved. In the passband, the measured slow-wave factor (β/k_o) is 1.2–2.4 times higher and insertion loss is at the same level compared to a conventional 50Ω-line. Another advantage of this structure is that it can be built using standard planar fabrication techniques without any modification.

Several application examples had been demonstrated, including a non-leaky conductor-backed coplanar waveguide (CB-CWG), a compact spurious-free bandpass filter, TEM waveguides, amplifiers, and Low-pass filters.

The advantage of using this structure over the conventional CB-CPW is that the conventional CPW is often backed with another ground plane to increase mechanical strength, realize mixed CPW microstrip circuits, or to provide a heat sink. The conductor-backed CPW (CB-CPW), however, excites the parallel-plate mode and deteriorates the CPW performance. The energy will leak along a particular angle once the wave is launched. This leakage is significant even at low frequencies, which will cause a severe effect, such as crosstalk, with neighboring circuits. The stopband of a UC-PBG structure are used to suppress the propagation of this parallel-plate mode.

Another application is the compact microstrip bandpass filters (BPFs) with intrinsic spurious suppression. Parallel-coupled microstrip lines are widely used to design bandpass filters (BPF). However, they exhibit spurious passbands at harmonic frequencies, which may degrade overall system performance. This limitation can be overcome by designing the passband of the BPF inside the passband of the UC-PBG, while simultaneously placing the spurious passband of the BPF in the stopband.

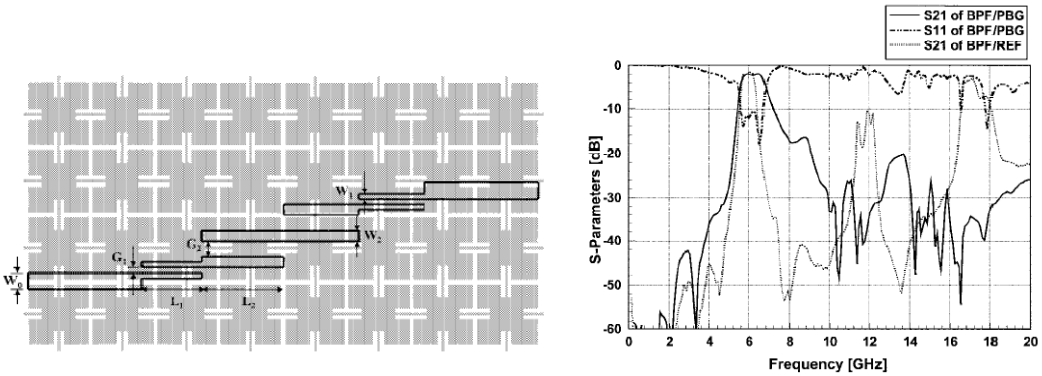

(a) (b)

Fig. 2.7. (a) Schematic diagram and (b) measured insertion loss (S_{21}) of the BPF on UC-PBG ground [26].

Fig. 2.7 shows the schematic diagram and the measured results of the proposed filter compared to that of the conventional edge-coupled filter. It can be seen that the proposed UC-PBG filter exhibits 20 dB to 25 dB spurious rejection in the second and third passband. Moreover, the slow-wave effect reduces the resonator length of the filter integrated with the UC-PBG ground plane by 20% when compared to a conventional filter.

Additional applications, is the spurious-free lowpass microstrip filters. The broad stopband shown by the UC-PBG structure can be exploited to suppress spurious passbands always present in conventional microstrip filters. The sharp cutoff of the UC-PBG structure can also be used to improve the roll-off of a lowpass filter (LPF). The prototype shows stopband attenuation 38 dB better than that of a conventional LPF.

As for active devices, harmonic tuning in power amplifier is also achieved using the UC-PBG structure [28]. Power amplifier is the main power consumption block in any advanced wireless communication system. The most crucial factor in power amplifier design is to increase the power-added efficiency (PAE) and output

power. It is possible to tune both the second and third harmonics in order to achieve higher PAE. The output levels of the second and third harmonics have been reduced from -11 dB and -30 dB to -48 dB and -60 dB, respectively, as compared to a reference amplifier terminated with a standard 50Ω load. A 10% increase in PAE and 1.3 dB increase in output power is also realized.

UC-PBG structure has also proved its advantage for radiating elements and antennas. Patch antennas are usually built on low permittivity substrates for optimum performance, since surface waves are usually excited on high dielectric constant substrate. The stopband provided by the UC-PBG structure can be employed to reduce surface-wave losses of patch antennas on high permittivity substrates. It was seen that excitation of surface waves was strongly reduced in the E-plane and that directive gain at broadside of the UC-PBG antenna was 3-dB higher than that of the reference patch [29].

Rectangular waveguides with uniform field distributions are of great concern for applications in quasi-optical power combining. A TEM-waveguide can be realized by placing perfect magnetic conductor (PMC) on the two sidewalls of a waveguide, creating a magnetic boundary condition to suppress the parallel-plate mode. The UC-PBG structure has already been demonstrated to behave like a PMC within its stopband and therefore can be applied to build a TEM waveguide [17], [30].

Although this UC-PBG structure has demonstrated easy manufacturability, stopband bandwidth through a variety of applications, no detailed study or extraction of an accurate equivalent circuit that explains the field propagation inside the structure has been conducted. All the applications of the structure have been designed using FDTD software, fabricated and measured.

The famous structure that is presented in the same year is the high impedance grounded metallic plates electromagnetic surface, known by the mushroom structure [25]. It consists of an array of metal protrusions on a flat metal sheet. They are arranged in a two-dimensional lattice, and can be visualized as mushrooms or thumbtacks protruding from the surface as shown in Fig. 2.8. The structure is easily fabricated using printed-circuit board technology. The protrusions are formed as metal patches on the top surface of the board, connected to the solid lower conducting surface by metal plated vias. Although it is made of continuous metal, and conducts DC currents, it does not conduct AC currents within a forbidden

frequency band. Unlike normal conductors, this surface does not support propagating surface waves, and its image currents are not phase reversed. The geometry is analogous to a corrugated metal surface in which the corrugations have been folded up into lumped-circuit elements, and distributed in a two-dimensional lattice. The surface was described using solid-state band theory concepts, even though the periodicity is much less than the free-space wavelength.

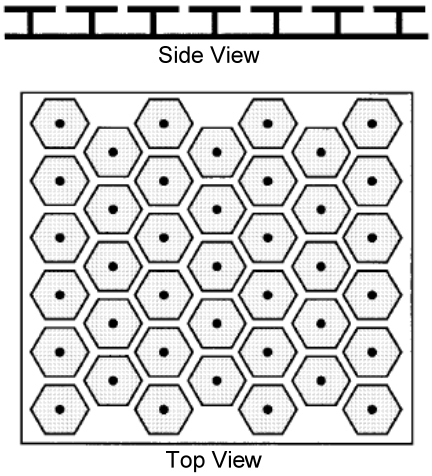

Fig. 2.8. Cross section of a high-impedance surface, fabricated as a printed circuit board. The top view of the high-impedance surface shows a triangular lattice of hexagonal metal plates [25].

The high-impedance surface has proven useful as an antenna ground plane [25]. Using high-impedance ground planes, antennas have been demonstrated that take advantage of both the suppression of surface waves, and the unusual reflection phase. An antenna on a high-impedance ground plane produces a smoother radiation profile than a similar antenna on a conventional metal ground plane, with less power wasted in the backward direction. Furthermore, radiating elements can lie directly adjacent to the high-impedance surface without being shorted out. These antennas can take on a variety of forms, including straight wires to produce linear polarization, or various other shapes to generate circular polarization. Patch antennas are also improved if they are embedded in a high impedance surface.

The high-impedance surface is particularly applicable to the field of portable hand-held communications, in which the interaction between the antenna and the user can have a significant impact on antenna performance. Using this new ground

plane as a shield between the antenna and the user in portable communications equipment can lead to higher antenna efficiency, longer battery life, and lower weight.

In 2001, the interest in the implementation of more compact bandgap structures started to appear while more requirements and degrees of freedom start to impose themselves in the domain. For example, the interest towards the implementation of bandgap structures employing multi-layers in order to achieve more compact and enhanced structure towards better selectivity and further suppression of surface waves started to show up.

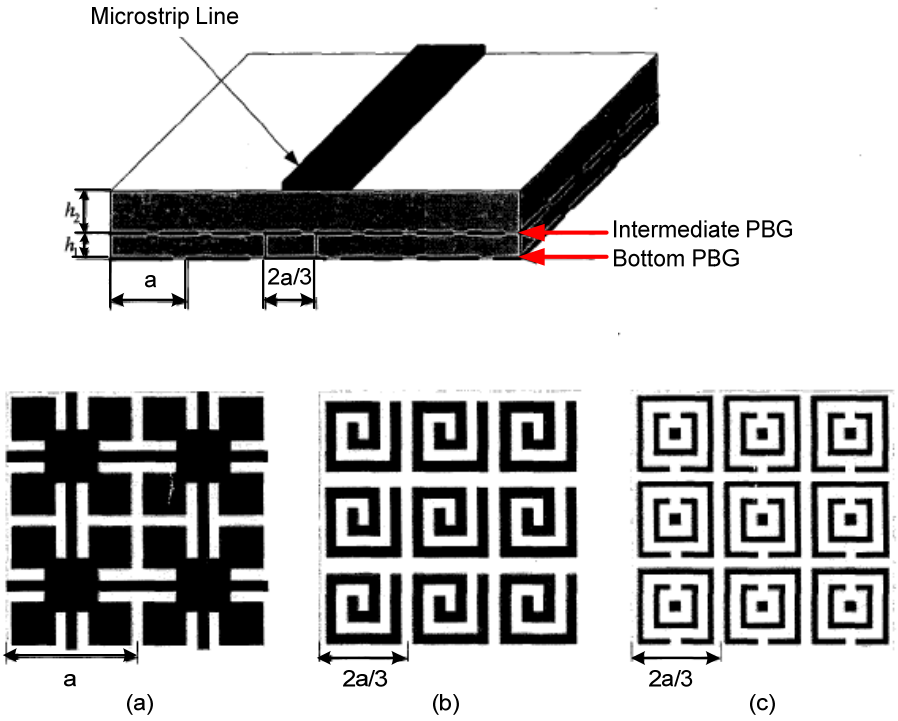

Fig. 2.9. Schematic view of the two layer EBG structure. (a) Bottom UC-PBG configuration, (b) Intermediate bandgap L-configuration, (c) Intermediate bandgap C-configuration [31].

One of the most remarkable papers in this domain is the bi-periodic bandgap structure proposed by Itoh et al. in [31]. It consists of two-layer bi-periodic bandgap microstrip structure, characterized by periods in an inharmonic ratio and by the use of highly reactive elements (printed inductors and capacitors), as shown in Fig. 2.9. The inharmonicity of the periods (a and 2a/3) gives rise to a resulting configuration of larger period (2a) which, in conjunction of the loading effect of the reactive

elements, leads to an extremely low cutoff frequency and makes therefore the structure super compact. Moreover, the existence of three different effective periods, controlling each a different frequency range, yields a huge stopband. Two different configurations, including inductors and capacitor elements in the intermediate plate, were proposed. These structures exhibit a low-pass filter behavior with cutoff frequency corresponding to a=λ/8 and a gap of width exceeding 150% than the UC-PBG structure, presented previously, with an excellent transmission in the passband.

In 2004, the MIT introduced the PBG structure to high power microwave applications [32]. The advantages of using photonic band gap structures in vacuum electron devices and transmission lines were discussed. Actually, the excellent mode selectivity in PBG structures permits them to be employed as over-moded interaction structures in microwave tubes for either high power (>l0 MW) or extremely high frequency (>l00 GHz) operation. A 140 GHz highly over-moded gyrotron oscillator was experimentally demonstrated. The simulations of PBG structures for high power microwave devices were carried out using HFSS. These theoretical results have been used to design a gyrotron device interaction circuit and a 90 GHz, oversized, highly mode-selective PBG waveguide.

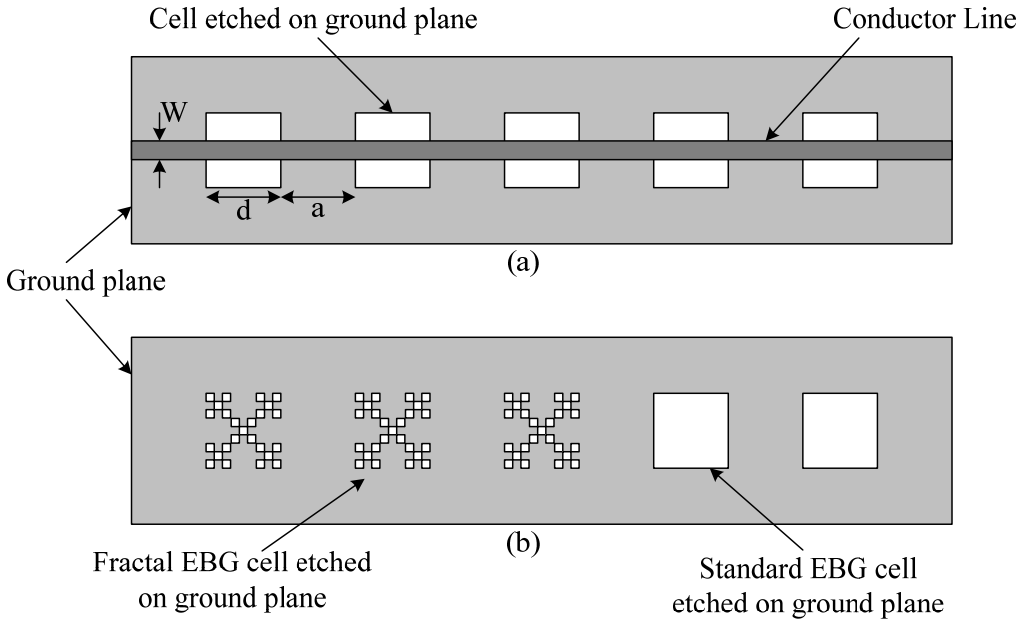

Fig. 2.10. (a) Top view of the standard PBG structure, (b) ground view of the proposed wide stopband PBG structure [26].

In 2006, EBG structures with fractal features were introduced for the first time [26]. The proposed structure has the same size as the conventional EBG structure, but boasts the characteristic of ultra-wide stopband and low ripple level in the passband. Fig. 2.10 (a) and (b) show the top view of the standard square EBG structure and the ground view of the proposed wide stopband EBG structure with fractal features, which is generated by subtracting. Both the standard EBG structure and the fractal EBG structure with different iteration orders were simulated. The proposed fractal EBG structure displays the characteristic of multi-stopband, and the center frequency of the second stopband is twice of the center frequency of the first stopband. With the increase of the iteration order, the bandwidth of the parasitic passband becomes narrower.

From that time on, an enormous number of structures and applications have been introduced for the EBG structures. Most of these new structures are improvements for previously implemented structures which make them more suitable for certain applications. Giving some examples of these new structures, in 2006, another planar EBG scheme was presented for size reduction [27]. The proposed structure can be considered as a kind of distorted uniplanar compact-photonic bandgap (DUC-PBG) but more compact in size. One unit cell of the proposed DUC-PBG, together with that of the conventional UC-PBG, is shown in Fig. 2.11.

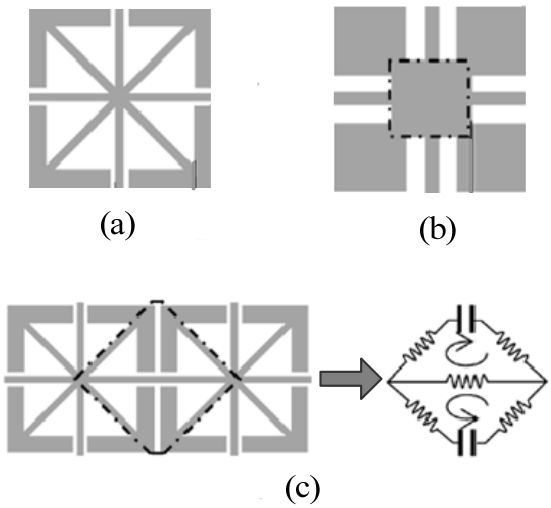

Fig. 2.11. Schematic diagram of the (a) DUC-PBG, (b) conventional UC-PBG, (c) cascaded DUC-PBG [27].

The unit cell of the conventional UC-PBG lattice consists of square pads and narrow lines with insets. The gaps between the conductor edges of two adjacent cells introduce equivalent capacitance (C) and the narrow strips, together with insets at connections, introduce equivalent inductance (L). In order to achieve a more compact structure, the equivalent capacitance and inductance should be increased. The novel DUC-PBG structure is proposed for the demerits mentioned above. The DUC-PBG is just a distorted UC-PBG where the insets have been distorted and introduced into the center part of the pad. As shown in Fig. 2.11 (a), there are only several conductor lines left, therefore the space over the center part has been utilized efficiently. Additional inductances, which are related with the extra magnetic flux flowing around the conductor lines, are introduced in the design. Since both inductance and capacitance per unit cell are increased, a more compact PBG structure has been realized with a lower frequency bandgap.

Also, a number of papers introduced the concept of using spiral structures in the implementation of the EBG structures like [28], and [29]. One of the recent papers which introduces the spiral EBG structures is [30]. In some practical applications, such as in antenna array, the spacing of neighboring antenna element has to be less than a half wavelength of the operating frequency, the mushroom EBG structure is still too large.

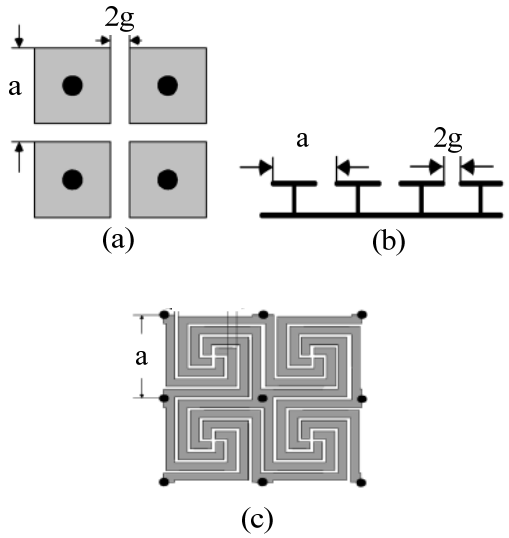

Fig. 2.12. Conventional mushroom EBG (a) top view, (b) side view.
(c) Proposed spiral EBG [30].

In [30], they propose a novel EBG structure, which can be considered as an extension of mushroom EBG structure, and report its application in the antenna field. The structure of spiral-like metal patch is more complicated than other EBGs although it is more compact in size as shown in Fig. 2.12. The simulations and experimental results have proved that the size of the spiral structure is only 30.9% of the conventional EBG structure. Two applications have been introduced, including patch antenna with the spiral EBG structure and a double-element microstrip antenna array with low mutual coupling. The measured results show that a gain improvement over 3 dB and a significant reduction of cross polarization in H-plane are obtained. A 6 dB reduction of mutual coupling is achieved in a double-element EBG microstrip antenna array.

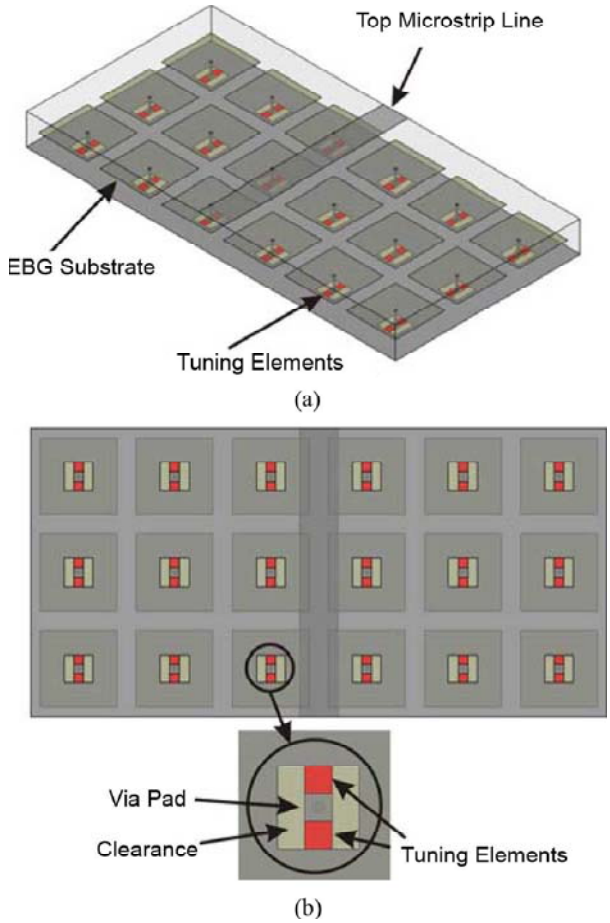

Fig. 2.13 (a) Prospective view and (b) bottom view of tuning element loaded EBG microstrip line [33].

Also another paper which is recently published in this domain is that of Yang et al. in 2009 [33]. In this paper, a novel tunable EBG structure is proposed and applied to a switchable microstrip antenna where a patch proximity fed by an open-end microstrip line is on top of an EBG substrate loaded with arrays of diode switches.

A microstrip line on a tunable EBG structure is shown in Fig. 2.13. The structure consists of a microstrip line etched on top of a dielectric slab, under which there is another dielectric slab with mushroom-like EBG units fabricated on top. These two slabs are laminated together to form a multilayer printed circuit board (PCB). In addition, from the bottom view of the structure in Fig. 2.13, the EBG plate-through vias are not directly connected to the RF ground plane, but rather on square conducting pads with clearance around. With this topology, the tuning device, such as PIN diode switches or varactor diodes, are able to be attached between the RF ground plane and via pads. By changing the states of the tuning devices (open or short circuit), the characteristics of the EBG substrate thus can be varied dynamically, and as a result, the propagation constant of the top microstrip line is electrically tunable.

Using this technique, the microstrip patch antenna operation frequency is dynamically controlled by tuning the EBG substrate characteristics. The switches are in between the EBG vias and the substrate ground plane. When the switches are on, the EBG surface is electrically shorted to the ground through vias and the geometry is almost identical to the EBG loaded microstrip patch. When the switches are off, the EBG surface is disconnected from the ground plane and the EBG surface acts like arrays of floating patches. The novelty here is to tune the printed antenna radiation properties by changing the EBG substrate characteristics rather than the antenna radiating element itself.

In this section, we covered most of the important work done in EBG structures. In the following section, the emergence of DGS and their properties, development and applications are going to be considered.

2.3.2. Defected Ground Structures (DGSs)

As mentioned before, although EBG structures proved itself in the implementation of many structures and applications, the EBG structures suffered from difficulty in their modeling which made their design extremely dependent on

the electromagnetic simulations. On the other hand, the electromagnetic simulation of EBG structures takes very long time on commercial simulation tools due to its complexity and many design parameters. All these disadvantages gave rise to the emergence of the defected ground structures (DGS).

The DGS is a one single defect in the ground plane of microstrip transmission line or coplanar waveguide which is capable of producing a transmission zero in the response of the structure. The resonant frequency of this transmission zero depends on the physical dimensions of the defect. The main advantage of DGS over EBG structures, that they are easier to model and therefore to use in more complex structures than EBG.

The first DGS structure is the well-known dumbbell shaped DGS shown in Fig. 2.5, published in 1998 [34]. Although this is the first paper to introduce the concept of DGS, it categorized the structure as a photonic bandgap unit cell. In this paper, by using the field analysis method, the equivalent circuit of the proposed DGS was derived. Since the electromagnetic simulations of the structure shows an attenuation pole at a certain resonance frequency, the DGS is modeled as parallel *LC* resonance circuit, as will be shown in Chapter four. The equivalent circuit parameters are extracted based on the circuit analysis theory.

In order to show the validity of the proposed DGS and the derived equivalent circuit, two three-pole low-pass filters are designed by employing the proposed PBG structures and the equivalent circuit. Although this paper is a breakthrough in the design of EBG and DGS, it suffered two drawbacks in the design. The first is the losses introduced by the DGS unit cell, especially radiation losses, which are not considered at all in the *LC* model of the DGS cell. The second drawback is the coupling effect that might take place between two adjacent DGS cells in the implementation of a filter.

In 2000, the expression defected ground structures or DGS started to appear for the first time [35], [36]. The first paper using this term is devoted to make a parametric study on the dumbbell shaped DGS [35]. The main aim of this study is to find out which physical dimensions of the introduced defect affect the equivalent parallel inductance and capacitance values. The conclusion of this parametric study is that the etched square area of the dumbbell is responsible for the equivalent inductance while the etched gap beneath the microstrip line is responsible for the equivalent capacitance.

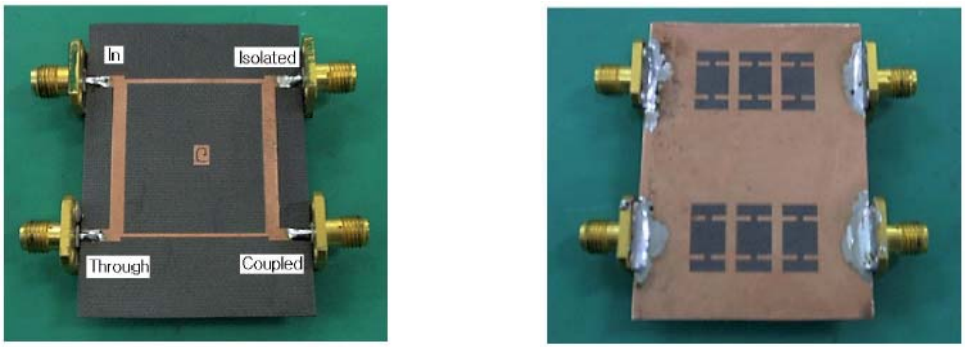

(a) (b)

Fig. 2.14. Photograph of (a) top and (b) bottom sides of the fabricated 90° branch-line coupler with DGS cells [36].

By the end of the same year, the DGSs started to appear in microwave applications. The first application where DGS is introduced is a 10 dB branch line coupler [36]. A photograph of the presented coupler is shown in Fig. 2.14. The authors used the DGS in this case to control the line impedance and therefore to control the conductor width of the microstrip line. In this case, the width of a 150Ω line is five times its conventional case using these DGSs, which facilitate the fabrication process and increases the power handling capability.

DGSs also prove themselves for active devices as EBG structures [37]. In 2001, DGSs have been used for the enhancement of the efficiency of power amplifiers. It has been verified that the microstrip line with DGS has a very wide stopband and therefore may be used for tuning all harmonics in power amplifiers. A power amplifier showed improved output power and power added efficiency 1~5% compared to conventional power amplifiers. For the amplifier with DGS, the second harmonic is not detected up to -45 dBm level at the output.

In both previously mentioned applications, the model or the equivalent circuit used to present the DGS is the parallel *LC* resonant circuit. Although this simplified equivalent circuit is sufficient to perform an initial design of the required application, the structure still needs enhancement on electromagnetic simulation tools to overcome the parameters not considered in the equivalent circuit model.

In 2002, a number of authors started to provide more complex equivalent circuits of the DGS cell, while keeping its simplicity to be able to use these equivalent circuits in more sophisticated structures. The first enhancement that is considered in the equivalent circuit is the radiation loss that is provided by the defect.

This radiation loss is considered in the equivalent circuit by a resistance (*R*) in the parallel *LC* resonator, which converts the structure into a parallel *RLC* resonator. This loss, or this parallel resistance, is considered for the first time in [38] for the harmonic control of active microstrip antenna.

In the same year, a more complicated equivalent circuit is published in [39]. This equivalent circuit is in the form of a π-section. The series part of this π-section is the parallel *RLC* resonator, where the inductance and the capacitance form the resonance circuit and the resistance counts for the radiation loss of the structure. On the other hand, the parallel part consists of a parallel *RC* circuit to represent the relatively large fringing field at the step discontinuity plane on the metallic ground plane of the microstrip line. Although this equivalent circuit is the closest to the physical structure as it takes most of the parameters into account, most of the researchers after that preferred the simple *RLC* resonance circuit, as it is accurate enough for the design process.

It should be mentioned also that till this moment, novel equivalent circuits of the DGSs are emerging everyday considering other parameters like the coupling between adjacent DGSs [40]-[42], and the different conductors and dielectric losses in a quasi-static model for the dumbbell-DGS [41].

In 2005, Lim et al. published a paper which is considered one of the most important building blocks in the development of DGSs [43]. In this paper, the authors generalize the design technique of the three order low pass filter presented before to N-order low-pass filter, and as an example, the complete design procedures of a five order LPF having DGS is demonstrated, with accurate curve fitting results and successive design process. In addition, the proposed LPF with DGS, called a DGS-LPF, included transmission line elements with low impedance instead of open stubs in realizing the required shunt capacitance. The main advantage of this paper is that it proves that the DGSs with its equivalent circuit can be really put into action as a building block of a multistage structure with clear understanding and straight forward design process.

So far, we have given a brief view on the development of the equivalent circuit of DGS. A more detailed understanding of these equivalent circuits with the advantages and disadvantages of each will be given in Chapter Three.

On the other hand, it should be noted that the development of the DGSs was not only in the equivalent circuit model of the structure, but also in the

implementation of novel compact DGSs, and the use of these structures in different applications. Of these structures, there are the U-shaped DGS [43], the arrow-head DGS [44], the multi-layer DGS [45], the cross-head DGS [46], the deformed DGS [47] and others. Each DGS has its advantage either compact size, better rejection skirt, better electric and magnetic coupling between adjacent structures or minimized losses.

The following part of this state of the art of DGS focuses on the development of the DGS in two different directions. The first is the implementation of Multi-band DGSs, while the second direction is devoted for the evolution of the reconfigurable DGSs.

2.3.2.1. Multi-Band DGSs

In this section, we are going to present a number of DGSs that have two or more resonant frequencies. Recently, DGSs which have more than one resonance frequencies started to attract the attention of many researchers. Having more than one resonance that means that using one single defect enables the suppression of multiple undesired harmonics. In addition, structures with multiple harmonics usually have the advantage of better rejection skirt which enables better design of filters.

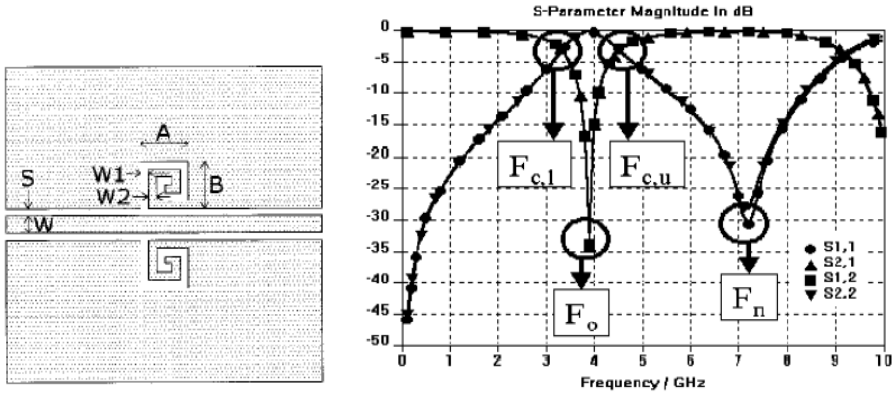

(b)

Fig. 2.15 (a) Layout of the spiral DGS. (b) Its simulated response [48].

Starting from 2002, spiral defected ground structures started to prove itself in a number of articles. Lim et al. suggested this spiral-shaped defected ground structure for CPW (spiral-DGS CPW) [48]. The spiral-DGS CPW is composed of a

standard CPW line and spiral-shaped defected ground structure on both ground planes. Fig. 2.15 (a) shows the unit cell of the proposed spiral-DGS CPW, which has five variable dimensions which are A, B, W1, W2, and the distance between spirals in series. Additionally, the number of turns of defected-slot and number of spiral-DGS elements are factors for determining the characteristics. The shape of spiral is not limited only to rectangle, but circular or octagonal shape can be used. Fig. 2.15 (b) shows the predicted performances for Fig. 2.15 (a). The larger the size of defect, the lower the cutoff frequency as can be expected easily. The required area for spiral-DGS CPW is much smaller than other conventional DGSs for the same frequency response due to the increased equivalent inductance and slow-wave effects. Additionally, the slope of cutoff characteristics is very steep compared to other structures.

Due to the great advantages provided by the spiral-shaped DGS presented previously, Woo and Lee, in 2005, introduced the asymmetric spiral DGS for the suppression of harmonics in Wilkinson power divider [49].

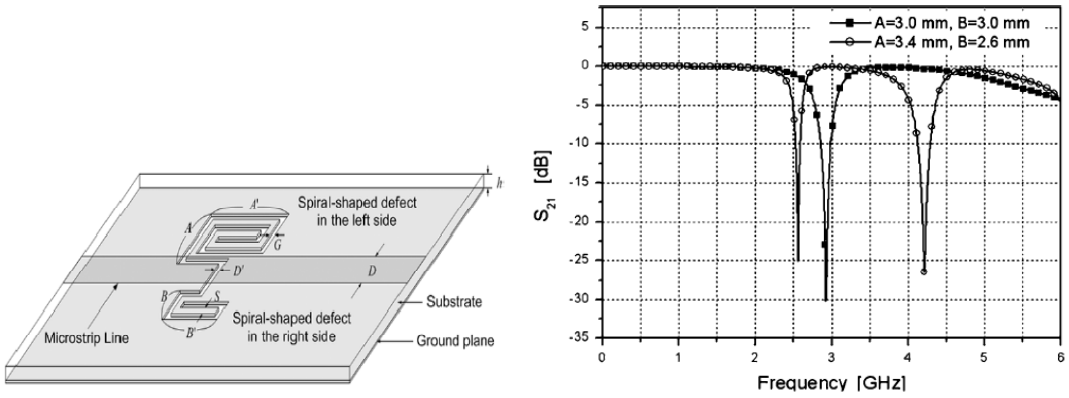

(a) (b)

Fig. 2.16 (a) Layout of the asymmetric spiral DGS. (b) Its simulated response [49].

Fig. 2.16 (a) shows the geometry of an asymmetric spiral DGS on the ground plane of the microstrip line, where the dimensions of the spiral-shaped defects on the right- and left-hand sides are different. For an asymmetric spiral DGS, there are two different resonance frequencies corresponding to the left-hand-side defect and the right-hand-side defect, respectively. The resonance frequencies may be adjusted by changing the dimensions of the spiral defects independently.

The transfer characteristics of the symmetric spiral DGS and asymmetric spiral DGS are compared in Fig. 2.16 (b). For the symmetric spiral DGS there is one resonance frequency. However, when the DGS becomes asymmetric, the resonance frequency splits into two different frequencies. For an asymmetric DGS, it can be seen that there are two different resonance frequencies. In the same paper, it is illustrated that by the insertion of asymmetric spiral DGS into a quarter-wave line of the Wilkinson power divider; the second and third harmonics are suppressed simultaneously. In experimental results, 18-dB suppression for the second harmonic and 15-dB suppression for the third harmonic, respectively, are achieved using one single defect in the ground plane. In addition, the size of a quarter-wave line is reduced by 9.1% compared to that of the conventional divider without a DGS.

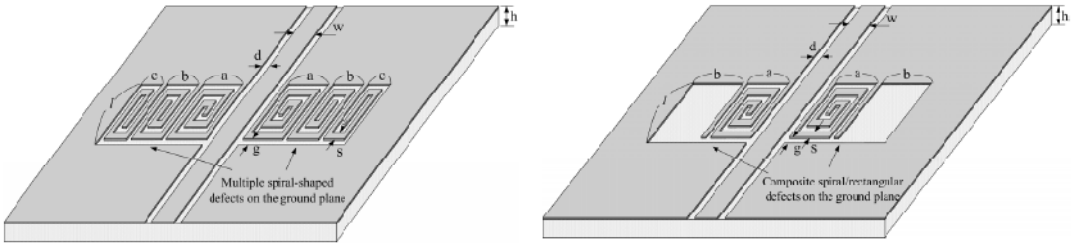

(a) (b)

Fig. 2.17. (a) SS-DGS with three pairs of defects on the ground plane of the CPW. (b) CPW with composite spiral-rectangular DGS [50].

The single asymmetric DGS effectively suppresses two frequency bands and it requires a small area. However, the asymmetric spiral DGS provides only two different resonance frequencies by its limited configuration. Recently, in 2008, a newly developed stacked spiral DGS and composite spiral-rectangular DGS to provide multi-band rejection properties have been published [50]. Fig. 2.17 (a) shows the schematic of the stacked spiral DGS (SS-DGS) pattern etched on the ground plane in both sides of a coplanar waveguide. The proposed SS-DGS, in which the defects on the ground plane consist of three spirals aligned in the transverse direction to the coplanar waveguide, is symmetric and provides three different resonance frequencies due to the fact that each spiral defect has different size. Because the sizes of defect-pair decrease to the outer direction, the resonance frequency due to the closest defect to the signal line is lower than the others, as can be expected easily.

On the other hand, it is well known that the conventional dumbbell-shaped DGS has wide band-gap property while the attenuation pole of the spiral shaped DGS shifts much lower than that of the dumbbell shaped DGS in the same occupied defect area. In the same paper, the composite spiral-rectangular DGS (CSR-DGS), which has two frequency characteristics of the dumbbell- and spiral shaped DGS, is presented. In the CSR-DGS, the spiral- and the rectangular-shaped defects are stacked in same unit, as shown in Fig. 2.17 (b), benefiting from the advantages of both structures.

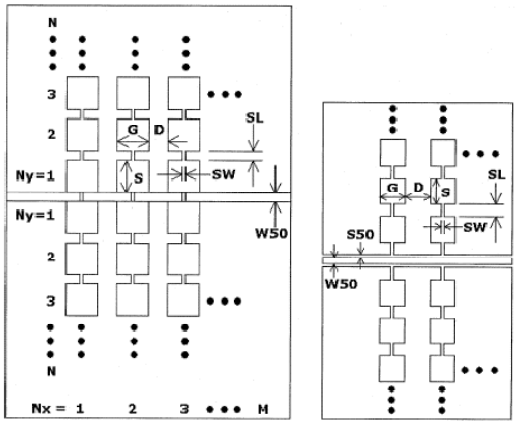

Fig. 2.18. The proposed VPDGS (a) Microstrip line, (b) CPW [51].

In parallel with the evolution of the spiral DGS, a number of articles were published to achieve dual resonance by applying simple modifications on the conventional dumbbell DGS.

In December 2002, the vertically periodic defected ground structure has been proposed by Lim et al. [51]. The prominent feature of the proposed structure is that it is possible to organize the periodicity along the vertical direction as well as the horizontal direction. On the other hand, the conventional PBG and DGS for planar transmission lines have the only horizontally periodic (HP) structure, i.e., serially cascading structure along the transmission direction. In addition vertically periodic (VP) structures produce much higher slow-wave factor (SWF) than conventionl structures. Fig. 2.18 (a) and (b) show the generalized structure of the proposed VPDGS on the ground planes of the microstrip and CPW lines. N_x and N_y mean the number of periodic defects along the horizontal and vertical direction, respectively.

VPDGS is the extended DGS along the vertical direction from the basic dumb-bell shape structure, which was previously presented.

It should also be noted that the SWF grows rapidly by increasing the number N_y for the fixed N_x, although the frequency dispersion is also proportional to N_x and N_y. However, the dispersion, impedance variation, and loss problems are getting serious only at high-frequency region around the resonance or higher. Hence, those problems at the desired application frequency can be avoided by selecting proper substrate and dimensions because the resonant frequency depends on the dielectric material and the dimensions of VPDGS.

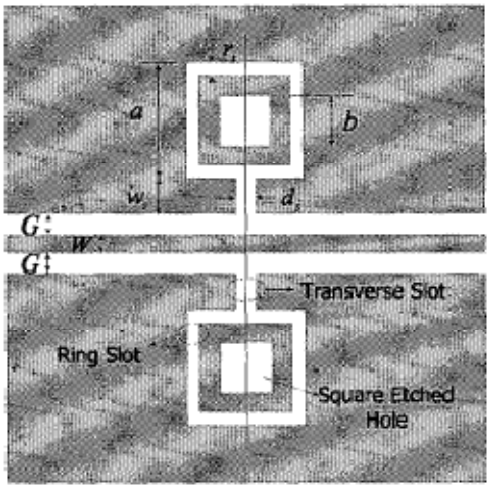

Fig. 2.19. One unit cell of proposed CPW DGS structure [52].

In 2004, another modification was introduced to the conventional dumbbell-DGS to produce multi-resonance [52]. The proposed structure is shown in Fig. 2.19. In proposed CPW DGS unit cell, a ring slot was etched in the ground plane. The ring slot is connected to the gap by a narrow transverse slot. In addition, a square etched hole is etched in the center of the ring slot. When the ring slot side length equates to the side length of the square etched hole (a=b), the ring slot and the square etched hole will then merge to form a square aperture. When that happens, the unit cell becomes the conventional unloaded CPW PBG structure. The proposed CPW DGS structure includes a ring slot and a square etched hole and hence, it is named as a loaded CPW PBG structure. However, as can be clearly noticed that from the EM simulation results of a typical loaded CPW DGS cell, there exists two resonant frequencies.

This structure has two basic advantages over the conventional dumbbell DGS; first, the structure has two resonance frequencies instead of only one single resonance; second, the structure has more degrees of freedom in its design.

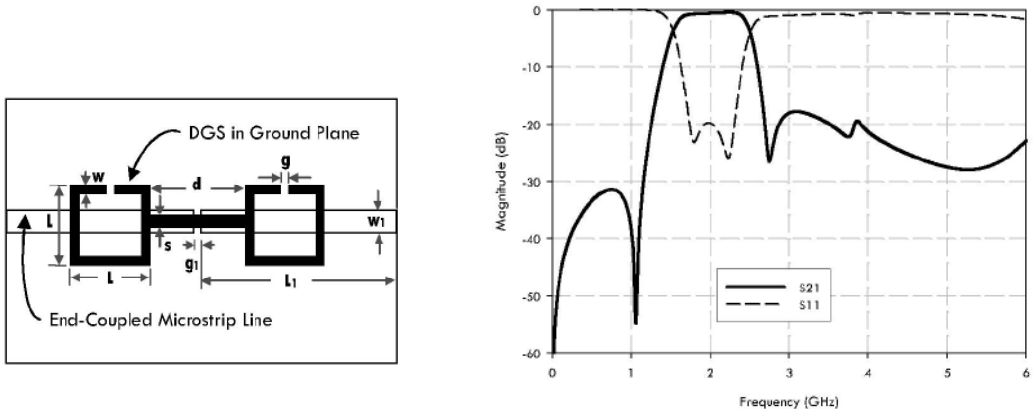

(a) (b)

Fig. 2.20. (a) Open-loop dumbbell-shaped bandpass DGS unit.
(b) Bandpass characteristic with finite transmission zeros [53].

Another structure that is considered one of the most innovative structures presented is the open-loop dumbbell-shaped DGS published in 2006 [53]. The proposed open-loop dumbbell-shaped bandpass DGS unit is shown in Fig. 2.20 (a). It has a pair of end-coupled microstrip lines with equal-length on the top and a dumbbell-shaped outline symmetrically etched in the ground plane. The etched pattern consists of two identical square-loops having open-loop edge length (L) together with open-ends (g) and a slot-line (named dumbbell-arm) connecting between them. In this configuration, the dumbbell-arm is aligned with the microstrip line on the top. In contrast to the conventional dumbbell DGS configurations, this DGS unit has a 90° difference in the geometrical orientation.

The simulation result is illustrated in Fig. 2.20 (b). As seen from the simulated responses, the structure gives three different transmission zeros. The first zero is at DC and it is obtained by the end-coupled microstrip line. Beside the zero at DC, the passband of the filter is bounded by two finite transmission-zeros. These two zeros can be varied by the DGS dimensions. Investigating the response of the structure, we may say that it offers a quasi-elliptic bandpass characteristic bounded by dual finite controllable transmission-zeros. It is found that these two zeros can be controlled by the DGS dimensions, so that BPFs with different center frequencies

and bandwidths can be easily designed. All these advantages are done by one single defect in the ground plane.

There are many other structures that have been published regarding multi-band DGS. In this state of the art, we have mentioned only some of these structures. Some other multi-band structures developed into reconfigurable structures using different reconfigurability elements such as PIN diodes, varactor diodes, or MEMS switches. In the next section, we will focus on this type of reconfigurable structures and their development.

2.3.2.2. Tunable and Reconfigurable DGSs

When defected ground structures proved itself as a promising building block in many applications, a number of researchers started towards the implementation of reconfigurable or tunable DGS. Although the work that has been published in this domain is not much, the achievements in terms of reconfigurable structures are relevant. In this section, we are going to show some of this work and its advancement.

The first two reconfigurable DGSs appeared in 2005. The first is by Kim et al. from the Korea University, for the implementation of tunable bandstop filter [54] and the other by Mansour et al. from Waterloo University, for the implementation of a tunable lowpass filter [55]-[56].

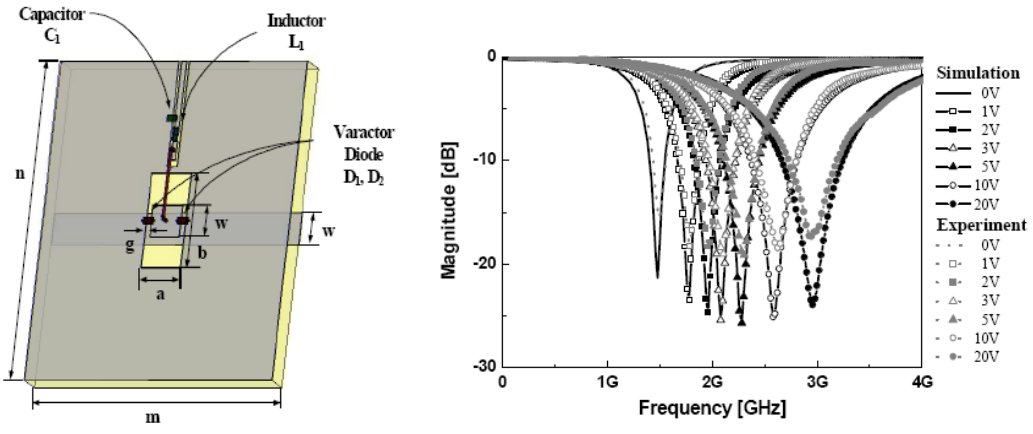

(a) (b)

Fig. 2.21 (a) The proposed DGS, (b) its simulated response [54].

The first to discuss is the tunable bandstop filters using DGS reported in [54]. To adjust the stopband, voltage controlled variable capacitor diodes (VVC) are equipped on the DGS section. The proposed structure is depicted in Fig. 2.21 (a). In Fig. 2.21 (b), the simulated and measured results are shown. Two VVC diodes are placed on the two gaps. Such a structure may be explained as follows. In general, a conventional DGS cell is modeled as a resonant cell which is composed of parallel inductance and parallel capacitance. If either both of them or one is changed, the frequency response can be changed. The gap on the DGS is treated as a parallel capacitor. The VVC diode on the gap also acts as a parallel capacitor, so the total capacitance is increased. By adjusting the reverse voltage, the total capacitance is varied and the frequency response is also changed.

The disadvantage of such a structure is the wire bonding to bias, as more places is needed and the inner resistances of VVC diodes make undesired effect such as lower quality factor and inner power consumption.

The second tunable DGS is the folded slots DGS presented by Zhang and Mansour [55]. The same structure is then represented with complete explanation and equivalent circuit in 2007 [56]. These articles present a new technique for implementing tunable lowpass filters by employing slot resonators etched in the ground plane [55]. When RF MEMS switches are used to short-circuit the slots in the ground plane, the effective length of the slots can be varied to achieve tunability at discrete frequencies.

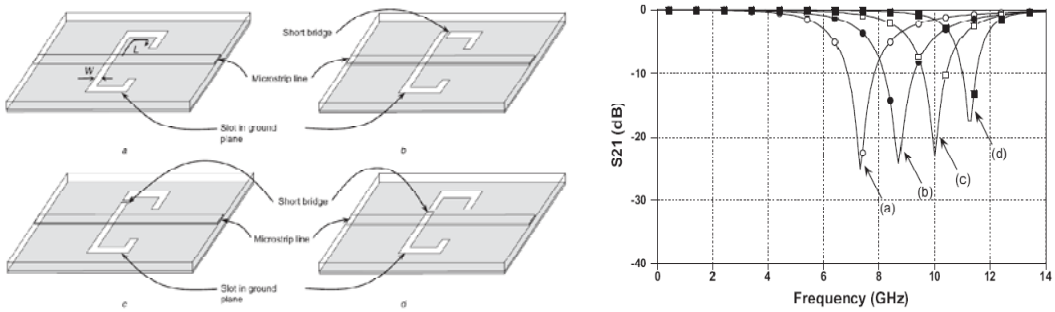

(a) (b)

Fig. 2.22 (a) Schematic of slot resonator. (b) Simulation results [55].

Fig. 2.22 (a) illustrates three configurations of the structure where short bridges are placed across the slot at different locations. The RF performance of these structures is also shown in Figs. 2.22 (b). It can be seen clearly that, on moving the short bridge from the slot edge, the corresponding resonances are shifted to higher frequencies demonstrating a tuning range of 4 GHz.

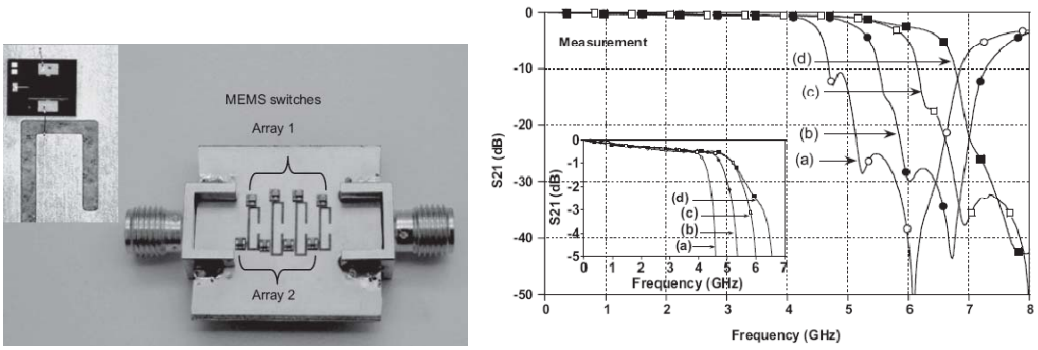

(a) (b)

Fig. 2.23 (a)Photograph of the digital tunable LPF. (b) Measured results.

The proposed concept is used to design higher-order digital tunable lowpass filters [56]. A higher-order lowpass filter can be achieved by cascading a specific number of slot resonators. In principle, if switches are used on the slots of the filter instead of the short bridges, it is expected that the cutoff frequency of the filter can be digitally adjusted by activating the switches between their ON and OFF states. In addition, increased flexibility in the tuning range of the filter is achievable by an appropriate combination of the ON/OFF states of the switches. Fig. 2.23 (a) shows a photograph of the fabricated digital tunable lowpass filter loaded with two arrays of switches, four for each array. This design leads to a switched tunable filter with 4 states. The simulated and measured S-parameters of the tunable filter are shown in Fig. 2.23 (b). The experimental results show a broad tuning range of 2 GHz.

In 2006, Karim et al. started using vertically periodic DGSs (VPDGSs) to produce a reconfigurable bandpass/bandstop filter at the same frequency [57]. The reconfigurable filter structure consists of three unit cells designed in a CPW configuration as shown in Fig. 2.24. PIN diodes are used for switching from bandpass to bandstop filter. The measurement results are shown in Fig. 2.25 (a) and (b). It shows that when diode is off, then a band pass filter is operating at 7.3 GHz

and when the diode is switched ON, the top transverse slot and bigger square slot, b will be shorted to ground, and it will show a bandstop characteristic.

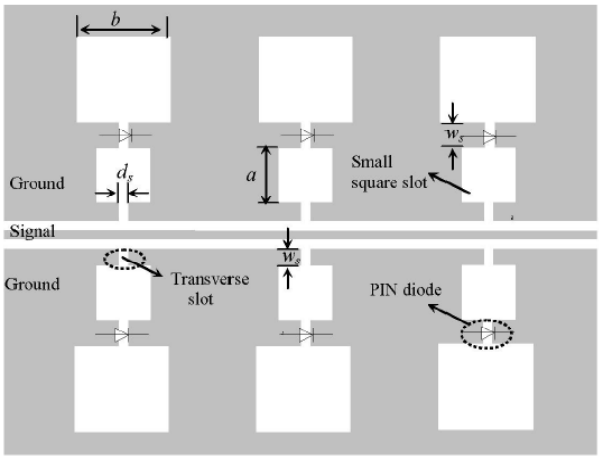

Fig. 2.24. Schematic of the Reconfigurable Structure [57].

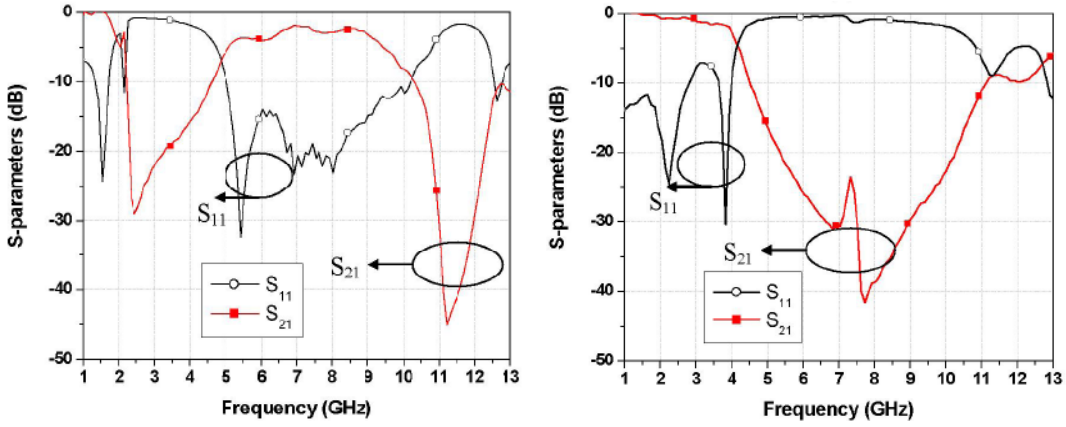

(a) (b)

Fig. 2.25. Measurement results of the reconfigurable filter (a) PIN diode is OFF, bandpass filter. (b) PIN diode is ON, bandstop filter [57].

Using the same structure explained above, reconfigurability may be done using MEMS switches instead of PIN diodes [58]. The tunable filters based on the MEMS switching technique offer several advantages in terms of low loss, low power consumption, high linearity, and small size compared to other varactor devices.

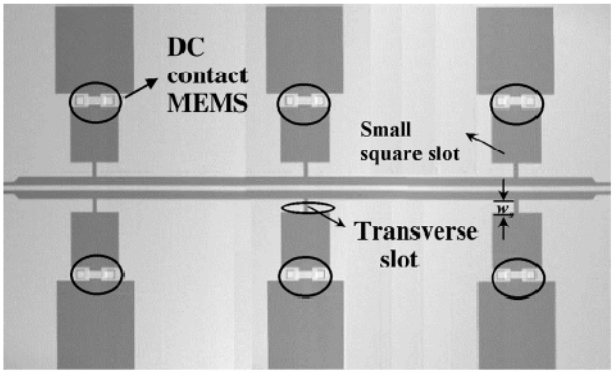

Fig. 2.26. Photograph of the reconfigurable filter with MEMS switches [58].

A photograph of the fabricated structure is shown in Fig 2.26. The reconfigurable filter is fabricated using gold material. The reconfigurable filter structure with DC contact MEMS switches is fabricated for 50Ω of the CPW transmission line. The switch resistance is 1Ω and the up-state capacitance is 50 fF. For providing the DC voltage, the bias lines are designed and have a resistance of 1 kΩ. The MEMS switch is used as a metal-to-metal contact and is used for switching from the bandpass to bandstop filter.

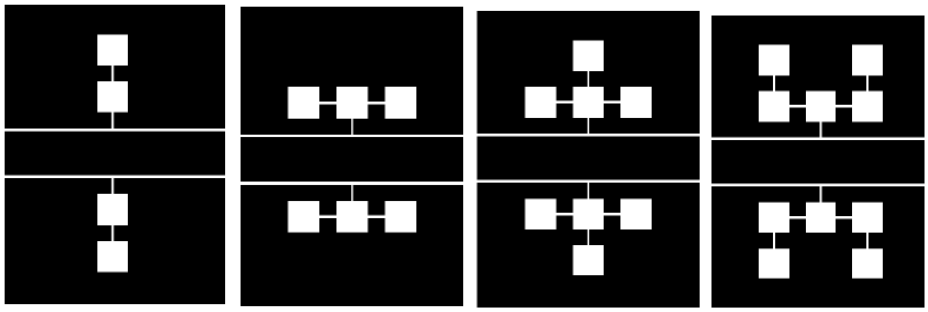

Fig. 2.27. Schematic diagram of the proposed periodic DGS with 2-cells, 3-cells, 4-cells, and 5-cells [60].

In 2006, another MEMS reconfigurable DGS resonator, using two-dimensional (2-D) periodic DGS for CPW and RF MEMS series-resistive switches, is reported [59]. The periodic DGS structure is based on the standard dumbbell structure and is reported for the first time in 2005 [60].The cells are added such that the symmetry along the axes of the dumbbell is kept unchanged. Thus, for the two-cells structure, the cell is added above cell one. For three-cells, two-cells are placed to the left and to the right of the original cell. The same process is applied for larger number of cells. The schematic diagrams of 2, 3, 4, 5-cells are shown in Fig. 2.27.

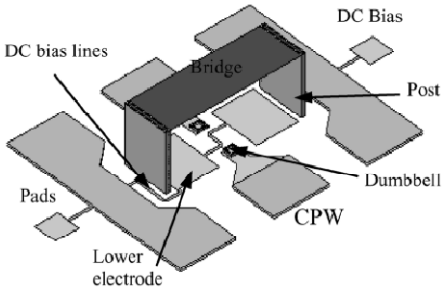

(a)

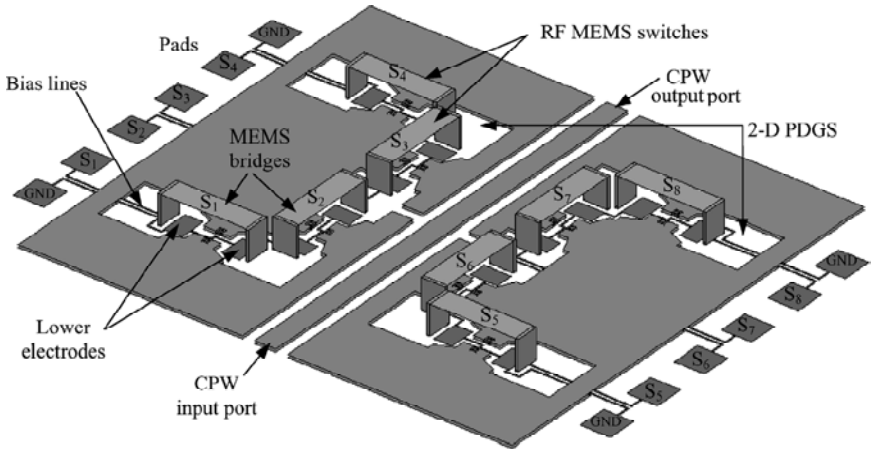

(b)

Fig. 2.28. (a) Schematic diagram of fixed-fixed beam RF MEMS series-resistive switch [60].

In 2006, these periodic DGS are converted by the same group to reconfigurable structures using MEMS switches. Fig. 2.28 (a) shows the schematic diagram of the fixed-fixed beam, series-configured, and resistive-contact RF-MEMS switch, which has been investigated in [61] and used by [60]. These switches are combined with the 2D periodic DGS as shown in Fig. 2.28 (b). It consists of five cells of the 2-D PDGS in CPW environment and eight RF MEMS series-resistive switches based on fixed-fixed beam to cover the whole K-band for automotive applications and transceivers. The substrate used is high-resistivity silicon coated by a SiO_2 layer. The bridge of the MEMS switches is made of Au to improve the mechanical and electrical performances.

Having eight switches, which can be actuated individually, 28 states can be principally obtained. However, because the structure has vertical and horizontal symmetries, only 26 states are available. It should be mentioned here that when all

switches are actuated, the defected ground structure would be nearly completely destroyed and the total structure behaves as a simple coplanar transmission line, i.e., there is no filter resonance in this case.

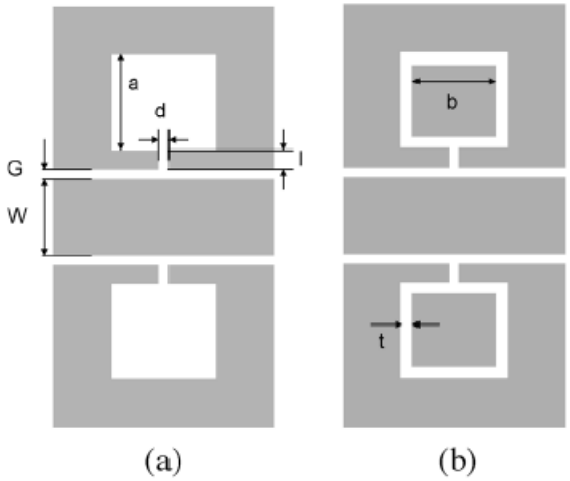

Fig. 2.29. Schematic diagram of: (a) conventional dumbbell-shaped DGS, (b) modified dumbbell-shaped DGS [62].

Another tunable structure that is published in 2006 and is cited by a number of publications in the same domain is the modified-DGS or M-DGS [62]. In the M-DGS, shown in Fig. 2.29 (b) instead of removing the metal from inside the defect, only a strip of width *t* is removed along the circumference keeping a smaller metal square (patch) inside the defect. Both structures were simulated and fabricated using the same dimensions, which show that the conventional DGS and M-DGS have the same response with a slight shift in the central frequency.

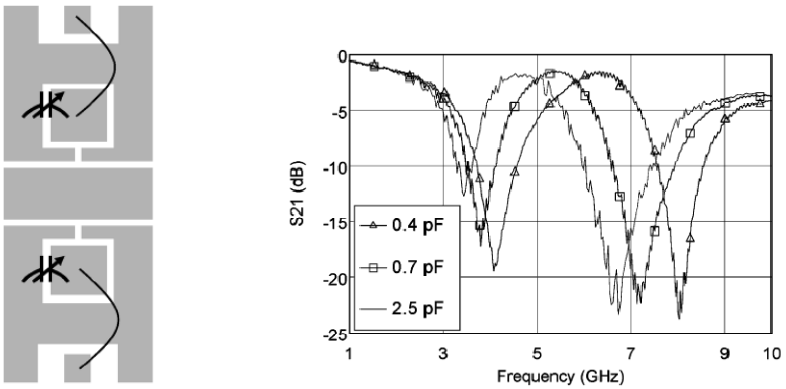

Fig. 2.30 (a) Schematic of the tunable bandstop filter. (b) Measured response of the M-DGS with the capacitors [62].

The advantage of using such a structure is that tunability of the M-DGS can be achieved if a reconfigurability element is added between the patch and the ground plane as shown in Fig. 2.30 (a). However, in this case, the resonance frequency will not be determined by the DGS only, but by the combination of the equivalent circuit of the DGS and the equivalent circuit of the varactors. Bias is provided through a wire bonding that connects the bias pad to the patch. As an alternative, bias can also be provided by connecting the patch to a thin metal strip, which can be realized on the bottom plane of the substrate and carries the bias through the vias. Fig. 2.30 (b) shows measured response.

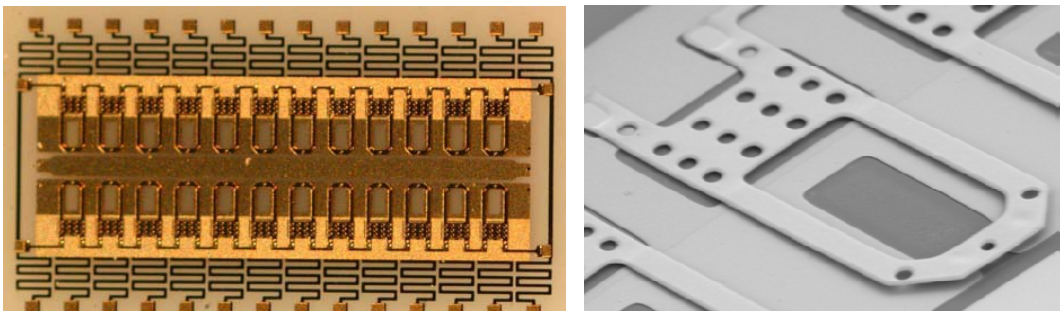

(a) (b)

Fig. 2.31. (a) Picture of the fabricated reconfigurable impedance matching network. (b) SEM image of the MEMS series-contact switch.

The last work that should be added to this state of the art is the structure reported in [63]. The novelty of this structure is not in its proposed DGS unit cell, on the contrary it uses the conventional dumbbell-DGS, but in the reconfigurability element and in the proposed application. In this work, a novel approach for developing RF MEMS impedance matching networks and tuners using periodic DGSs is presented. Unlike existing designs, the proposed structure employs MEMS series-contact type switches on the CPW ground planes which do not suffer from self-actuation. The insertion loss of the tuner is also limited by only the loss of the transmission line and not the number of MEMS tuning elements used for the maximum impedance coverage. The application of DGSs results in an improved insertion loss and power handling capability compared to the conventional RF MEMS impedance tuning networks. The proposed structure consists of 12 DGSs and RF MEMS series-contact switches producing 4096 (2^{12}) impedance states. The tunable matching network was fabricated on an alumina substrate and is only 1.3×3.6

mm in size. The measured results demonstrate wide coverage of the Smith chart with a maximum VSWR of 12:1 at 60 GHz. The measured loss of the network when used to match a 10 Ω load to 50 Ω from 22 GHz up to 40 GHz is only 0.5 dB. A photograph of the fabricated structure is shown in Fig. 2.31.

2.4. Conclusion

In this chapter, we presented the state of the art of electromagnetic bandgap (EBG) and defected ground structures (DGS). As much as possible, we tried to cover all the main topics and the important work that have been published so far in this domain. The chapter started by defining what is meant by bandgap structures and their evolution in the microwave domain after their invention in the optical domain. Then, the most important work that has been published from that time till now was covered. No doubt that bandgap structures are progressing everyday towards better equivalent circuit models and better characteristics that make them good candidates for many applications.

In the following chapters, more details regarding the different numerical techniques towards the investigation of bandgap structures, and the different equivalent circuit models and their extraction will be discussed.

References of Chapter Two

[1] E. Yablonovitch, "Photonic band-gap structures," *J. Optical Soc. America B*, Vol. 10, No. 2, pp. 283–295, Feb. 1993.

[2] J. D. Joannopoulos, R. D. Meade, and J. N. Winn, "Electromagnetic modeling for microwave imaging of cylindrical buried inhomogeneities," *Photonic Crystals*, Princeton Univ. Press, Princeton, NJ, 1995.

[3] D. F. Sievenpiper, M. E. Sickmiller, and E. Yablonovitch, "3D wire mesh photonic crystals," *Phys. Rev. Lett*., Vol. 76, No. 14, pp. 2480–2483, Apr. 1996.

[4] J. Shumpert, T. Ellis, G. Rebeiz, and L. Katehi, "Microwave and millimeter wave propagation in photonic band-gap structures," *Proceeding of Ant. Prop. Symp. (AP-S)*, p. 678, 1997.

[5] Y. Qian, V. Radisic, and T. Itoh, "Simulation and experiment of photonic band-gap structures for microstrip circuits," *Proceeding of Asia-Pacific Microw. Conf. (APMC)*, pp. 585–588, 1997.

[6] E. R. Brown, C. D. Parker, and E. Yablonovitch, "Radiation properties of a planar antenna on a photonic-crystal substrate," *J. Optical Soc. America B*, Vol. 10, No. 2, pp. 404–407, Feb. 1993.

[7] M. M. Sigalas, R. Biswas, and K. M. Ho, "Theoretical study of dipole antennas on photonic band-gap materials," *Microwave Opt. Technol. Lett.*, Vol. 13, No. 4, pp. 205–209, Nov. 1996.

[8] H. Y. D. Yang, N. G. Alexopoulos, and E. Yablonovitch, "Photonic band-gap materials for high-gain printed circuit antennas," *IEEE Trans. Ant. Prop.,* Vol. 45, No. 1, pp.185–187, Jan. 1997.

[9] R. D. Meade, K. D. Brommer, A. M. Rappe, and J. D. Joannopoulos, "Photonic bound states in periodic dielectric materials," *Phys. Rev. B.,* Vol. 44, No. 24, pp. 13772–13774, Dec. 1991.

[10] C. C. Chang, Y. Qian, and T. Itoh, "Analysis and applications of uniplanar compact photonic band gap structures," *Progress In Electromagnetics Research (PIERS)*, Vol. 41, pp. 211–235, 2003.

[11] C. K. Wu, H. S. Wu, and C. K. C. Tzuang, "Electric–magnetic–electric slow-wave microstrip line and bandpass filter of compressed size," *IEEE Trans. Microw. Theory Tech.,* Vol. 50, No.8, pp.1996-2004, Aug. 1999.

[12] V. Radisic, Y. Qian, R. Coccioli, and T. Itoh, "Novel 2-D Photonic Bandgap Structures for Microstrip Lines," *IEEE Microw. Guided Wave Lett.,* Vol. 8, No. 2, pp.69-71, Feb., 1998.

[13] V. Radisic, Y. Qian, and T. Itoh, "Broadband power amplifier using dielectric photonic bandgap structure," *IEEE Microwave Guided Wave Lett.,* Vol. 8, No. 1, pp. 13–14, Jan. 1998.

[14] V. Radisic, Y. Qian, and T. Itoh, "Broad-band power amplifier integrated with slot antenna and novel harmonic tuning structure," *Proceedings of IEEE MTT-S Int. Microwave Symp. Dig.*, pp. 1895–1898, June 1998.

[15] F. R. Yang, Y. Qian, R. Coccioli, and T. Itoh, "A novel low loss slow-wave microstrip structure," *IEEE Microw. Guided Wave Lett.,* Vol. 8, No. 11, pp. 372–374, Nov. 1998.

[16] K. P. Ma, K. Hirose, F. R. Yang, Y. Qian, and T. Itoh, "Realization of magnetic conducting surface using novel photonic bandgap structure," *Electron. Lett.,* Vol. 34, No. 21, pp. 2041–2042, Nov. 1998.

[17] F. R. Yang, K. P. Ma, Y. Qian, and T. Itoh, "A novel TEM waveguide using uniplanar compact photonic-bandgap (UC-PBG) structure," *IEEE Trans. Microw. Theory Tech.,* Vol. 47, No. 11, pp. 2092–2098, Nov. 1999.

[18] C. S. Kim, J. S. Park, D. Ahn, J. B. Lim, "A novel 1-D periodic defected ground structure for planar circuits," *IEEE Microw. Wireless Comp. Lett.,* Vol. 10, No. 4, pp. 131 – 133, April 2000.

[19] J. S. Lim, C. S. Kim, J. S. Park, D. Ahn, S. Nam, "Design of 10 dB 90° branch line coupler using microstrip line with defected ground structure," *Electron. Lett.,* Vol. 36, No. 21, pp. 1784 – 1785, Oct. 2000.

[20] I. Chang and B. Lee, "Design of defected ground structures for harmonic control of active microstrip antenna," *Proceedings of IEEE Ant. Prop. Symp. (AP-S),* Vol. 2, pp.852-855, June 2002.

[21] F. R. Yang, K. P. Ma, Y. Qian, and T. Itoh, "A uniplanar compact photonic-band gap (UC-PBG) structure and its applications for microwave circuits," *IEEE Trans. Microw. Theory Tech.,* Vol. 47, No. 8, pp. 1509–1514, Aug. 1999.

[22] F. R. Yang, Y. Qian, and T. Itoh, "A novel uniplanar compact PBG structure for filter and mixer applications," *Proceedings of IEEE MTT-S Int. Microw. Symp. Dig.,* pp. 919–922, Anaheim, CA, June 1999.

[23] C. Hang, V. Radisic, Y. Qian, and T. Itoh, "High efficiency power amplifier with novel PBG ground plane for harmonic tuning," *Proceedings of IEEE MTT-S Int. Microw. Symp. Dig.*, pp. 919–922, Anaheim, CA, June 1999.

[24] R. Coccioli, F. R. Yang, K. P. Ma, and T. Itoh, "Aperture coupled patch antenna on UC-PBG substrate," *IEEE Trans. Microw. Theory Tech.*, Vol. 47, No. 11, pp. 2123–2130, Nov. 1999.

[25] D. Sievenpiper, L. Zhang, F. J. Broas, N. G. Alexopolous, and E. Yablonovitch, "High-impedance electromagnetic surface with a forbidden frequency gap," *IEEE Trans. on Microw. Theory Tech.*, Vol. 47, No. 11, pp. 2059-2074, Nov. 1999.

[26] W. Chen, G. Wang, Y. Qi and J. Liang, "A novel wide stopband PBG structure with fractal features and its application to the design of microstrip low-pass filter," *Proceedings of Int. Symp. Ant., Prop. & EM Theory (ISAPE)*, Oct. 2006 .

[27] B. Lin, Q. Zheng and N. Yuan, "A novel planar PBG structure for size reduction," *IEEE Microw. Wireless Comp. Lett.,* Vol. 16, No. 5, pp. 269–271, May 2006.

[28] O. IsiK, Y. Ge, and K. Esselle, "Novel spiral EBG structure," *Proceedings of Int. Symp. Ant. Tech. Applied Electromagnetics (ANTEM)*, Montreal, Canada, pp. 561–564, July 2006.

[29] F. Q. Shan and B. X. Gao, "Novel compact photonic bandgap structures using rectangular increasing distance spiral slots," *Microw. Optical Technol. Lett.,* Vol. 43, No. 6, pp. 537–539, Dec. 2004.

[30] Q. R. Zheng, Y. Q. Fu and N. C. Yuan, "A novel compact electromagnetic band-gap (EBG) structure," *IEEE Trans. Ant. Prop.,* Vol. 56, No. 6, June 2008.

[31] C. Caloz, C. Chang, Y. Qian and T. Itoh, "A novel multilayer photonic band-gap (PBG) structure for microstrip circuits and antennas," *Proceedings of IEEE Ant. Prop. Symp., Vol. 2, pp. 502 - 505, July 2001*.

[32] M. A. Shapiro, C. Chen, J. R. Sirigiri, E. I. Smirnova and R. J. Temkin, "Photonic bandgap structures for high power microwave applications," *Proceedings of IEEE MTT-S Int. Microw. Symp. Dig.,*Vol. 2, pp.1005–1008, June 2004.

[33] J. Liang and H. Y. David Yang, "Microstrip patch antennas on tunable electromagnetic bandgap substrates," *IEEE Trans. Ant. Prop.,* Vol. 57, No. 6, pp. 1612-1617, June 2009.

[34] J. I. Park, C. S. Kim, J. Kim, J. S. Park, Y. Qian, D. Ahn, and T. Itoh, "Modeling of a photonic bandgap and its application for the low-pass filter design," *Proceedings of Asia Pacific Microw. Conf. (APMC),* pp. 331–334, Singapore 1999.

[35] C. S. Kim, J. S. Park, Dal Ahn, and J. B. Lim, "A novel 1-D periodic defected ground structure for planar circuits," *IEEE Microw. Guided Wave Lett.,* Vol. 10, No. 4, pp. 131–133, April. 2000.

[36] C. S. Kim, J. S. Lim, J. S. Park, Dal Ahn, and S. Nam, "A 10 dB branch line coupler using defected ground structures," *Proceedings of Europ. Microw. Conf. (EuMC),* France, Sep. 2000.

[37] J. S. Lim, H. S. Kim, J. S. Park, Dal Ahn, and S. Nam, "A power amplifier with efficiency improved using defected ground structure," *IEEE Microw. Wire. Comp. Lett.,* Vol.11, No.4, pp. 170–172, April 2001.

[38] I. Chang and B. Lee, "Design of defected ground structures for harmonic control of active microstrip antenna," *IEEE Ant. Prop. Sypm. (AP-S),* Vol. 2, pp.852-855, June 2002.

[39] J. S. Park, J. H. Kim, J. H. Lee, S. H. Kim, and S. H. Myung, "A novel equivalent circuit and modeling method for defected ground structure and its application to optimization of a DGS lowpass filter," *Proceedings of IEEE MTT-S Int. Microw. Symp. Dig.,* Vol. 1, pp. 417-420, June 2002.

[40] A. Rahman, A. Boutejdar, A. K. Verma, G. Nadim, A. S. Omar, "Improved circuit model for DGS based lowpass filter," *Proceedings of IEEE Ant. Prop. Int. Symp.,* Vol.1, pp. 998-1001, June 2004.

[41] N. C. Karmakar, S. M. Roy, and I. Balbin, "Quasi-Static Modeling of Defected Ground Structure," *IEEE Trans. Microw. Theory Tech.,* Vol. 54, No. 5, pp. 2160-2168, May 2006.

[42] J. S. Lim, C. S. Kim, Dal Ahn, Y. C. Jeong and S. Nam, "Design of low-pass filters using defected ground structure," *IEEE Trans. Microw. Theory Tech.,* Vol. 53, No.8, pp. 2539–2545, Jan. 2005.

[43] A. Boutejdar, A. Ramadan, M. Makkey and A. S. Omar, "Design of compact microstrip lowpass filters using a U-shaped defected ground structure and compensated microstrip line" *Proceedings of Europ. Microw. Conf. (EuMC)*, Manchester, UK, pp. 267-270, Sep. 2006.

[44] A. Boutejdar, A. Elsherbini and A. S. Omar , "Control of bandstop response of cascaded microstrip low-pass bandstop filters using arrow-head slots in backside metallic ground plane" *Proceedings of IEEE Ant. Prop. Symp. (AP-S),* Vol. 1B, pp. 574 – 577, 2005.

[45] A. Boutejdar, A. Elsherbini and A. S. Omar, "A Compact Microstrip Multi-Layer Low-pass Filter Using Triangle Slots Etched in the Ground Plane" *Proceedings of Europ. Microw. Conf. (EuMC),* Manchester, UK, pp. 271-274, Sep. 2006.

[46] A. Boutejdar, A. Elsherbini, and A. Omar, "A new cross-head defected ground structure (CDGS) for a compact lowpass filter with a wide stopband", *Proceedings of Europ. Microw. Conf. (EuMC),* Munich, Germany, Oct. 2007.

[47] A. Boutejdar, M. Makkey, A. Elsherbini, O. Luxor et A. Omar, "Design of compact extended-stopband microstrip low-pass filter by employing new mutual-coupling technique for DGSs", *Proceedings of Europ. Microw. Conf. (EuMC),* Munich, Germany, Oct. 2007.

[48] J. S. Li, C. S. Kim, Y. T. Lee, D. Ahn, S. Nam; "A spiral-shaped defected ground structure for coplanar waveguide*," IEEE Microw. Wireless Comp. Lett.,* Vol.12, No. 9, pp. 330-332, Sep. 2002.

[49] D. J. Woo, T. K. Lee; "Suppression of harmonics in Wilkinson power divider using dual-band rejection by asymmetric DGS," *IEEE Trans. Microw. Theory Tech.,* Vol. 53, No. 6, Part 2, pp.2139-2144, June 2005.

[50] D. J. Woo, J. W. Lee and T. K. Lee, "Multi-band rejection DGS with improved slow-wave effect," *Proceedings of Europ. Microw. Conf. (EuMC),* Amsterdam, Netherlands, Oct. 2008.

[51] J. S. Li, C. S. Kim, Y. T. Lee, D. Ahn, S. Nam, "A vertically periodic defected ground structure and its application in reducing the size of microwave circuits", *IEEE Microw. Wireless Comp Lett.,* Vol. 12, No. 12, pp. 479-481, Dec. 2002.

[52] X. J. Zhang, A. Q. Liu, M. F. Karim, A. B. Yu, Z. X. Shen, " MEMS-based photonic bandgap (PBG) band-stop filter," *Proceedings of IEEE MTT-S Int. Microw. Symp. Dig.,* Vol. 3, pp. 1463- 1466, June 2004.

[53] S. Ting; K. Tam, R. P. Martins; "Compact Microstrip Quasi-Elliptic Bandpass Filter Using Open-Loop Dumbbell Shaped Defected Ground Structure," *Proceedings of IEEE MTT-S Int. Microw. Symp. Dig.,* pp.527-530, June 2006.

[54] J.D. Park, Y.J. Sung, S.H. Lee, Y.S. Kim; "Tunable bandstop filters using defected ground structure with active devices," *Proceedings of Asia-Pacific Microw. Conf. (APMC)*, Vol. 1, Dec. 2005.

[55] R. Zhang and R. R. Mansour, "Novel tunable lowpass filters using folded slots etched in the ground plane," *Proceedings of IEEE MTT-S Int. Microw. Symp. Dig.,* Vol. 3, pp. 1311-1314, June 2005.

[56] R. Zhang and R. R. Mansour; "Novel digital and analogue tunable lowpass filters", IET Microw. Ant. Prop., Vol. 1, No. 3, pp. 549-555, June 2007.

[57] M. F. Karim, A. Q. Liu, A. Alphones, A. B. Yu; "A Novel Reconfigurable Filter Using Periodic Structures," *Proceedings of IEEE MTT-S Int. Microw. Symp. Dig.,* pp. 943 – 946, June 2006.

[58] M. F. Karim, A. Q. Liu, A. Alphones, A. B. Yu; "A Reconfigurable Micromachined switching filter using periodic structures," *IEEE Trans. on Microw. Theory Tech.,* Vol. 55, No. 6, Part 1, pp.1154-1162, June 2007.

[59] E. K. I. Hamad, A. M. E. Safwat, A. S. Omar, "A MEMS reconfigurable DGS resonator for K-band applications," *Journal of Microelectromechanical Systems,* Vol. 15, No. 4, pp. 756-762, Aug. 2006.

[60] E. K. I. Hamad, A. M. E. Safwat, and A. S. Omar, "2-D periodic defected ground structure for coplanar waveguide," *Proceedings of German Microw. Conf. (GeMiC),* Ulm, Germany, pp. 25–28, April 2005.

[61] J. B. Muldavin and G. M. Rebeiz, "All-metal high-isolation series and series/shunt MEMS switches," *IEEE Microw. Wireless Comp. Lett.,* Vol. 11, No. 9, pp. 373–375, Sept. 2001.

[62] A. M. E. Safwat, F. Podevin, P. Ferrari, A. Vilcot, "Tunable Bandstop Defected Ground Structure Resonator Using Reconfigurable Dumbbell-Shaped Coplanar Waveguide," *IEEE Trans. Microw. Theory Tech.,* Vol. 54, No. 9, pp. 3559 – 3564, Sep. 2006.

[63] S. Fouladi, A. Akhavan, and R. R. Mansour, "A novel reconfigurable impedance matching network using DGS and MEMS switches for MM-wave applications," *Proceedings of IEEE MTT-S Int. Microw. Symp. Dig.,* pp. 145 – 148, June 2008.

CHAPTER THREE

STUDY OF THE ELECTROMAGNETIC BANDGAP (EBG) AND DEFECTED GROUND STRUCTURES (DGS) PHENOMENA

3.1. Introduction

As mentioned before, the Photonic Bandgap (PBG) research was done in the optical fields originally, but recently, there has been an increasing interest in microwave and millimeter-wave applications of EBG circuits [1] - [8]. Many passive and active microwave and millimeter devices have been developed to suppress the harmonics and realize compact physical dimensions of circuits. Several efforts have been made to realize such devices using various bandgap circuits, such as, power amplifiers [9], [10], slow-wave circuits [11], and magnetic walls in waveguides [12], [13]. Their experimental results are sufficient to show the validity of bandgap circuit applications. On the other hand, defected ground structures (DGS) have recently attracted the attention of many researchers due to their attractive features and ease of modeling and design. Different equivalent circuits and modeling methods have been used to represent these DGS and to use them in more complex structures and applications.

In this chapter, our aim is to understand the different approaches used to explain EBG structures. We will explain in details the bandgap theory using the Coupled-Mode Theory and the Bloch Wave-Formalism. Using analysis and wave propagation equations, both approaches will reach the conclusion that any periodic structure leads to a band of frequency where propagation is not allowed, referred to as the "bandgap phenomenon". In addition, we will investigate the different equivalent circuits used to represent the dumbbell shape DGS, their extraction methods and choose the most suitable circuit for the implementation of higher order filters.

This chapter is organized as follows; Section 3.2.1 introduces briefly the evolution of the bandgap structures in the optical domain for the first time. Section 3.2.2 will study a periodic layered medium using the Coupled Mode Theory while Section 3.2.3 will study the same structure using the commonly used Bloch-wave Formalism. Then, Section 3.2.4 will draw the conclusion of both analysis techniques. On the other hand Section 3.3 is devoted for the equivalent circuit models of the dumbbell-shaped DGS. Section 3.3.1 investigates the effect of the different physical dimensions of the dumbbell DGS on the dispersion diagram of the structure. Section 3.3.2 is devoted to the modeling and parameter extraction of the equivalent circuit of the DGS unit section. The equivalent-circuit parameters are extracted based on the circuit analysis theory. By employing the extracted parameters and the circuit analysis theory, the bandgap effect for the provided DGS section can be explained. In this section, we have examined three different equivalent circuits, the parallel *LC*-circuit, the parallel *RLC*-circuit and the π-equivalent circuit. In Section 3.3.3, three-pole low-pass filters are designed by using this DGS section and its equivalent circuit on microstrip transmission line and coplanar waveguide. Finally, Section 3.3.4 gives a quick and brief idea on the use of DGSs as periodic structures, and Section 3.4 draws the conclusion of the whole chapter.

3.2. EBG phenomenon

3.2.1. Introduction

The study of wave propagation in periodic structures has a long history, which stretches back to, at least, Lord Rayleigh classical article on the influence of obstacles arranged in rectangular order upon the properties of a medium [13]. This work was soon followed by work of Kasterin [14], who studied reflection and refraction of low frequency sound by an orthorhombic grid of hard spheres (an acoustic crystal). Another early paper on photonic crystals is that of Ewald [15]. Ewald studied if the optical birefringence can be caused by lattice structure alone, i.e. if it requires anisotropy of the atomic scatterers. Later on, wave propagation in periodic structures was a subject of the book [16] of the same title by Brillouin and Parodi. The use of two-dimensional distributed feedback periodic structures in thin

film optical devices and lasers is disclosed in the US patent publication US-3,884,549 [17].

The phenomenon of bandgap structures appeared in the late 1960's in the optical domain. The first to give an explanation to this phenomenon were Kogelnik and Shank in their explanation to the dispersion characteristics of the Distributed Feedback Lasers (DFB) [18]. At that time, they did not value the phenomenon of the bandgap produced by the periodic variations in the refractive index, but they just focused on explaining the phenomenon. They proved that the periodic variations in the refractive index of a structure produced forward and backward propagating waves that interact with each other through coupled wave equations. By solving these coupled wave equations, they found through the dispersion relation that there existed a certain frequency band along which there was no wave propagation due to the presence of evanescent waves.

In the 1980's, Yoblonovitch stated that this PBG, produced by periodic variation in the refractive index of the structure, can be very useful as it can be used to eliminate the spontaneous emission of photons at certain frequency bands. The motivation after this was that the performance of semiconductor lasers, heterojunction bipolar transistors and solar cells was limited by spontaneous emission, but each in a characteristically different way [19]. In 1987, he published the first physical review letter discussing how to establish this three dimensional periodic variations using PBG crystals.

By the 1990's, the idea of bandgap structures started to find its way in microwave and millimeter wave domains. Applications of EBG materials at microwave frequencies have been proposed, such as microstrip antennas, resonant cavities, and filters; and from that time on, EBG structures became a major interest in the research fields.

Two approaches are generally used to obtain the solution of the propagation of electromagnetic waves in a periodic layered medium. One is the Coupled-Mode Theory and the other is the Bloch-Wave Formalism [20]. In this section, we are going to explain both techniques and how both of them indicate the existence of a frequency gap in a periodic structure.

3.2.2. Coupled-Mode Theory

The periodic variation of the dielectric tensor is considered as a perturbation that couples the unperturbed normal modes of the structure. Let us express the dielectric tensor as a function of space in the form of [20]:

$$\varepsilon(x,y,z) = \varepsilon_0(x,y) + \Delta\varepsilon(x,y,z) \tag{3.1}$$

where $\varepsilon_o(x,y)$is the unperturbed part of the dielectric tensor, and $\Delta\varepsilon(x,y,z)$ is periodic in the z-direction and is the only periodically varying part of the dielectric tensor.

We assume that the normal modes of propagation in the unperturbed dielectric medium described by the dielectric tensor $\varepsilon_o(x,y)$ are known. Since the unperturbed dielectric medium is homogeneous in the z-direction (i.e. $\partial\varepsilon_o(x,y)/\partial z = 0$), the normal modes can be written in the form of:

$$E_m(x,y)e^{j(\omega t-\beta_m z)} \tag{3.2}$$

where the m is the mode subscript, which can be either continuous for unbounded modes, such as plane waves, or discrete for confined modes, such as waveguide modes. These normal modes satisfy:

$$\left[\frac{\partial^2}{\partial x^2}+\frac{\partial^2}{\partial y^2}+\omega^2\mu\varepsilon_0-\beta_m^2\right]E_m(x,y)=0 \tag{3.3}$$

where we assume that $\nabla.E = 0$. If an arbitrary field of frequency ω is excited at $z=0$, the propagation of this field in the unperturbed medium can always be expressed in terms of a linear combination of normal modes,

$$E=\sum_m A_m E_m(x,y)e^{j(\omega t-\beta_m z)} \tag{3.4}$$

Where the $A_m's$ are constants. Such an expansion is possible because these normal modes form a complete set.

Let us consider the propagation of an unperturbed mode $E_1(x,y)e^{j(\omega t-\beta_1 z)}$ in the perturbed medium described by the dielectric tensor $\varepsilon_o(x,y)+\Delta\varepsilon(x,y,z)$. The

presence of the dielectric perturbation $\Delta\varepsilon(x,y,z)$ gives rise to a new perturbation polarization:

$$\Delta P = \Delta\varepsilon(x,y,z)E_1(x,y)e^{j(\omega t-\beta_1 z)} \tag{3.5}$$

If this polarization wave, acting as a distributed source, can feed energy into some other mode $E_2(x,y)e^{j(\omega t-\beta_2 z)}$, then we say that the dielectric perturbation $\Delta\varepsilon(x,y,z)$ couples between mode E_1 and E_2.

By substituting Eq.(3.4) into the wave equation, we get:

$$\left\{\nabla^2+\omega^2\mu\left[\varepsilon_0(x,y)+\Delta\varepsilon(x,y,z)\right]\right\}E = 0 \tag{3.6}$$

And using Eq. (3.3), we reach:

$$\sum_k\left[\frac{d^2}{dz^2}A_k - 2j\beta_k\frac{d}{dz}A_k\right]E_k(x,y)e^{-j\beta_k z} = -\omega^2\mu\sum_l\Delta\varepsilon(x,y,z)A_lE_1(x,y)e^{-j\beta_1 z} \tag{3.7}$$

We now assume further that the dielectric perturbation is weak, so that the variation of the mode amplitude is slow and satisfies the condition:

$$\left|\frac{d^2}{dz^2}A_k\right| << \left|\beta_k\frac{d}{dz}A_k\right| \tag{3.8}$$

This condition is known as parabolic approximation and is often used when the perturbation is small. Thus, neglecting the second derivative in Eq. (3.7) leads to:

$$-2j\sum_k\beta_k\left[\frac{d}{dz}A_k\right]E_k(x,y)e^{-j\beta_k z} = -\omega^2\mu\sum_l\Delta\varepsilon(x,y,z)A_lE_1(x,y)e^{-j\beta_1 z} \tag{3.9}$$

We next take the scalar product of Eq. (3.9) and integrate it over *x* and *y*. The result, using the orthogonal property of the normal modes, is:

$$\langle k|k\rangle\frac{d}{dz}A_k(z) = \frac{\omega^2\mu}{2j\beta_k}\sum_l\langle k|\Delta\varepsilon|l\rangle A_l(z)e^{j(\beta_k-\beta_l)z} \tag{3.10}$$

where

$$\langle k|k\rangle \equiv \int E_k^*(x,y).E_k(x,y)dxdy = \frac{2\omega\mu}{|\beta_k|} \tag{3.11}$$

$$\langle k|\Delta\varepsilon|l\rangle \equiv \int E_k^*(x,y).\Delta\varepsilon(x,y,z)E_l(x,y)dxdy \tag{3.12}$$

Since the dielectric perturbation $\Delta\varepsilon(x,y,z)$ is periodic in *z*, we can expand it as a Fourier series:

$$\Delta\varepsilon(x,y,z) = \sum_{m\neq 0} \varepsilon_m(x,y)\exp\left(-jm\frac{2\pi}{\Lambda}z\right) \tag{3.13}$$

where the summation is over all values of *m* except *m=0* because of the definition of $\Delta\varepsilon(x,y,z)$ in Eq. (3.1).

Substitution of Eq. (3.11-3.13) in Eq. (3.9) leads to:

$$\frac{d}{dz}A_k(z) = -j\frac{\beta_k}{|\beta_k|}\sum_l\sum_m C_{kl}^{(m)}A_l e^{j\left(\beta_k-\beta_l-\frac{m2\pi}{\Lambda}\right)z} \tag{3.14}$$

Where the coupling coefficient $C_{kl}^{(m)}$ is defined as:

$$C_{kl}^{(m)} \equiv \frac{\omega}{4}\langle k|\Delta\varepsilon|l\rangle = \frac{\omega}{4}\int E_k^*(x,y).\Delta\varepsilon(x,y,z)E_l(x,y)dxdy \tag{3.15(a)}$$

The coupling coefficient $C_{kl}^{(m)}$ reflects the magnitude of coupling between the k^{th} and the l^{th} modes due to the m^{th} Fourier component of the dielectric perturbation. Eq. (3.14) presents a set of coupled linear differential equations. In principle, an infinite number of mode amplitudes are involved. However, in practice, especially near the condition of resonant coupling, only two modes are strongly coupled, and Eq. (3.14) reduces to two equations for the two mode amplitudes.

In the event that the dielectric tensor ε of Eq. (3.1) is a function of z only, the normal modes of the unperturbed medium are plane waves and the Fourier coefficients ε_m of the dielectric perturbation are constants. The coupling coefficients for this specific case become:

$$C_{kl}^{(m)} = \frac{\omega^2 \mu}{2\sqrt{|\beta_k \beta_l|}} P_k^* \varepsilon_m P_l^* \tag{3.15(b)}$$

By resonant coupling, we mean a mode coupling at the phase matching condition given by:

$$\Delta\beta = \beta_k - \beta_l - m\frac{2\pi}{\Lambda} = 0 \tag{3.16}$$

for some integer m.

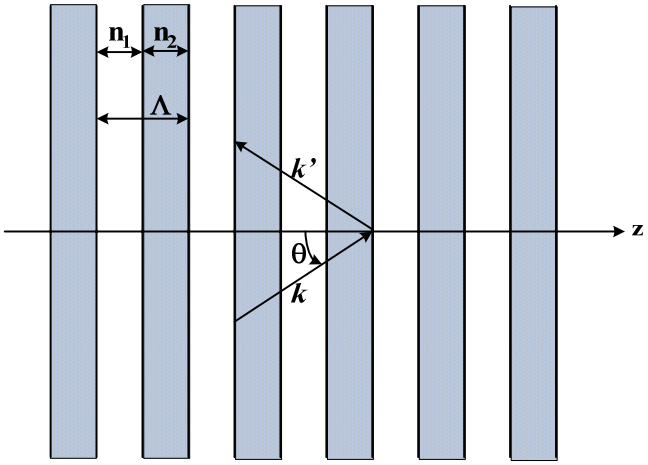

Fig. 3.1. The geometry of a typical N-period Bragg reflector.

Now consider a Bragg reflector as shown in Fig. 3.1. We will now analyze this Bragg reflector using the coupled-mode theory. For the sake of simplicity, we will assume that the layer thicknesses are the same and the dielectric constant as a function of z is:

$$\varepsilon(z) = \begin{cases} \varepsilon_0 n_2^2, & 0 < z < \frac{1}{2}\Lambda \\ \varepsilon_0 n_1^2, & \frac{1}{2}\Lambda < z < \Lambda \end{cases} \tag{3.17}$$

with

$$\varepsilon(z) = \varepsilon(z + \Lambda) \tag{3.18}$$

This dielectric constant can be decomposed according to Eq. (3.1) as:

$$\varepsilon(z)=\frac{\varepsilon_0\left(n_1^2+n_2^2\right)}{2}+\frac{\varepsilon_0\left(n_2^2-n_1^2\right)}{2}f(z) \tag{3.19}$$

where $f(z)$ is a periodic square wave function given by:

$$f(z)=\begin{cases}1, & 0<\mathrm{z}<\frac{1}{2}\Lambda\\ -1, & \frac{1}{2}\Lambda<\mathrm{z}<\Lambda\end{cases} \tag{3.20(a)}$$

The period Λ is exactly twice the thickness of a crystal plate.

The periodic function $f(z)$ can be written as a Fourier Series:

$$f(z)=\sum_{m\neq 0}\frac{j\left(1-\cos(m\pi)\right)}{m\pi}\exp\left(-jm\left(\frac{2\pi}{\Lambda}\right)z\right) \tag{3.20(b)}$$

The normal modes of the unperturbed medium are plane waves $e^{-jk.r}$ with a wave number given by:

$$k^2=\left(\frac{\omega}{c}\right)^2\left(\frac{n_1^2+n_2^2}{2}\right)=\left(\frac{\bar{n}\omega}{c}\right)^2 \tag{3.21}$$

where $\bar{n}$ is the (geometric) averaged refractive index of the medium. The plane waves are divided into TE waves and TM waves according to their polarization states. Since both the perturbed and the unperturbed dielectric constants are scalars, mode coupling between TE waves and TM waves does not exist. Consequently, only coupling between waves of the same polarization can exist; this is possible only in the contradirectional coupling, because the phase matching condition for codirectional coupling can never be satisfied $[\Delta\beta=\beta_1-\beta_2-m(2\pi/\Lambda)\neq 0$ for finite $\Lambda]$.

The mode coupling for TE waves and TM waves are similar. The only difference is the coupling coefficients. Let θ be the angle between the wave vector k and the z axis, and k' be the wave vector of the reflected wave as shown in Fig.3.1. The coupling constants according to Eq. 3.15(b), 3.20(b) and 3.21 are given by:

$$\kappa = \begin{cases} \dfrac{j(1-\cos(m\pi))}{2m\lambda\cos(\theta)} \dfrac{\sqrt{2}\left(n_2^2 - n_1^2\right)}{\sqrt{n_2^2 + n_1^2}}, & \text{TE waves} \\ \dfrac{j(1-\cos(m\pi))}{2m\lambda\cos(\theta)} \dfrac{\sqrt{2}\left(n_2^2 - n_1^2\right)}{\sqrt{n_2^2 + n_1^2}} \cos(2\theta), & \text{TM waves} \end{cases} \tag{3.22}$$

Note that the difference between the two coupling constants is only a directional factor $cos(2\theta)$, which is the cosine of the angle between the polarization vectors of TM waves.

The phase matching factor is given by:

$$\Delta\beta = 2k\cos(\theta) - m\left(\frac{2\pi}{\Lambda}\right) = 2\left(\bar{n}\frac{\omega}{c}\right)\cos(\theta) - m\frac{2\pi}{\Lambda} \tag{3.23}$$

where Λ is the period of the layered structure and k is the wave number .

Now, let us assume that light is incident at $z=0$, so that the boundary condition is:

$$\begin{aligned} A_1(0) &= 1 \\ A_2(L) &= 0 \end{aligned} \tag{3.24}$$

where A_1 is the amplitude of the incident wave and A_2 is the amplitude of the reflected wave. The solution of the coupled equation given by (3.14) is:

$$A_1(z) = e^{j\left(\frac{\Delta\beta}{2}\right)z} \frac{s\cosh(s(L-z)) + j\left(\frac{\Delta\beta}{2}\right)\sinh(s(L-z))}{s\cosh(sL) + j\left(\frac{\Delta\beta}{2}\right)\sinh(sL)} \tag{3.25}$$

$$A_2(z) = e^{-j\left(\frac{\Delta\beta}{2}\right)z} \frac{-j\kappa^*\sinh(s(L-z))}{s\cosh(sL) + j\left(\frac{\Delta\beta}{2}\right)\sinh(sL)} \tag{3.26}$$

where s is given by:

$$s^2 = \kappa\kappa^* - \left(\frac{\Delta\beta}{2}\right)^2 \tag{3.27}$$

We find that the z-dependent part of the wave solution in the periodic layered medium is an exponential with propagation constant:

$$K = k\cos(\theta) \pm js = \frac{m\pi}{\Lambda} \pm j\sqrt{\kappa\kappa^* - \left(\frac{\Delta\beta}{2}\right)^2} \tag{3.28}$$

We note that for a range of frequencies such that $|\Delta\beta| < 2|\kappa|$, K has an imaginary part. This is called "forbidden" region, as shown in Fig. 3.2. Note that for each value of m *(m=1, 2, 3...)* there exists a gap whose center frequency ω_o satisfies $kcos(\theta) = m\pi/\Lambda$.

Returning to Eq. (3.28) and by using Eq. (3.21), we have:

$$K = \frac{m\pi}{\Lambda} \pm j\sqrt{kk^* - \left(\frac{\bar{n}}{c}\right)^2 (\omega - \omega_0)^2 \cos^2(\theta)} \tag{3.29}$$

where ω_o, the midband frequency, is the value of ω for which $kcos(\theta) = m\pi/\Lambda$ or $\Delta\beta = 0$. A plot of *Re(K)* for m=1 and θ=0 versus ω, based on Eq. (3.29), is shown in Fig. 3.2.

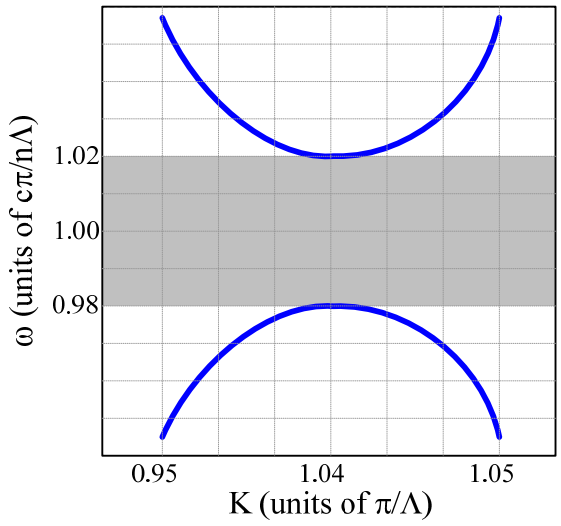

Fig. 3.2. Dispersion relation (ω versus K) for a periodic medium.

3.2.3. Bloch-Wave Formalism

Now, we are going to validate the same phenomenon of bandgap structures and the existence of a forbidden band using the Bloch-Wave Formalism.

The properties of a periodic medium are described by its dielectric and permeability tensors, which are periodic functions of *x*, reflecting the translational symmetry of the medium:

$$\varepsilon(x) = \varepsilon(x+a), \qquad \mu(x) = \mu(x+a) \tag{3.30}$$

where a is an arbitrary lattice vector. These equations merely state that the medium "looks" exactly the same to an observer at *x* as at $x + a$. In a three dimensional periodic medium, there exist permittivity vectors a_1, a_2, a_3 which define the periodicity of the lattice, such that the medium remains invariant under translation through any vector a which is the sum of integral multiples of these vectors.

The propagation of the electromagnetic waves in a periodic medium is described by Maxwell's equations, which in the simplified harmonic form (no conductive mechanisms taken into account) are as follows:

$$\nabla \times \overline{H} = j\omega\varepsilon\,\overline{E} \tag{3.31}$$

$$\nabla \times \overline{E} = -j\omega\mu\,\overline{H} \tag{3.32}$$

These equations remain the same after we have substituted $x + a$ for *x* in the operator ∇ and ε, μ. The translational symmetry of the medium allows us to take its normal modes as:

$$E = E_{\mathrm{K}}(x)e^{-j\mathrm{K}.x} \tag{3.33}$$

$$H = H_{\mathrm{K}}(x)e^{-j\mathrm{K}.x} \tag{3.34}$$

where $E_K(x)$ and $H_K(x)$ are both periodic, that is:

$$E_{\mathrm{K}}(x) = E_{\mathrm{K}}(x+a) \tag{3.35}$$

$$H_{\mathrm{K}}(x) = H_{\mathrm{K}}(x+a) \tag{3.36}$$

This is known as the Floquet (or Bloch) theorem. The subscript K indicates that the functions E_K and H_K depend on K, which is known as the Bloch wave vector. A dispersion relation exists between ω and K:

$$\omega = \omega(K) \tag{3.37}$$

In the event that the periodicity disappears, the functions $E_K(x)$ and $H_K(x)$ become constant and the normal modes become plane waves with the Bloch wave vector equals to the plane wave propagation vector. Our main task is to determine the dispersion relation $\omega(K)$.

Now let us consider a one-dimensional periodic medium such that:

$$\varepsilon(z) = \varepsilon(z + l\Lambda) \tag{3.38}$$

where ε is the permittivity tensor, Λ is the period and l is an integer, Fig. 3.1. We will limit our discussion to a one-dimensional, nonmagnetic media. Assume that the incident electromagnetic wave on the periodic medium has an incidence angle θ. The wave will be reflected and refracted at each interface. Constructive interference occurs when the condition:

$$m\lambda = 2\Lambda\cos(\theta) \tag{3.39}$$

is satisfied. This is known as the Bragg condition. It can be easily derived by considering the phase difference between the waves reflected from successive lattice planes. Constructive interference occurs when the path difference between rays reflected from successive lattice planes contain an integer number of wavelengths. The propagation of electromagnetic radiation in these media obeys the wave equation:

$$\nabla \times (\nabla \times E) - \omega^2 \mu\varepsilon E = 0 \tag{3.40}$$

Since the medium is periodic then we can expand the dielectric tensor ε in a Fourier series:

$$\varepsilon(z)=\sum_{G}\varepsilon_{G}e^{-jG.z} \tag{3.41}$$

where G runs over all the reciprocal lattice vectors, including G=0. In our one dimensional case:

$$G = l\ g = l\frac{2\pi}{\Lambda}\hat{z} \qquad l = 0,\pm 1,\pm 2,\pm 3,... \tag{3.42}$$

and

$$\varepsilon(z)=\sum_{l}\varepsilon_{l}e^{-jl\frac{2\pi}{\Lambda}z} \tag{3.43}$$

The vector G is known as the reciprocal lattice vector in solid-state physics and plays a fundamental role in crystal physics. In a one-dimensional periodic medium, g is parallel to z. The electric field vector in this periodic medium may be expressed in general as a Fourier integral:

$$E=\int A(k)e^{-jk.z} \tag{3.44}$$

Submitting Eq. (3.44) and Eq. (3.41) in Eq. (3.40), we obtain:

$$k\times[k\times A(k)]+\omega^{2}\mu\sum_{G}\varepsilon_{G}A(k-G)=0 \qquad for\ \ all\ k \tag{3.45}$$

where the summation is over all the reciprocal lattice vectors. This is an infinite set of homogeneous equations for the unknown coefficient $A(k)$. Each equation in the set has a different value of k. By inspecting Eq. (3.45), we note that not all the coefficients of $A(k)$ are coupled. In fact, only the coefficients of the form $A(k-G)$ are coupled. This makes it possible to divide the whole set of equations into many subsets, each labeled by a wave vector K and containing equations that involve $A(K)$and $A(K-G)$ with all the possible G's. Each subset can be solved separately. Using this fact, the solution of the subset K can be written as:

$$E_{\mathrm{K}}=\sum_{G}A(K-G)e^{-j(K-G).r}=e^{-jK.r}\sum_{G}A(K-G)e^{jG.r}=e^{-jK.r}E_{K}(r) \tag{3.46}$$

In the one-dimensional case,

$$E_{\mathrm{K}}(r)=\sum_{l} A(K-l\,\mathrm{g})e^{-jl\frac{2\pi}{\Lambda}z} \tag{3.47}$$

Eqs. (3.46) and (3.47) represent a normal mode of propagation. The general solution given in Eq. (3.45) now becomes a linear superposition of these normal modes. Given a frequency ω, Eq. (3.45) can be used to obtain the K vector. If the medium is homogeneous in the x and y directions, then the Bloch mode of the electric vector becomes:

$$E = e^{-j\left(K_x x+K_y y\right)}e^{-jK_z z}E_K(z) \tag{3.48}$$

where $E_K(z)$ is a periodic function of z.

It is assumed that the wave is propagating in the direction of z (i.e., $K_x = K_y = 0$) and the field vector is transverse to the propagation vector ($k.E = 0$). In addition, we assume that the medium is isotropic, so that the ε_l's are scalar. This Eq. (3.45) becomes:

$$k^2 A(k)-\omega^2\mu\sum_{l}\varepsilon_l A(k-l\,g)=0 \tag{3.49}$$

To find the Bloch wave with the wave number K (here we drop the subscript z for the sake of simplicity) we need to solve the set of equations (3.49) with $k = K, K \pm g, K \pm 2g, \ldots$. Since there are an infinite number of equations involving $A(K)$, $A(K \pm g)$, $A(K \pm 2g)$,…, an approximation is required to obtain an explicit result. To make the correct approximation, we need to inspect all the terms involved and neglect the small ones. Writing out the first few terms in Eq. (3.49) for $k = K$, we obtain:

$$K^2 A(K)-\omega^2\mu\varepsilon_0 A(K)-\omega^2\mu\varepsilon_1 A(K-g)-\omega^2\mu\varepsilon_{-1}A(K+g)-\ldots=0 \tag{3.50}$$

which can also be written as:

$$A(K)=\frac{1}{K^2-\omega^2\mu\varepsilon_0}\left[\omega^2\mu\varepsilon_1 A(K-g)+\omega^2\mu\varepsilon_{-1}A(K+g)+\ldots\right] \tag{3.51}$$

Similarly, for $k = K - g$ and $k = K + g$:

$$A(K-g) = \frac{1}{(K-g)^2 - \omega^2\mu\varepsilon_0}\left[\omega^2\mu\varepsilon_1 A(K-2g) + \omega^2\mu\varepsilon_{-1}A(K) + \ldots\right] \tag{3.52}$$

and

$$A(K+g) = \frac{1}{(K+g)^2 - \omega^2\mu\varepsilon_0}\left[\omega^2\mu\varepsilon_1 A(K) + \omega^2\mu\varepsilon_{-1}A(K+2g) + \ldots\right] \tag{3.53}$$

Eq. (3.51, 3.52 and 3.53) show that if:

$$|K-g| \cong K \tag{3.54}$$

and

$$K^2 \cong \omega^2\mu\varepsilon_0 \tag{3.55}$$

the dominant terms are $A(K)$ and $A(K-g)$. Physically, this means that the plane wave components $A(K)$ and $A(K-g)$ are resonantly coupled. Neglecting all other coefficients, the series of equations (3.49) for the Bloch wave with wave number K becomes:

$$\left(K^2 - \omega^2\mu\varepsilon_0\right)A(K) - \omega^2\mu\varepsilon_1 A(K-g) = 0 \tag{3.56}$$

$$-\omega^2\mu\varepsilon_{-1}A(K) + \left\{(K-g)^2 - \omega^2\mu\varepsilon_0\right\}A(K-g) = 0 \tag{3.57}$$

Notice that $\varepsilon_o$here denotes the 0th Fourier component of the dielectric tensor, and $\varepsilon_{-1} = \varepsilon_1^*$ if ε is a real dielectric function.

Eqs. (3.56 and 3.57) are two coupled linear equations in the field amplitudes $A(K)$ and $A(K-g)$. A nontrivial solution exists only when the determinant vanishes:

$$\begin{vmatrix} K^2 - \omega^2\mu\varepsilon_0 & -\omega^2\mu\varepsilon_1 \\ -\omega^2\mu\varepsilon_{-1} & (K-g)^2 - \omega^2\mu\varepsilon_0 \end{vmatrix} = 0 \tag{3.58}$$

or

$$\left(K^2-\omega^2\mu\varepsilon_0\right)\left((K-g)^2-\omega^2\mu\varepsilon_0\right)-\left(\omega^2\mu|\varepsilon_1|\right)^2=0 \tag{3.59}$$

This is an explicit form of the dispersion relation between ω and K. The Bragg condition is satisfied at exactly $K=\frac{1}{2}g=\pi/\Lambda$. At this K value, two roots for ω^2 may be obtained from Eq. (3.59).

$$\omega_{\pm}^2=\frac{K^2}{\mu\left(\varepsilon_0\pm|\varepsilon_1|\right)} \tag{3.60}$$

These are the spectral band edges. At frequencies between ω_+ and ω_-, the roots of K are complex, with real part equals to π/Λ. The waves are evanescent and this spectral regime is the "forbidden band" proved previously by the Coupled Wave equations.

3.2.4. Conclusion

In this section, the electromagnetic wave propagation in a periodic structure, where the refractive index of the propagation medium is periodically changing in one direction and constant in the other two directions, has been discussed. This periodic structure has been analyzed using two different approaches, the Coupled-Mode Wave Equation and the Bloch-Wave Formalism. Both approaches validated that periodic structures have a certain forbidden band where no propagation is allowed due to its complex propagation constant in this frequency band.

Starting from this important conclusion, a lot of researchers started to investigate the ability to use this bandgap phenomenon in more complex structures in order to have full control of the dispersion diagram of the structure and tailor it as required [21]-[25].

As mentioned before in Chapter Two, due to the difficulty in modeling electromagnetic bandgap structures, a large number of researchers resolves to defected ground structures, where two or three defects may be used to achieve the required stopband [26]-[28]. In the following section of this chapter, the different models for the representation of these DGSs and the extraction method of each will be considered, pointing out the advantages and the disadvantages of each equivalent circuit.

3.3. Defected Ground Structures

In the previous section of this chapter, the different methods used for understanding the EBG structure properties providing the passband and stopband properties of these structures have been explained. However, it should be noted that it is difficult to use an EBG structure for the design of microwave or millimeter-wave components due to the difficulties of their modeling, as there are too many design parameters which affect the bandgap property, such as the number of lattice, lattice shapes, lattice spacing, and relative volume fraction. On the other hand, one single etched DGS unit cell is easier to model and use in more complex designs.

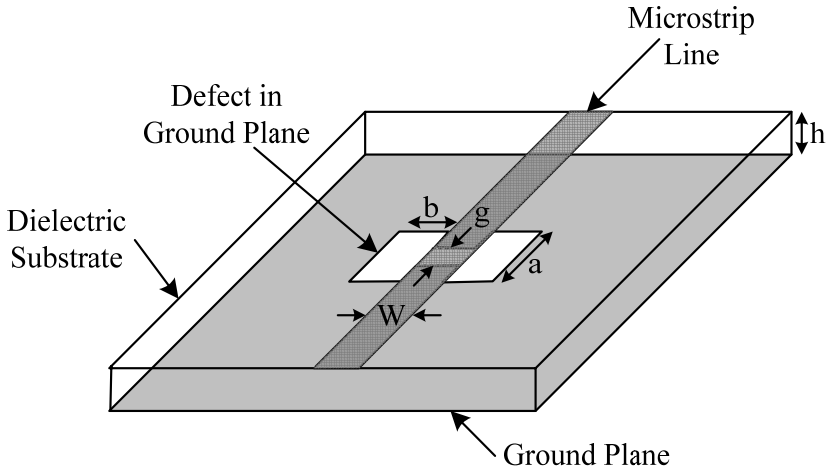

Fig. 3.3. Three-dimensional view of the dumbbell shaped DGS.

In this section, we have taken the dumbbell shaped DGS unit cell as an example to explore the different equivalent circuits and models of DGSs. Any etched defect in the ground plane disturbs the shield current distribution in the ground plane. This disturbance can change characteristics of a transmission line, such as line capacitance and inductance. DGSs consist of narrow and wide etched areas in the metallic ground plane as shown in Fig. 3.3, which gives rise to increasing the effective capacitance and inductance of a transmission line, respectively. Thus, an *LC* equivalent circuit can represent any unit DGS circuit. The effects of physical dimensions of the proposed DGS on these equivalent-circuit parameters will be demonstrated. It is the purpose of this section to show the potential of applying DGSs to practical circuits. In order to design a circuit with a DGS section, the equivalent circuit parameters for the DGS section should be extracted.

3.3.1. Frequency Characteristics of the Dumbbell Shaped DGS

Fig. 3.3 shows the etched unit shape of the dumbbell DGS section, which is located on the backside metallic ground plane of a microstrip line. The DGS unit section can provide cutoff frequency and attenuation pole in some frequencies without any periodic array of DGSs. In order to investigate the frequency characteristics of this DGS section, we simulated it by Zeland IE3D version 12.1.

The simulation results show one-pole low-pass filter characteristics, as expected. The existence of the cutoff frequency and the attenuation pole means that employing the DGS section increases the effective permeability so that the effective inductance of the microstrip line is also increased. The cutoff frequency is mainly dependent on the etched square area in ground plane. There is also an attenuation pole, which is due to the etched gap distance. Actually, it is well known that an attenuation pole can be generated by combination of the inductance and capacitance elements. Thus, to explain the frequency characteristic of the proposed DGS section, the presence of a capacitance is needed. The etched gap area, which is placed under a conductor line, as shown in Fig. 3.3, provides the parallel capacitance with effective line inductance. Thus, the proposed DGS section is fully described by two parameters: the etched lattice dimension and gap distance. We will show the influences of these two parameters on the frequency characteristics of a microstrip line.

3.3.1.1. Influence of the Square Lattice Dimension

In order to investigate the influence of the square lattice dimension, three DGS unit cells of different dimensions are simulated. The line width is chosen to attain a characteristic impedance of 50Ω. The etched gap, which is related with the gap capacitance, is kept constant to 0.637 mm for all three cases and the etched square area is varied. The substrate used for all simulations is Teflon substrate of thickness 0.635 mm, dielectric constant of 9.5 and loss tangent 0.0035. The simulation results are shown in Fig. 3.4.

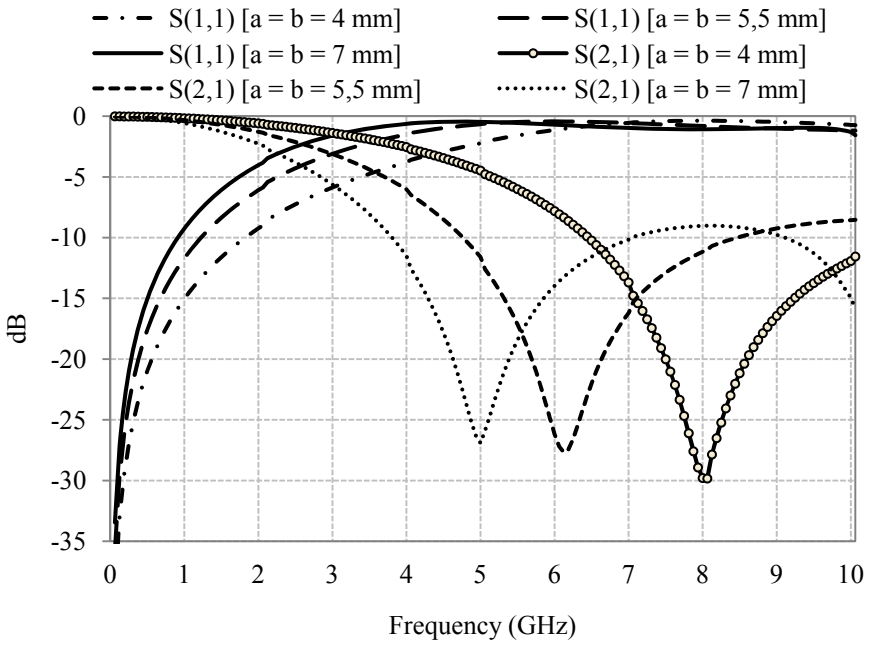

Fig. 3.4. Simulated S-parameters for the DGS unit cells.
The gap distance (g) is 0.637 mm for all cases.

From Fig. 3.4, one clearly observes that employing the proposed etched lattice increases the series inductance of the microstrip line. This effective series inductance introduces the cutoff characteristic at certain frequency. As the etched area of the unit lattice is increased, the rotation of the backward current in the ground plane around the etched square lattice increases, causing the increase of the effective series inductance, giving rise to a lower cutoff frequency, as shown in Fig. 3.4.

There are attenuation poles in the simulation results on the etched unit lattices. These attenuation poles can be explained by parallel capacitance with the series inductance, as was explained previously. This capacitance depends on the etched gap below the conductor line. The capacitance values are identical for all cases due to the identical gap distance. However, the attenuation pole location, which corresponds to the resonance frequency of the parallel *LC* circuit, also becomes lower because as the series inductance increases, the resonance frequency of the equivalent parallel *LC* circuit decreases [29]-[30].

3.3.1.2. Influence of the Gap Distance

We now investigate the influence of the etched gap distance. The lattice dimension is kept constant to 5.5 x 5.5 mm for all three cases and the etched gap distance is varied. The simulation results are shown in Fig. 3.5.

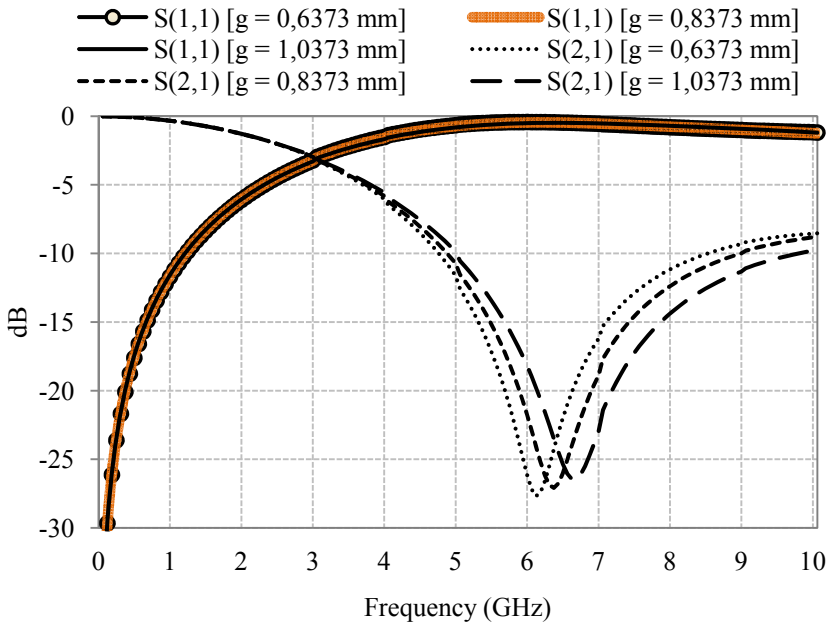

Fig. 3.5. Simulated S-parameters for the DGS unit cells.
The lattice dimensions (*a* and *b*) are 5.5 and 5.5 mm, respectively.

Due to the constant lattice dimensions, we can expect that the effective series inductances are also constant for all cases. Unlike the influence of lattice dimension, there is nearly no change in cutoff frequency despite the variation of the gap distance. This means that the gap distance does not affect the effective series inductance of a microstrip. Variation of the effective capacitance only affects the attenuation pole location, as seen in Fig. 3.5. As the etched gap distance increases, the effective capacitance decreases so that the attenuation pole location moves up to higher frequency.

Simulation results seen in Fig. 3.4 and Fig. 3.5 show the influences of the proposed DGS section on frequency characteristics. This equivalent circuit of the proposed DGS unit can explain the bandgap effect. The series inductance, due to the DGS section, increases the reactance of a microstrip with increasing the frequency. Thus, the rejection of the certain frequency range can be achieved. The parallel capacitance with the series inductance provides the attenuation pole location, which is the resonance frequency of the parallel *LC* resonator. However, as the operating frequency increases, the reactance of the capacitance decreases. Thus, the bandgap between the propagating frequency bands occurs.

3.3.2. Modeling and Parameter Extraction

3.3.2.1. Parallel *LC*-Circuit

In the previous section, we have shown that the parallel *LC* circuit can represent the equivalent circuit of the proposed DGS section. Furthermore, effects of the proposed DGS parameters on the frequency characteristics have been investigated.

It is clear that the resonant frequency (ω_o) of the DGS and 3-dB cutoff frequency ($\omega_{c,\ 3\ dB}$) exist as shown in Fig. 3.4 and Fig. 3.5. The equivalent *LC* – circuit of the DGS can be extracted because this kind of electrical characteristic is observed from a typical *LC* – parallel resonant circuit. The equivalent circuit of the DGS and one-pole Butterworth prototype of the LPF are presented in Fig. 3.6.

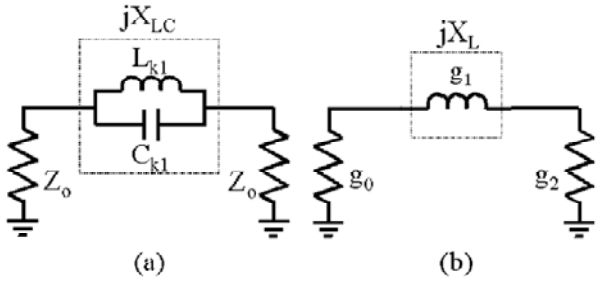

Fig. 3.6. (a) Equivalent circuit of the microstrip line with unit DGS. (b) Butterworth prototype of one pole LPF [31].

The equivalent *LC* – elements are calculated by Eq.(3.61)–(3.63) because the two reactance values of Fig. 3.6 (a) and (b) must be equal at $\omega_{c,\ 3\ dB}$ as follows [31]:

$$X_{LC} = \frac{1}{\omega_o C_{k1}\left(\frac{\omega_o}{\omega} - \frac{\omega}{\omega_o}\right)} \tag{3.61}$$

$$X_L = \omega' Z_o g_1 \tag{3.62}$$

$$X_{LC}\Big|_{\omega=\omega_{c,3dB}} = X_L\Big|_{\omega'=1} \tag{3.63}$$

where ω' (=1), g_1(=2), and Z_o (=50 Ω) are the normalized 3-dB cutoff frequency, element value of one-pole Butterworth prototype LPF, and port impedance, respectively, and $\omega_o = \left(1/\sqrt{L_{k1}C_{k1}}\right)$.

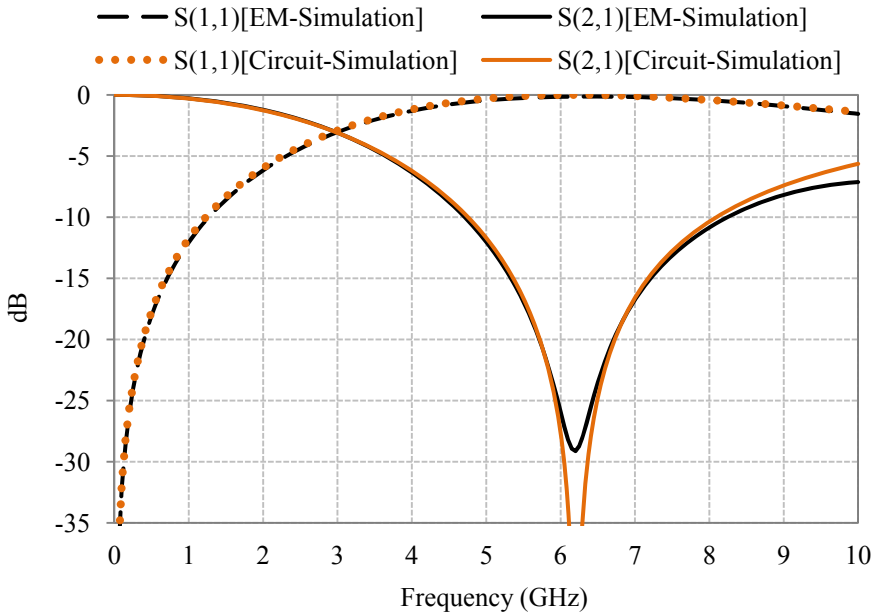

Fig. 3.7. S-parameters of the equivalent *LC* network with the EM simulation results.

As an example of the parameter-extraction procedure, *a*, *b*, *w*, and *g*, which are the dimensions of the DGS section shown in Fig. 3.3, have been chosen to be 5.5, 5.5, 0.637, and 0.637 mm, respectively. The substrate for simulations is Teflon with 0.635-mm-thick and a dielectric constant of 9.5. The simulation result is shown in Fig. 3.7. There is an attenuation pole near 6.06 GHz in the field simulation result. The circuit parameters for the derived equivalent circuit can be extracted from the simulation result as explained before. The simulation result of the proposed DGS unit section can be matched to the one-pole Butterworth-type low-pass response, which has 3-dB cutoff frequency at 2.96 GHz. The series reactance value shown in Fig. 3.6 can be easily calculated by using the prototype element value of the one-pole Butterworth response. The prototype element value is given by various references [32], [33]. The parallel capacitance value for the given DGS unit dimension can be extracted from the attenuation pole location.

TABLE 3.1

Extracted equivalent circuit parameters for the unit DGS section presented in Fig. 3.4

	DGS Dimensions (g = 0.6373 mm, w = 0.6373 mm)		
	a = b = 7 mm	a = b = 5.5 mm	a = b = 4 mm
Cutoff frequency (GHz)	2.2	2.96	4.194
Attenuation pole location (GHz)	4.93	6.204	7.956
Inductance (nH)	5.794	4.146	2.74
Capacitance (pF)	0.179	0.159	0.146

TABLE 3.2

Extracted equivalent circuit parameters for the unit DGS section presented in Fig.3.5

	DGS Dimensions (a = b =5.5 mm)		
	g = 0.637 mm	g = 0.837 mm	g = 1.032 mm
Cutoff frequency (GHz)	2.96	2.85	2.9
Attenuation pole location (GHz)	6.204	6.3	6.54
Inductance (nH)	4.146	4.333	4.4
Capacitance (pF)	0.159	0.147	0.134

The calculated inductance and capacitance of the DGS are 4.146 nH and 0.159 pF, respectively. Fig. 3.7 shows an excellent agreement between the EM simulated S-parameters and the new ones calculated using LC circuit. Advanced Design System (ADS), a circuit simulator from Agilent Technologies, has been used for the calculation. This agreement means that the modeling technique is valid in extracting the equivalent-circuit elements. It should be noted that this is one of the great advantages of DGS because it is possible to define the unit element of the DGS and to establish its equivalent circuit, while the conventional planar transmission lines with a periodic structure such as a EBG have difficulty in defining the unit element and to extract the modeled circuit element.

Tables 3.1 and 3.2 show the extracted equivalent circuit parameters for the defected ground structure unit section which are simulated in Fig. 3.4 and 3.5. By these results, it is clear that the dimensions a and b influence the inductance value while the gap distance (g) controls the value of the capacitance.

3.3.2.2. Parallel *RLC*-Circuit

In the previous section, we discussed the equivalent circuit of the dumbbell DGS based on the lumped elements, L and C extracted from EM simulations [30-31]. In this section, we also consider the radiation and surface wave losses by including the parallel resistance *R* in the equivalent circuit [28], as shown in Fig. 3.8.

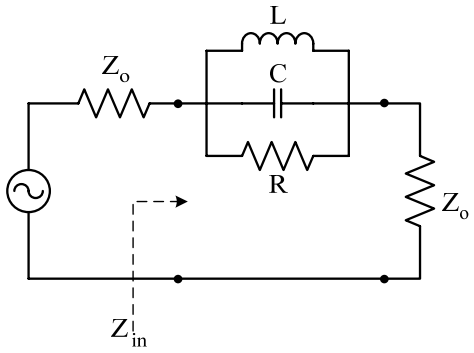

Fig. 3.8. The equivalent circuit of the DGS with parallel resistance [28].

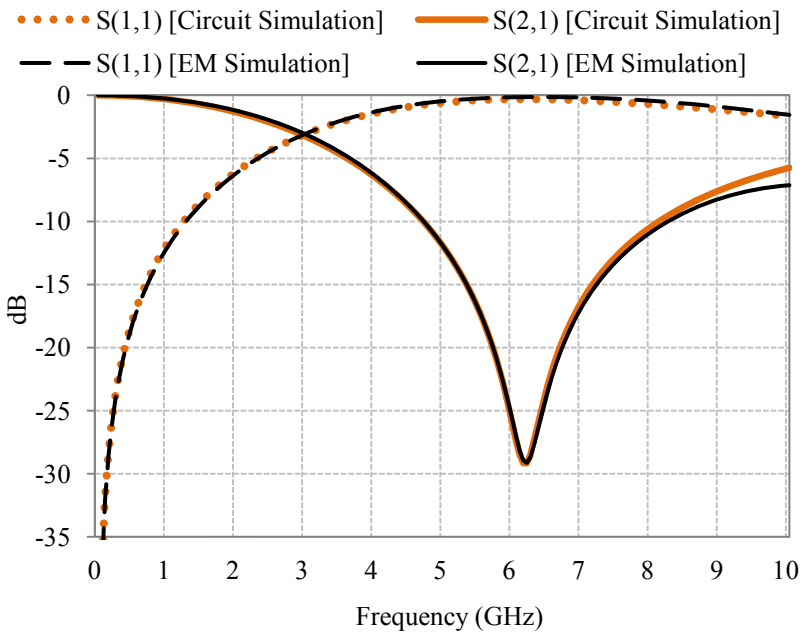

Fig. 3.9. S-parameters of the equivalent parallel *RLC*-circuit and the EM simulation responses.

As explained previously, the values of the extracted *L* and *C* are obtained from the electromagnetic simulation using the center angular frequency of the

stopband (ω_o) and 3-dB cutoff angular frequency ($\omega_{c,\ 3\ dB}$) taken from the S_{21} curve, using Eqs. (3.61), (3.62) and (3.63).

Using $S_{11}(\omega)$ obtained from EM simulation, the resistance R is determined by equating $S_{11}(\omega) = (Z_{in} - Z_o)/(Z_{in}+Z_o)$ at $\omega=\omega_o$ giving

$$R = \frac{2Z_o}{\sqrt{\frac{1}{|S_{11}(\omega)|^2} - \left(2Z_o\left(\omega C - \frac{1}{\omega L}\right)\right)^2} - 1} \tag{3.64}$$

As an example of this equivalent circuit, we present the equivalent circuit of the same structure presented in Fig. 3.7, but with a parallel resistance to compensate the losses. Fig. 3.9 shows a comparison between the circuit simulation using ADS and the EM simulation using Zeland IE3D. The extracted parameters are: L=4.146 nH, C=0.159 pF and R=2.8 kΩ.

3.3.2.3. π – Equivalent Circuit

A more complicated equivalent circuit was presented by Park at al. in 2002 [34]. The proposed equivalent circuit includes the parallel capacitance that is due to the relatively large fringing field at the step discontinuity plane on metallic ground surface.

Since the parallel capacitance might change the characteristic impedance level and electrical length of the DGS unit section, it should be considered as a part of equivalent circuit for more accurate modeling procedure. Fig. 3.10 shows the newly proposed equivalent circuit.

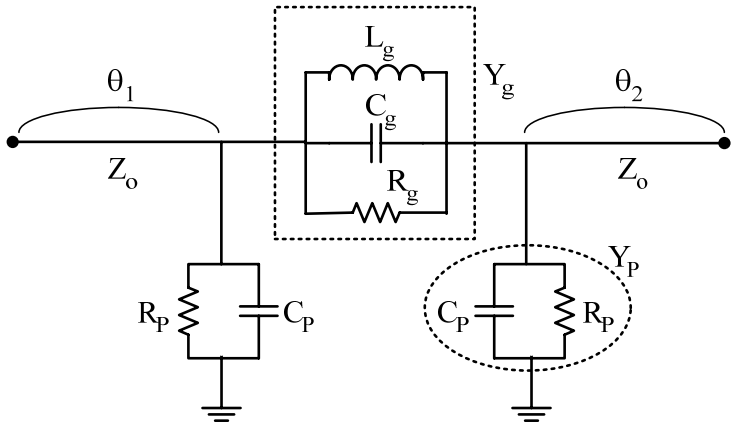

Fig. 3.10. The π-equivalent circuit of the dumbbell DGS [34].

In order to derive the equivalent circuit elements, the S-parameters of unit DGS cell at the reference plane should be calculated by EM-simulation. Once the S-parameters are calculated, by using the relation between the S-parameter and ABCD-parameter the equivalent circuit parameter can be extracted as follows.

$$A = \frac{(1+S_{11})(1-S_{22})+S_{12}S_{21}}{2S_{21}} = 1+\frac{Y_g}{Y_p} \tag{3.65}$$

$$B = \frac{(1+S_{11})(1+S_{22})-S_{12}S_{21}}{2S_{21}} = \frac{1}{Y_g} \tag{3.66}$$

$$C = \frac{1}{Z_o}\frac{(1-S_{11})(1-S_{22})-S_{12}S_{21}}{2S_{21}} = 2Y_p + \frac{Y_p^2}{Y_g} \tag{3.67}$$

$$D = \frac{(1-S_{11})(1+S_{22})+S_{12}S_{21}}{2S_{21}} = 1+\frac{Y_p}{Y_g} \tag{3.68}$$

The resulting equivalent circuit parameters are given by:

$$Y_g = \frac{1}{B} = \frac{1}{R_g} + jB_r \tag{3.69}$$

$$Y_p = \frac{A-1}{B} = \frac{1}{R_p} + jB_p \tag{3.70}$$

$$C_g = \frac{B_r}{\omega_o\left(\frac{\omega}{\omega_o}-\frac{\omega_o}{\omega}\right)} \;,\; L_g = \frac{1}{\omega_o^2 C_g} \;,\; C_p = \frac{B_p}{\omega} \tag{3.71}$$

Fig. 3.11 shows the example for the extraction of the equivalent circuit parameter of the same circuit shown in Fig. 3.9. The extracted parameters are: L_g=4.146 nH, C_g=0.159 pF, R_g=2762 Ω, R_p=111890 Ω, C_p=0.026 pF.

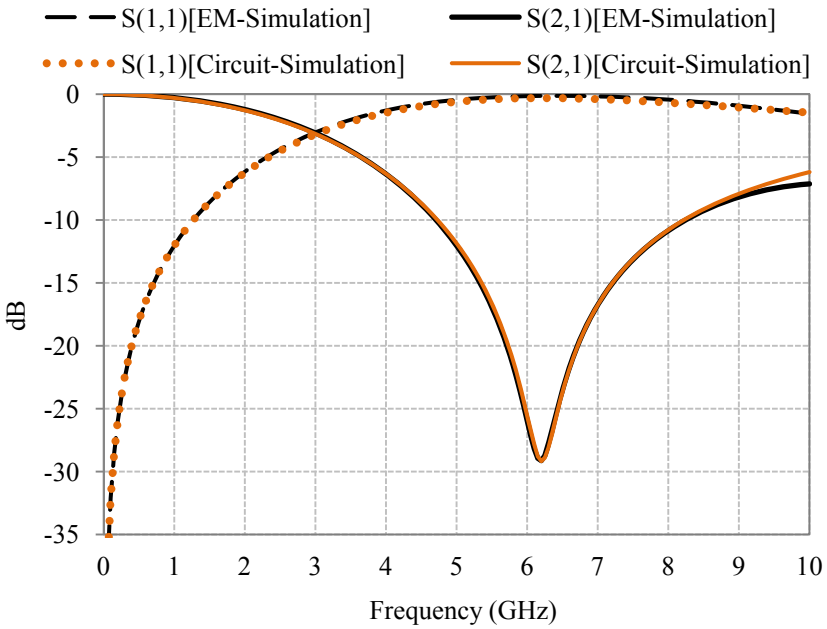

Fig. 3.11. EM and circuit simulations of the π-equivalent circuit.

3.3.2.4. Conclusion

Through this section, we have explained the equivalent circuit of the dumbbell defected ground structure. First, a simple single pole, parallel *LC*-circuit is presented. Then to consider the radiation and surface wave losses of the structure, a parallel resistance is added to the structure. Finally, the fringing capacitance of the structure is considered in the π-equivalent circuit.

Although the π-equivalent circuit is the most accurate, as it takes all effects into consideration, the parallel *RLC*-circuit is accurate enough to be used to represent the DGS section and simpler to calculate.

On the other hand, if the losses are not to be considered in a design process, then the first parallel *LC*-circuit might be used in the design due to its simplicity, in addition, it contains the main required data needed in the design, as will be shown in the following section.

3.3.3. Low-Pass Filter Design

3.3.3.1. Low-Pass Filter of Order Three

The low-pass filter using the DGS circuit has a number of attractive features, which include the following [30]:

1) Simple structure.
2) Very wide and deep stopband compared to that of conventional low-pass filters.
3) Low insertion loss.
4) Extremely small element values for implementation of low-pass filters can be realized.

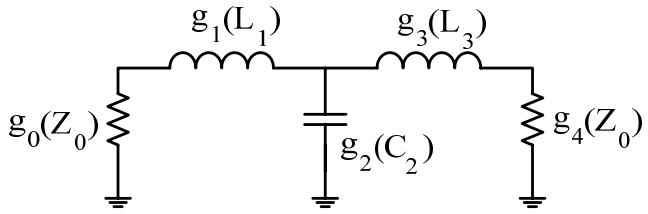

Fig. 3.12. Three-pole Chebychev prototype LPF.

The method of designing a three-pole LPF using the DGS is discussed here. Fig. 3.12 depicts the prototype circuit of a three-pole LPF, where element values represent the normalized element values of a Chebychev prototype LPF for the given ripple. According to the design theory of filters, in order to transform the prototype LPF to the LPF composed of lumped elements, the values of *L* and *C* can be determined owing to the impedance and frequency scaling rules expressed in [32].

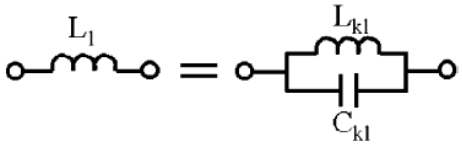

Fig. 3.13. Equality of the series inductor to a parallel LC circuit.

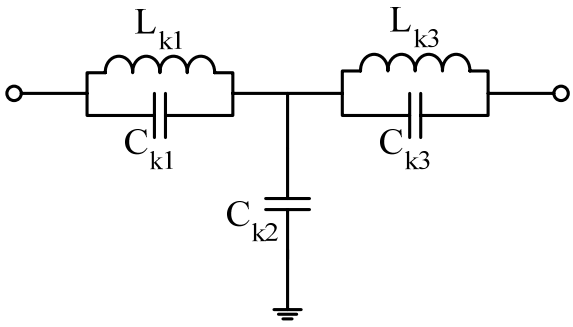

Fig. 3.14. Modified three-pole prototype LPF using parallel LC circuit.

In order to replace L_1 by the DGS shown in Fig. 3.3, the equivalence illustrated in Fig. 3.13 should be satisfied at ω_c; hence, two reactance values must be equal, as expressed in Eq. (3.63). Fig. 3.14 shows the new prototype three-pole LPF of which two inductors have been replaced by the parallel *LC*-equivalent circuit of the DGS. Since L_1 is equal to L_3, the parallel resonator of $L_{k1} - C_{k1}$ is exactly the same as the $L_{k3} - C_{k3}$ resonator.

The parallel capacitance in a lumped low-pass filter prototype can be realized by using the parallel open stub. These open stubs are realized either with a T-junction structure or a cross-junction structure.

It should be noted that for the implementation of high-impedance inductance with a conventional microstrip, the conductor width becomes narrow. This is a limitation in using microstrip low-pass filter configuration for high-power applications. By employing the proposed DGS sections, extremely small element values for implementation of a low-pass filter can be realized. The high-impedance inductance sections are realized by using DGS sections with a conductor width corresponding to a 50 Ω microstrip so that it can be expected that DGS low-pass filters improve the power-handling capability.

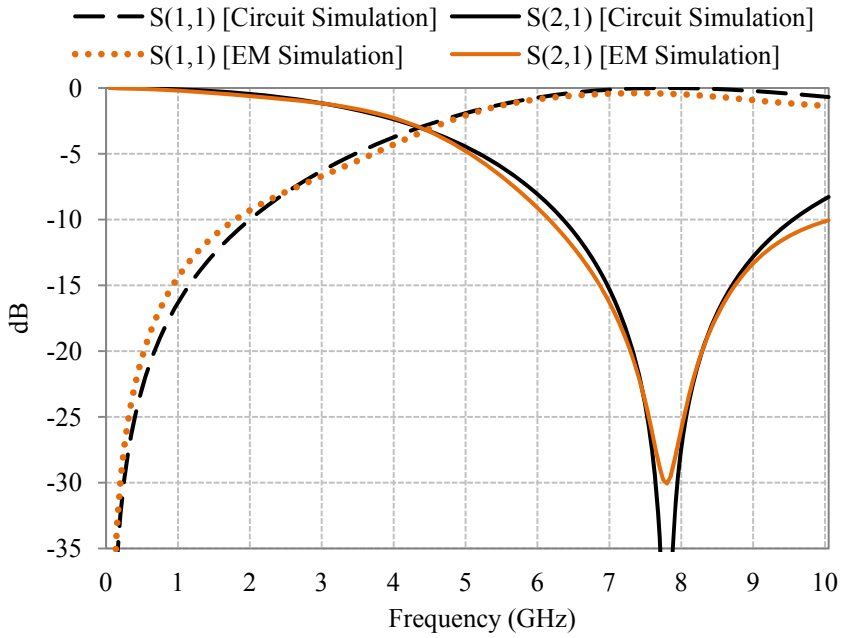

Fig. 3.15. EM and circuit simulations of the dumbbell structure used in the filter design.

Considering a dumbbell structure with a=b=4 mm, w=0.637 mm, and g=0.5 mm, the equivalent L_{k1} and C_{k1} are 2.548 nH and 0.166 pF as shown in Fig. 3.15, then f_c is 4.19 GHz. Now the values of L_1, C_2 and L_3 can be calculated after having been transformed by frequency and impedance scaling. The resultant values for the three-pole Chebyshev with a 0.01-dB ripple are summarized in Table 3.3, while the dimensions of the filter and its simulated responses are shown in Fig. 3.16 and Fig. 3.17, respectively.

TABLE 3.3

Prototype elements of the three-pole Chebychev LPF

Prototype Elements		Scaled Elements		Final elements	
g_0	1	Z_0	50		
g_1	0.629	L_1	2.703 nH	$L_{k1} - C_{k1}$	2.548 nH -0.166 pF
g_2	0.97	C_2	1.667 pF	C_{k2}	1.667 pF
g_3	0.629	L_3	2.703 nH	$L_{k1} - C_{k1}$	2.548 nH -0.166 pF
g_4	1	Z_0	50		

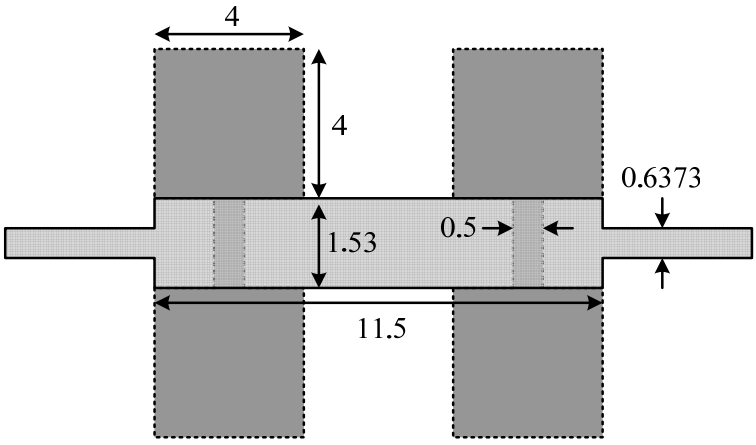

Fig. 3.16. Complete dimensions of the LPF of order three of the prototype elements in Table 3.3.

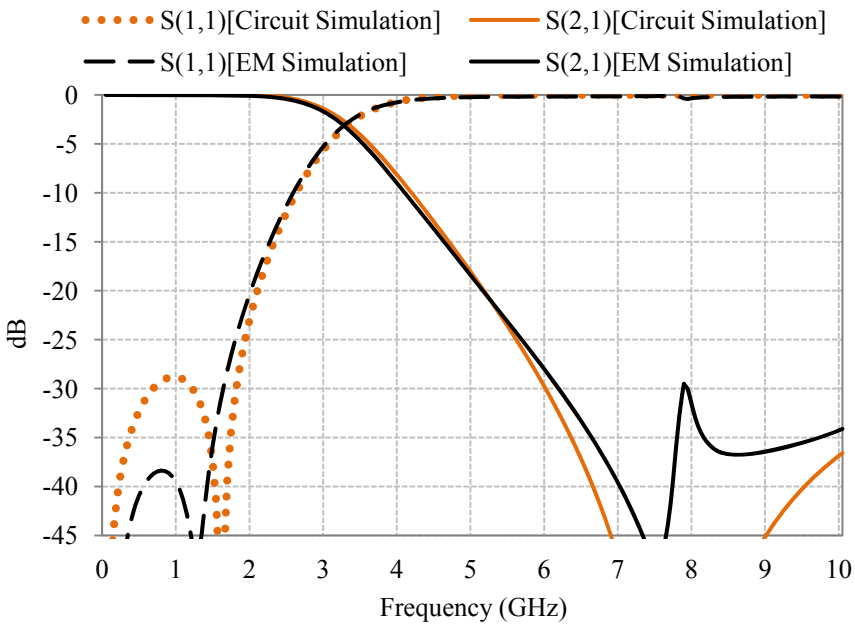

Fig. 3.17. EM and circuit simulations of the LPF of order three.

As mentioned previously, the capacitance may be implemented using different techniques, an open circuited stub through a T-junction or a cross-junction may be used as in [30] and [36]. Here, the capacitance has been implemented using a simple microstrip line with a compensated width in order to get the proper capacitance element as in [31].

According to the basic theories of transmission lines, a transmission line of low characteristic impedance has a capacitive element equivalency. The equivalent capacitance of a transmission line with the characteristic impedance (Z_o) and length (ℓ) is expressed as [30]:

$$C = \frac{1}{\omega Z_o} \sin^{-1}\left(\frac{2\pi\,\ell}{\lambda_g}\right) \tag{3.72}$$

However, additional equivalent inductance of the transmission line does also exist at the same time and is expressed as L_a by:

$$L_a = \frac{Z_o}{2\omega} \sin\left(\frac{2\pi\,\ell}{\lambda_g}\right) \tag{3.73}$$

which might be the main cause of the shift in the frequency.

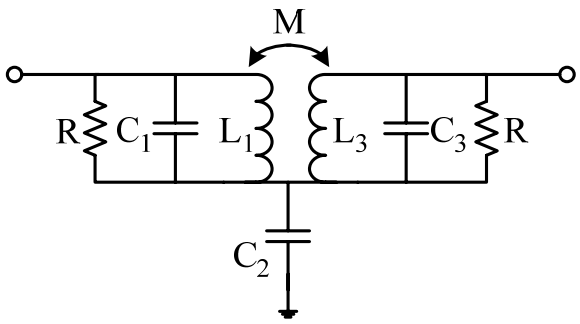

Fig. 3.18. Improved circuit model for the DGS in LPF design [37].

In [37], a more accurate equivalent circuit is proposed for the filter where the effect of coupling between the two defected ground structures is considered. The resistance R, in Fig. 3.18, represents the loss of the slot due to radiation and surface waves. The interaction between the slots is accounted by the mutual inductance, $M = K_{12}\sqrt{L_1 L_3}$. In our case due to the symmetrical slots, L_1=L_3, and the capacitance C_1=C_3, calculated by Eq. (3.61)-(3.63). The mutual inductance M is optimized using a ready-made software package and there are no accurate equations for it, which is considered the basic disadvantage of this equivalent circuit.

3.3.3.2. DGS Based Filter on Coplanar Waveguide Technology

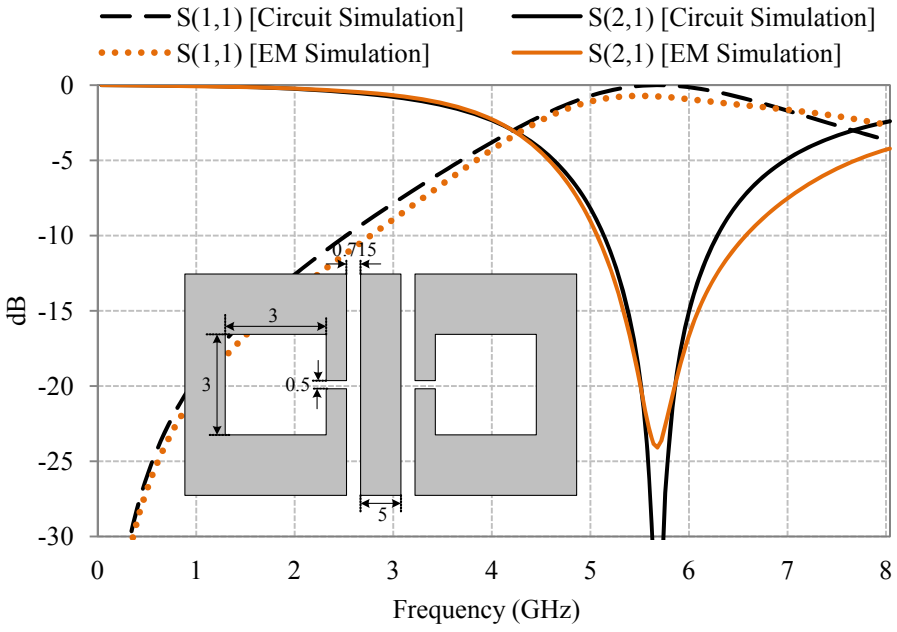

Fig. 3.19. EM and circuit simulations of the dumbbell DGS on CPW. The layout of the structure with dimensions in mm.

The same design procedure can be applied to design a LPF using DGS on CPW ("DGSCPW"). Fig. 3.19 shows the response of a single DGS on CPW. The equivalent *LC*-circuit parameters are given by: L=1.724 nH, and C=0.461 pF.

To implement the shunt capacitance, this is done by using transmission lines with lower impedance. A CPW section with lower impedance may be implemented by narrowing the gap between the signal line and ground planes without touching the main signal line. This is great advantage because the width of signal line is constant. At least, there are no discontinuity elements in the main signal line in CPW structure. Only the gaps are changed so that the line impedance is much lower than 50 Ω, for example 30 Ω in this work, by moving the ground plane towards the signal line. Therefore, the air-bridged bonding wires, which are essential in CPW discontinuity elements such as T-junctions or cross-junctions, are not required.

TABLE 3.4

Prototype elements of the three-pole Chebychev LPF for Coplanar Waveguide

Prototype Elements		Scaled Elements		Final elements	
g_0	1	Z_0	50		
g_1	0.629	L_1	2.703 nH	$L_{k1} - C_{k1}$	1.724 nH -0.461 pF
g_2	0.97	C_2	1.667 pF	C_{k2}	1.295 pF
g_3	0.629	L_3	2.703 nH	$L_{k1} - C_{k1}$	1.724 nH -0.461 pF
g_4	1	Z_0	50		

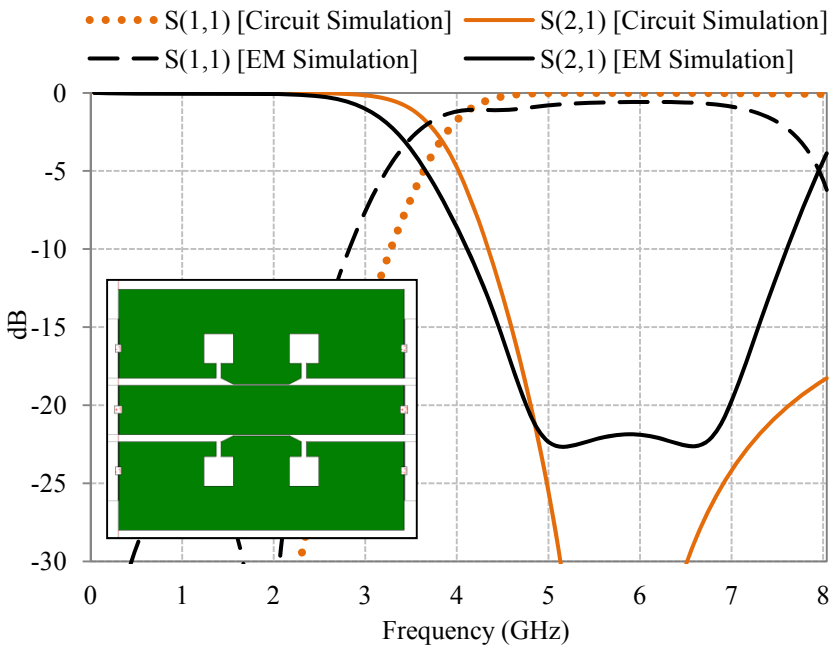

Fig. 3.20. EM and circuit simulations of the dumb-bell DGS filter on CPW.

Using the same technique in the previous section, Table 3.4 shows the prototype element values of the structure while Fig. 3.20 shows the circuit and the EM simulated response.

3.3.4. Defected Ground Structures as Periodic Structures

Since 2001, a lot of researchers have been trying to use periodic defected ground structures to enhance the performance of amplifiers, power dividers, and oscillators [37, 38]. They proposed the use of a microstrip line with periodic defected ground structures (DGS) at the output for harmonic tuning of different components.

In [39], they applied a periodic uniform dumbbell shaped DGS etched in the ground plane of a microstrip line as shown in Fig. 3.21 (a), in order to supress the higher order modes of a power amplifier. Later in 2004, they started considering the non-uniform periodic defected ground structure with relative amplitude distribution following a Chebychev or binomial distribution [40, 41] or exponential function as in [42], Fig. 3.21 (b), (c)).

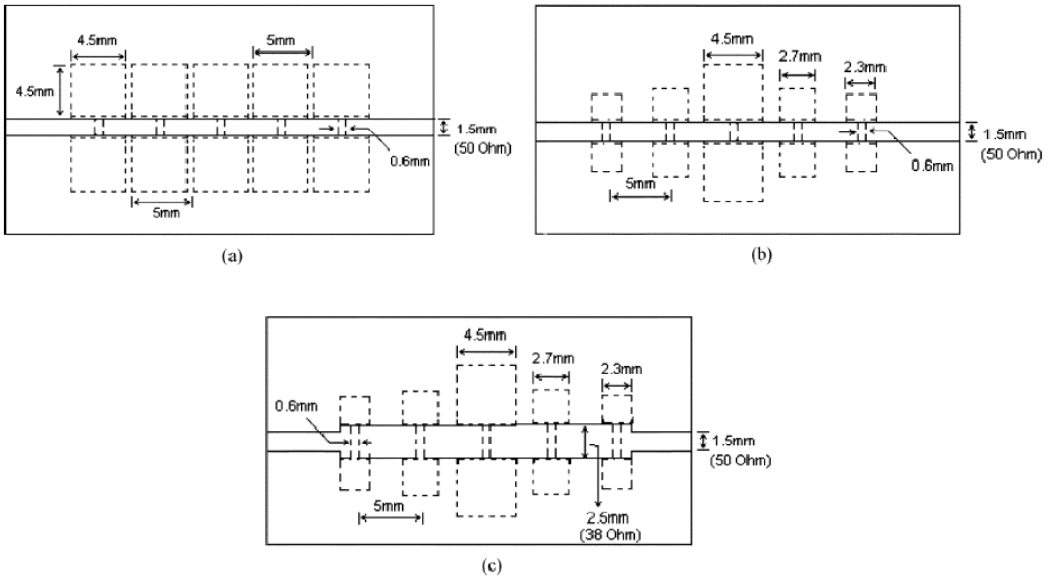

Fig. 3.21 (a) A dumbbell shaped DGS etched in the ground plane of a microstrip line (a) with periodic uniform distribution, (b) binomial distribution, (c) exponential distribution.

3.4. Conclusion

In the first part of this chapter, two different analytical approaches are used for understanding the bandgap phenomenon, the Coupled-Wave Theory and the Bloch-Wave Formalism. Both techniques led to the same conclusion, which is, all periodic structures would lead to inhibit the propagation of electromagnetic waves in a certain band of frequency.

In the second part of this chapter, the different equivalent circuits of defected ground structures are investigated based on the observations and study for the dumbbell shape DGS. The drawn conclusion is that the *LC* equivalent circuit is useful enough for representing the DGS in the design of more complicated structures; still it represents neither losses nor coupling of the structure with adjacent ones. Using this equivalent circuit, the design procedures for the implementation of higher order low-pass filters on microstrip transmission line and coplanar waveguide are demonstrated.

References of Chapter Three

[1] T. J. Ellis and G. M. Rebeiz, "MM-wave tapered slot antennas on micro-machined photonic bandgap dielectrics," proceedings of *IEEE MTT-S Int. Microw. Symp. Dig.*, pp. 1157–1160, June 1996.

[2] M. M. Sigalas, R. Biswas, and K. M. Ho, "Theoretical study of dipole antennas on photonic–crystal substrate," *Microw. Opt. Tech.. Lett.*, Vol. 13, No. 4, pp. 205–209, Nov. 1996.

[3] M. P. Kesler, J. G. Maloney, and B. L. Shirley, "Antenna design with the use of photonic bandgap material as all dielectric planar reflectors," *Microw. Opt. Tech. Lett.*, Vol. 11, No. 4, pp. 169–174, Mar. 1996.

[4] V. Radisic, Y. Qian, R. Coccioli, and T. Itoh, "Novel 2-D photonic bandgap structure for microstrip lines," *IEEE Microw. Guided Wave Lett.*, Vol. 8, No. 2, pp. 69–71, Feb. 1998.

[5] E. Yablonovitch, "Photonic band-gap structures," *J. Opt. Soc. Amer. B, Opt. Phys.*, Vol. 10, pp. 283–295, Feb. 1993.

[6] Y. Qian, F. R. Yang, and T. Itoh, "Characteristics of microstrip lines on a uniplanar compact PBG ground plane," proceedings of *Asia Pacific Microw. Conf. (APMC)*, pp. 589–592, Dec. 1998.

[7] Y. Qian and T. Itoh, "Planar periodic structures for microwave and millimeter wave circuit applications," proceedings of *IEEE MTT-S Int. Microwave Symp. Dig.*, pp. 1533–1536, June 1999.

[8] Y. Qian, F. R. Yang, and T. Itoh, "Characteristics of microstrip lines on a uniplanar compact PBG ground plane," proceedings of *Asia Pacific Microw. Conf.*., pp. 589–592, Dec. 1998.

[9] V. Radisic, Y. Qian, and T. Itoh, "Broadband power amplifier using dielectric photonic bandgap structure," *IEEE Microw. Guided Wave Lett.*, Vol. 8, No.1, pp. 13–14, Jan. 1998.

[10] V. Radisic, Y. Qian, and T. Itoh, "Broad-band power amplifier integrated with slot antenna and novel harmonic tuning structure," proceedings of *IEEE MTT-S Int. Microwave Symp. Dig.*, pp. 1895–1898, June 1998.

[11] F. R. Yang, Y. Qian, R. Coccioli, and T. Itoh, "A novel low loss slow-wave microstrip structure," *IEEE Microw. Guided Wave Lett.*, Vol. 8, No. 11, pp. 372–374, Nov. 1998.

[12] K. P. Ma, K. Hirose, F. R. Yang, Y. Qian, and T. Itoh, "Realization of magnetic conducting surface using novel photonic bandgap structure," *Electron. Lett.*, Vol. 34, No. 21, pp. 2041–2042, Nov. 1998.

[13] Lord Rayleigh, "On the influence of obstacles arranged in rectangular order upon the properties of a medium", Philos. Mag., Vol.34, pp.481-502, 1892.

[14] N. P. Kasterin, Vers. Akad. Van Wetenschappen Amsterdam, Vol. 6, p. 460, 1897-8; Diss. Moscow, 1903.

[15] P. P. Ewald, “Zur Begrundung der Kristalloptik,” Ann. Phys. (Lepzig), Vol. 49, pp.1-38, 1916.

[16] L. Brillouin and M. Parodi, Wave Propagation in Periodic Structures, Dover, New York, 1953.

[17] S. Wang and S. K. Sheem, “Two dimensional distributed feedback devices and lasers”, US patent publication US-3,884,549 A, May 20, 1975.

[18] H. Kogelnik and C.V. Shank, “Coupled wave theory of distributed feedback lasers,” J. of Appl. Phys., Vol. 43, No.5, pp. 2327-2335, May 1972.

[19] E. Yablonovitch, "Inhibited spontaneous emission in solid state physics and electronics", Phys. Rev. Lett., Vol. 58, No. 20, p. 2059, 1987.

[20] A. Yariv and P. Yeh, Optical Waves in Crystals, Wiley & Sons, 1984.

[21] D. F. Sievenpiper, M. E. Sickmiller, and E. Yablonovitch, “3D wire mesh photonic crystals,” Phys. Rev. Lett., Vol. 76, No. 14, pp. 2480–2483, Apr. 1996.

[22] J. Shumpert, T. Ellis, G. Rebeiz, and L. Katehi, “Microwave and millimeter wave propagation in photonic band-gap structures,” proceedings of Ant. Prop. Symp. (AP-S), p. 678, 1997.

[23] E. R. Brown, C. D. Parker, and E. Yablonovitch, “Radiation properties of a planar antenna on a photonic-crystal substrate,” J. Optical Soc. America B, Vol. 10, pp. 404–407, Feb. 1993.

[24] H. Y. D. Yang, N. G. Alexopoulos, and E. Yablonovitch, “Photonic band-gap materials for high-gain printed circuit antennas,” IEEE Trans. Ant. Prop., Vol. 45, No. 1,185–187, Jan. 1997.

[25] R. D. Meade, K. D. Brommer, A. M. Rappe, and J. D. Joannopoulos, “Photonic bound states in periodic dielectric materials,” Phys. Rev. B., Vol. 44, pp. 13772–13774, Dec. 1991.

[26] C. S. Kim, J. S. Park, D. Ahn, J. B. Lim, “A novel 1-D periodic defected ground structure for planar circuits,” IEEE Microw. Wireless Comp. Lett., Vol. 10, No. 4, pp. 131 – 133, April 2000.

[27] J. S. Lim, C. S. Kim, J. S. Park, D. Ahn, S. Nam, “Design of 10 dB 90° branch line coupler using microstrip line with defected ground structure,” Electron. Lett, Vol. 36, No. 21, pp. 1784 – 1785, Oct. 2000.

[28] I. Chang and B. Lee, “Design of defected ground structures for harmonic control of active microstrip antenna,” proceedings of IEEE Ant. Prop Symp. (AP-S), Vol. 2, pp. 852-855, June 2002.

[29] F. R. Yang, K. P. Ma, Y. Qian, and T. Itoh, “A novel TEM waveguide using uniplanar compact photonic-bandgap (UC-PBG) structure,” *IEEE Trans. Microw. Theory Tech.*, Vol. 47, No. 11, pp. 2092–2098, Nov. 1999.

[30] J. S. Lim, C. S. Kim, D. Ahn, Y. C. Jeong and S. Nam, “Design of low-pass filter using novel microstrip DGS,” *IEEE Trans. Microw. Theory Tech.*, Vol. 49, No.1, pp. 86–93, Jan. 2001.

[31] J. S. Lim, C. S. Kim, D. Ahn, Y. C. Jeong and S. Nam "Design of low-pass filters using defected ground structure," *IEEE Trans. Microwave Theory Tech.*, Vol. 53, No.8, pp. 2539–2545, Jan. 2005.

[32] D. M. Pozar, *Microwave Engineering*. Reading, MA: Addison-Wesley, 1990, pp. 486–517.

[33] J. I. Park, C. S. Kim, J. Kim, J. S. Park, Y. Qian, D. Ahn, and T. Itoh, "Modeling of a photonic bandgap and its application for the low-pass filter design," proceedings of Asia Pacific Microw. Conf. (*APMC)*, pp. 331–334, Dec. 1999.

[34] J. S. Park, J. H. Kim, J. H. Lee, S. H. Kim, and S. H. Myung, "A novel equivalent circuit and modeling method for defected ground structure and its application to optimization of a DGS lowpass filter," proceedings of IEEE MTT-S Int. Microw. Symp. Dig., Vol.1, pp. 417-420, June 2002.

[35] J. Park, C. S. Kim, J. Kim, J. S. Park, Y. Qian, D. Ahn, and T. Itoh, "A design of low-pass filter using the novel microstrip defected ground structure," *IEEE Trans. Microw. Theory Tech.*, Vol. 49, No.1, pp. 86–93, Jan. 2001.

[36] J. S. Lim, C. S. Kim, Y. T. Lee, D. Ahn, S. Nam, "A new type of low pass filter with defected ground structure," proceedings of *Europ. Microw. Conf (EuMC),* pp. 1 – 4, Oct. 2002.

[37] A. Rahman, A. Boutejdar, A. K. Verma, G. Nadim, A.S. Omar, "Improved circuit model for DGS based lowpass filter," proceedings of *IEEE Ant. Prop. Symp.,* Vol.1, pp. 998-1001,June 2004.

[38] J. S. Lim, H. S. Kim, D. Ahn, and S. Nam, "A power amplifier with efficiency improved using defected ground structure," *IEEE Microwave Guided Wave Lett.*, Vol. 11, No. 4, pp. 170–172, Apr. 2001.

[39] Y. T. Lee, J. K. Lim, J. S. Park, A. Dal, and S. Nam, "A novel phase noise reduction technique in oscillator using defected ground structure," *IEEE Microw. Guided Wave Lett.*, Vol. 12, No. 2, pp. 39–41, Feb. 2002.

[40] N. C. Karmakar, "Improved performance of photonic band-gap microstripline structures with the use of Chebyshev distributions," *Microw. Opt. Tech. Lett.*, Vol. 33, No. 1, pp. 1–5, April 2002.

[41] N. C. Karmakar, "Theoretical investigations into binomial distributions of photonic bandgaps in microstrip line structures," *Microwave Opt. Tech. Lett.*, Vol. 33, No. 3, pp. 191–196, May 2002.

[42] H. W. Liu, Z. F. Li, X. W. Sun, J. F. Mao, "An improved 1D periodic defected ground structure for microstrip line," *IEEE Microw. Wireless Comp. Lett.,* Vol. 14, No. 4, pp. 180 – 182, April 2004.

CHAPTER FOUR

NOVEL RECONFIGURABLE DEFECTED GROUND STRUCTURE RESONATOR FOR MULTI-STOPBAND FILTER ON COPLANAR WAVEGUIDE TECHNOLOGY

4.1. Introduction

Since the late 1980's, electromagnetic bandgap (EBG) structures [1]-[7] and defected ground structures (DGS) [7]-[14] have attracted the interest of many researchers, due to their interesting properties in terms of size miniaturization, suppression of surface waves and arbitrary stopbands. Since then, they have been used in many applications like lowpass filters [8], bandpass filters [6], [9], [10], antennas [7], waveguides [3] and others.

Recently, a great trend towards the implementation of a reconfigurable DGS where the location of the transmission zeros can be controlled and tuned may be seen from a number of recent publications [11]-[13]. However, still not a large amount of work has been published in this domain. In addition, most of the work that has been published so far has considered the structures by means of parallel *RLC* equivalent circuit to represent the transmission zeros in the response [8], [11], providing no insight into the underlying electromagnetic wave propagation principle and hence providing no design rules. On the other hand, some work used complicated methods like the Floquet's theorem [12], the Linpar method [10], or neural networks [14]. The disadvantages of these methods are their mathematical complexity and hence their limitations in providing initial design rules.

In this chapter, a novel reconfigurable Defected Ground Structure (DGS) resonator on Coplanar Waveguide (CPW) technology is presented. The resonator is endowed with an original design which enables the generation of multiple transmission zeros at arbitrary frequencies. The chosen design is indeed based on a slot defect created on the lateral ground planes of the CPW with the double

advantage to allow a simple reconfiguration, by means of surface mounted (or fabricated) components, and a very compact solution, by exploiting the transversal dimension of the CPW-TL.

The cell contains a number of diodes on each side of the coplanar waveguide ground planes. Four different states corresponding to four different diode configurations are presented here. The equivalent circuit of each state is obtained using the conventional circuit parameter extraction method. In addition to the parallel *RLC* equivalent circuit, electromagnetic explanation of the structure, using the slotline design equations of Janaswamy and Schaubert [15], is hereby presented providing simple and efficient design rules. These rules have been applied to the design of the structures centered at different arbitrary frequencies and validated by the simulated magnetic field distribution inside the etched slots using an FEM (Ansoft HFSS) simulation tool.

In this work, the reconfigurability is first proven by means of short bridges mounted in specific locations of the slot patterns. These bridges are then replaced by PIN diodes to give the switch effect. Simulated and measured results are presented in each case, where the effects of the PIN diode capacitance and resistance have also been studied.

This chapter is organized as follows; Section 4.2 presents briefly the description of the novel reconfigurable DGS. Section 4.3 addresses the design, fabrication, characterization and modeling of the reconfigurable DGS with the different configurations. Section 4.4 presents the final measurements of the reconfigurable DGS resonator using PIN diodes as tuning components. Finally, conclusions are outlined in Section 4.5 of this chapter.

4.2. Structure Description

The structure consists of a DGS resonator based on coplanar waveguide. The unit cell of the proposed DGS is shown in Fig. 4.1. The cell is made of two square resonators of different sizes, *a* and *b*, whose patterns are etched in the ground plane of the CPW with a slot width *t*. The smaller square is connected to the slot of the coplanar waveguide by means of a transverse gap of length w_1, while another is used to connect the bigger square to the smaller one of length w_2. The structure contains three diodes in each side of the ground plane. The first diode (S_1) is used to

disconnect the bigger square from the rest of the structure. The second diode (S_2) is used to divide the smaller resonator (smaller square) into two resonators of different lengths. Adding another degree of freedom, a third diode (S_3), is used to divide the bigger ring resonator into two.

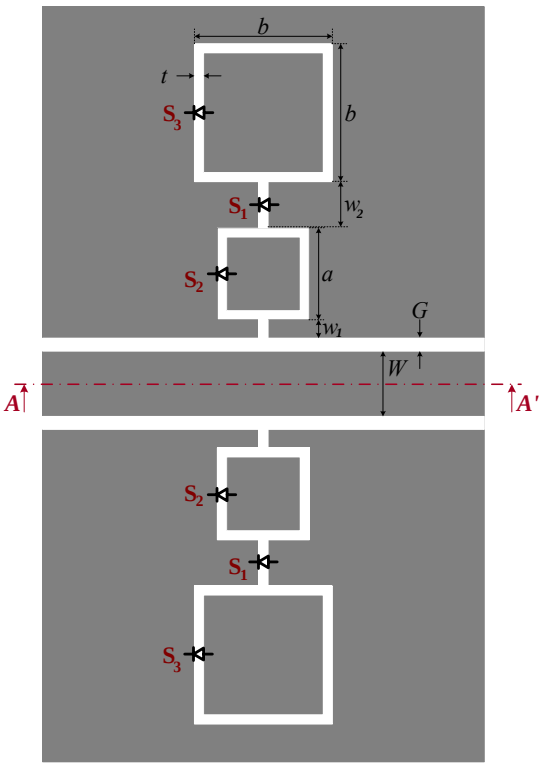

Fig. 4.1. Unit cell of the proposed DGS resonator.

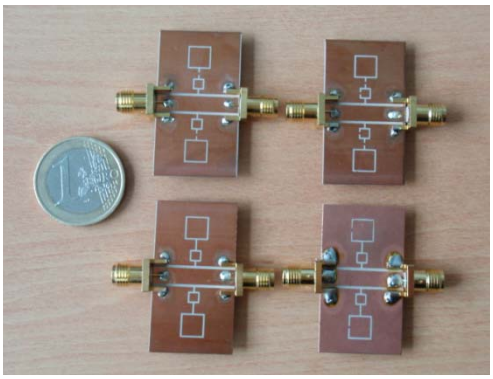

Fig. 4.2. Fabricated structure in four different cases.

This structure is designed and fabricated on Teflon substrate of dielectric constant ε_r=9.5, dielectric thickness h=0.635mm, and loss tangent 0.0035. The dimensions of the fabricated structure are: a=3 mm, b=6 mm, t=0.5 mm, w_1=1 mm and w_2=2.5 mm, where the CPW parameters are G/W/G =0.715/4/0.715 mm in order to attain 50 Ω of input line characteristic impedance. In the fabrication of these structures, as a first iteration, we modeled the diodes as ideal ones, i.e. the diodes are presented by either open circuits or short bridges as shown in Fig. 4.2, and then PIN diodes have been used to allow reconfigurability.

4.3. Study of the Reconfigurable DGS Resonator

In the previous section, we explained the structure of the DGS resonator. As mentioned, there are three diodes in each side of the ground plane, consequently different responses according to the different diode configurations will be considered. In each configuration, we will give the EM simulation, measured response and the equivalent circuit model of the DGS. Then using the slotline equations and the magnetic field distribution inside the slot, the resonant frequency of the transmission zeros will be proven.

The four different configurations that we are going to study are: S_1 is ON while S_2 and S_3 are OFF, S_1 and S_2 are ON while S_3 is OFF, all switches are OFF, and finally S_1 and S_2 are OFF while S_3 is ON.

4.3.1. Configuration One: S_1: ON, S_2: OFF and S_3: OFF

4.3.1.1. Simulation and Measurements Responses

In this case, the upper larger square resonator is isolated from the rest of the structure and therefore it is totally excluded from the structure transfer function, as shown in Fig. 4.3 (a). The structure has a transmission zero at 6 GHz as shown from the simulated and measured responses in Fig. 4.3 (b).

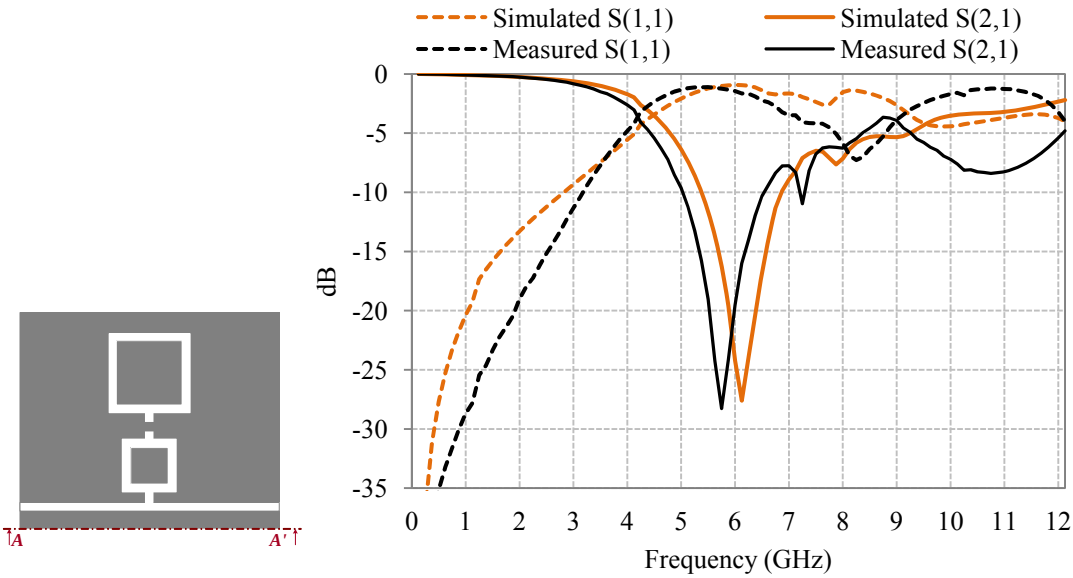

(a) (b)

Fig. 4.3. (a) Layout of the DGS when S_1 is ON, S_2 and S_3 are OFF. (b) Simulated and measured responses of the DGS when S_1 is ON, S_2 and S_3 are OFF.

4.3.1.2. Equivalent Circuit Extraction

Since the structure gives a single transmission zeros then it can be represented by one parallel *RLC* resonator as shown in Fig. 4.4.

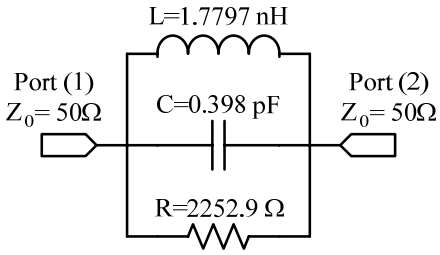

Fig. 4.4 Parallel *RLC* equivalent circuit model of configuration one.

To extract the parameters of the parallel *RLC* equivalent circuit model, the resonant frequency ω_0 and the 3-dB cutoff frequency ω_c are first determined from the EM simulations. The resonant frequency in terms of the parallel resonant circuit elements is given by:

$$\omega_0 = \frac{1}{\sqrt{LC}} \tag{4.1}$$

where L and C are the inductance and capacitance of the parallel inductor and capacitor, respectively. The 3-dB cutoff frequency is determined using the S_{21} curve. The equivalent impedance of the parallel resonance is given by

$$Z = \frac{1}{1/R + 1/j\omega L + j\omega C} \tag{4.2}$$

and from the circuit theory

$$S_{21} = \frac{2Z_0}{2Z_0 + Z} = \frac{2Z_0}{2Z_0 + \dfrac{1}{1/R + 1/j\omega L + j\omega C}} \tag{4.3}$$

at the 3 dB cutoff frequency point

$$|S_{21}| = \frac{2Z_0}{\sqrt{4Z_0^2 + \left(\dfrac{\omega_c / C}{\omega_0^2 - \omega_c^2}\right)}} = \frac{1}{\sqrt{2}}, \qquad \text{assuming } R >> Z_0 \tag{4.4}$$

Rearranging (4.4), the capacitance of the equivalent circuit model is given by

$$C = \frac{\omega_c}{2Z_0\left(\omega_0^2 - \omega_c^2\right)} \tag{4.5}$$

Substituting back in Eq. (4.1), the inductance value can be determined.

The resistance in the equivalent circuit model is best fitted around the resonant frequency ω_0. In this case, the equivalent impedance is $Z=R$ and the transmission loss S_{21} is

$$S_{21}\big|_{\omega_0} = \left|\frac{2Z_0}{2Z_0 + Z}\right| = \frac{2Z_0}{2Z_0 + R} \;\Rightarrow\; R = 2Z_0 \frac{1 - S_{21}\big|_{\omega_0}}{S_{21}\big|_{\omega_0}} \tag{4.6}$$

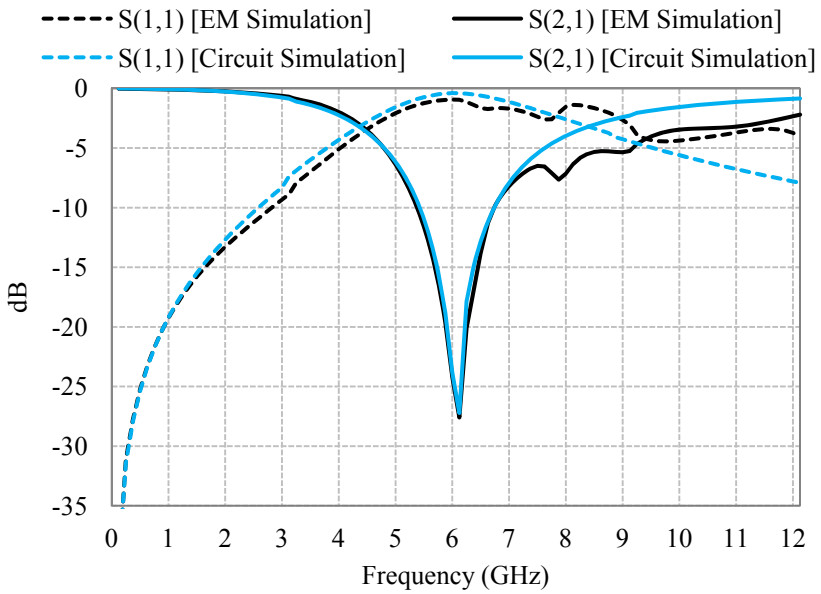

Fig. 4.5. EM and circuit simulated S-parameters of configuration one.

The extracted *R, L* and *C* for case two are 2.25 kΩ, 1.78 nH, and 0.4 pF, respectively, as shown in Fig. 4.4 for f_o=6 GHz, f_c=4.3 GHz and S_{21}=0.043 at f_o. EM simulation using Zeland IE3D version 12 and circuit simulation using Advanced Design Systems (ADS) are shown in Fig. 4.5.The two simulation results are in very good agreement.

4.3.1.3. EM Explanation and Design Rules

In the previous section, the response of the structure using the cascaded parallel *RLC* circuits is explained, as done in most of the defected ground structure literature. Although it is a very good step to represent the structure by lumped elements, this equivalent circuit doesn't give any insight to the electromagnetic wave propagation in the structure nor any design rules. In this section, the existence of the transmission zeros in the structure will be explained using the slotline transmission line design equations.

To investigate the EM wave propagation in the CPW structure, it is considered as two slotline structures in parallel to each other, then considering the upper part of the structure as shown in Fig. 4.6 (a), it is found that the path difference between path (1), denoted by the continuous blue line, and path (2), denoted by the

dotted red line, is 14 mm. This electrical path difference is equal to $\lambda_g/2$ at 6 GHz according to the slotline equations used; therefore a transmission zero is produced due to 180° phase difference obtained at point 'P'. Fig. 4.6 (b) shows the magnetic field distribution in the slot, using the HFSS software, which validates the theory that this path difference corresponds to $\lambda_g/2$ at 6 GHz causing the existence of a transmission zero.

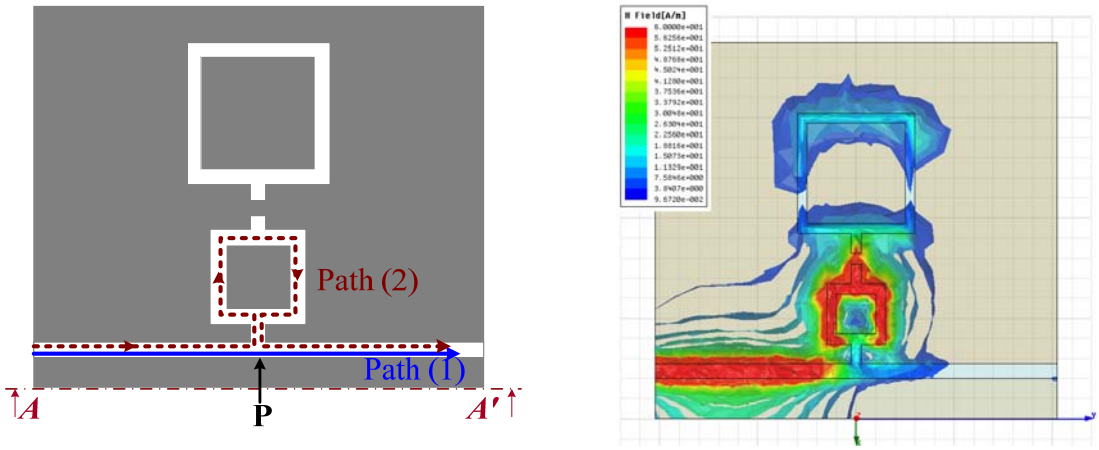

(a) (b)

Fig. 4.6. (a) Magnetic current paths when S_1 is ON, S_2 and S_3 are OFF. (b) H-field distribution at 6 GHz.

The equations of the slotline used to explain the structure are the closed form expressions of Janaswamy and Schaubert [15] for low ε_r substrates obtained by curve-fitting the numerical results of Galerkin's method in the Fourier transform domain (Appendix One). For $0.0015 \le W/\lambda_0 \le 0.075$ and $3.8 \le \varepsilon_r \le 9.8$ (the range where our design exists):

$$\frac{\lambda_g}{\lambda_0} = 0.9217 - 0.277\ln(\varepsilon_r) + 0.0322\frac{W}{h}\left(\frac{\varepsilon_r}{0.435 + W/h}\right)^{1/2} - 0.01\left(4.6 - \frac{3.65}{\varepsilon_r^{\,2}(9.06 - 100W/\lambda_0)\sqrt{W/\lambda_0}}\right)\ln\left(\frac{h}{\lambda_0}\right) \tag{4.7}$$

Maximum absolute error = 3%

$$Z_0 = 73.6 - 2.15\varepsilon_r + (638.9 - 31.37\varepsilon_r)(W/\lambda_0)^{0.6} + \left(36.23\sqrt{\varepsilon_r^{\,2} + 41} - 225\right)\frac{W/h}{W/h + 0.879\varepsilon_r - 2} + 0.51(\varepsilon_r + 2.12)(W/h)\ln(100h/\lambda_0) - 0.753\varepsilon_r(h/\lambda_0)\sqrt{W/\lambda_0} \quad (4.8)$$

Maximum absolute error = 5.4 %

4.3.2. Configuration Two: S_1: ON, S_2: ON and S_3: OFF

4.3.2.1. Simulation and Measurements Responses

In this case, the upper square resonator is isolated as in the previous configuration, and the smaller resonator is divided into two unequal resonators as shown in Fig. 4.7 (a). Each resonator forms a transmission zero at the corresponding frequency (4.8 and 10.9 GHz). Simulated and measured responses are shown in Fig. 4.7 (b).

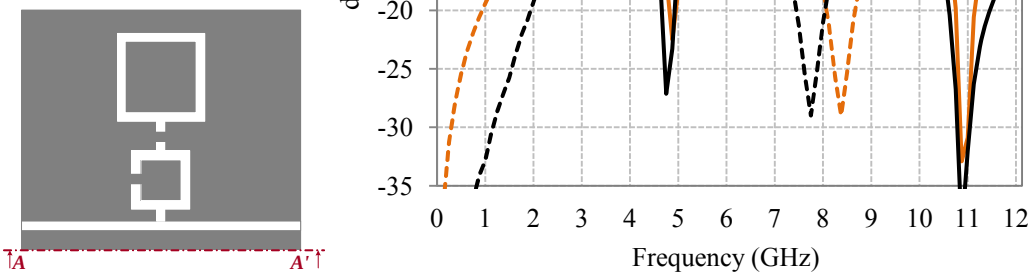

(a) (b)

Fig. 4.7. (a) Layout of the DGS when S_1 and S_2 are ON, S_3 is OFF. (b) Simulated and measured responses of the DGS when S_1 and S_2 are ON, S_3 is OFF.

4.3.2.2. Equivalent Circuit Extraction

In configuration two, the EM simulations show two transmission zeros, therefore the equivalent circuit consists of two cascaded parallel resonance circuits as shown in Fig. 4.8.

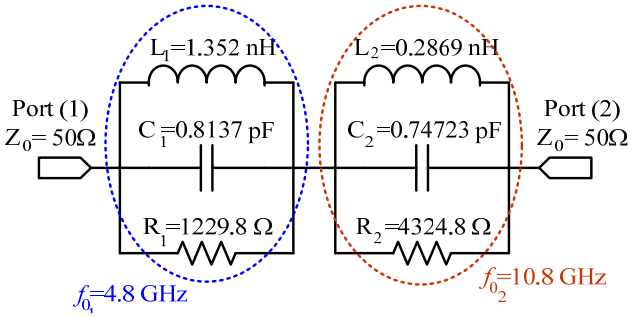

Fig. 4.8. The RLC equivalent circuit of configuration two.

The equivalent impedance of the cascaded parallel resonance circuits is:

$$Z = \frac{1}{1/R_1 + 1/j\omega L_1 + j\omega C_1} + \frac{1}{1/R_2 + 1/j\omega L_2 + j\omega C_2} \tag{4.9}$$

The reflection coefficient is given by:

$$S_{11} = \frac{\left(\dfrac{1}{1/R_1 + 1/j\omega L_1 + j\omega C_1} + \dfrac{1}{1/R_2 + 1/j\omega L_2 + j\omega C_2}\right)}{2Z_0 + \left(\dfrac{1}{1/R_1 + 1/j\omega L_1 + j\omega C_1} + \dfrac{1}{1/R_2 + 1/j\omega L_2 + j\omega C_2}\right)} \tag{4.10}$$

Assuming that $R>>Z_0$, S_{11} is reduced to:

$$S_{11} = \frac{Z}{2Z_0 + Z} = \frac{\left(\dfrac{j\omega L_1}{1-\omega^2 L_1 C_1} + \dfrac{j\omega L_2}{1-\omega^2 L_2 C_2}\right)}{2Z_0 + \left(\dfrac{j\omega L_1}{1-\omega^2 L_1 C_1} + \dfrac{j\omega L_2}{1-\omega^2 L_2 C_2}\right)} \tag{4.11}$$

The above expression has two poles at:

$$\omega_{0_1} = \frac{1}{\sqrt{L_1 C_1}} \quad \text{and} \quad \omega_{0_2} = \frac{1}{\sqrt{L_2 C_2}} \tag{4.12}$$

The transmission coefficient is given by:

$$S_{21} = \frac{2Z_0}{2Z_0 + Z} = \frac{2Z_0}{2Z_0 + \left(\frac{j\omega L_1}{1 - \omega^2 L_1 C_1} + \frac{j\omega L_2}{1 - \omega^2 L_2 C_2} \right)} \tag{4.13}$$

It has full transmission at ω_p , which is given by:

$$\left(\frac{j\omega L_1}{1 - \omega^2 L_1 C_1} + \frac{j\omega L_2}{1 - \omega^2 L_2 C_2} \right) = 0 \tag{4.14}$$

Hence, the full transmission frequency is given by:

$$\omega_p = \frac{\sqrt{C_1 \omega_1^2 + C_2 \omega_2^2}}{\sqrt{C_1 + C_2}} \tag{4.15}$$

Similarly the 3-dB cutoff frequency ω_c is determined by $|S_{21}| = 1/\sqrt{2}$, which leads to:

$$\left| 1 + \frac{\left(\frac{j\omega_c L_1}{1 - \omega_c^{\,2} L_1 C_1} + \frac{j\omega_c L_2}{1 - \omega_c^{\,2} L_2 C_2} \right)}{2Z_0} \right| = \sqrt{2} \tag{4.16}$$

$$\frac{\omega_c}{2Z_0} \left(\frac{1/C_1}{\omega_{0_1}^2 - \omega_c^2} + \frac{1/C_2}{\omega_{0_2}^2 - \omega_c^2} \right) = 1 \tag{4.17}$$

From (5.16) and (5.17) the capacitances C_1 and C_2 of the equivalent circuit model are given by:

$$C_1 = \frac{\omega_c}{2Z_0} \left(\frac{\left(\omega_p^2 - \omega_c^2\right)\left(\omega_{0_2}^2 - \omega_{0_1}^2\right)}{\left(\omega_{0_1}^2 - \omega_c^2\right)\left(\omega_{0_2}^2 - \omega_c^2\right)\left(\omega_p^2 - \omega_{0_1}^2\right)} \right) \tag{4.18}$$

$$C_2 = \frac{\omega_c}{2Z_0}\left(\frac{\left(\omega_p^2-\omega_c^2\right)\left(\omega_{0_2}^2-\omega_{0_1}^2\right)}{\left(\omega_{0_1}^2-\omega_c^2\right)\left(\omega_{0_2}^2-\omega_c^2\right)\left(\omega_{0_2}^2-\omega_p^2\right)}\right) \tag{4.19}$$

The inductances L_1 and L_2 of the equivalent circuit model can be directly determined from Eq. (5.12). The resistances R_1 and R_2 of the circuit model are best fitted around the resonant frequencies ω_{0_1} and ω_{0_2}, respectively. In this case, the impedance around the first resonant frequency ω_{0_1} is dominated by the first parallel resonance where the equivalent impedance is $Z_{S1} \approx R_1$ and the transmission loss S_{21} is given by:

$$S_{21}\big|_{\omega_{0_1}} = \left|\frac{2Z_0}{2Z_0+Z_{S1}}\right| = \frac{2Z_0}{2Z_0+R_1} \Rightarrow R_1 = 2Z_0\frac{1-S_{21}\big|_{\omega_{0_1}}}{S_{21}\big|_{\omega_{0_1}}} \tag{4.20}$$

The impedance around the second resonant frequency ω_{0_2} is dominantly by the second parallel resonance where the equivalent impedance is $Z_{S2} \approx R_2$ and the transmission loss is given by

$$S_{21}\big|_{\omega_{0_2}} = \left|\frac{2Z_0}{2Z_0+Z_{S2}}\right| = \frac{2Z_0}{2Z_0+R_2} \Rightarrow R_2 = 2Z_0\frac{1-S_{21}\big|_{\omega_{0_2}}}{S_{21}\big|_{\omega_{0_2}}} \tag{4.21}$$

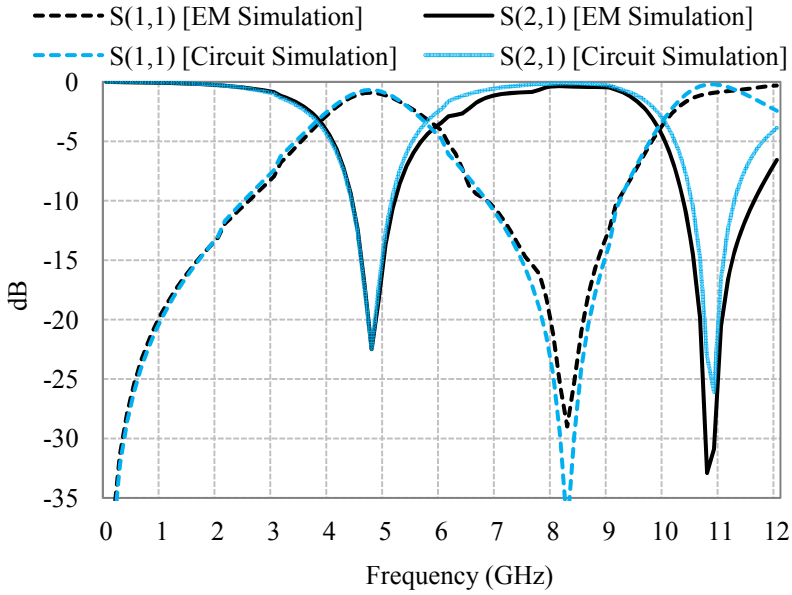

Fig. 4.9. EM and circuit simulations of configuration two.

The extracted values for case two are L_1=1.352 nH, C_1=0.8137 pF and R_1=1.23 kΩ to represent the resonant frequency f_{01} =4.8 GHz and L_2=0.287 nH, C_2=0.747 pF and R_2=4.32 kΩ to represent the resonant frequency f_{02} =10.8 GHz, as shown in Fig. 4.8. Both circuit and EM simulations are shown in Fig. 4.9, and they are in very good agreement.

4.3.2.3. EM Explanation and Design Rules

In this case, the upper square resonator is isolated as in the previous case, and the smaller resonator is divided into two unequal resonators as shown in Fig. 4.10. Each portion forms a $\lambda_g/4$ resonator that is terminated by a short circuit directly connected to the ground. Each resonator forms a transmission zero at the corresponding frequency as illustrated in the measured and simulated responses of the filter in Fig. 4.7 (b). This explanation is confirmed with the slotline design equation Eq. (4.7) at both frequencies.

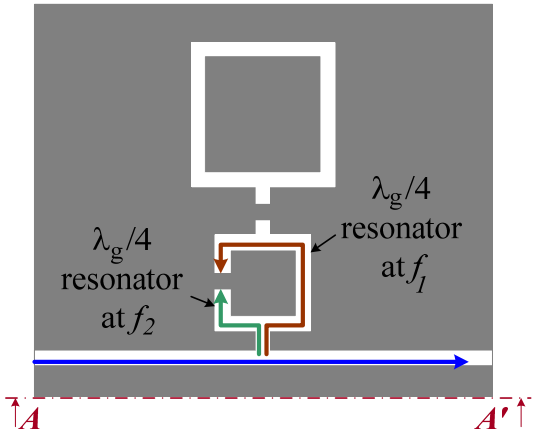

Fig. 4.10. Magnetic current paths when S_1 and S_2 are ON, while S_3 is OFF.

Fig. 4.11 (a) and (b) show the magnetic field distribution in the slot at the transmission zero frequencies. It is clear that the longer resonator is the cause of the first transmission zero, which means that its length corresponds to $\lambda_g/4$ at this frequency, while the shorter resonator is the cause of the second transmission zero, which again emphasizes our theory.

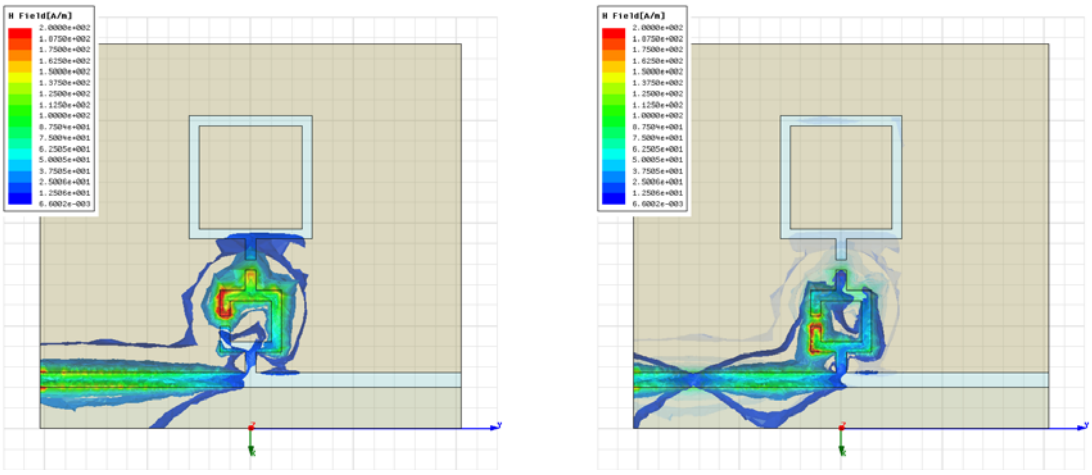

(a) (b)

Fig. 4.11. H-field distribution at (a) 4.8 GHz, and (b) 10.9 GHz.

4.3.3. Configuration Three: S_1: OFF, S_2: OFF and S_3: OFF

4.3.3.1. Simulation and Measurements Responses

In this case, all switches will act as open circuits leading to the structure illustrated in Fig. 4.12 (a), where both squares are connected to the CPW slots through the transverse gaps w_1 and w_2.

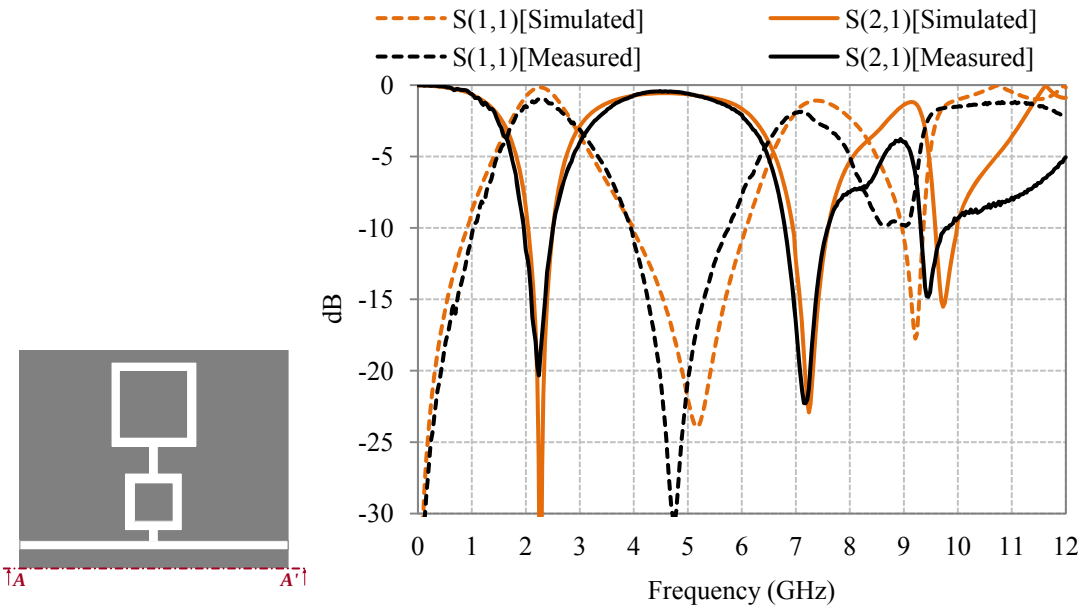

(a) (b)

Fig. 4.12. (a) Layout of the DGS when all switches are OFF. (b) Simulated and measured responses of the DGS when all switches are OFF.

The simulated and measured responses of the structure with all switches OFF are shown in Fig. 4.12 (b). They are in good agreement with each other. The structure provides three transmission zeros at 2.28, 7.26 and 9.72 GHz.

4.3.3.2. Equivalent Circuit Extraction

For configuration three, as we have three transmission zeros, the equivalent circuit consists of three cascaded parallel resonance circuits as shown in Fig. 4.13.

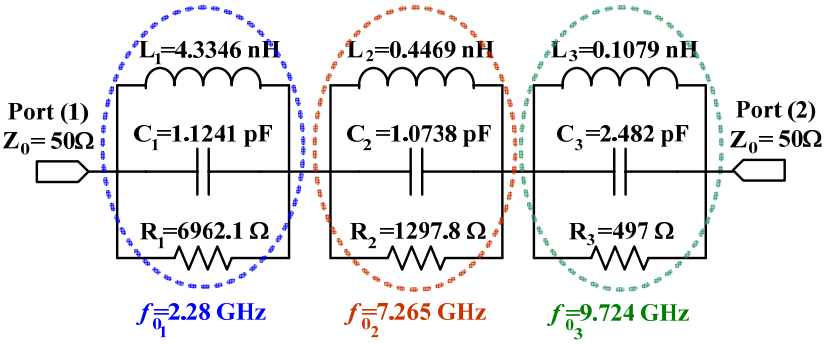

Fig. 4.13. The *RLC* equivalent circuit of configuration three.

The equivalent impedance of the cascaded parallel resonance circuits shown in Fig. 4.13 (a) is:

$$Z = \frac{1}{1/R_1 + 1/j\omega L_1 + j\omega C_1} + \frac{1}{1/R_2 + 1/j\omega L_2 + j\omega C_2} + \frac{1}{1/R_3 + 1/j\omega L_3 + j\omega C_3} \tag{4.22}$$

The reflection coefficient is given by:

$$S_{11} = \frac{\left(\frac{1}{1/R_1 + 1/j\omega L_1 + j\omega C_1} + \frac{1}{1/R_2 + 1/j\omega L_2 + j\omega C_2} + \frac{1}{1/R_3 + 1/j\omega L_3 + j\omega C_3}\right)}{2Z_0 + \frac{1}{1/R_1 + 1/j\omega L_1 + j\omega C_1} + \frac{1}{1/R_2 + 1/j\omega L_2 + j\omega C_2} + \frac{1}{1/R_3 + 1/j\omega L_3 + j\omega C_3}} \tag{4.23}$$

Assuming that R_1, R_2, $R_3 >> Z_0$, S_{11} is reduced to:

$$S_{11} = \frac{\left(\frac{j\omega L_1}{1-\omega^2 L_1 C_1} + \frac{j\omega L_2}{1-\omega^2 L_2 C_2} + \frac{j\omega L_3}{1-\omega^2 L_3 C_3}\right)}{2Z_0 + \left(\frac{j\omega L_1}{1-\omega^2 L_1 C_1} + \frac{j\omega L_2}{1-\omega^2 L_2 C_2} + \frac{j\omega L_3}{1-\omega^2 L_3 C_3}\right)} \tag{4.24}$$

The above expression has three poles at:

$$\omega_{0_1} = \frac{1}{\sqrt{L_1 C_1}}, \omega_{0_2} = \frac{1}{\sqrt{L_2 C_2}} \quad \text{and} \; \omega_{0_3} = \frac{1}{\sqrt{L_3 C_3}} \tag{4.25}$$

The transmission coefficient is given by:

$$S_{21} = \frac{2Z_0}{2Z_0 + Z} = \frac{2Z_0}{2Z_0 + \left(\dfrac{j\omega/C_1}{\omega_{0_1}^2 - \omega^2} + \dfrac{j\omega/C_2}{\omega_{0_2}^2 - \omega^2} + \dfrac{j\omega/C_3}{\omega_{0_3}^2 - \omega^2} \right)} \tag{4.26}$$

It has full transmission at ω_{p_1} and ω_{p_2}, which is given by:

$$\left(\frac{1/C_1}{\omega_{0_1}^2 - \omega_{p_1}^{\;2}} + \frac{1/C_2}{\omega_{0_2}^2 - \omega_{p_1}^{\;2}} + \frac{1/C_3}{\omega_{0_3}^2 - \omega_{p_1}^{\;2}} \right) = 0 \tag{4.27}$$

$$\left(\frac{1/C_1}{\omega_{0_1}^2 - \omega_{p_2}^{\;2}} + \frac{1/C_2}{\omega_{0_2}^2 - \omega_{p_2}^{\;2}} + \frac{1/C_3}{\omega_{0_3}^2 - \omega_{p_2}^{\;2}} \right) = 0 \tag{4.28}$$

Similarly the 3-dB cutoff frequency ω_c is determined by $|S_{21}| = 1/\sqrt{2}$, which leads to:

$$\left| 1 + \frac{j\omega_c}{2Z_0} \left(\frac{1/C_1}{\omega_{0_1}^2 - \omega_c^{\;2}} + \frac{1/C_2}{\omega_{0_2}^2 - \omega_c^{\;2}} + \frac{1/C_3}{\omega_{0_3}^2 - \omega_c^{\;2}} \right) \right| = \sqrt{2} \tag{4.29}$$

$$\frac{\omega_c}{2Z_0} \left(\frac{1/C_1}{\omega_{0_1}^2 - \omega_c^{\;2}} + \frac{1/C_2}{\omega_{0_2}^2 - \omega_c^{\;2}} + \frac{1/C_3}{\omega_{0_3}^2 - \omega_c^{\;2}} \right) = 1 \tag{4.30}$$

From Eq. (5.27), (5.28) and (5.30), the capacitances C_1, C_2 and C_3 can be obtained.

The inductances L_1, L_2 and L_3 of the equivalent circuit model can be directly determined from Eq. (5.25). Similarly, the resistances R_1, R_2 and R_3 of the circuit model are best fitted around the resonant frequencies ω_{0_1}, ω_{0_2} and ω_{0_3}, respectively.

In this case, the impedance around the first resonant frequency ω_{0_1} is dominated by the first parallel resonance where the equivalent impedance is $Z_{S1} \approx R_1$ and the transmission loss S_{21} is given by

$$S_{21}\big|_{\omega_{0_1}} = \left|\frac{2Z_0}{2Z_0 + Z_{S1}}\right| = \frac{2Z_0}{2Z_0 + R_1} \Rightarrow R_1 = 2Z_0 \frac{1 - S_{21}\big|_{\omega_{0_1}}}{S_{21}\big|_{\omega_{0_1}}} \tag{4.31}$$

The impedance around the second resonant frequency ω_{0_2} is dominated by the second parallel resonance where the equivalent impedance is $Z_{S2} \approx R_2$ and the transmission loss is given by

$$S_{21}\big|_{\omega_{0_2}} = \left|\frac{2Z_0}{2Z_0 + Z_{S2}}\right| = \frac{2Z_0}{2Z_0 + R_2} \Rightarrow R_2 = 2Z_0 \frac{1 - S_{21}\big|_{\omega_{0_2}}}{S_{21}\big|_{\omega_{0_2}}} \tag{4.32}$$

Similarly,

$$S_{21}\big|_{\omega_{03}} = \left|\frac{2Z_0}{2Z_0 + Z_{S3}}\right| = \frac{2Z_0}{2Z_0 + R_3} \Rightarrow R_3 = 2Z_0 \frac{1 - S_{21}\big|_{\omega_{0_3}}}{S_{21}\big|_{\omega_{0_3}}} \tag{4.33}$$

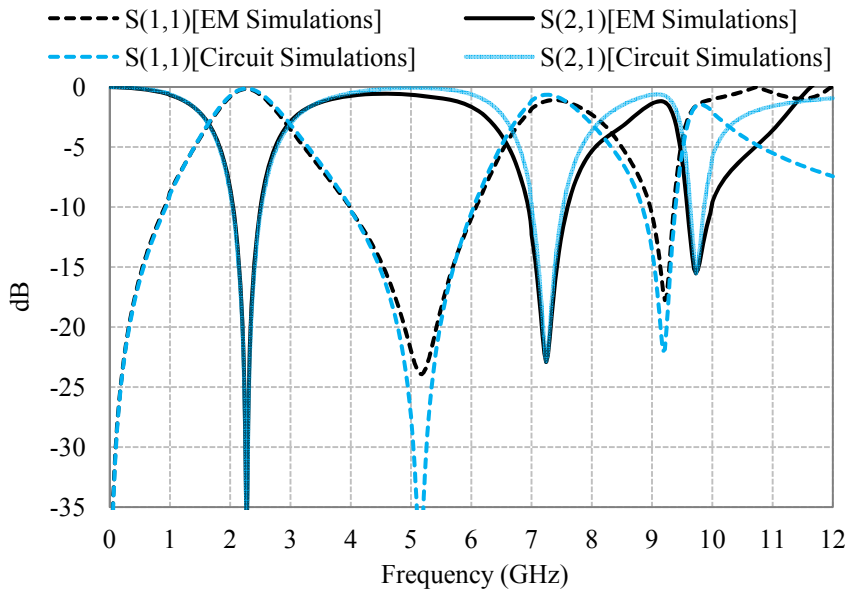

Fig. 4.14. EM and circuit simulations of configuration three.

Therefore, the extracted values for case three are L_1=4.335 nH, C_1=1.124 pF and R_1=6.962 kΩ to represent the resonant frequency f_{01} =2.28 GHz , L_2=0.447 nH, C_2=1.074 pF and R_2=1.297 kΩ to represent the resonant frequency f_{02} =7.26 GHz, and L_3=0.108 nH, C_3=2.482 pF and R_3=0.497 kΩ to represent the resonant frequency f_{03} =9.72 GHz. Both simulations are shown in Fig. 4.14, and they are in very good agreement.

4.3.3.3. EM Explanation and Design Rules

As mentioned before, in this case, all diodes will act as open circuits leading to the structure in Fig. 4.15, where both squares are connected to the coplanar waveguide slots. The response of the structure shows three transmission zeros at 2.28, 7.44 and 9.85 GHz. The existence of these transmission zeros may be explained as follows; it is found that the path difference between path (1), denoted by the continuous blue line, and path (2) denoted by the dotted red line, is 41.5 mm. When this electrical path difference equals to odd multiples of half the guided wavelength, a transmission zero is produced due to 180° phase difference obtained at point "P".

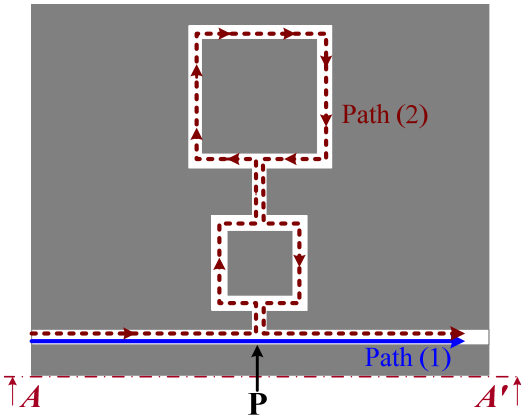

Fig. 4.15. Magnetic current paths inside the slot when S_1, S_2 and S_3 are OFF.

In Fig. 4.16 (a, b and c), the magnetic field distribution in the slot is illustrated using the HFSS software package. Fig. 4.16 (a) shows the magnetic field distribution in the slot at 2.28 GHz. We have only one maximum for the field, and no field in the CPW slot after the point "P", which illustrates our theory presented above. At 2.28 GHz, the path difference is $\lambda_g/2$ causing a phase difference at point

"P" equals to 180°, forming a transmission zero at this frequency. Fig. 4.16 (b) shows the H-field at 7.44 GHz. In this case we have three maxima corresponding to $3(\lambda_g/2)$, causing the second transmission zero. Finally, in Fig. 4.16 (c), the magnetic field has 5 maxima, which means that the path difference corresponds to $5(\lambda_g/2)$, causing the third transmission zero at 9.85 GHz.

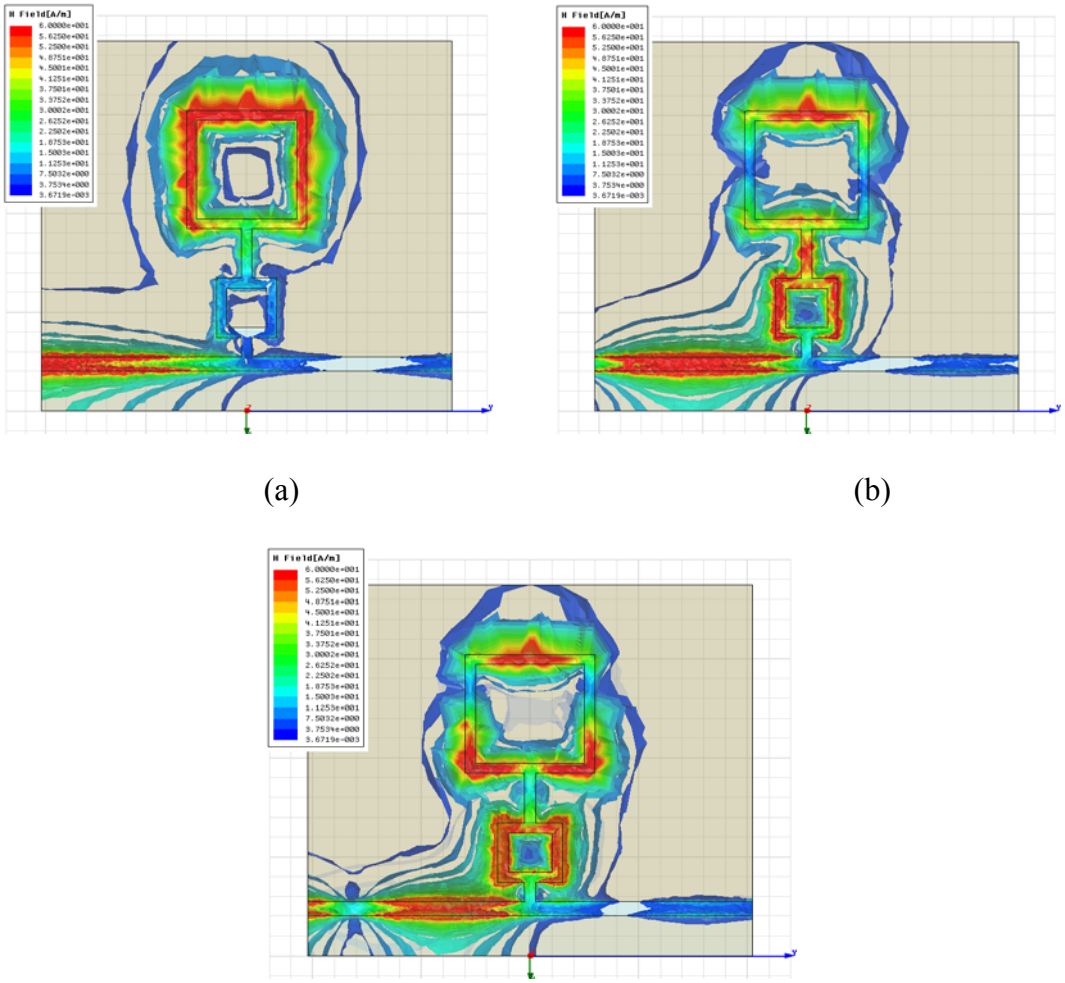

(a) (b)

(c)

Fig. 4.16. H-Field distribution at (a) 2.28 GHz, (b) 7.44 GHz and (c) 9.85 GHz of configuration three.

4.3.3. Configuration Four: S_1: OFF, S_2: OFF and S_3: ON

4.3.3.1. Simulation and Measurements Responses

Adding another degree of freedom, we considered adding another switch along the bigger ring resonator. When S_3 is ON, the structure will be as shown in Fig.

4.17 (a). The structure has three resonance frequencies at 2.04 GHz, 4.26 GHz, and 8.39 GHz as shown in Fig. 4.17 (a).

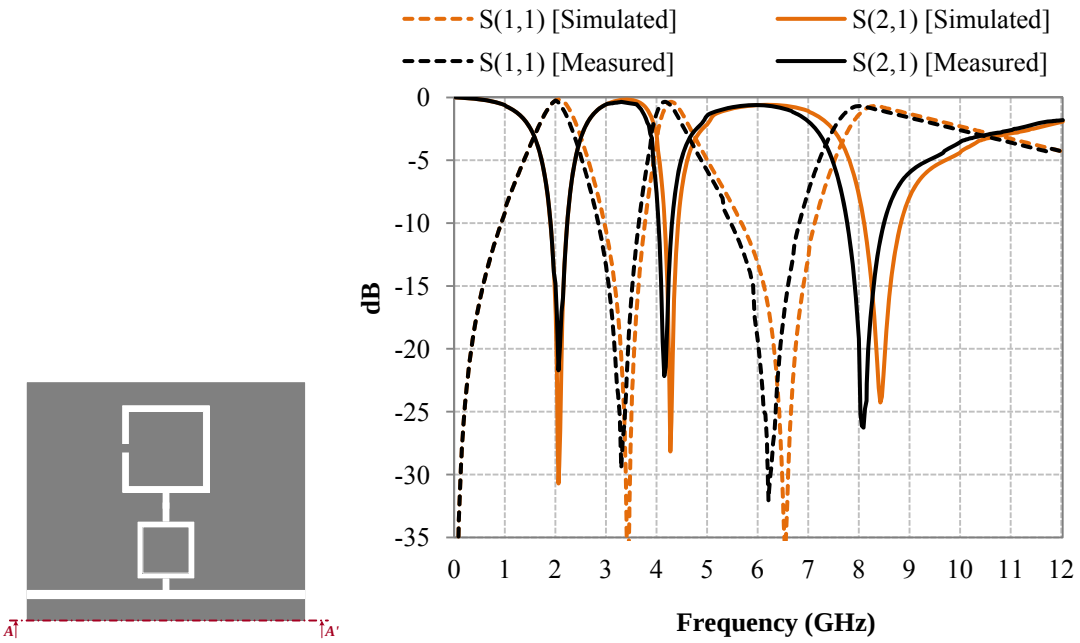

Fig. 4.17. (a) Layout of the DGS when S_1 and S_2 are OFF and S_3 is ON. (b) Simulated and measured responses.

4.3.3.2. Equivalent Circuit Extraction

Using the same equations in configuration three, the extracted values for case four are L_1=3.786 nH, C_1=1.606 pF and R_1=3.068 kΩ to represent the resonant frequency f_{01} =2.04 GHz, L_2=0.635 nH, C_2=2.196 pF and R_2=2.41 kΩ to represent the resonant frequency f_{02} =4.261 GHz, and L_3=0.354 nH, C_3=1.015 pF and R_3=1.527 kΩ to represent the resonant frequency f_{03} =8.397 GHz, as shown in Fig. 4.18 (a). Both simulations are in good agreement, as shown in Fig. 4.18 (b).

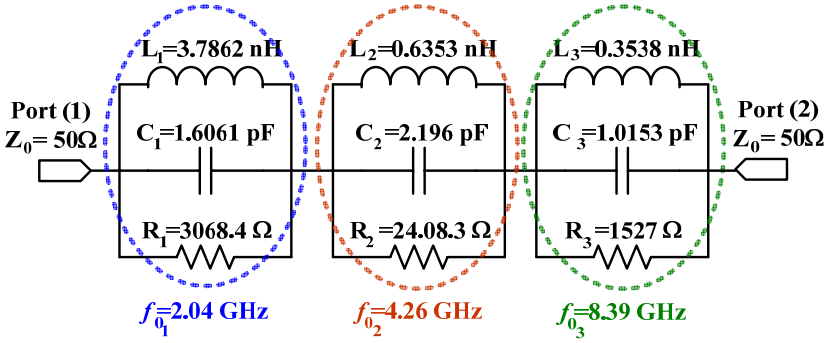

(a)

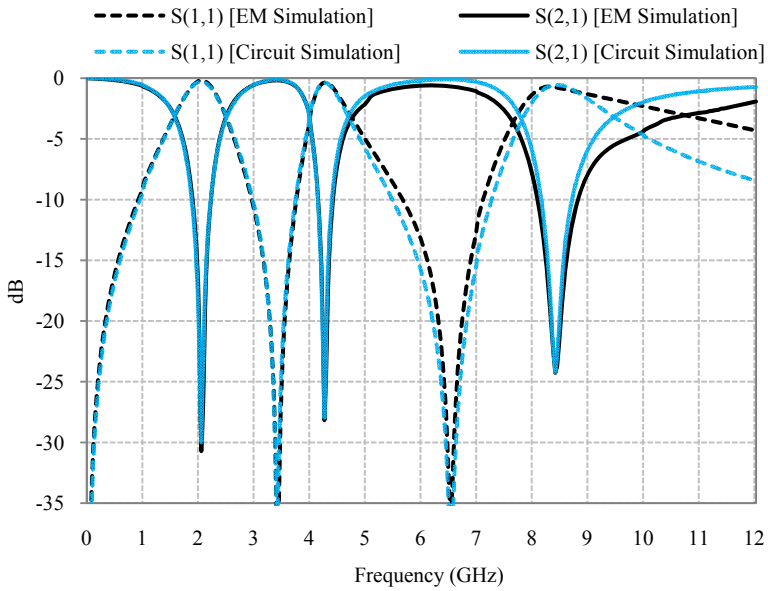

(b)

Fig. 4.18 (a) The *RLC* equivalent circuit of case four. (b) EM and circuit simulations.

4.3.3.3. EM Explanation and Design Rules

In this case the bigger square has a short bridge along its path causing the whole structure to divide into two basic resonators. The first resonator, denoted by the red path, is a $\lambda_g/4$ resonator ending by a short circuit, as in the previous case, producing a 180° phase shift at point "P" which causes the first resonant frequency at f_1= 2.04 GHz. The same goes for the second resonator, denoted by the green path, giving the second transmission zero at frequency f_2=4.26 GHz, Fig. 4.19. The third transmission zero at f_3=8.39 GHz occurs when the branch, starting from point "M" to the short circuits, corresponds to $\lambda_g/4$ and $3\lambda_g/4$ forming a transmission zero at point "M", and consequently a zero in the whole structure response as illustrated in Fig. 4.20 (c). All these results have been validated using Eq. (4.7) of the slotline transmission line.

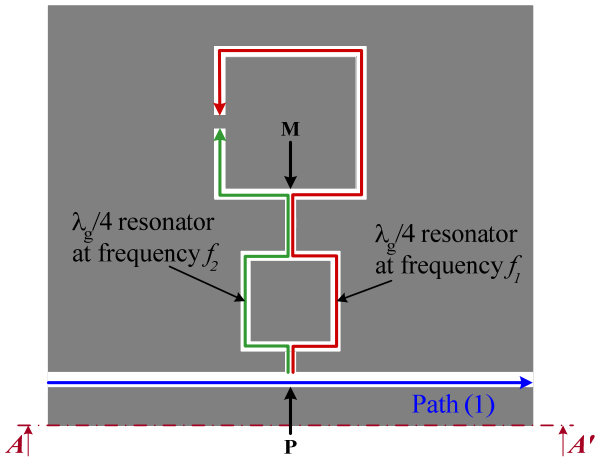

Fig. 4.19. Magnetic current paths when S_1 and S_2 are OFF, while S_3 is ON.

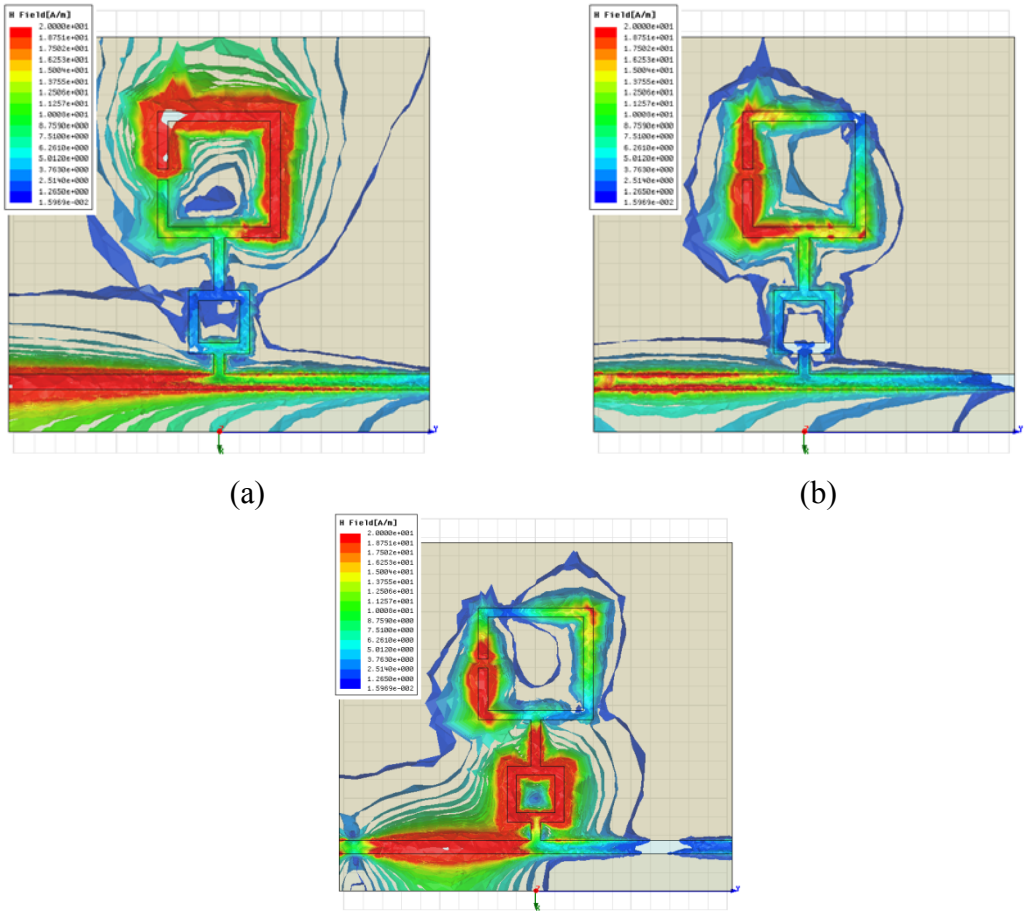

(a) (b)

(c)

Fig. 4.20. H-field distribution at (a) 2.04 GHz, (b) 4.26 GHz and (c)8.39 GHz.

4.4. Reconfigurability by Using PIN Diodes

In this section, the measurement results when these short and open bridges are replaced by PIN diodes are presented. The PIN diodes used here are the Philips silicon PIN diodes BAP 63-02. They have been chosen due to their low diode capacitance ($C_d \approx 0.36$ pF), low forward resistance ($r_d \approx 2\ \Omega$) and very low series inductance ($L_s \approx 0.6$ nH), in addition to their small size (1.1 x 0.7 mm) which makes them compatible with our design. A photograph of the fabricated structure is shown in Fig. 4.21.

4.4.1. PIN Diode Biasing

As illustrated before, in this structure, there are three PIN diodes in each ground plane of the coplanar waveguide. Two of these diodes (S_2 and S_3) are connected between the inner patch of the square resonators and the ground plane. Fixing these diodes is as shown in Fig. 4.1. The voltage needed for biasing these diodes is applied on the inner square patch.

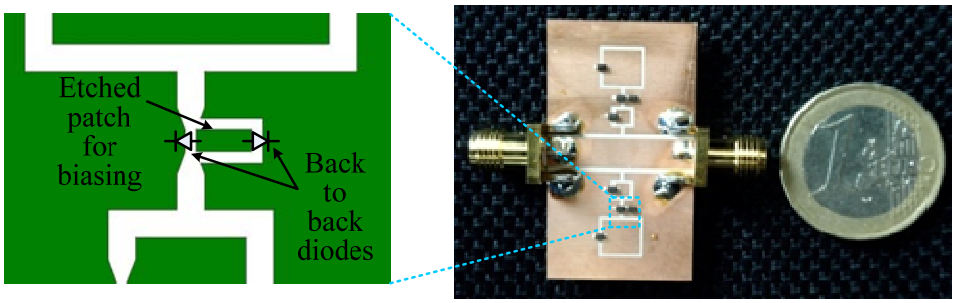

Fig. 4.21. Photograph of the fabricated structure with PIN diodes illustrating the biasing technique across the transverse slot.

For the diodes across the transverse slot between the two square resonators (S_1), the biasing is more complex. According to the initial structure in Fig. 4.1, the two terminals of the diodes are connected to the ground plane of the coplanar waveguide; therefore the biasing in this case is impossible. To solve this problem, a small rectangular patch is etched in the ground plane where two back to back diodes are connected, as shown in Fig. 4.21. When the voltage is applied to this square patch, both diodes will be ON, short circuiting the upper resonator. On the other

hand, when no biasing is applied, the path is open for the signal to pass to the outer larger square resonator.

It should be noted that the etching is done as small as possible in order not to cause large perturbation in the ground plane for the calculated signal, at the same time to provide high impedance, and so to prevent the signal from passing in the other paths instead of the main designed path.

4.4.2. Measurement Setup

In this section, the complete setup to measure the response of the DGS resonator with PIN diodes is presented. Fig. 4.22 shows a schematic diagram of the measurement setup, while Fig. 4.23 (a) and (b) show photographs of the measurement setup.

To bias the diodes, probes with the required applied voltages are used. These four probes, which are connected in parallel, are connected to the voltage source by means of a large series resistance to protect the diodes from any access current as not to cause breakdown. To monitor the voltage and current across the diodes, we use a voltmeter and an ammeter connected across the terminals of the diodes. It should be noted that we have one common ground for the whole circuit, the voltage source, the voltmeter, the ammeter, and vector network analyzer and the circuit under test. The biasing voltage of the diode is set to 0.95~1 V and the biasing current is 40~50 mA.

In order to measure the scattering parameters the DGS resonator, the Anritsu ME7808A network analyzer is used through SMA cables and SMA connectors as illustrated in Fig. 4.22 and Fig. 4.23. We measured the response in each biasing configuration in the range of frequency from 0-12 GHz, and the calibration of the VNA is done using the SOLT technique.

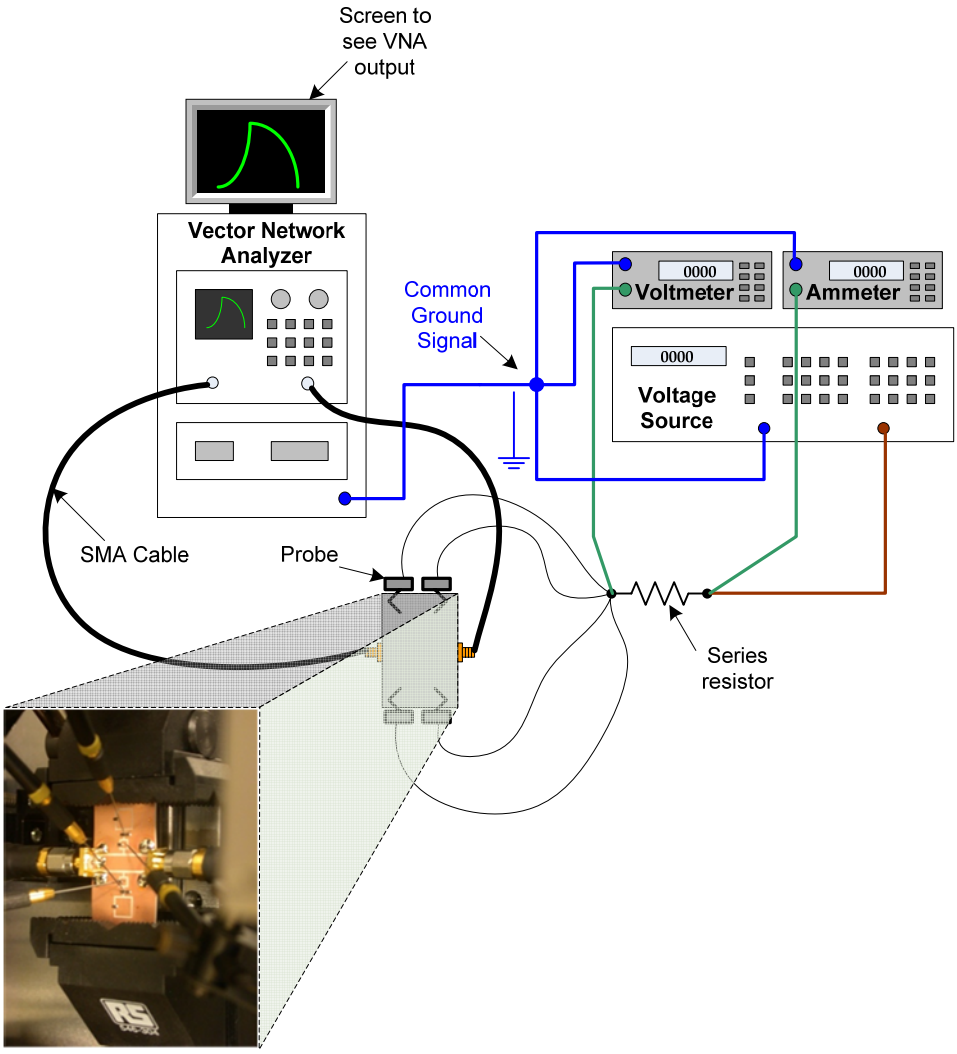

Fig. 4.22. Schematic diagram of the fabricated structure with PIN diodes while measurement.

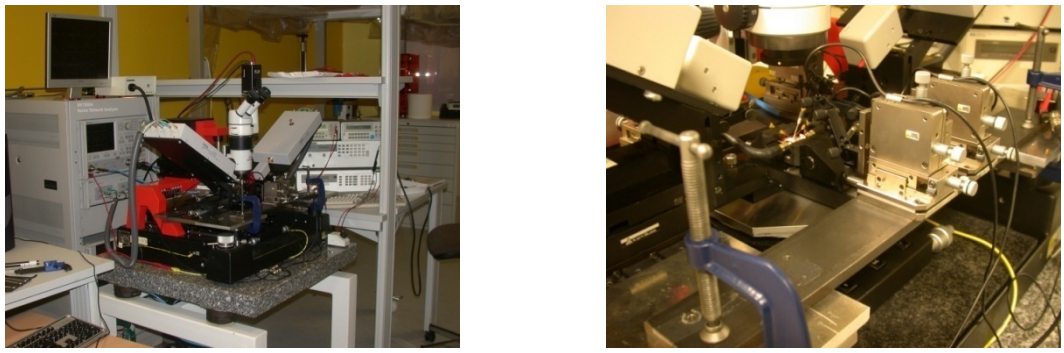

(a) (b)

Fig. 4.23 (a) Photograph of the complete measurement setup. (b) Photograph of the DGS circuit with probes for biasing the diodes.

4.4.3. Measured Results

Measured results are shown in Fig. 4.24. In configuration one, there is one transmission zero at 4.35 GHz of -16.4 dB, and a 10-dB bandwidth of 0.88 GHz, Fig. 4.24 (a). In configuration two, two transmission zeros exist at 3.75 GHz and 8.47 GHz of -16.96 dB, and -17.51 dB, and 10-dB bandwidth of 0.36 and 1.29 GHz, respectively, Fig. 4.24 (b). In configuration three, we have three transmission zeros at 1.86, 6.75 and 8.34 GHz, of -18.05, -21.15, and -12 dB, and 10-dB bandwidth of 0.36, 0.52, and 0.09 GHz, respectively, Fig. 4.24 (c). In configuration four, three transmission zeros exist at 1.68, 3.48, and 7.17 GHz, of -16.8, -15.83, and -24.62 dB, and 10-dB bandwidth of 0.27, 0.18 and 0.84 GHz, respectively, Fig. 4.24 (d).

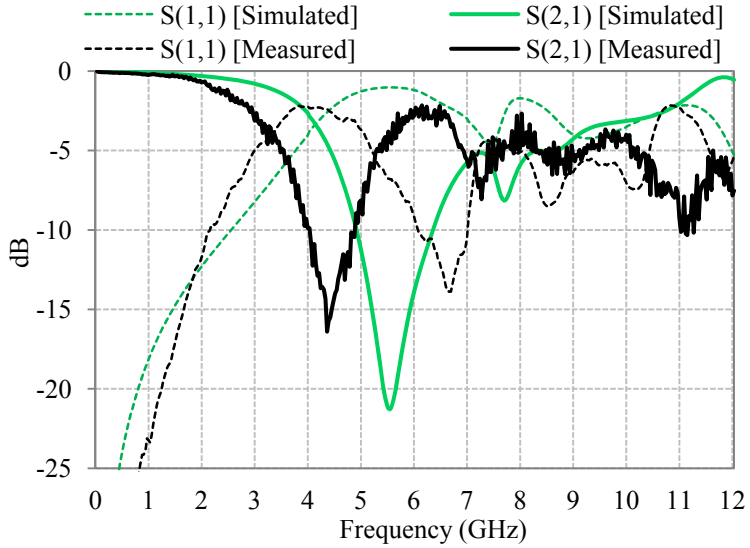

(a)

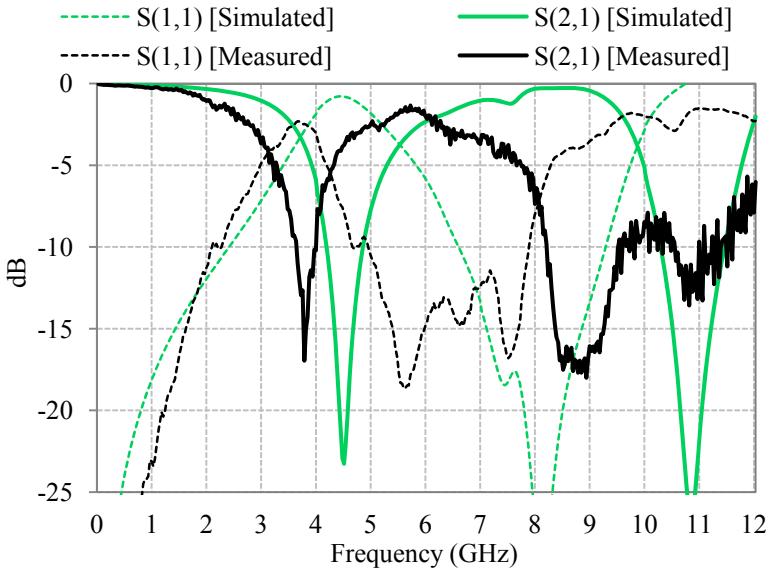

(b)

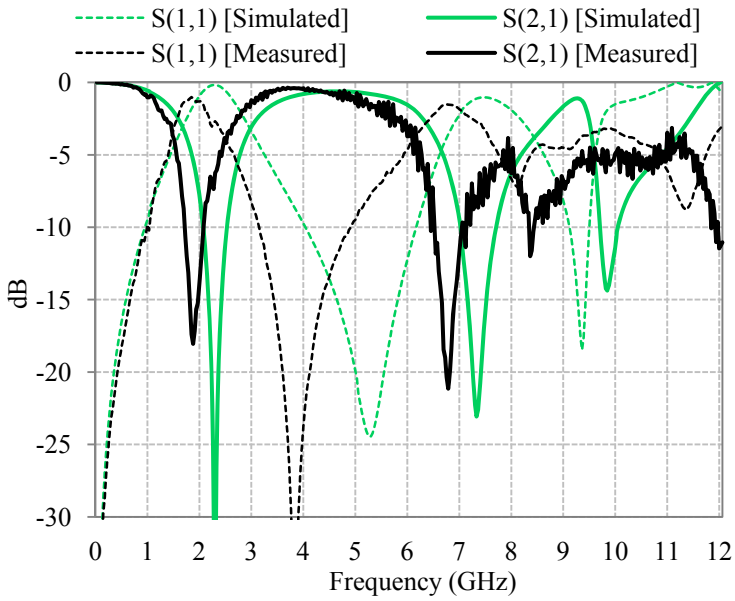

(c)

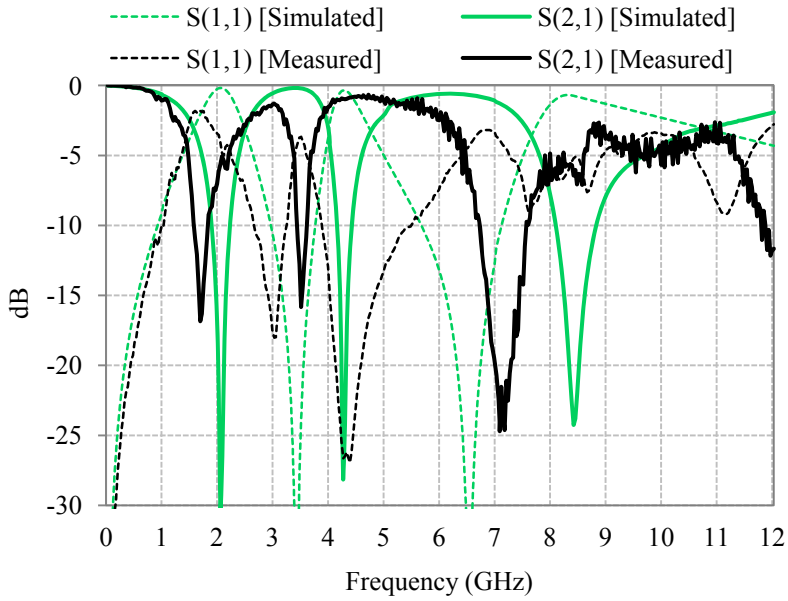

(d)

Fig. 4.24 Measured results after adding the PIN diodes compared to simulation results with open and short bridges (a) configuration one, (b) configuration two, (c) configuration three and (d) configuration four.

A shift in the resonance frequencies of the transmission zeros, between the measured results with PIN diodes and simulation results when diodes have been modeled as open and short circuits, can be observed. This can be explained due to the fact that the effect of the diodes has not been previously considered, in order to facilitate obtaining clear design rules for the transmission zeros using the slotline

design equations. No doubt that adding the diodes shifts the resonant frequencies to lower frequencies due to the diode capacitance and inductance. This shift is not fixed for a definite value as this depends on which diodes are biased and which are not, in addition to their location in the circuit.

Also the quality factor of the transmission zeros has decreased due to the diode resistance introduced. All these factors may be neglected in a first design iteration, then after obtaining the location of the transmission zeros using the introduced slotline theory, the effect of the diode may then be considered to obtain final tuning in the structure.

Table 4.1

Summary of simulated and measured results of the proposed DGS resonator

Config-urations	**Trans-mission Zero**	**Simulated Results without diodes**			**Measured Results with PIN diodes**		
		Frequency (GHz)	Insertion Loss (dB)	10-dB band-width (GHz)	Frequency (GHz)	Insertion Loss (dB)	10-dB band-width (GHz)
One	TZ-1	5.65	-21.87	1.4	4.35	-16.4	0.88
Two	TZ-1	4.5	-23.4	0.7	3.75	-16.96	0.36
	TZ-2	10.98	-27.8	1.13	8.47	-17.51	1.29
Three	TZ-1	2.27	-31	0.4	1.86	-18.05	0.36
	TZ-2	7.3	-23.3	0.62	6.75	-21.15	0.52
	TZ-3	9.89	-14.3	0.26	8.34	-12	0.09
Four	TZ-1	2.08	-30.9	0.34	1.68	-16.8	0.27
	TZ-2	4.33	-27.8	0.21	3.48	-15.83	0.18
	TZ-3	8.45	-24.5	0.72	7.17	-24.62	0.84

By observing the first zero of the four configurations, it is evident that there is a shift of less that 4% in all cases between measured results with open/short circuits and theory (model); and a much larger shift (15-25%) between measured results with diodes and those with open/short circuits. This means that there are two mechanisms taking part to this drift which sum to each other. The first is the unavoidable over-etching of the metal (affecting both cases; open/short and diodes), the second is the parasite capacitance associated with the diodes package (SMD metal pads), beside

those aforementioned. This drift is frequency dependent and seems to validate the above hypothesis. All these factors may be neglected in a first design iteration, and considered afterwards once the location of the transmission zeros have been found by means of the aforeintroduced slotline theory. Eventually the effect of the diodes can be considered for a final tuning of the structure. It should be clear that these reported results are obtained with a single iteration and no redesign has been done. All simulated and measured results are summarized in Table 4.1.

4.5. Conclusion

In this chapter, a novel reconfigurable DGS resonator capable of producing arbitrary transmission zeros is presented. The structure was studied using the slotline design equations which give insight of the EM propagation inside the structure in addition to design rules for the resonator which are provided for the first time. A good agreement has been observed between simulation and measurement results.

The reconfigurability of the structure presented here is achieved by PIN diodes. In case of slight tuning requirements, varactor diodes are to be used instead. Also for better performance, MEMS switches may be used.

This reconfigurable DGS resonator is a good candidate for a number of applications where suppression of passbands and reconfigurability are required. For example, this DGS cell may be used after a multiband antenna to allow or suppress one of the bands according to the need, or after a wideband antenna to obtain a controllable reconfigurable bandwidth, or after a bandpass filter to suppress higher order harmonics, as will be demonstrated in the next chapter.

References of Chapter Four

[1] E. Yablonovitch, "Photonic band-gap structures," J. Optical Soc. America B, Vol. 10, No. 2, pp. 283–295, Feb. 1993.

[2] F. Yang, K. Ma, Y. Qian and T. Itoh, "A uniplanar compact photonic bandgap (UC-EBG) structure and its applications for microwave circuits," *IEEE Trans. Microw. Theory Tech*., Vol. 47, No. 8, pp. 1509-1514, August 1999.

[3] F. R. Yang, K. P. Ma, Y. Qian, and T. Itoh, "A novel TEM waveguide using uniplanar compact photonic-bandgap (UC-PBG) structure," *IEEE Trans. Microw. Theory Tech.*, Vol. 47, No. 11, pp. 2092–2098, Nov. 1999.

[4] T. Y. Yun, and K. Chang, "Uniplanar one-dimensional photonic-bandgap structures and resonators*," IEEE Trans. Microw. Theory Tech.*, Vol. 49, No. 3, pp. 549 - 553, March. 2001.

[5] C. Caloz and T. Itoh, "Multilayer and anisotropic planar compact PBG structures for microstrip applications," *IEEE Trans. Microw. Theory Tech.*, Vol. 50, No. 9, pp. 2206-2208, Sept. 2002.

[6] S.-G. Mao and Y. Zhi, "Coplanar waveguide BPF with compact size and wide spurious free stopband using electromagnetic bandgap resonators," *IEEE Micro. Wireless Comp. Lett.,* Vol. 7, No. 3, pp. 181-183, Mar. 2007.

[7] H. Liu, Z. Li, X. Sun and J. Mao, "Harmonic suppression with photonic band gap and defected ground structure for a microstrip patch antenna," *IEEE Microw. Wireless Comp. Lett.,* Vol. 15, No. 2, pp. 55 – 56, Feb. 2005.

[8] J. Lim, C. Kim, D. Ahn, Y. Jeong, and S. Nam, "Design of low-pass filters using defected ground structure," *IEEE Trans. Microw. Theory Tech.*, Vol.53, No.8, pp. 2539–2545, Jan. 2005.

[9] H. B. El-Shaarawy, F. Coccetti, R. Plana, M. El-Said and E. A. Hashish, "Compact bandpass ring resonator filter with enhanced wide-band rejection characteristics using defected ground structures," *IEEE Microw. Wireless Comp. Lett.*, Vol. 18, No. 8, pp. 500-503, Aug. 2008.

[10] M. Abdelaziz, A. M. E. Safwat, F. Podevin, A. Vilcot, "Narrow bandpass filter based on the modified DGS," proceedings of *Europ. Microw. Conf. (EuMC)*, pp. 75 – 78, Oct. 2007.

[11] E. K. I. Hamad, A. M. E. Safwat, A.S. Omar, "A MEMS reconfigurable DGS resonator for K-band applications," *IEEE Journal of Microelectromechanical Systems,* Vol. 15, No. 4, pp. 756 – 762, Aug. 2006.

[12] M. F. Karim, A. Q. Liu, A. Alphones, A. B. Yu; "A Reconfigurable Micromachined switching filter using periodic structures," *IEEE Trans. Microw. Theory Tech.,* Vol. 55, No. 6, Part 1, pp. 1154 – 1162, June 2007.

[13] A. M. E. Safwat, F. Podevin, P. Ferrari, A. Vilcot, "Tunable bandstop defected ground structure resonator using reconfigurable dumbbell-shaped coplanar waveguide," *IEEE Trans. Microw. Theory Tech.,* Vol. 54, No. 9, pp. 3559 – 3564, Sept. 2006.

[14] L. Yuan, L. Jiao, Y. Chunhui, "The back propagation neural network model of non-periodic defected ground structure," *Global Symp. Millimeter Waves (GSMM),* pp. 29 – 32, April 2008.

[15] R. Janaswamy and D. H. Shaubert, “Characteristic impedance of a wide slot line on low permittivity substrates,” *IEEE Trans. Microw. Theory Tech.,* Vol. 34, No. 6, Part 1, pp. 900 – 902, June 1986.

CHAPTER FIVE

ALTERNATIVE APPLICATIONS OF BANDGAP STRUCTURES IN THE MICROWAVE RANGE

5.1. Introduction

Recently, as wireless communications systems get smaller and lighter and are able to perform multi-functions, microwave components that have a small size and better performance are required. Bandpass filters (BPF) are one of the most rapidly developing components in modern microwave communications systems. Miniaturization and suppression of multi-harmonic responses are the preliminary challenges in advanced BPF design. Recently there has been considerable interest in the development of a high-performance microwave component using a slow-wave structure, such as Electromagnetic Bandgap (EBG) structures [1]-[4], and Defected Ground Structures (DGS) [5]-[12].

The previous chapters of this thesis give a complete explanation of the bandgap structures, their advantages, disadvantages, equivalent circuits and recent developments; followed by proposing a novel reconfigurable defected ground structure resonator. The simulated and measured responses of this DGS cell has been obtained, then the equivalent circuit using parallel *RLC* resonators has been extracted from the simulated responses. Finally, EM explanation of the structure has been obtained using the slotline design equations.

In this chapter, two applications of the defected ground structures in the implementation of bandpass filters are presented. The first application is based on the coplanar waveguide technology, while the second is on microstrip transmission lines.

In the first application, we introduce a novel defected ground structure cell in the middle of an inductively coupled resonator filter. First, the design process of the shunt inductances between the resonators is explained using Matthaei, Young, and Jones technique [13]. Then, we show how to design the defect between the two

coupling inductive stubs such that the structure resonates at the required frequency. Adding the defect to the bandpass filter reduces the length of the resonator designed at 5 GHz from 12.9 mm for the conventional case to 5.5 mm with the DGS. To validate our theory, a second order filter with a better rejection skirt and wider bandwidth is designed and fabricated showing good agreement between simulated and measured results.

Finally, to enhance the ability of the filter, another square resonator is added to the DGS cell that is connected and/or disconnected to the structure by means of a capacitive MEMS switch. This reconfigurability element changes the structure from a single resonance filter to a multiband filter. All filters are simulated, fabricated and measured, showing good agreement within each other.

The second application that is introduced in this chapter is the enhancement of the response of microstrip ring resonator filters using different types of defected ground structures. It has been demonstrated that ring resonator filters suffer from two drawbacks. The first one is their large size due to the two tuning stubs which occupy about 72 % of the filter area, while the second is the existence of higher order modes which limit the out-of-band rejection. In this chapter, two different design approaches are considered. The first is at the filter layout level, through a space saving redesign of the tuning stubs [6], while the second is at the wave propagation level, through the exploitation of Defected Ground Structures (DGS) and Uniplanar Compact-Photonic Bandgap (UC-PBG) Structures properties [16], reaching 84 % of size reduction while keeping the overall filter characteristics with respect to insertion and return loss values.

This chapter is organized as follows; Section 5.2 introduces the DGS based inductively coupled resonator bandpass filters. After giving a brief introduction in Section 5.2.1, the design process of the conventional inductively coupled BPF is explained in Section 5.2.2. Section 5.2.3 discusses how the DGS cell is introduced in the resonator and how this affects the filter response. Section 5.2.4 deals with the reconfigurability of the BPF from single resonance to multi-resonance filter, while all results are summed up in Section 5.2.5.

Section 5.3 is devoted for the microstrip ring resonator filter with different bandgap structures. In Section 5.3.1, a brief introduction for the ring resonator filters and their attractive features which make a good candidate to a number of applications is given. In Section 5.3.2, the design procedures of the conventional ring resonator

filters and its disadvantages with respect to its tuning stubs and higher order harmonics are explained with a filter designed at 1.5 GHz. Section 5.3.3 deals with the redesign process of the stubs to occupy a smaller area, using two different design approaches. Sections 5.3.4 and 5.3.5 investigates the use of DGSs and EBG structures for the suppression of the higher order harmonics, respectively. Finally, Section 5.3.6 is devoted for the conclusion.

5.2. Defected Ground Structure Based Inductively Coupled Resonator Bandpass Filters

5.2.1. Introduction

In this section, compact DGS based inductively coupled resonator bandpass filters are introduced. Each filter consists of two basic parts. The first part is the conventional inductively coupled resonator which is responsible for the transmission pole effect (passband effect) [9], while the second is the defected ground structure resonator which is responsible for size miniaturization and reconfigurability.

First, the inductively coupled resonator, design procedure and why such type of resonators is preferred more than capacitively coupled resonators are presented. Then we will study the effect of adding the DGS cell to the resonator with respect to the insertion and return loss values, size miniaturization and reconfigurability. In each case, simulation and measurement results are illustrated showing good agreement with each other.

5.2.2. Conventional Inductively Coupled Resonator Bandpass Filters

The main building block of the bandpass filters is the inductively coupled resonators introduced in [9].

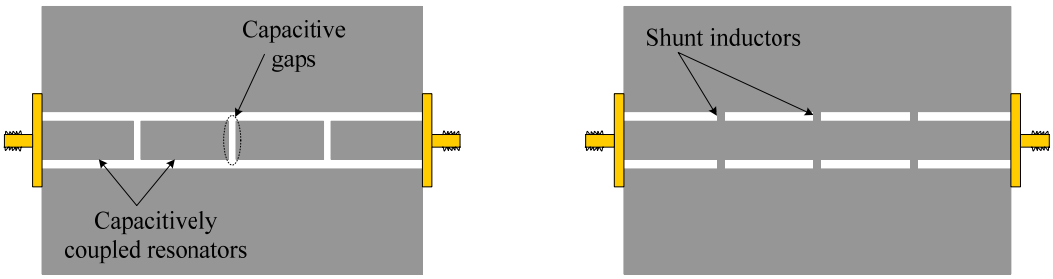

(a) (b)

Fig. 5.1 (a) Capacitively coupled resonant section bandpass filter. (b) Inductively coupled resonant sections bandpass filter.

This type of resonators is preferred more than coplanar end-coupled bandpass filters introduced in [10]. This is due to the fact that the capacitive coupling scheme between the resonators is realized by cutting gaps in the coplanar waveguide signal line as shown in Fig. 5.1 (a). The electric field in the gaps radiates as two simple dipoles, one at each end of the resonant section, in a way similar to a patch antenna, consequently, these gaps produce high radiation losses degrading the whole system performance. This type of filters has been produced elsewhere on coaxial and fin lines [11] and helical lines [12].

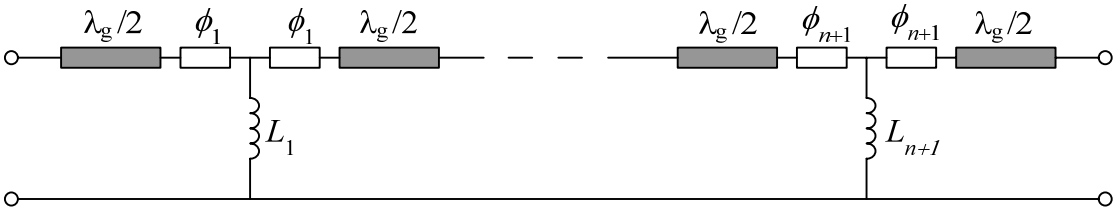

Fig. 5.2. Schematic diagram of a shunt inductively coupled bandpass filter.

The shunt inductively coupled CPW filter structure is designed using the filter synthesis technique as described by Matthaei, Young, and Jones [13]. The filter is composed of half-wave transmission lines and immittance inverters as shown in Fig. 5.2. The immittance inverters are realized by embedding shunt inductors between uniform transmission lines. For easy fabrication, all the half-wave transmission lines are chosen to have identical characteristic impedance Z_T. Furthermore, without loss of generality, a symmetric filter structure is assumed. Thus, the circuit parameters $X_j(\omega_0 L_j)$ and Φ_j are given by:

$$\frac{Z_0}{X_j} = \left(\frac{Z_0}{S}\right)^{1/2} - \left(\frac{S}{Z_0}\right)^{1/2} \qquad j = 1, n+1 \tag{5.1}$$

$$\frac{Z_0}{X_j} = \frac{Z_0}{S}\frac{\sqrt{g_{j-1} - g_j}}{g_0 g_1} - \frac{S}{Z_0}\frac{g_0 g_1}{\sqrt{g_{j-1} - g_j}} \qquad j = 2,3,\ldots,n \tag{5.2}$$

$$S = \frac{\pi Z_T}{2 g_0 g_1}\frac{\omega_2 - \omega_1}{\omega_0} \tag{5.3}$$

$$\phi_j = -\tan^{-1}\left(\frac{2X_j}{Z_0}\right) \tag{5.4}$$

where ω_0, ω_1, and ω_2 are the center, lower cut-off and upper cut-off angular frequencies; n is the number of resonant sections in the bandpass filter and g_i are the prototype element values of the corresponding lowpass equivalent, and Z_0 is the source and load impedance. The first two equations are used to calculate the shunt inductor values, providing that the design parameters (Z_T, bandwidth and ω_0) are known in advance. Note that the negative length of transmission lines of the immittance inverters are simply absorbed in the half wavelength resonant sections.

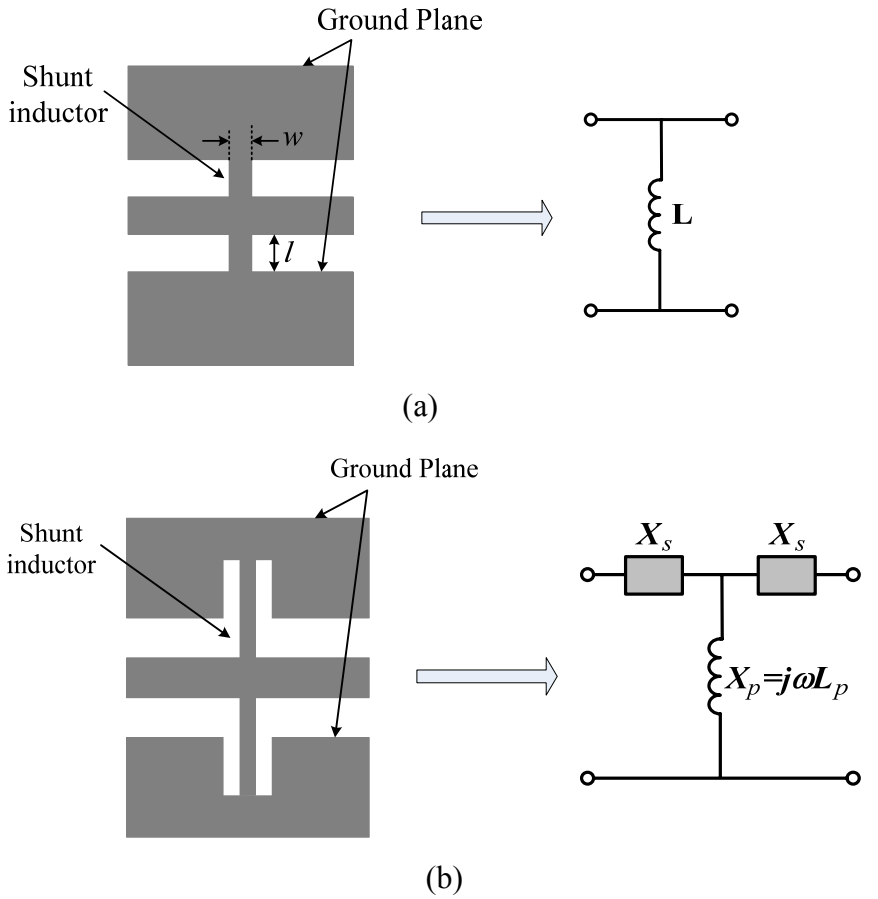

Fig. 5.3. Structure used to realize (a) small, (b) large shunt inductors.

One method to realize the shunt inductors is to use the classical formula for (ribbon) straight inductors:

$$L = 2l\left\{\ln\left(\frac{2\pi l}{w}\right) - 1 + \frac{w}{\pi l}\right\} \qquad nH \tag{5.5}$$

where *w* and *l*, measured in cm, are the width and length of the stub, respectively, as shown in Fig. 5.3 (a). However, it should be noted that the accuracy of this formula is quite poor with an error greater than 10% for wide lines (small inductance).

Another technique to realize the large inductance value at both ends of the filter is to adopt the structure shown in Fig. 5.3 (b) in the design. This configuration shown is represented by a T-circuit rather than a simple inductor, to take into account the phase shifts introduced by the series elements. An accurate model for this structure is not available; therefore, the design was improved iteratively, using the electromagnetic MoM-based simulator Zeland IE3D version 12.1, to adjust the end inductors.

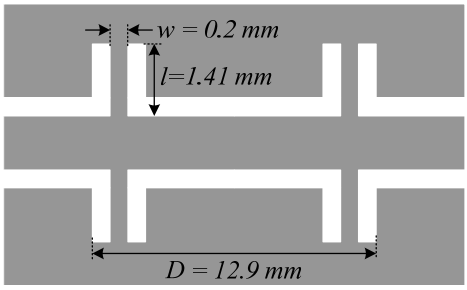

(a)

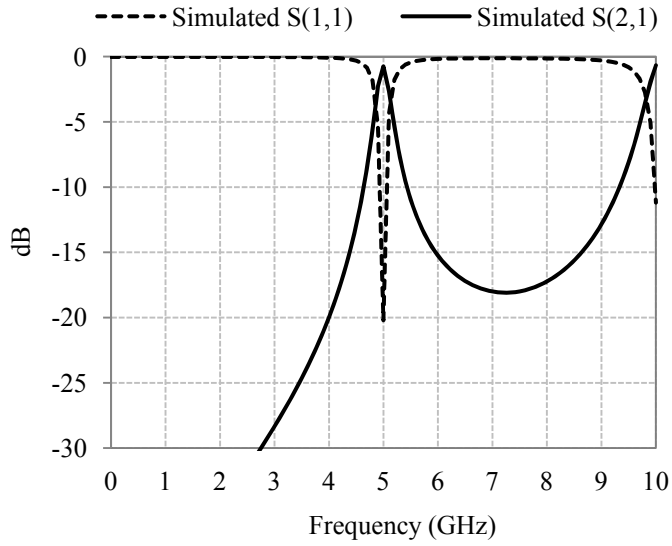

(b)

Fig. 5.4 (a) Layout of the conventional inductively coupled BPF. (b) Simulated response of the filter designed at 5 GHz.

Using the previously mentioned technique, the narrow bandpass filter composed of one half waveguide wavelength resonator terminated by short circuited

stubs to produce the inductively coupled scheme has been implemented as shown in Fig. 5.4 (a). The resonator is designed on Teflon substrate of dielectric constant ε_r= 9.5, thickness 0.635mm, loss tangent 0.0035 and L=0.72 nH (based on the Chebychev prototype with 0.01 ripple factor) with CPW dimensions G/W/G = 0.45/1.4/0.45 mm corresponding to 50Ω. The structure resonates at 5 GHz, with insertion loss of -0.645 dB, return loss -21.1 dB and 3-dB fractional bandwidth of 4.48 %, as shown from the simulated response in Fig. 5.4 (b).

5.2.3. Defected Ground Structure Based Bandpass Filter

In the previous section, the design procedures for the conventional inductively coupled resonator BPF is presented with one designed at 5 GHz using 0.01 ripple factor Chebychev response.

In this section, we will introduce a DGS in the middle of the resonator between the two stub inductors. The same design equations are to be used to find the values of the inductances, as the introduced DGS will only influence the effective length of the resonator, but has no great effect on the coupling scheme between different resonators. This section is devoted to the design procedures and the effect of this defect on the inductively coupled resonators.

The design process of the DGS cell introduced in the middle of the inductively coupled resonator is as follows:

For the structure to resonate at the required resonant frequency (in our case: 5 GHz), the analytical phase angle of the whole resonator (the DGS cell and the two stubs) should equal to 180° at 5 GHz. The short-circuited CPW shunt stub is represented by the inductive T-network extracted from the full wave simulator, thus the electrical length of the CPW short-circuited stubs θ_{stub} may be calculated. Therefore, the electrical length of the DGS cell is given by:

$$\theta_{DGS} = 180^{\circ} - 2\theta_{stub} \tag{5.6}$$

Fig. 5.5 (a) shows the layout of the DGS based BPF designed on the same previously mentioned substrate, while Fig. 5.5 (b) shows a photograph of the fabricated structure. By comparing the layout of the conventional inductively coupled resonator BPF in Fig. 5.4 (a), and that of the DGS based BPF in Fig. 5.5 (a), it is clear that the length of the resonator is reduced from 12.9 mm to 5.5 mm,

making use of the lateral ground planes of the CPW. Fig. 5.6 shows the simulated and measured responses of the DGS based filter. All electromagnetic simulations are done by the full wave MoM-based simulator Zeland IE3D Ver.12.1, and they show good agreement with the measurement results. The filter resonates at 5 GHz with insertion loss of -0.6613 dB, return loss -17.61 dB and fractional bandwidth of 4 %, which is comparable to results obtained by the conventional inductively coupled resonator filter.

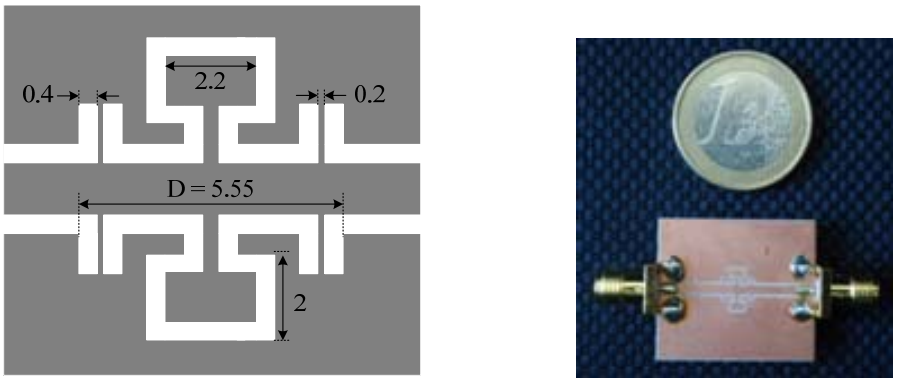

(a) (b)

Fig. 5.5 (a) Layout of the DGS based inductively coupled BPF of order one. Dimensions are in mm. (b) Photograph of the fabricated structure.

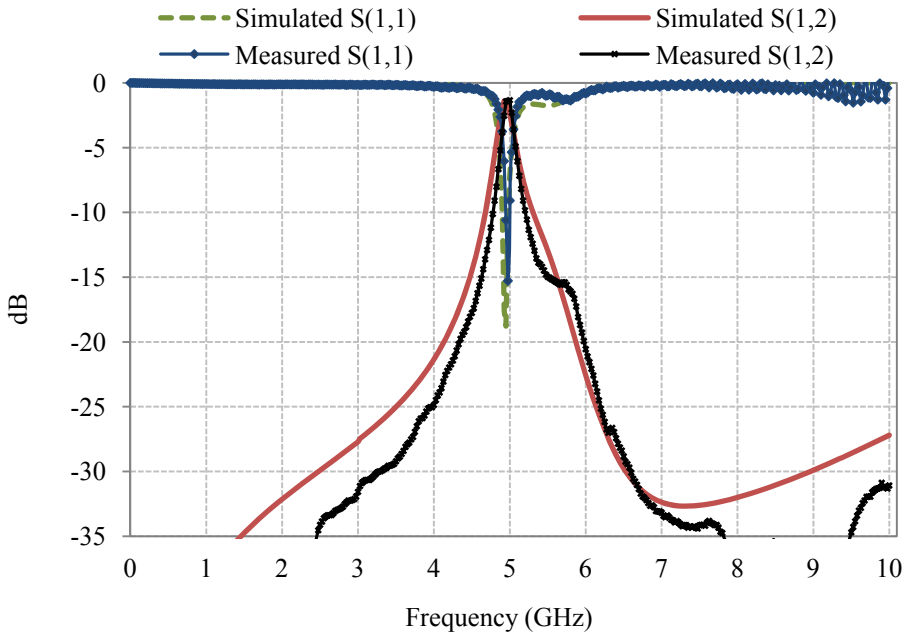

Fig. 5.6. Simulated and measured responses of the first order DGS based bandpass filter.

To validate the presented technique and design procedures, a second order filter of the same type is implemented to achieve a better rejection skirt. The filter is designed on the same substrate using also the 0.01 ripple level Chebychev response. The layout of the filter is shown in Fig. 5.7 (a), while the simulated and measured responses are shown in Fig. 5.7 (c). The same DGS cell with the same dimensions is used for the second order filter, while the dimensions of the stubs are changed according to the values of the shunt inductances needed.

The length of the filter is 12.82 mm as illustrated in Fig. 5.7 (a) for both resonators with the coupling shunt stub inductors. Simulation and measurement results are in good agreement. The filter has insertion loss of -1.446 dB, return loss -12.52 dB, and a fractional bandwidth of 5.46 %.

A comparison between the simulated response of the three presented filters is shown in Fig. 5.8, where it is clear that the responses of the conventional and the first order filter are nearly identical, while the second order DGS based BPF shows a flat passband width with better rejection characteristics.

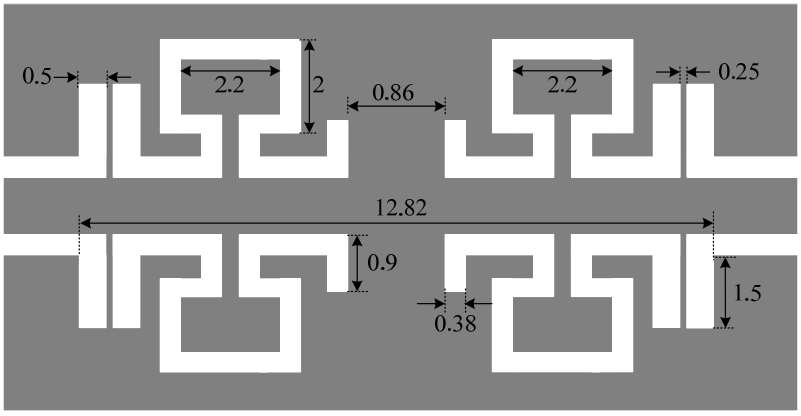

(a)

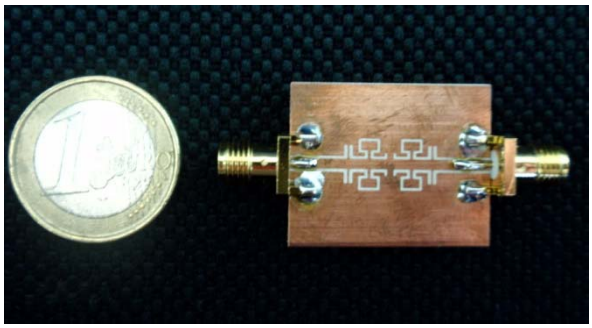

(b)

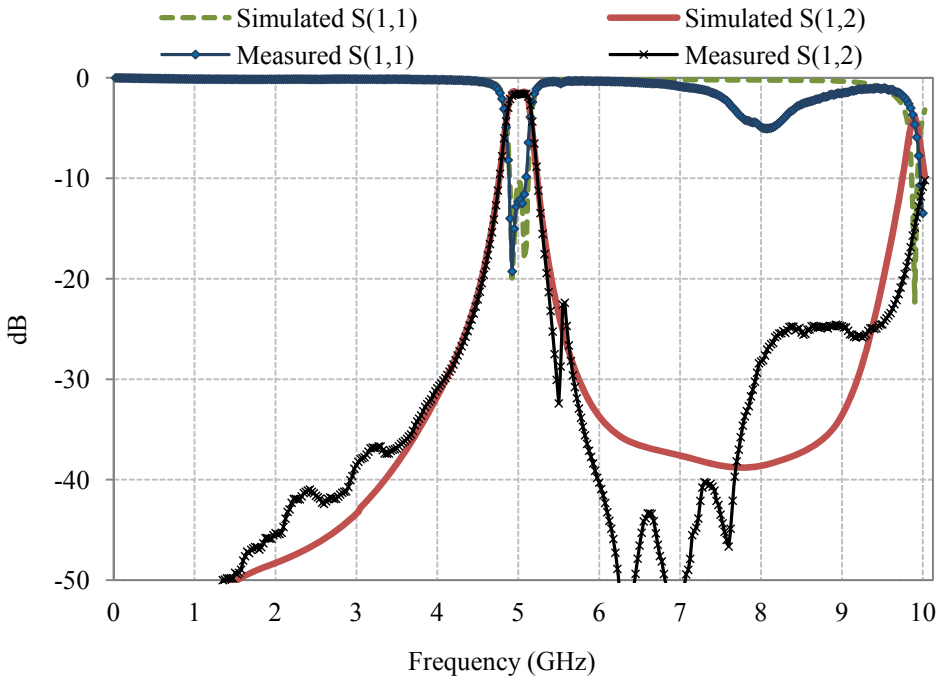

(c)

Fig. 5.7. (a) Layout of the DGS based BPF of order two. Dimensions are in mm. (b) Photograph of the fabricated filter. (c) Simulated and measured responses.

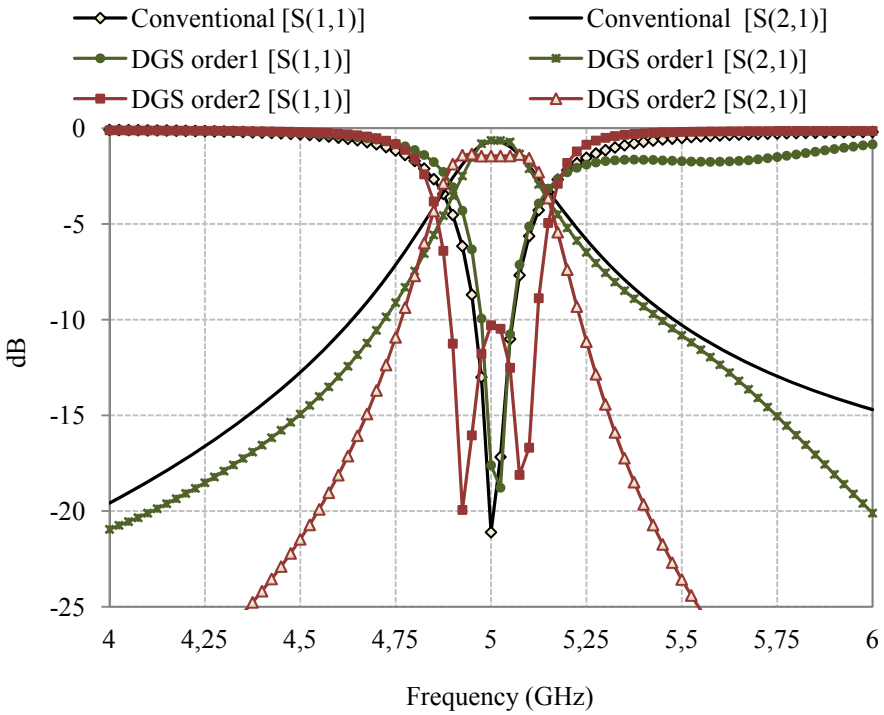

Fig. 5.8. Simulated S-parameters of the conventional inductively coupled resonator in comparison with the novel first and second order DGS based inductively coupled resonator bandpass filters designed at 5 GHz.

5.2.4. Inductively Coupled Resonator Bandpass Filter with a Reconfigurable Defected Ground structure

In this section, we present a reconfigurable multiband bandpass filter as an enhancement for the previously presented filters. The reconfigurability is introduced by means of the DGS implemented in the middle of the inductively coupled resonator as shown in Fig. 5.9 (a). The reconfigurable bandpass filter presented here consists of two parts. The first part is the inductively coupled resonator which is explained in the Section 5.2.2 and the second is the reconfigurable defected ground structure resonator which is responsible for size miniaturization and reconfigurability effect.

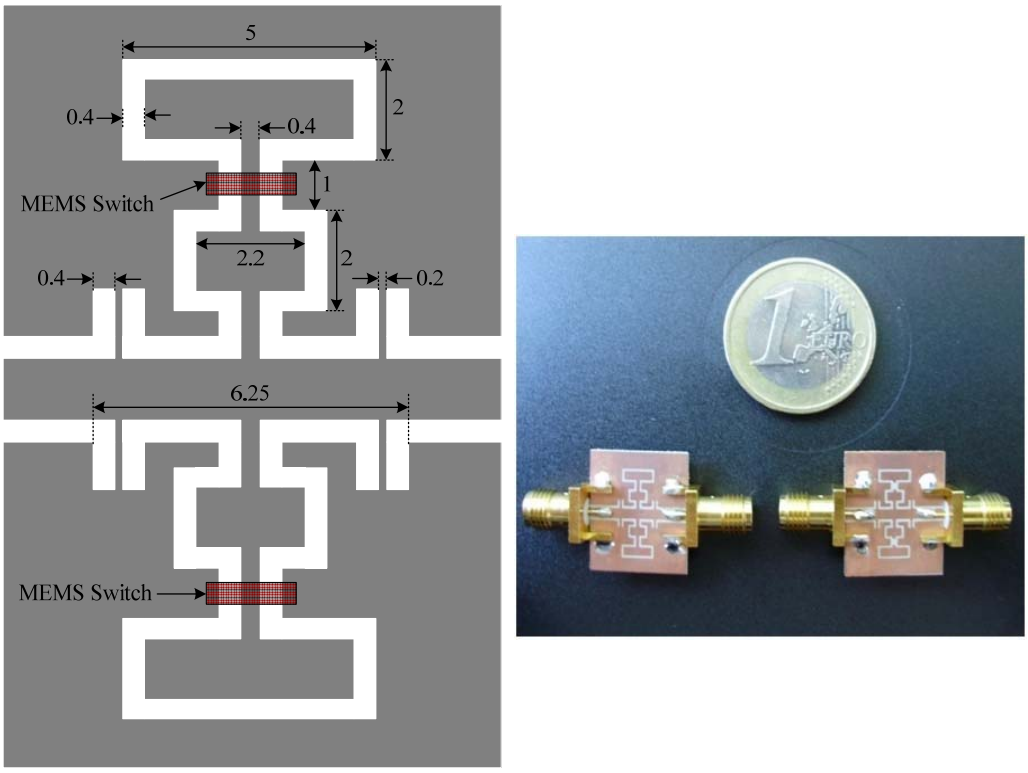

(a) (b)

Fig. 5.9 (a) Layout of the proposed inductively coupled BPF with DGS (Dimensions in mm). (b) Photograph of the fabricated structure.

The DGS presented here consists of two rectangular resonators of different sizes, Fig. 5.9 (a). The first resonator is directly connected to the CPW signal line, and then the second resonator is fed through the first one. There is a MEMS switch used to connect and disconnect the second resonator from the structure allowing the reconfigurability of the resonant frequency. In this work, the reconfigurability element used (MEMS capacitive switch) is assumed to be an ideal switch, which

means it is modeled as an open circuit in the OFF state and capacitive short circuit in the ON state. Therefore, two structures have been fabricated as shown in Fig. 5.9 (b) representing the ON and OFF states of the switch.

In this section, simulated and measured results of the reconfigurable BPF are presented with explanation of the shown phenomena. Results concerning the introduced DGS as a standalone element have been explained before with design equations for the transmission zeros using slotline equations in Chapter Four.

Fig. 5.10 and Fig. 5.11 show the simulated and measured responses of the reconfigurable BPF in two cases. In the first case, the MEMS switch is ON, which means a virtual capacitive short circuit introduced by it at this point impedes the signal transfer to the second resonator. Hence only one single resonator is involved in the transfer function of the filter. This corresponds to one resonance frequency, at 5 GHz as in the case of conventional inductively coupled resonator, except that, the length of the resonator is reduced from 12.9 mm, as shown in Fig. 5.4 (a), to 6.25 mm due to the slow wave effect introduced by the DGS. The insertion loss at 5 GHz is -1.24 dB, return loss is -18.43 dB, and 3-dB fractional bandwidth is 4.26 %, which makes the results comparable with those of the conventional inductively coupled BPF. In addition, the second harmonic at 10 GHz is completely suppressed.

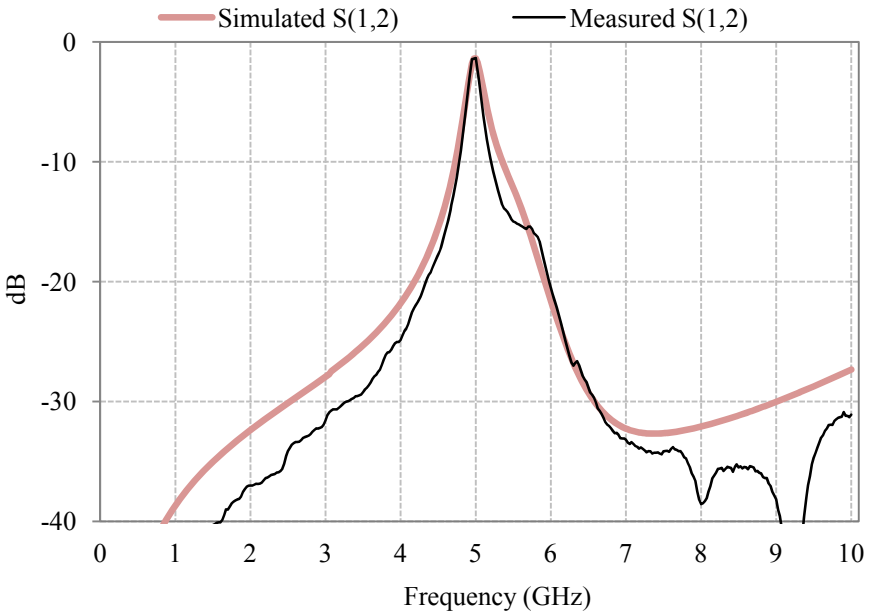

(a)

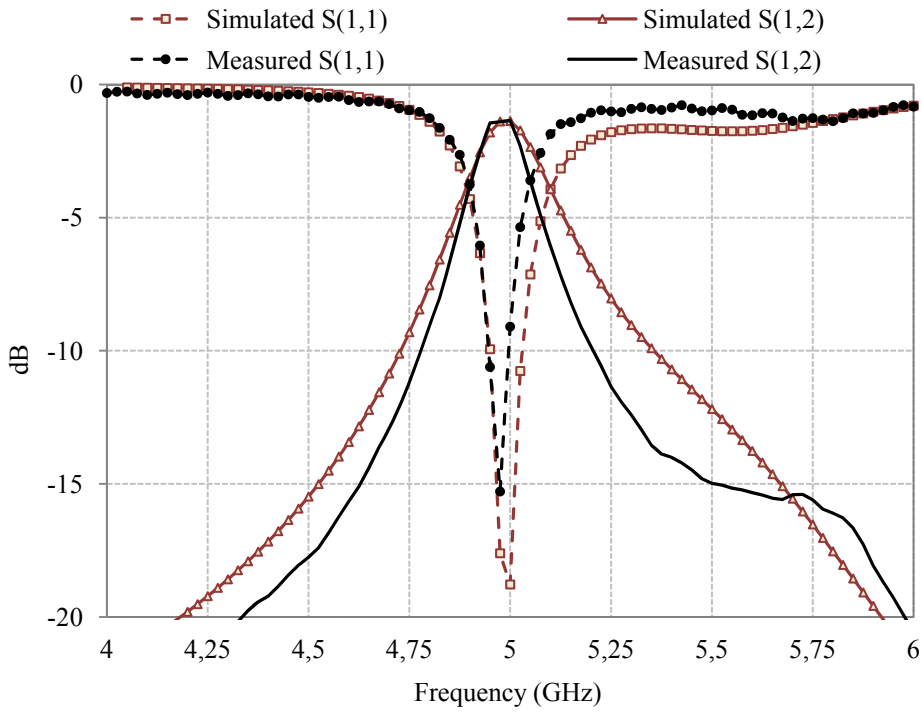

(b)

Fig. 5.10 Simulated and measured responses of the reconfigurable BPF when the MEMS switch is ON (a) from 0-10 GHz; (b) from 4-6 GHz.

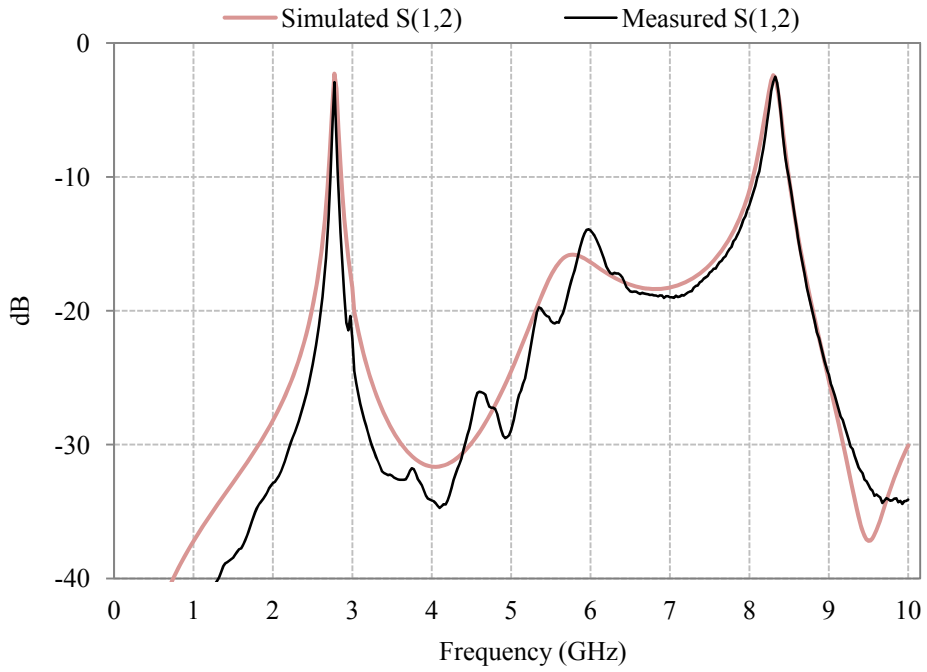

(a)

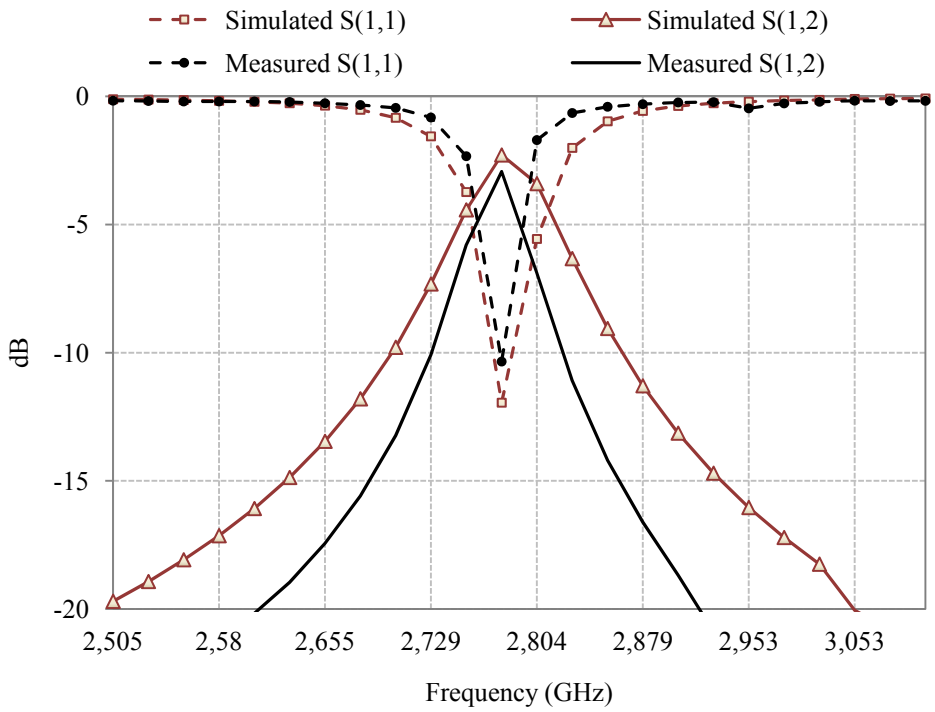

(b)

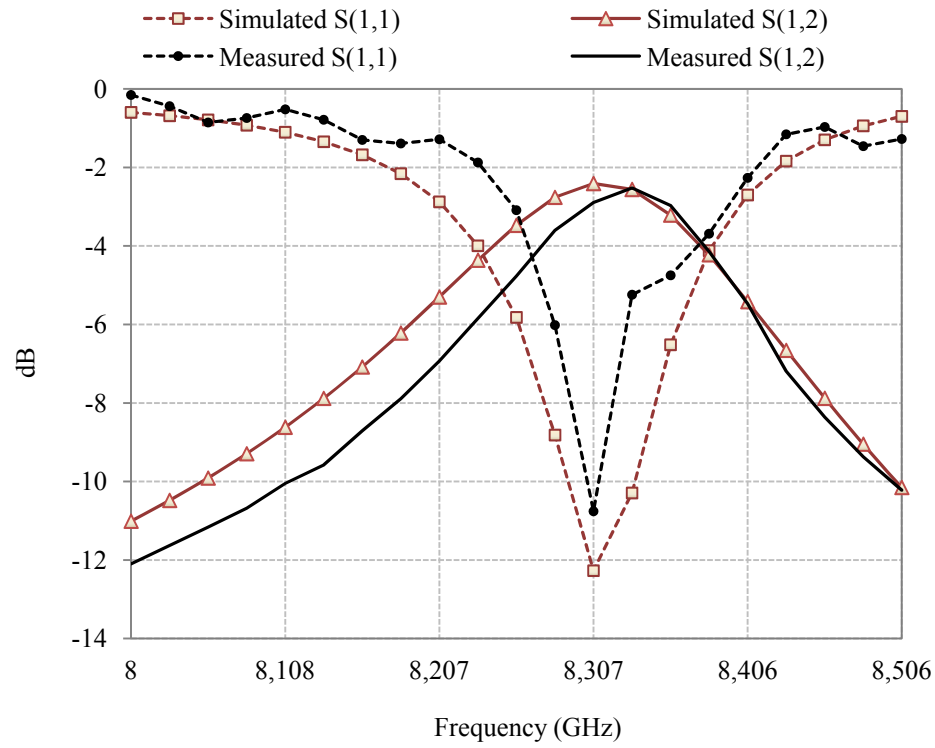

(c)

Fig. 5.11 Simulated and measured responses of the reconfigurable BPF when the MEMS switch is OFF (a) from 0-10 GHz; (b) from 4-6 GHz; (c) from 8-8.5 GHz.

The second case is when the MEMS switch is OFF, that means that the second resonator is connected along with the first one, yielding two resonant frequencies at 2.8 GHz and 8.3 GHz. At 2.8 GHz, the insertion loss is -2.36 dB and return loss is -10.5dB and at 8.3 GHz, the insertion loss is -2.2 dB and return loss is -10.9 dB. The simulated and measured responses are shown in Fig. 5.11.

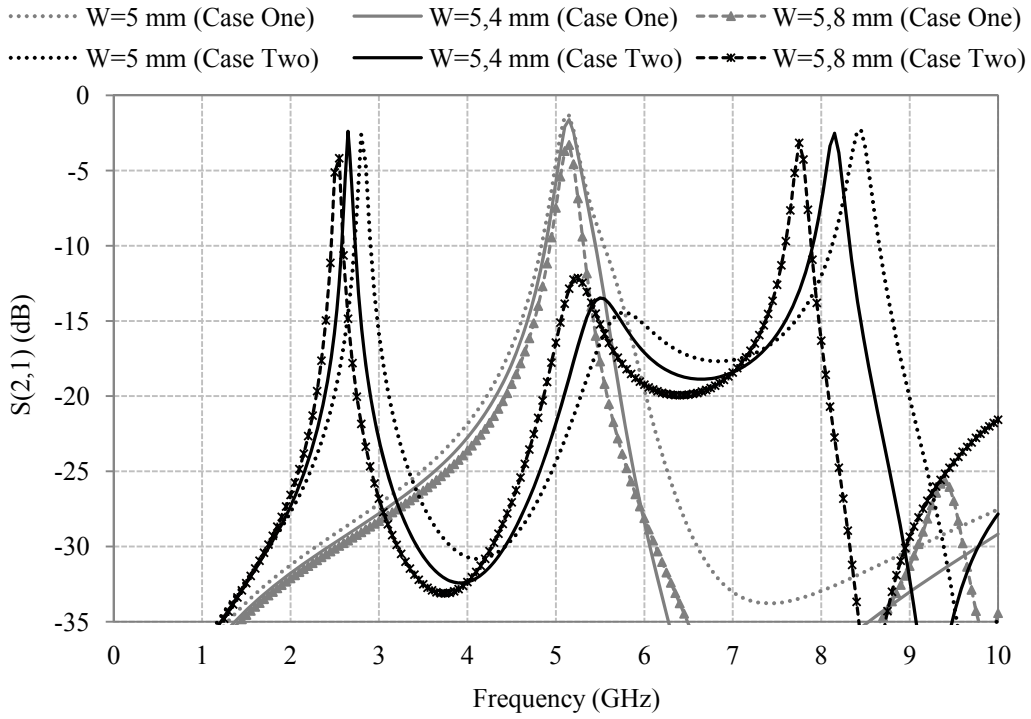

Fig. 5.12 Simulated results of the reconfigurable BPF for different values of "W".

Fig. 5.12 shows the effect of changing the width of the bigger resonator, denoted by "W" (in Fig. 5.9 (a)), on the resonance frequencies in both cases. It is clear that changing the width of the outer resonator has nearly no effect on the resonance frequency in case one, but it shifts those of case two as expected. This is very important in the design of reconfigurable structures as this shows that both cases can be independently designed and controlled. It is also important to note that the number of resonance frequencies depends on the number of resonators, i.e. if three passbands are required, have three resonators will be needed, but on the other hand this will increase the insertion loss values.

5.2.5. Conclusion

This section addresses DGS based inductively coupled bandpass filters fabricated on Coplanar Waveguide (CPW) technology. The addition of the DGS to the conventional inductively coupled resonator BPF allows the miniaturization of the resonator by exploiting the transversal dimensions of the CPW, while maintaining its performance with respect to insertion and return loss values. On the other hand, the DGS cell allows reconfiguration of the structure from a single band to a multiband BPF. The design procedure of the filters with the DGS is explained with filters designed at 5 GHz. Simulated and measured results show good agreement.

5.3. Ring Resonator Filter with Different Bandgap Structures

5.3.1. Introduction

In this section, we address a modified bandpass ring resonator filter providing compact size, low insertion-loss, wide bandwidth, sharp rejection and suppressed higher order modes.

It has been demonstrated that ring resonator based filters feature attractive behavior [14], [15] but they suffer from two drawbacks that limit their implementation in real applications. The first one is their large size due to the two tuning stubs, while the second deals with the existence of higher order modes which limits the out-of-band rejection. Both issues degrade the whole system performance and need to be assessed to find solutions to overcome these drawbacks.

This section aims to propose some solutions to reduce the size and increase the rejection of the upper stopband of the ring resonator bandpass filter, while keeping its overall performances with respect to its wide bandwidth, sharp rejection and low insertion-loss. In order to do so, two different design approaches are considered. The first is at the filter layout level, through a space saving redesign of the tuning stubs [6], while the second is at the wave propagation level, through the exploitation of Defected Ground Structures (DGS) and Uniplanar Compact-Photonic Bandgap (UC-PBG) Structures properties [16].

The DGS, realized by etching patterns in the ground plane, enables higher order modes suppression through the introduction of a wide stopband in the frequency response of the filter, and on the other hand introduces slow wave effect

which translates into a reduction of the electrical length and hence the overall filter dimensions [17-19].

To our knowledge, the work reported to date has used the DGSs to suppress only the second order harmonic of multistage coupled ring resonator filter by etching the ground plane of the output feeding line [16]. The use of this technique yields general detrimental effects as; on the one hand it increases the filter size and the filter insertion loss while on the other it decreases the filter bandwidth due to the coupling of different stages. In the work presented here, by placing the DGSs directly under the ring resonator, the second and third harmonics are suppressed with a reduction in the filter size reaching 25.75 % of the conventional ring resonator filter.

We also investigated the use of UC-PBG structures [20] with the ring resonator filter. Despite that it is difficult to use EBG structures for the design of the microwave or millimeter-wave components due to the difficulty of their modeling and their too many design parameters that affect the bandgap properties; they give wider upper stopbands suppressing the second, third and forth harmonics with a greater size reduction reaching 45.5 %.

All filters are fabricated on Teflon substrate (CER 10-0250 CH/CH) of dielectric constant ε_r=9.5, dielectric thickness h=0.635mm and loss tangent 0.0035. Measurements show good agreement with simulation results.

5.3.2. Conventional Ring Resonator Filter

This section presents briefly the ring resonator bandpass filter proposed by [14]. The ring resonator bandpass filter consists of a ring resonator directly connected to a pair of two orthogonal tuning stubs and two orthogonal feeding lines as shown in Fig. 5.13. The circumference of the ring resonator ℓ_r is chosen according to the following expression:

$$\ell_r = n\lambda_g \tag{6.1}$$

where n is the mode number and λ_g is the guided wavelength. Each tuning stub is equal to one quarter of a guided wavelength designed at the center frequency and placed at the center of each side of the ring resonator. In order to increase the bandwidth of the stopbands of the filter, a square stub is added at the corner of the filter which gives rise to degenerate mode operation [22], [14].

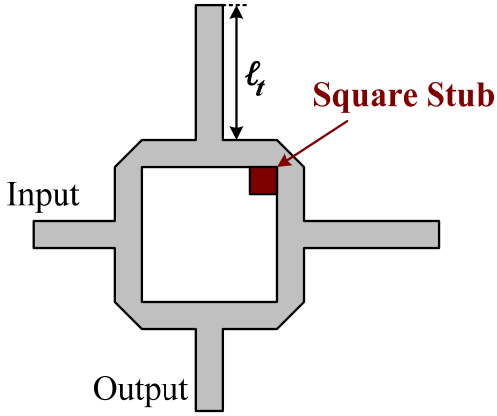

Fig. 5.13. Layout of the conventional microstrip ring resonator filter with two straight tuning stubs [14].

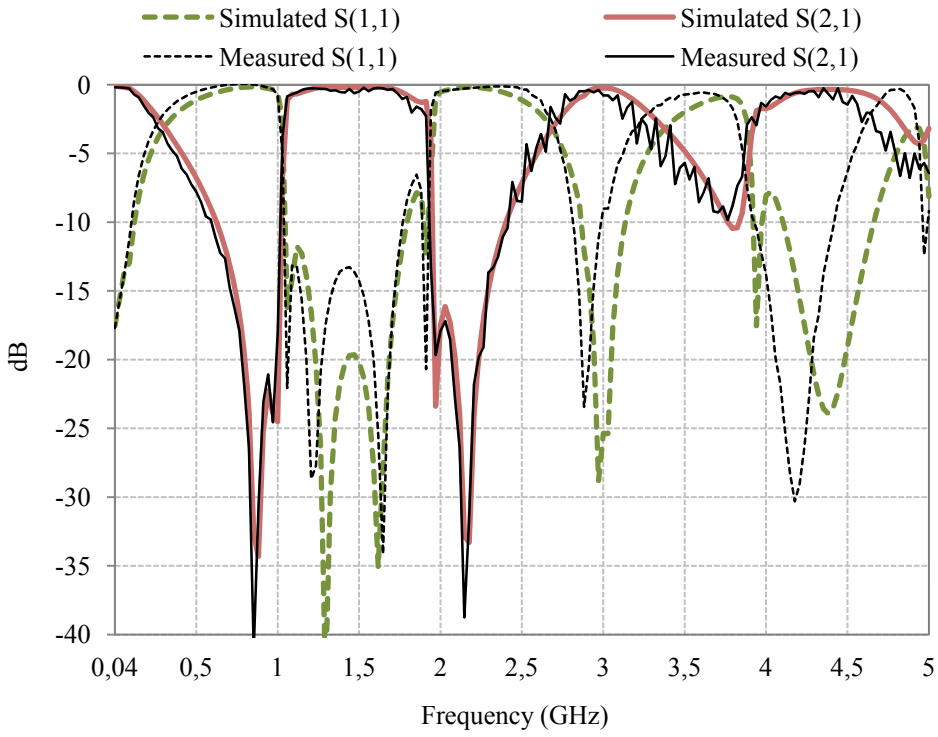

Fig. 5.14. Simulated and measured responses of the conventional ring resonator filter.

A filter using the previously discussed technique is designed and fabricated. The complete area of the filter is 40.47x 40.47 mm. Fig. 5.14 shows the simulated and measured response of the filter. Its response is measured using the Vector Network Analyzer VNA WILTRON 360B. The filter center frequency is at 1.49 GHz and return loss of -8 dB and an insertion loss of -1.2 dB (worst measured value

in the passband). The filter has a 3-dB fractional bandwidth of 60.6%, and has two attenuation poles at 0.85 GHz and 0.98 GHz of -35 dB and -24.7 dB, respectively, and another two attenuation poles at 1.98 GHz and 2.16 GHz of -20.2 dB and -40.3 dB, respectively.

It was found that the filter suffers from adjacent passbands due to the higher order modes at 3 GHz and 4.45 GHz, representing the second and third harmonics of the resonant frequency, respectively, consequently the filter 10-dB upper stopband is only 0.4612 GHz.

The filter also suffers from its large occupation area, due to its two tuning stubs that occupy about 72 % of the area of the filter. The following section addresses the large occupation area of the two stubs by two different techniques.

5.3.3. Miniaturization by Using Folded Stubs

In order to reduce the area occupied by the filter, a more compact design of the stubs is introduced. This has been previously considered by [15]. The disadvantage of the stub structure in [15] is its complex orientation and design parameters.

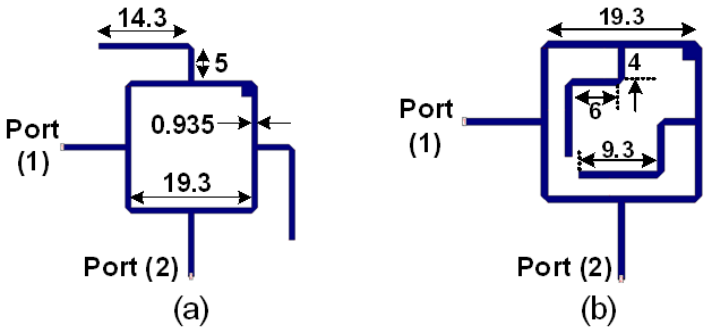

Fig. 5.15. Layout of the ring resonator filters with (a) external bent stubs; and (b) internal folded stubs. All dimensions are in mm.

This is done here by bending the stub along the filter ring profile in a first design iteration, as shown in Fig. 5.15 (a), and then reversing the stubs T-junction toward the interior of the ring in a second iteration, as shown in Fig. 5.15 (b). In the latter, the stubs need to be bent twice in order to fit in the ring internal area.

In both cases, parameters such as the losses introduced by the bend, and the coupling that might take place between the ring resonator and the bent stub need to be considered.

For a 90° microstrip bend, based on the study made by [23], this bend might cause up to 2.5 dB insertion loss in the form of radiation and surface-wave losses at this frequency range. On the other hand, a mitered bend provides about 0.1 to 0.3 dB losses. Therefore, to reduce the radiation and surface-wave losses, we use mitered bends in the stub.

The second issue that should be considered is the coupling between the stub and the ring. The design presented here is based on the quasi-TEM mode properties of the coupled microstrip line discussed in [24]. The coupling coefficient between the two lines is given by:

$$C = \frac{Z_c^e - Z_c^o}{Z_c^e + Z_c^o} \tag{5.6}$$

where Z_c^e and Z_c^o are the even- and odd-mode characteristic impedances. Although Eq. (5.6) provided by Bahl and Bhartia [24] produces an error that might reach 8% according to [25], we used this equation to reduce the coupling effect. It is enough to provide a distance that reduces the coupling coefficient up to -15dB.

The two solutions of Fig. 5.15 are designed on the same substrate mentioned above. The simulated and measured responses are presented in Fig. 5.16 (a) and (b). For the external bent stubs ring resonator filter, the complete area of the filter is 31.3 x 31.3 mm corresponding to a size reduction of 40.2 %. The filter center frequency is at 1.47 GHz with a worst measured return loss -8.2 dB and an insertion loss of -1.12 dB in the passband of the filter. The filter has a 3-dB fractional bandwidth of 57.8%, with two attenuation poles at 0.854 GHz and 0.956 GHz of -44.5 dB and -32.5 dB, respectively, and another two attenuation poles at 1.96 GHz and 2.16 GHz of -25.7 dB and -32.05 dB, respectively. The filter 10-dB upper stopband is 0.42 GHz.

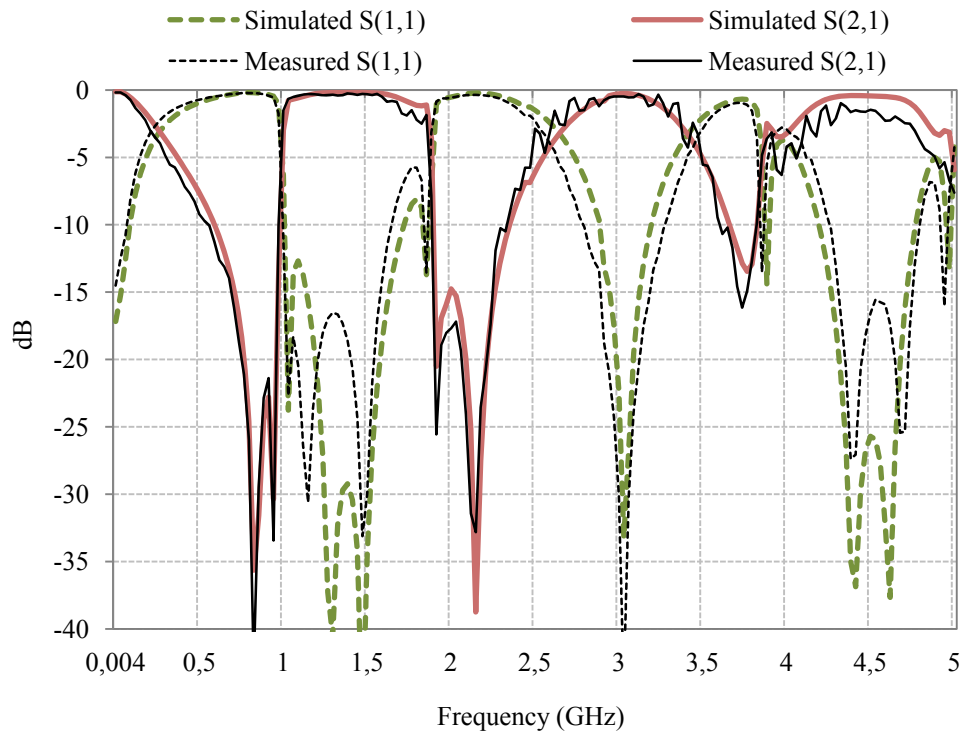

(a)

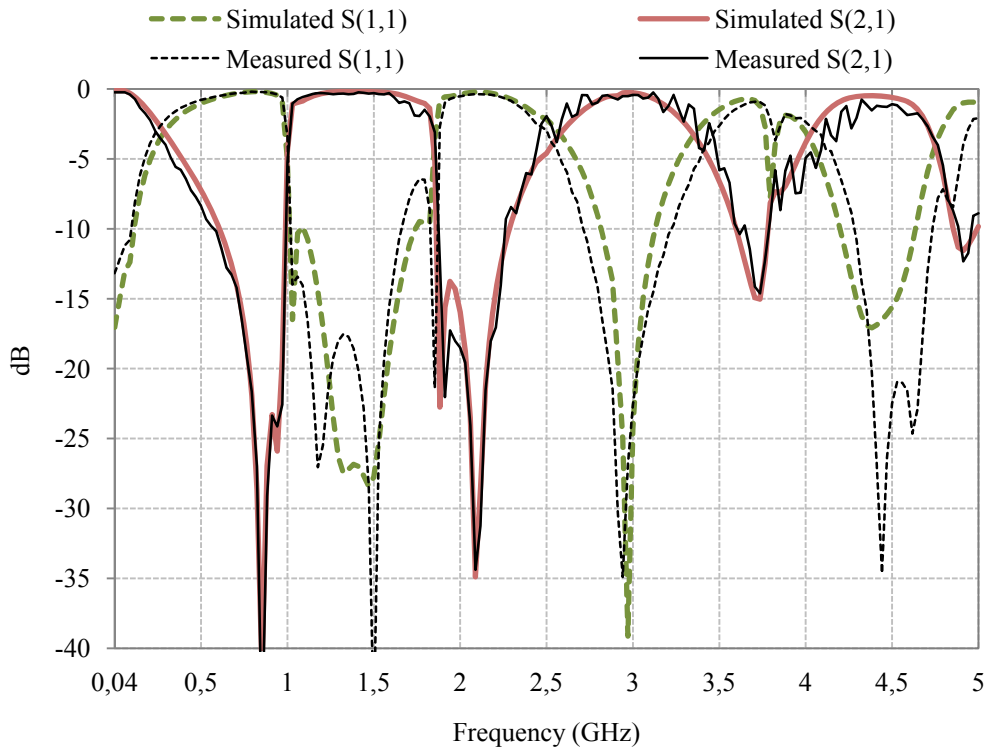

(b)

Fig. 5.16. Simulated and measured responses of the ring resonator filter (a) with external bent stubs and (b) with internal folded stubs.

Now we will consider the internal folded stubs to produce the maximum size reduction. The complete area of the filter is 19.3 x 19.3 mm corresponding to a size reduction of 73.4%. The filter center frequency is at 1.47 GHz with a worst measured return loss -9.6 dB and an insertion loss of -0.88 dB. The filter has a 3-dB fractional bandwidth of 55.8%, with two attenuation poles at 0.83 GHz and 0.94 GHz of -41.6 dB and -25.3 dB, respectively, and another two attenuation poles at 1.9 GHz and 2.1 GHz of -22.3 dB and -34.42 dB, respectively. The filter 10-dB upper stopband is 0.433 GHz. The properties of all demonstrated filters are summarized in Table 5.1.

Table 5.1

Characteristics of the Filters Presented in Section 5.3.3

Filter	Insertion Loss (dB)	Return Loss (dB)	Fractional Bandwidth	Upper Stopband (GHz)	Size (mm)	Size Reduction
Conventional Ring Resonator Filter	-1.2	-8	60.6 %	0.46	40.5 x 40.5	----------
Ring Filter with External Stubs	-1.12	-8.2	57.8 %	0.42	31.3 x 31.3	40.2 %
Ring Filter with Internal Stubs	-0.88	-9.6	55.8 %	0.43	21.1 x 21.1	72.6 %

From the comparison shown in Table 5.1, it is obvious that a great reduction in the size of the filter reaching up to 72.6% for internal folded stubs is achieved, keeping very good overall filter performance. However, the issue of higher harmonics is not solved yet, which will be the subject of the following section.

5.3.4. Microstrip Ring Resonator Bandpass Filter with Defected Ground Structures (DGSs)

The use of DGSs is hereby exploited to improve the harmonic rejection of the filter. DGSs produce variations in the refractive index of the medium to introduce a certain stopband in its frequency response. Following the original interpretation and analysis made by Yoblonovitch [26] this stopband is produced by the coupling between the forward and backward propagating waves due to periodic variations in the refractive index of the medium. This variation in the refractive index can be implemented by etching specific patterns in the ground plane.

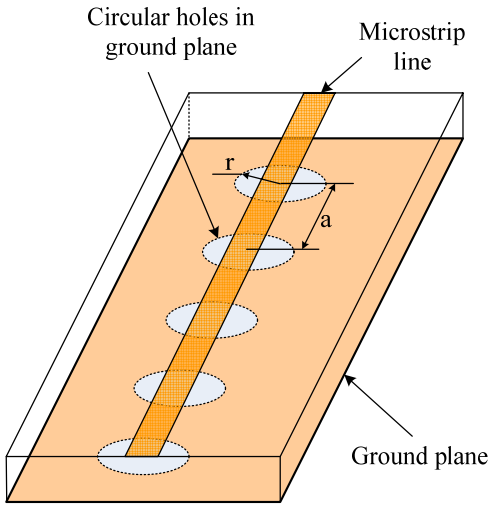

Fig. 5.17. Three-dimensional view of the proposed PBG structure.

The selected DGS, hereby presented, is a one dimensional lattice with circles etched in the ground plane as shown in Fig. 5.17 [27]. In order to investigate the stopband effect of the DGS structure, three circuits are simulated with circles of different radii. The substrate used is the aforementioned above. The period between the circle DGSs is kept constant to 14.3 mm (corresponding to $\lambda_g/2$ at 5 GHz) and the circle radius is varied. Simulated S-parameters for all three circuits are shown in Fig. 5.18 (a)–(c).

In our study, we fix the period of the structure (a) for 14.3 mm, and we varied the radius of the circle (r) in each case. In case (a), where r=1.79 mm, the center frequency of the stopband is 5 GHz, with a stopband of 1.36 GHz. In case (b), where r is doubled, the stopband is 3.87 GHz. Finally, in case (c), where r =6 mm, the stopband is 5.4 GHz.

As a conclusion, we may say that the stopband center frequency is a function of the period of the structure [27]. In particular, the guided wavelength is twice the period. Unfortunately, the propagation constant is not easily determined, and full-wave analysis is necessary to accurately characterize the structure. However, for small values of (r/a) the stopband center frequency can be assessed by using the propagation constant of the unperturbed microstrip.

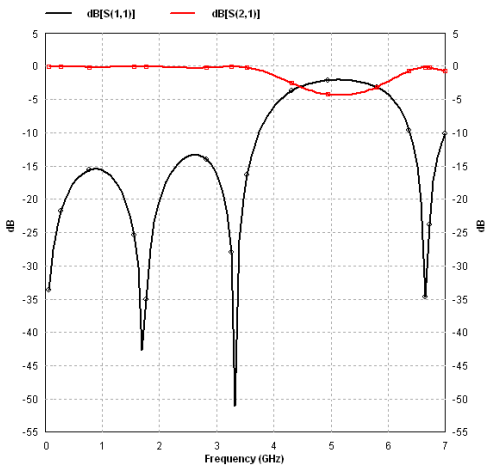

(a)

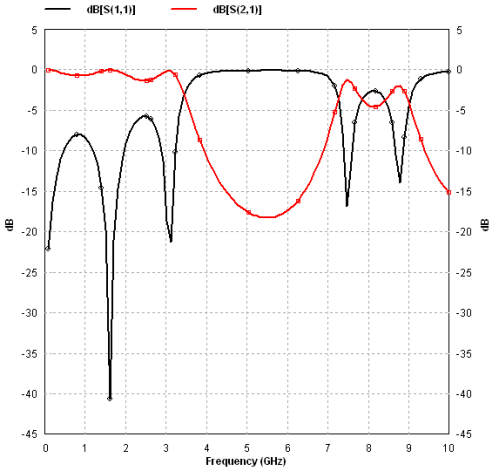

(b)

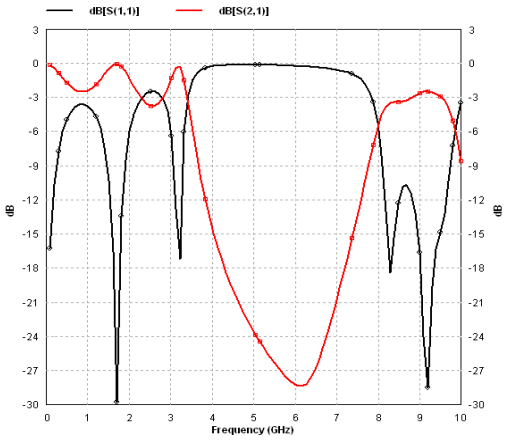

(c)

Fig. 5.18. Simulated S-parameters for the circle DGS microstrip transmission line. The ground plane has 1x3 etched circles. The hole radius is (a) r = 1.79 mm, (b) r = 3.58 mm, and (c) r = 6 mm. The period is 14.3 mm for all cases.

Based on previous results, depth and bandwidth of the stopband depend on the circle radius. For smaller circle radii the stopband is very small, as shown in Fig. 5.18 (a). In the limiting case ($r \to 0$) there is no stopband, and the structure is a standard microstrip line. As the circle radius is increased the stopband becomes more distinctive. A tradeoff is that for very large factor (r/a) the ripple in the passband is also increased, as shown in Fig. 5.18 (c).

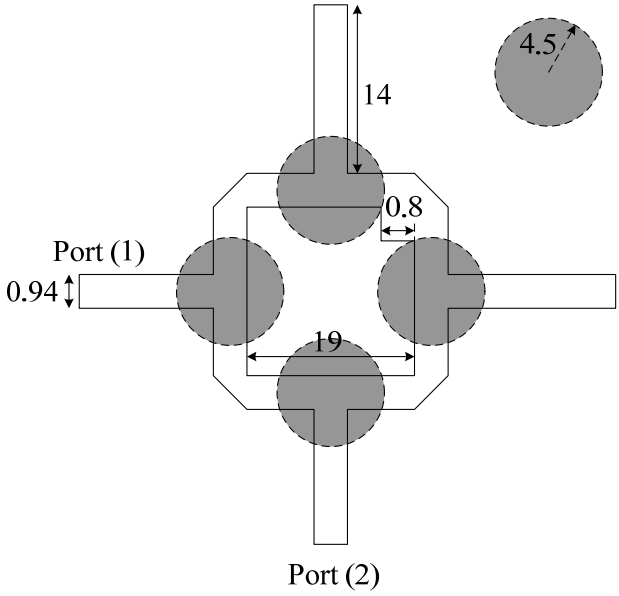

Fig. 5.19. Layout of the ring resonator filter with two straight stubs and circle DGSs etched in the ground plane. All dimensions are in mm.

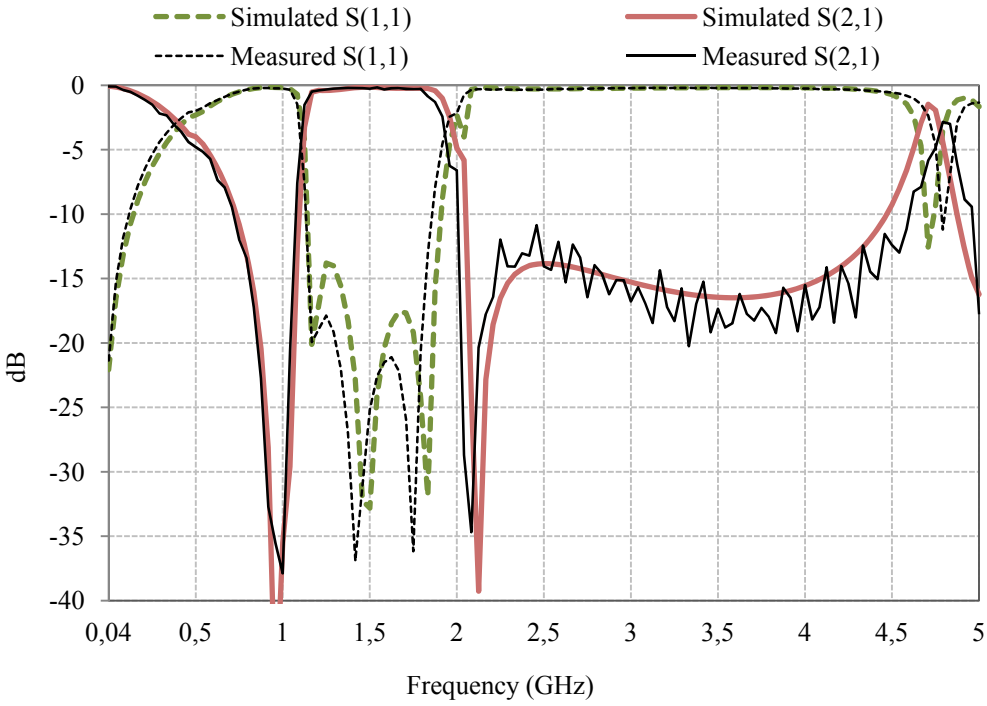

Fig. 5.20. Simulated and measured responses of the ring resonator filter with two unbent stubs and circle DGSs.

Based on these analysis and observations, circles are etched in the ground plane of the ring resonator filter. Simulations of a microstrip transmission line with a period between the etched circles corresponding to $\lambda_g/2$ at 3.5 GHz are first

performed to determine the dimensions of the DGS circles; period (a) and radius (r). The simulations show a stopband starting from 2 to 4.5 GHz, which is wide enough to clear the higher order harmonics of the filter. Using the obtained dimensions, circles are etched in the ground plane of the ring resonator filter; Fig. 5.19 shows the layout of the filter, while Fig. 5.20 shows the simulated and measured responses. The measured results show excellent agreement with the simulation results.

The filter center frequency is at 1.49 GHz and return loss -18 dB and insertion loss of -0.24 dB (worst measured values in the passband). The filter has a 3-dB fractional bandwidth of 57%.The area of the filter is 34.9 x 34.9 mm corresponding to a size reduction of 25.75% of its original size and upper stopband of 2.44 GHz.

The etching of DGSs in the ground plane solves the two problems of the original filter simultaneously. The size of the filter is reduced by 25.75% due to the slow wave effect introduced and the stopband of the filter has increased from 0.45 GHz to 2.44 GHz suppressing the second and third harmonics introduced by the original filter design. In addition, the insertion and return loss values of the filter are enhanced due to the suppression of surface waves provided by the DGSs.

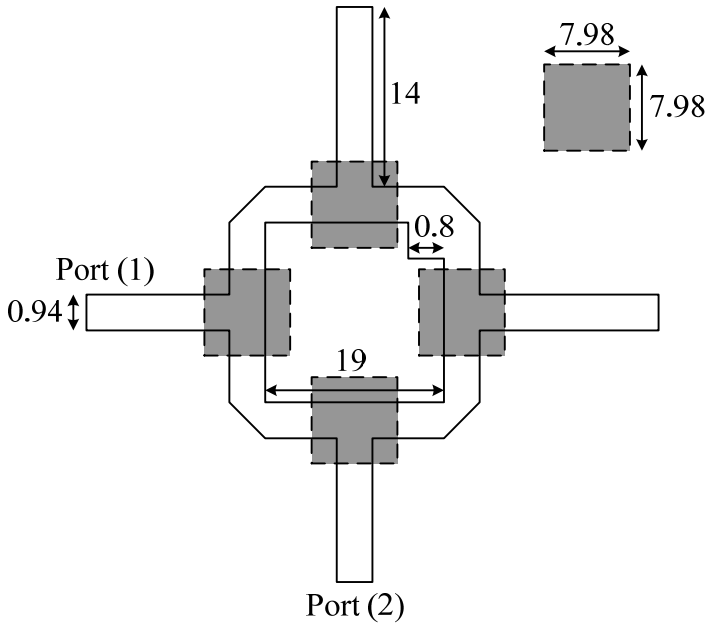

Fig. 5.21. Layout of the ring resonator filter with two straight stubs and square DGSs etched in the ground plane. All dimensions are in mm.

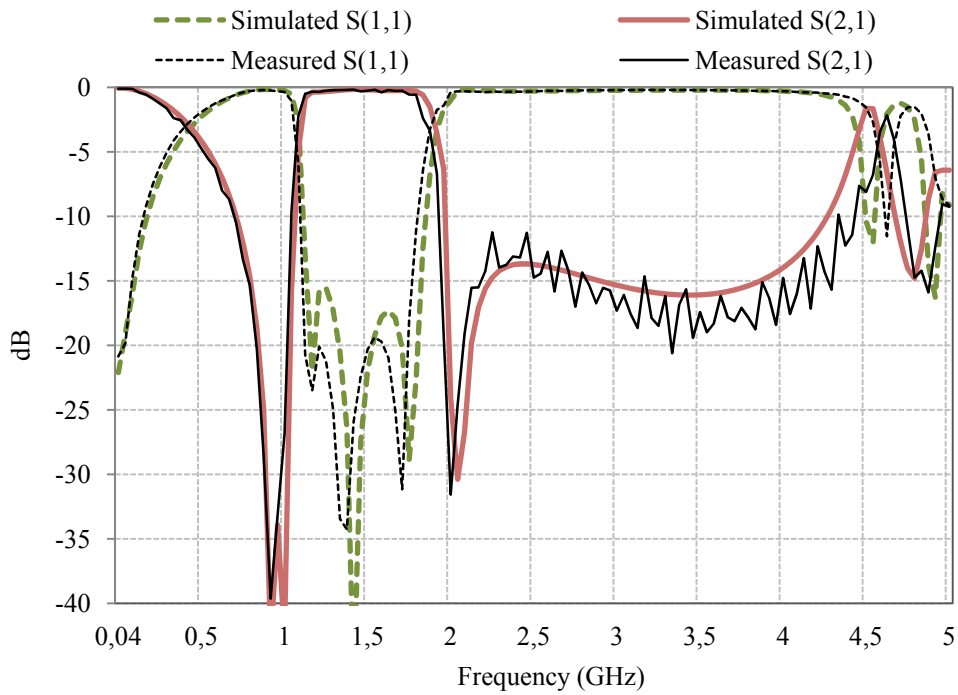

Fig. 5.22. Simulated and measured responses of the ring resonator filter with two straight stubs and square DGSs.

Etching periodic squares instead of etching periodic circles in the ground plane are also considered. The layout of the ring resonator filter with etched squares in the ground plane is shown in Fig. 5.21 and the simulated and measured responses are shown in Fig. 5.22. The filter center frequency is at 1.49 GHz with a worst measured return loss of -19 dB and an insertion loss of -0.23 dB in the passband. The filter has a 3-dB fractional bandwidth of 54.58%.The area of the filter is 34.9 x 34.9 mm corresponding to a size reduction of 25.75% of its original size and upper stopband of 2.4 GHz. It is found that the response of the filter is the same for circles and squares under the condition that we keep the same etched area [28].

(a) (b)

Fig. 5.23. Photograph of the BPF with DGSs (a) Top view, (b) bottom view.

Now, the two approaches described in Section 5.2.3 and Section 5.2.4. are combined together to yield an optimized filter design endowed with maximum size reduction, by using internal folded stubs and DGSs, and enhanced selectivity by suppressing higher order harmonics. A photograph of the fabricated filter is shown in Fig. 5.23, while the simulated and measured responses are shown in Fig. 5.24.

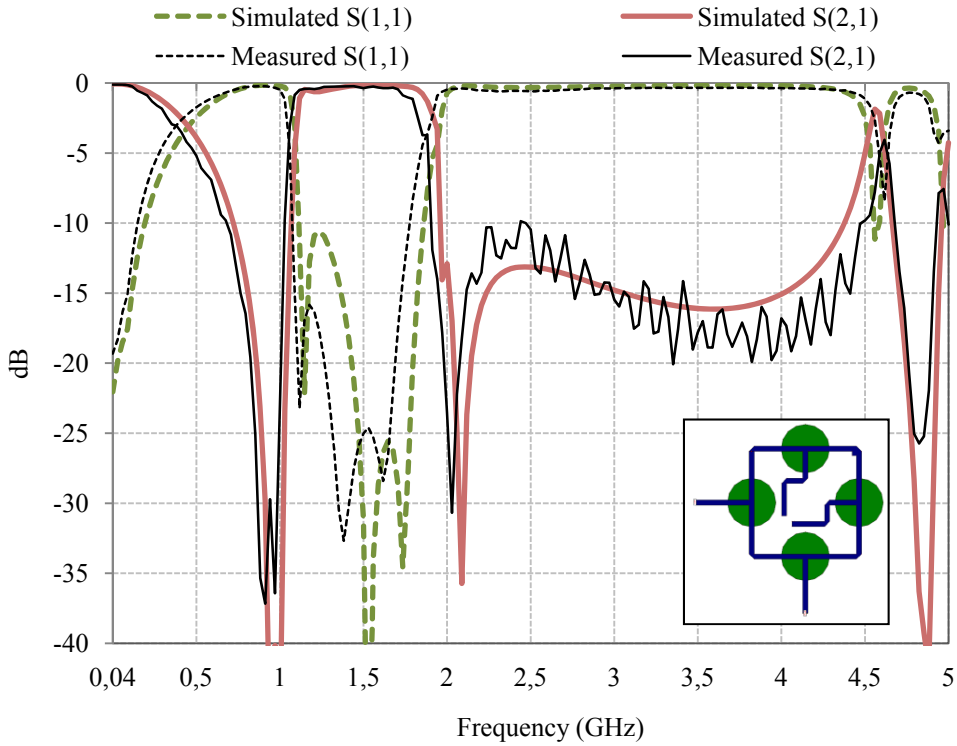

Fig. 5.24. Simulated and measured responses of the filter with internal folded stubs and DGSs. The inset shows the layout of the filter.

The filter center frequency is at 1.49 GHz with a return loss -16 dB and an insertion loss of -0.28 dB. The filter has a 3-dB fractional bandwidth of 56.1%.The area of the filter is 20.9 x 20.9 mm corresponding to a size reduction of 73.4% of its original size and upper stopband of 2.4 GHz. In addition, the filter performances have been further enhanced in terms of insertion and return loss values while keeping the wide bandwidth of the original filter design. The properties of all demonstrated filters are summarized in Table 5.2.

Table 5.2

Characteristics of the Filters Presented in Section 5.3.4

Filter	Insertion Loss (dB)	Return Loss (dB)	Fractional Bandwidth	Upper Stopband (GHz)	Size (mm)	Size Reduction
Conventional Ring Resonator Filter	-1.2	-8	60.6 %	0.46	40.5 x 40.5	----------
Ring Filter with Straight Stubs and Circle DGSs	-0.24	-18	57 %	2.44	34.9 x 34.9	25.75 %
Ring Filter with Straight Stubs and Square DGSs	-0.23	-19	54.58 %	2.24	34.9 x 34.9	25.75 %
Ring Filter with Internal Folded Stubs and Circle DGSs	-0.28	-16	56.1 %	2.4	20.9 x 20.9	73.4 %

5.3.5. Microstrip Ring Resonator Bandpass Filter with Uniplanar Compact-Photonic Bandgap (UC-PBG) Structures

The uniplanar compact-photonic band gap (UC-PBG) structure consists of a uniformly distributed periodic metallic pattern on one side of a dielectric slab. It exhibits some interesting features such as distinctive passband and stopband, slow-wave effects, low attenuation in the passband, and suppression of surface waves when serving as the ground plane of planar microstrip circuits. Moreover, the UC-PBG structure can also be used to realize a perfectly magnetic conducting (PMC) surface, which finds applications in designing a TEM waveguide and a low profile cavity backed slot antenna [20].

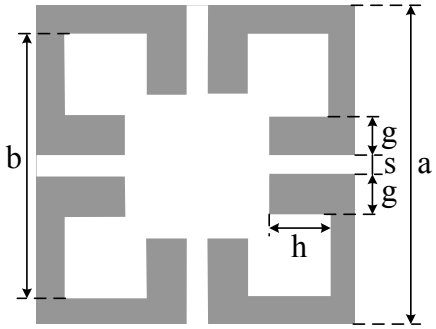

Fig. 5.25. One cell of the UC-PBG lattice.

The use of UC-PBG structures is hereby exploited to improve the harmonic rejection of the filter. The layout of the UC-PBG structure cell is shown in Fig. 5.25. The dimensions used for the UC-PBG structures are a=12 mm, b=10.968 mm, g=1.4 mm, s=1.032 mm and h=2.926 mm. The circumference of the ring resonator ℓ_r= 60 mm, the length of each tuning stub is 13 mm and the width of the line is 0.94 mm corresponding to a 50Ω line.

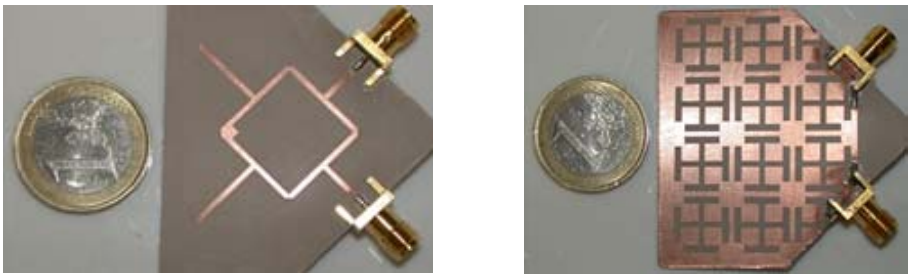

(a) (b)

Fig. 5.26. Photograph of the fabricated ring resonator BPF with UC-PBG structures in the ground plane (a) Top view, (b) bottom view.

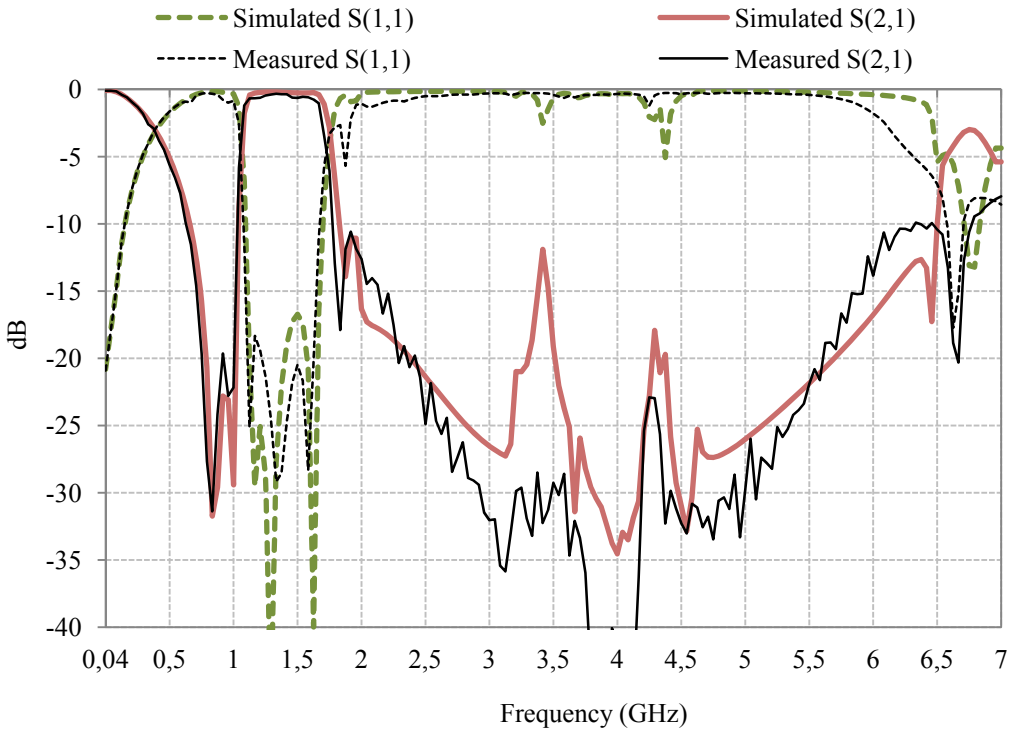

Fig. 5.27. Simulated and measured responses of the ring resonator filter with UC-PBG structures.

Fig. 5.26 shows a photograph of the fabricated ring resonator filter with UC-PBG structures etched in the ground plane and Fig. 5.27 shows the simulated and measured responses of the ring resonator filter with PBG structures. All filter specifications are found in Table 5.3.

The etching of UC-PBG structures in the ground plane also solves the two problems of the original filter simultaneously. Referring to the filter dimensions given in Table 5.3, the size of the filter is reduced by 45.52% and the stopband of the filter has increased from 0.46 GHz to 4.7 GHz suppressing the second, third and fourth harmonics introduced by the original filter design. Also, the insertion and return loss values of the filter are enhanced due to the suppression of surface waves provided by the UC-PBG structures. Compared to the results obtained by using defected ground structures presented previously on the same ring resonator filter, the DGSs introduces a size reduction of only 25.75 % and a narrower stopband of 2.44 GHz, which means that the UC-PBG structures are more efficient but suffer from the difficulty of their design and fabrication.

In this section we are going to study the ability of using both advantages of bent stubs and UC-PBG structures. As mentioned before, in bending the stubs, the coupling between the stubs and the ring resonator is one of the most effective parameters in the design. In our case, the quasi-TEM mode properties of the coupled microstrip lines provided by [24] are used. But for the case of UC-PBG structures etched in the ground plane, the amount of error provided by these equations increases, which makes the design more difficult, even though they still provide a reasonable initial guess. For further improvement in the design, a full electromagnetic wave simulator should be used.

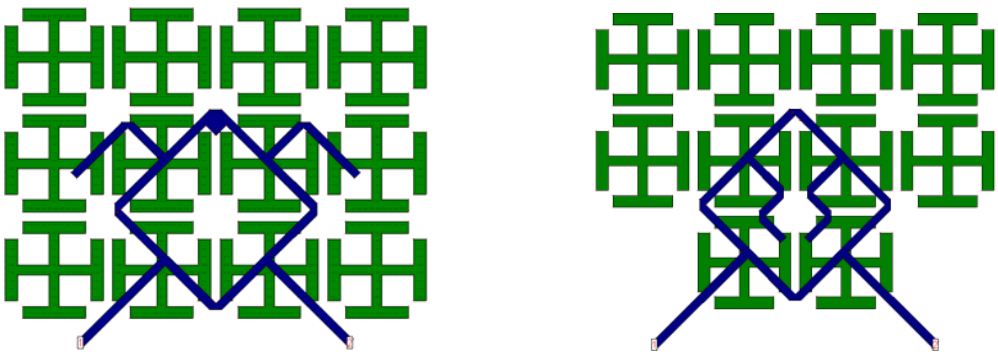

(a) (b)

Fig. 5.28. Layout of the ring resonator BPF with UC-PBG structures in the ground plane with (a) external bent stubs, (b) internal folded stubs.

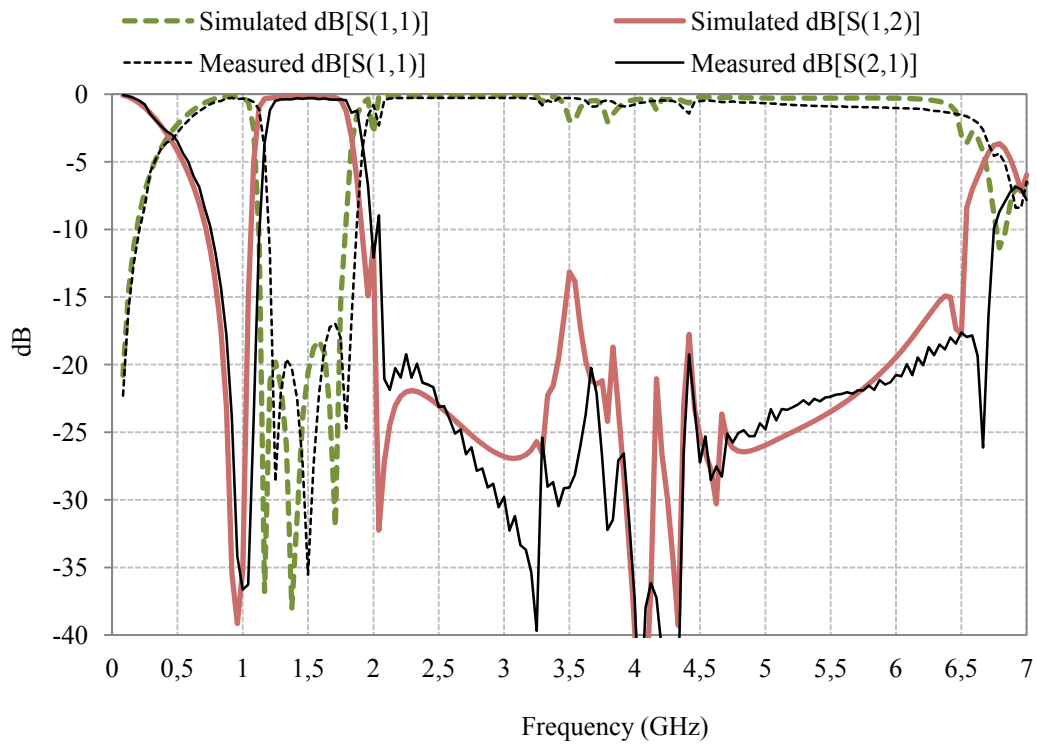

(a)

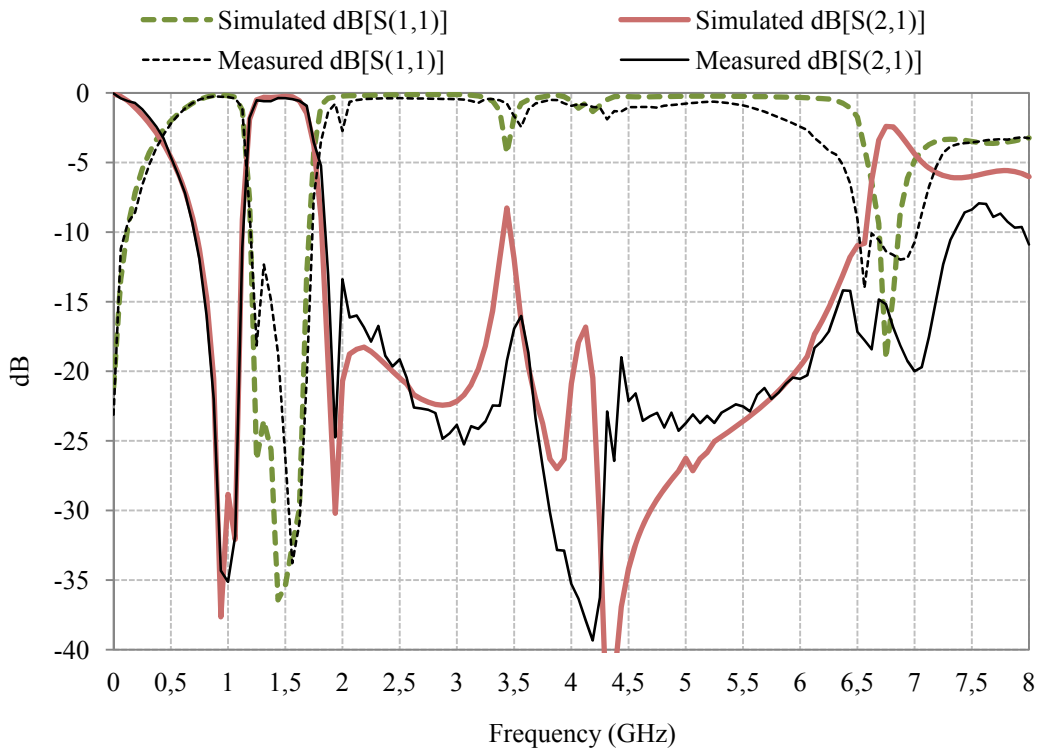

(b)

Fig. 5.29. Simulated and measured responses of the ring resonator filter with UC-PBG structures and (a) external bent stubs, (b) internal folded stubs.

The two solutions of Fig. 5.15 with external bent stubs and internal folded stubs with UC-PBG structures are designed on the same material mentioned above. The layouts of the structures are shown in Fig. 5.28 (a) and (b). The simulated and measured responses are presented in Fig. 5.29 (a) and (b). All filters specifications are shown in Table 5.3. We can see a great reduction in the size of the filter reaching up to 84.49 % for internal folded stubs (while 68.24% is attained for the external bent stubs), accompanied by very good overall filter performance. This means that bending the stubs has affected neither the good passband characteristics provided by the ring resonator filter, nor the wide stopband provided by the UC-PBG structures.

Table 5.3

Characteristics of the Filters Presented in Sections 5.3.5.

Filter	Insertion Loss (dB)	Return Loss (dB)	Fractional Bandwidth	Upper Stopband (GHz)	Size (mm)	Size Reduction
Conventional Ring Resonator Filter	-1.2	-8	60.6 %	0.46	40.5 x 40.5	----------
Ring Filter with Straight Stubs and UC-PBG	-0.21	-20	46.5 %	4.7	29.9 x 29.9	45.52 %
Ring Filter with External Bent Stubs and UC-PBG	-0.34	-17	50.73 %	4.66	22.9 x 22.9	68.24 %
Ring Filter with Internal Folded Stubs and UC-PBG	-0.59	-12.81	40.8 %	5.25	15.9 x 15.9	84.49 %

5.3.6. Conclusion

This section provided a general enhancement technique for ring resonator filters. The modifications presented here target two basic disadvantages in the ring resonator filters. The first is the large occupation area of the filter while the second is the narrow upper stopband due to its higher order passbands.

In order to reduce the area occupied by the filter, the first approach was to bend the tuning stubs of the filter along the ring resonator, and in a second design iteration, we tried the exploitation of the inner ring area using internal folded stubs. The advantage of this technique is that the area of the filter was reduced by a factor of 72% without affecting the good characteristics of the ring resonator filters.

To suppress the high order passbands of the filter, we investigated the use of both DGSs and UC-PBG structures. DGSs are easier in their design procedures than UC-PBG structures, but on the other hand UC-PBG structures provide a larger upper stopband. Both structures give additional advantage with respect to size.

References of Chapter Five

[1] K. M. Shum, T. T. Mo, Q. Xue, and C. H. Chan, "A compact bandpass filter with two tuning transmission zeros using a CMRC resonator," *IEEE Trans. Microw. Theory Tech*., Vol. 53, No. 12, pp. 895-900, Mar. 2005.

[2] A. Rahman, A. K. Verma, A. Boutejdar, and A. S. Omar, "Compact stub type microstrip bandpass filter using defected ground plane," *IEEE Microw. Wireless Comp. Lett.*, Vol. 14, No. 4, pp. 136-138, Apr. 2004.

[3] F. martin, J. Bonache, I. Gil, F. Falcone, T. Lopetegi, M. A. G. Laso, and M. Sorolla, "Compact spurious free CPW bandpass filter based on electromagnetic bandpass structures," *Microw. Opt. Technol. Lett.*, Vol. 40, No. 2, pp.146-148, Jan. 2004.

[4] F. Aryanfar and K. Sarabandi, "Compact millimeter-wave filter using distributed capacitively loaded CPW resonators," *IEEE Trans. Microw. Theory Tech*., Vol. 54, No. 3, pp. 1161-1165, Mar. 2006.

[5] J. Lim, C. Kim, D. Ahn, Y. Jeong, and S. Nam, "Design of low-pass filters using defected ground structure," *IEEE Trans. Microw. Theory Tech.,* Vol.53, No.8, pp. 2539–2545, Jan. 2005.

[6] H. B. El-Shaarawy, F. Coccetti, R. Plana, M. El-Said and E. A. Hashish, "Compact bandpass ring resonator filter with enhanced wide-band rejection characteristics using defected ground structures," *IEEE Microw. Wireless Comp. Lett.,* Vol. 18, No. 8, pp. 500-503, Aug. 2008.

[7] M. Abdelaziz, Amr M. E. Safwat, Florence Podevin, Anne Vilcot, "Narrow bandpass filter based on the modified DGS," proceedings of *Europ. Microw. Conf. (EuMC),* pp. 75 – 78, Oct. 2007.

[8] E. K. I. Hamad, A. M. E. Safwat, A. S. Omar, "A MEMS reconfigurable DGS resonator for K-band applications," *IEEE Journal of Microelectromechanical Systems,* Vol. 15, No. 4, pp. 756 – 762, Aug. 2006.

[9] J. K. A. Everard and K. K. M. Cheng, "High performance direct coupled bandpass filters on coplanar waveguide," *IEEE Trans. Microw. Theory Tech.*, Vol. 41, No. 9, pp.1568-1573, Sep. 1993.

[10] D. F. Williams and S. E. Schwarz, "Design and performance of coplanar waveguide bandpass filters," *IEEE Trans. Microw. Theory Tech*., Vol. 31, No. 7, pp. 558-566, July. 1983.

[11] F. Arndt , J. Bornemann, D. Grauerholz, and R. Vahldieck, "Theory and design of low-insertion loss fin-line filters," *IEEE Trans. Microw. Theory Techn.*, Vol. 30, No. 9, pp.155-163, Feb. 1982.

[12] J. K. A. Everard, K. K. M. Cheng and P. A. Dallas, "A high Q helical resonator for oscillators and filters in mobile communications systems," *Electron. Lett.*, Vol. 25, No. 24, pp.1648-1650, Nov. 1989.

[13] G. L. Matthaei, L. Young, and E. M. T. Jones, *Microwave Filters, Impedance Matching Networks, and Coupling Structures*. New York: McGraw-Hill, 1964.

[14] L. H. Hsieh, and K. Chang, "Compact, low-insertion loss, sharp-rejection and wide-band microstrip bandpass filter", *IEEE Trans. Microw. Theory Tech.*, Vol. 51, No. 4, pp.1241-1246, April 2003.

[15] S. Sun and L. Zhu, "Wideband microstrip ring resonator bandpass filters under multiple resonators", *IEEE Trans. Microw. Theory Tech*., Vol. 55, No. 10, pp. 1938-1948, Oct. 2007.

[16] A. Groil, D. Mira, A. Martinez, J. Marti and J. L. Corral, "Microstrip multistage coupled ring bandpass filters using photonic bandgap structures for harmonic suppression", *Electron. Lett.,* Vol. 39, No. 1, pp. 68-70, Jan. 2003.

[17] J. S. Park, D. Ahn, C. S. Kim, J. Kim, Y. Qian, and T. Itoh, "A design of the low-pass filter using the novel microstrip defected ground structure", *IEEE Trans. Microw. Theory Tech.*, Vol. 49, No. 1, pp. 86–93, Jan. 2001.

[18] J. Park, K. Park, S. Chang, D. Ahn, "A new equivalent transmission line modeling of dumbbell type defected ground structure", *WSEAS Trans. Communications*, Vol. 4, No. 2, pp.40-44, Feb. 2005.

[19] G. Lojewski, N. Militaru, M. G. Banciu, "Planar microwave bandpass filters with two and three-layer defected ground structures", *WSEAS Trans. Communications*, Vol. 5, No. 12, pp. 2129-2136, Dec. 2006.

[20] F. Yang, K. Ma, Y. Qian and T. Itoh, "A uniplanar compact photonic bandgap (UC-PBG) structure and its applications for microwave circuits", *IEEE Trans. Microwave Theory Tech.*, Vol. 47, No. 8, pp. 1509-1514, Aug. 1999.

[21] M. E. Mostafa and H. B. El-Shaarawy, "The use of vias for reducing the size and enhancing the response of microstrip filters", *WSEAS Trans. Circuits Syst*., Vol. 5, No. 9, pp.1424-1430, Sep. 2006.

[22] A. Görür, "Description of coupling between degenerate modes of a dual-mode microstrip loop resonator using a novel perturbation arrangement and its dual-mode bandpass filter application", *IEEE Trans. Microw. Theory Tech*., Vol. 52, No. 2, pp. 671-677, Feb. 2004.

[23] N. Feix, M. Lalande, and B. Jecko; "Harmonical characterization of a microstrip bend via the finite difference time domain method", *IEEE Trans. Microw. Theory Tech.,* Vol. 40, No. 5, pp. 955 – 961, May 1992.

[24] I. Bahl, and P. Bhartia, *Microwave Solid State Circuit Design*, New York: J. Wiley & Sons, 1988.

[25] R. Collin, *Foundation of Microwave Engineering*, McGraw Hill, 1992.

[26] E. Yablonovitch, "Inhibited spontaneous emission in solid state physics and electronics", *Phys. Rev. Lett*., Vol. 58, pp. 2059-2062, May 1987.

[27] V. Radisic et al., "Novel 2-D photonic bandgap structures for microstrip lines", *IEEE Microw. Guided Wave Lett.,* Vol. 8, No. 2, pp.69-71, Feb. 1998.

[28] A. B. Abdel-Rahman, A. K. Verma, A. Boutejdar, and A. S. Omar, "Control of bandstop response of hi-lo microstrip low-pass filter using slot in ground plane", *IEEE Trans. Microw. Theory Tech*., Vol. 52, No. 3, pp. 1008–1013, Mar. 2004.

CHAPTER SIX

CONCLUSION AND FUTURE WORK

6.1. Conclusion

The aim of this chapter is to sum up all the presented work in this thesis, and then obtain a constructive conclusion that would help in the development of this work and finally present the perspectives and future work.

The motivation of this thesis is to implement miniaturized filters with reconfigurable attributes to help in the miniaturization of nowadays rapidly developing transceiver architectures. To achieve this goal, first we had to choose the most suitable technique to provide structure miniaturization.

Studying electromagnetic bandgap (EBG) structures reveals that they have many interesting features that made them a good candidate for the implementation of miniaturized structures. The most important of these features is their "bandgap" property, where EM waves are not allowed to pass, while the second is the slow-wave effect that it introduced in the passband which helps in the miniaturization of the structure without added losses. These two features are the key points which we tried to investigate in the work presented here.

The following step of our research is to study the previous work that was presented in the same domain and how the EBG structures developed throughout the past years. In this state of the art, we covered both the main historical development of the EBG structures and recent achievements in the domain. From our readings, it is clear that EBG structures provided good results in the miniaturization of microwave devices, in addition to the enhancement of their performances, but they suffered one main disadvantage which is the difficulty of their modeling. From this point, like most of the other researchers, we turned our eyes towards defected ground structures (DGS) , as they have the same advantages in addition to the simple modeling, which enabled the development of more complex structures and applications.

From this point, we started to survey the different analysis and modeling techniques for both EBG and DGS. We first studied one dimensional periodic structure using the Coupled-Wave Theory and the Bloch-Wave Formalism. Both techniques proved that such periodic structures supported the "bandgap" phenomenon. On the other hand, both techniques showed the difficulty of the calculation process and the complexity of the analysis mechanism, in spite of the simplicity of the structure. Turning to DGSs, we presented the different equivalent circuits used to represent the dumbbell DGS. It was clear that the modeling of these DGSs is easier and more practical in the implementation of the reconfigurable structure.

Then, a novel reconfigurable multi-stopband DGS resonator was presented. The structure was first studied using the open and short circuit bridges. Fabrication and simulation results were in good agreement. We analyzed the structure after that using the slotline closed form expressions of Janaswamy and Schaubert for low ε_r substrates obtained by curve-fitting the numerical results of Galerkin's method in the Fourier transform domain. Using these expressions, design rules were obtained to produce the transmission zero in the required location. The structure was also modeled using the parallel *RLC* equivalent circuit, which was in good agreement with the EM simulation results.

After using the short bridges, and proving our theory, they were replaced with PIN diodes. First, the biasing mechanism was explained, and then, the measurement setup of the structures and the measurement results were presented and finally a discussion for the results was obtained.

Finally, the last step to reach our goal was to use the DGS in the implementation of the bandpass filters. Two applications of the DGSs were presented. First, a compact inductively coupled BPF using the DGS unit cell was implemented. Then to validate our theory, a second order filter of the same type was designed, and then, a reconfigurable bandpass filter using this structure was implemented. Using a MEMS switch, the structure would convert from a single resonance structure at 5 GHz to a multi resonance structure at 2.8 and 8 GHz.

The second application was the enhancement of the ring resonator filter with respect to size miniaturization and higher order harmonics suppression. First the structure was enhanced on the layout level by reconstructing the tuning stubs

achieving 72% size miniaturization, then on the propagation level by using different types of bandgap structures reaching 85% size miniaturization.

The conclusion of this study is that EBG structures and DGS still have a lot to offer and will still see a lot of development in the next decade. These structures provide both arbitrary stopbands and slow-wave effect that are the most important features cherished by any electromagnetic designer.

The final step in this work is to mention and explain the future work that we intend to develop as an enhancement of the work presented so far, making use of the study and understanding that we have developed through the work in the thesis.

6.2. Future Work

The future work, that is intended to be done, with respect to the presented defected ground structures consists of two aspects; first we intend to implement the novel DGS and bandpass filters at higher frequencies on silicon substrates using MEMS switches to produce better performance and integration capability with RF integrated circuits. Second, it is intended to design and fabricate tunable DGSs on barium strontium titanate (BST) which is a ferroelectric material still under investigation but showing promising results.

6.2.1. Fabrication on Silicon Substrates

In Chapters Four and Five, two novel structures were presented. In Chapter Four, we introduced the novel reconfigurable DGS resonator for multi-stopband filters. The structures were first implemented using open and short bridges instead of the reconfigurability element to illustrate our theory, then, PIN diodes were used for the implementation of the reconfigurable scheme. From the measurement results using the PIN diodes, it was clear that PIN diodes suffer two basic disadvantages. The first is the shift in the resonant frequency due to the internal diode capacitance and inductance. Moreover, this shift of frequency is not constant over the operating band of frequency of the PIN diode, which makes it difficult to estimate and prevent this shift in the resonant frequencies. Second, the losses produced by the PIN diode which causes a dramatic effect of the narrow fractional bandwidth, in other words, the quality factor of the resonator.

All these draw backs of PIN diodes push us towards the fabrication of the structures on silicon substrate using MEMS switches which provide lower internal resistances and produce less shift in the resonant frequencies.

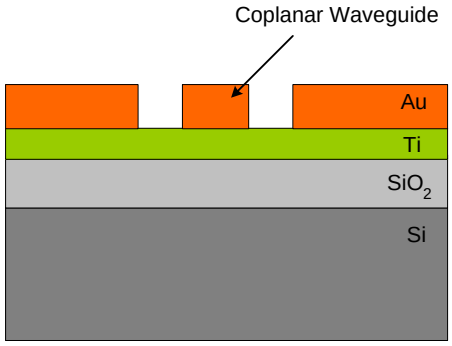

Fig. 6.1. The multi-layer structure of the fabrication process.

Following the same steps of our design process, we will first design the DGS using open and short bridges in place of the MEMS switches. The structures will be fabricated on high resistivity silicon of thickness 400µm, and dielectric constant ε_r= 11.9 and loss tangent 0.018. Over the HR silicon, there exists SiO_2 isolation layer of 200 nm thickness and dielectric constant ε_r=4 and loss tangent 0.001. To enhance the adhesion of gold on the SiO_2, a 50 nm layer of Titanium is added over the SiO_2. Finally gold is added as the conducting metal of thickness 2.5 µm and conductivity $4.1x10^7$ S/m. The layer structure is shown in Fig. 6.1 (a), while the complete fabrication process is described in (Appendix B).

6.2.2. Process Based on Ferroelectric (BST) Material

Another aspect that we intend to work on is the implementation of reconfigurable defected ground structure based on ferroelectric materials such as BST. Nowadays, a number of researchers are interested in the implementation of tunable microwave components using ferroelectric materials including filters, phase shifters and tunable resonators due to their properties of tunability and compatibility with RFIC process [1]-[3].

In the implementation of these devices, a thin layer of ferroelectric material is deposited over the substrate. The advantage of this layer is that it produces internal electric polarization that changes with an externally applied electric field. In other

words we may say that by changing the applied voltage across this layer, its effective dielectric constant changes, consequently producing a tunable behavior.

However, it should be noted that so far components implemented using this technique suffer from low-voltage tunability and also from the high transmission loss they exhibit with respect to conventional microwave components. These problems drove a lot of research towards the implementation of better ferroelectric materials by means of a more reliable and reproducible way.

The ferroelectric material that is used in our study is the $Ba_{0.6}Sr_{0.4}TiO_3$ over SiO_2, and then both layers are placed over high resistivity silicon wafer. The first step in this study is to identify the material characteristics of our material. To do this step, a TRL method based on two coplanar waveguides is chosen to identify the material dielectric constant and loss tangent [4], and an interdigital capacitor to determine the material performance in terms of tunability. Once the material characteristics are identified, the next step is to implement tunable DGSs.

References of Chapter Six

[1] G. Subruamanyam, F. V. Keuls, and F. A. Miranda, "A K-band tunable microstrip bandpass filter using a thin film conductor/ferroelectric/dielectric multilayer configurations," IEEE Microw. Guided Wave Lett., Vol. 8, No. 2, pp. 78–80, Feb. 1998.

[2] B. Acikel, T. R. Taylor, P. J. Hansen, J. S. Speck, and R. A. York, "A new high performance phase shifter using $BaSrTiO_3$ thin films," IEEE Microw. Wireless Compon. Lett., Vol. 12, No. 7, pp. 237–239, Jul. 2002.

[3] S. S. Gevorgian, E. F. Carlsson, S. Rudner, U. Helmersson, E. L. Kollberg, E. Wikborg, and O. G. Vendik, "HTS/ferroelectric devices for microwave applications," IEEE Trans. Appl. Supercond., Vol. 7, No. 2, pp. 2458–2461, Jun. 1997.

[4] M. Ouaddari, S. Delprat, F. Vidal, M. Chaker, and K. Wu, "Microwave Characterization of ferroelectric thin-film materials," IEEE Trans. Microw. Theory Tech., Vol. 53, No. 4, pp. 1390–1397, Apr. 2005.

APPENDIX ONE

WAVELENGTH AND CHARACTERISTIC IMPEDANCE OF SLOTLINE

Effective dielectric constant and impedance properties of a slotline have been thoroughly treated in the literature by a number of authors. This appendix presents the closed form expressions of the slotline reported by Janaswamy and Schaubert for low ε_r substrates obtained by curve-fitting the numerical results of Galerkin's method in the Fourier transform domain.

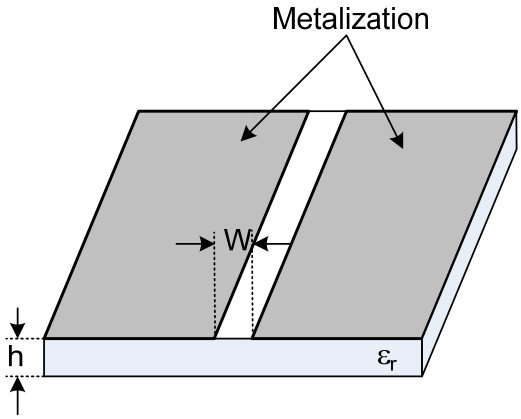

Fig. A2.1. Geometry of the slotline.

The geometry of the slotline is shown in Fig. A2.1 where ε_r is the substrate dielectric constant, h is the substrate thickness and W is the line width.

For $0.0015 \le W/\lambda_0 \le 0.075$ and $2.22 \le \varepsilon_r \le 3.8$:

$$\frac{\lambda_g}{\lambda_0} = 1.045 - 0.365\ln(\varepsilon_r) + 6.3\frac{W}{h}\left(\frac{\varepsilon_r^{\,0.945}}{238.64 + 100W/h}\right) - \left(0.148 - \frac{8.81(\varepsilon_r + 0.95)}{100\varepsilon_r}\right)\ln\left(\frac{h}{\lambda_0}\right) \tag{A1.1}$$

Maximum absolute error = 2.2 %.

$$Z_0 = 60 + 3.69\sin\left[\frac{(\varepsilon_r - 2.22)\pi}{2.36}\right] + 133.5\ln(10\varepsilon_r)\sqrt{W/\lambda_0}$$
$$+ 2.81[1 - 0.011\varepsilon_r(4.48 + \ln(\varepsilon_r))](W/h)\ln(100h/\lambda_0)$$
$$+ 131.1(1.028 - \ln(\varepsilon_r))\sqrt{h/\lambda_0} \qquad \text{(A1.2)}$$
$$+ 12.48(1 + 0.18\ln(\varepsilon_r))\frac{W/h}{\sqrt{\varepsilon_r - 2.06 + 0.85(W/h)^2}}$$

Maximum absolute error = 2.7 %.

For $0.075 \le W/\lambda_0 \le 1.0$ and $2.22 \le \varepsilon_r \le 3.8$ (the range where exists our design):

$$\frac{\lambda_g}{\lambda_0} = 1.194 - 0.24\ln(\varepsilon_r) - 0.621\left(\frac{W}{\lambda_0}\right)^{0.48}\left(\frac{\varepsilon_r^{\,0.835}}{1.344 + W/h}\right)$$
$$- 0.0617\left(1.91 - \frac{(\varepsilon_r + 2)}{\varepsilon_r}\right)\ln\left(\frac{h}{\lambda_0}\right) \qquad \text{(A1.3)}$$

Maximum absolute error = 2.6 %

$$Z_0 = 133 - 10.34(\varepsilon_r - 1.8)^2 + 2.87(2.96 + (\varepsilon_r - 1.582)^2)$$
$$\times\left[(W/h + 2.32\varepsilon_r - 0.56)(32.5 - 6.67\varepsilon_r)(100h/\lambda_0)^2 - 1\right]^{1/2} \qquad \text{(A1.4)}$$
$$- (\varepsilon_r + 1.35)^2(684.45h/\lambda_0) + 13.23[(\varepsilon_r - 1.722)W/\lambda_0]^2$$

Maximum absolute error = 5.4 %.

For $0.0015 \le W/\lambda_0 \le 0.075$ and $3.8 \le \varepsilon_r \le 9.8$ (the range where exists our design):

$$\frac{\lambda_g}{\lambda_0} = 0.9217 - 0.277\ln(\varepsilon_r) + 0.0322\frac{W}{h}\left(\frac{\varepsilon_r}{0.435 + W/h}\right)^{1/2}$$
$$- 0.01\left(4.6 - \frac{3.65}{\varepsilon_r^{\,2}(9.06 - 100W/\lambda_0)\sqrt{W/\lambda_0}}\right)\ln\left(\frac{h}{\lambda_0}\right) \qquad \text{(A1.5)}$$

Maximum absolute error = 3 %.

$$Z_0 = 73.6 - 2.15\varepsilon_r + (638.9 - 31.37\varepsilon_r)(W/\lambda_0)^{0.6}$$
$$+ \left(36.23\sqrt{\varepsilon_r^{\,2} + 41} - 225\right)\frac{W/h}{W/h + 0.879\varepsilon_r - 2} \qquad \text{(A1.6)}$$
$$+ 0.51(\varepsilon_r + 2.12)(W/h)\ln(100h/\lambda_0) - 0.753\varepsilon_r(h/\lambda_0)\sqrt{W/\lambda_0}$$

Maximum absolute error = 5.4 %.

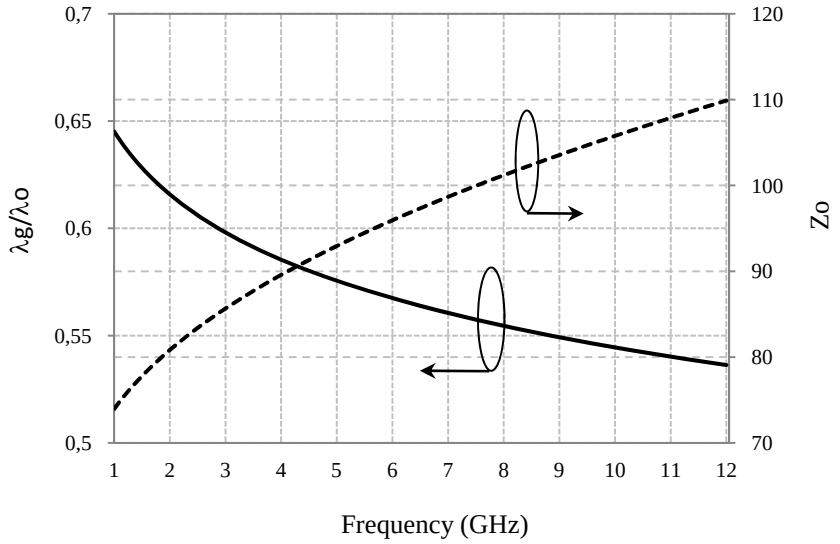

Fig. A1.2. Slotline waveguide wavelength and characteristic impedance for the substrate used versus frequency.

For $0.075 \le W/\lambda_0 \le 1.0$ and $3.8 \le \varepsilon_r \le 9.8$:

$$\frac{\lambda_g}{\lambda_0} = 1.05 - 0.04\varepsilon_r + 0.01411(\varepsilon_r - 1.421)\ln\left(\frac{W}{h} - 2.012(1 - 0.146\varepsilon_r)\right) + 0.111(1 - 0.366\varepsilon_r)\sqrt{W/\lambda_0} - 0.139(1 + 0.52\varepsilon_r \ln(14.7 - \varepsilon_r))\left(\frac{h}{\lambda_0}\right)\ln\left(\frac{h}{\lambda_0}\right) \quad \text{(A1.7)}$$

Maximum absolute error = 3.2 %.

$$Z_0 = 120.75 - 3.74\varepsilon_r + 50\left[\tan^{-1}(2\varepsilon_r) - 0.8\right](W/h)^{[1.11+(0.132(\varepsilon_r - 27.7)/(100h/\lambda_o + 5))]} \times \ln\left((100h/\lambda_0) + \sqrt{(100h/\lambda_0)^2 + 1}\right) + 14.21(1 - 0.458\varepsilon_r)(100h/\lambda_0 + 5.1\ln(\varepsilon_r) - 13.1) \times (W/\lambda_0 + 0.33)^2 \quad \text{(A1.8)}$$

Maximum absolute error = 5.8 %

APPENDIX TWO

LAAS RF MEMS PROCESS

As shown in Fig. A2.1, the LAAS process has the general features of a surface micromachining technology: (1) electroplated gold is used as the structure material and (2) photo resist is used as the sacrificial layer. The CPW lines are implemented using electroplated gold. Silicon dioxide is used for electrical isolation between the RF MEMS devices and the substrate while Silicon Nitride is used as a dielectric layer.

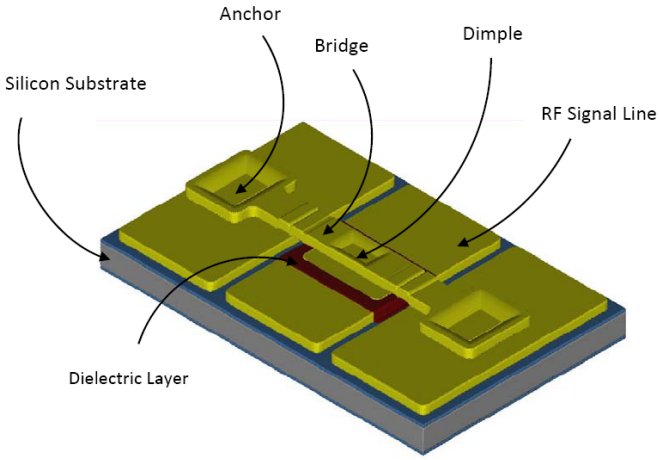

Fig. A2.1. 3D model of the RF MEMS switch built in MEMulatorTM using the LAAS process.

Step (1): Cleaning and Electrical Isolation

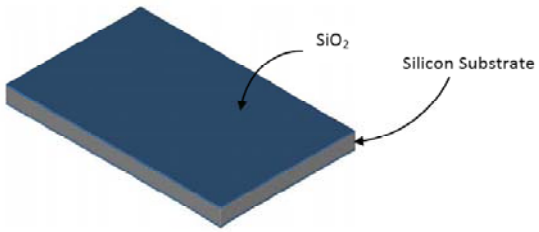

Fig. A2.2. The substrate after thermal oxidation.

The LAAS process begins with a 4 inch, (100) orientation, double side polished and high resistivity silicon wafers. First the wafers are cleaned using RCA cleaning method. Then, a 800 nm thermal silicon oxide is grown on the substrate as an electrical isolation, Fig. A2.2.

Step (2): Defining the CPW circuit

Electroplated gold is used to form the CPW lines. First, Ti/Au layers of 50nm/200nm are evaporated in order to be used as a seed layer for the gold electroplating. Then the wafers are coated with a Photo-resist layer of 10μm thickness. This is followed by using the first mask (**CPW**) in the process in order to build the mould for the gold electroplating.

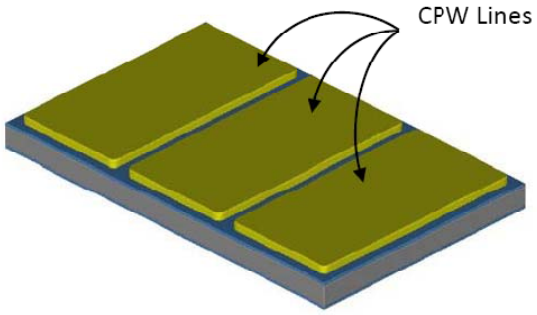

Fig. A2.3. The CPW lines after the metal etching of the seed layer.

The wafers are then electroplated with a 2.5 μm gold and the photo-resist mould is then removed using Acetone to obtain the CPW lines. This is followed by an evaporation of 50 nm of Ti in order to improve the adhesion between the electroplated gold layer and the dielectric layer which will be deposited later. Then, the second mask in the process (**SEEDETCH**) is applied and followed by wet metal etching in order to remove the seed layer and the previously evaporated Ti layer from the gaps between the CPW lines, Fig A2.3. It should be mentioned that the user should leave the **SEEDETCH** layer blank without any drawn objects. The **SEEDETCH** physical mask will be fabricated by inverting the **CPW** drawn mask during the masks fabrication process.

Step (3): Defining the Dielectric

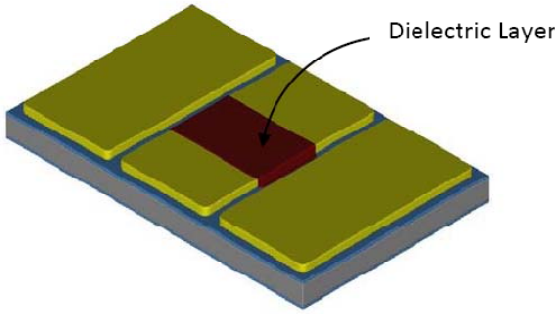

Fig A2.4. The switch with silicon nitride over the signal line

After the CPW circuit is patterned, a 400 nm silicon nitride is deposited using a low frequency PECVD process in order to be used as a dielectric layer. Silicon Nitride is then lithography patterned with the **(DIEL)** mask using RIE process, Fig A2.4. This is followed by wet etching of the Ti layer using the same mask in order to increase the adhesion between the CPW lines an the anchor areas.

Step (4): Defining the MIM capacitor (Floating Metal)

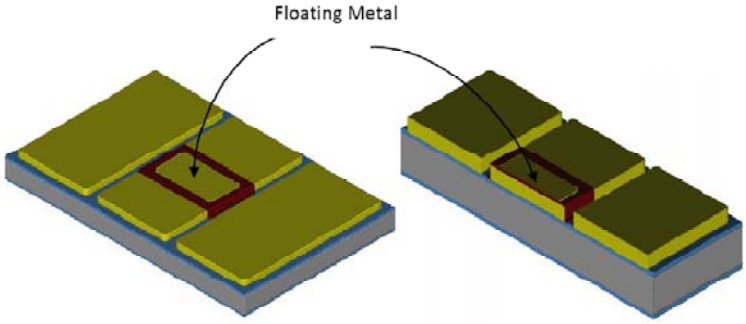

Fig A2.5. The MEMS switch with the floating metal layer.

In order to create the second plate for the MIM capacitor, a lift-off process is utilized. First, the wafers are coated with a Photo-resist layer and then lithography patterned with the **(MIM)** mask. This is followed by a metal evaporation step in order to obtain a Ti/Au layer of 20nm/200nm thickness. Finally, the PR is removed using acetone in order to obtain the

required metal plate, Fig A2.5. It should be also mentioned that, this floating metal layer is used in the capacitive MEMS switch in order to increase the On/Off capacitance ratio.

Step (5): Sacrificial layer patterning

The next step is to create the sacrificial layer which should be very planar in order not to deteriorate the switch performance That is why the sacrificial layer is created through two consecutive steps in order to obtain the optimum planarization.

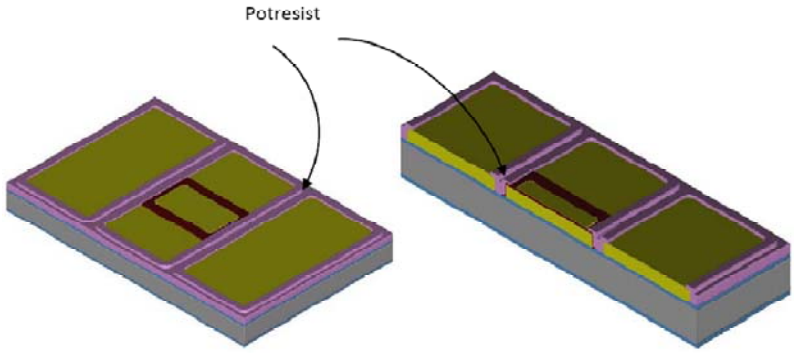

Fig. A2.6: The gaps between the CPW lines are filled with photo-resist for planarization purposes.

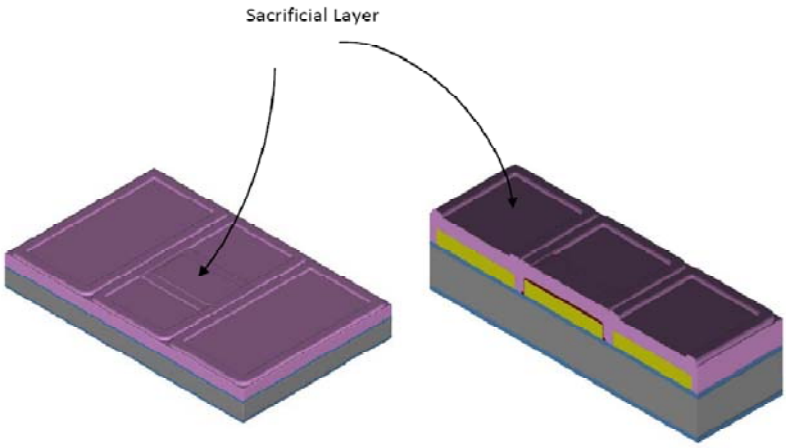

Fig. A2.7: The sacrificial layer after the second photo-resist coating.

First, the wafers are coated with a 2.5 μm photo-resist and the first mask (**CPW**) is used again in order to fill the gaps between the CPW lines with Photo-resist in order to have a flat surface, Fig. A2.6. The second step

is to coat the wafers again with another 2.5 μm layer of Photo-resist which represents the actual sacrificial layer, Fig. A2.7.

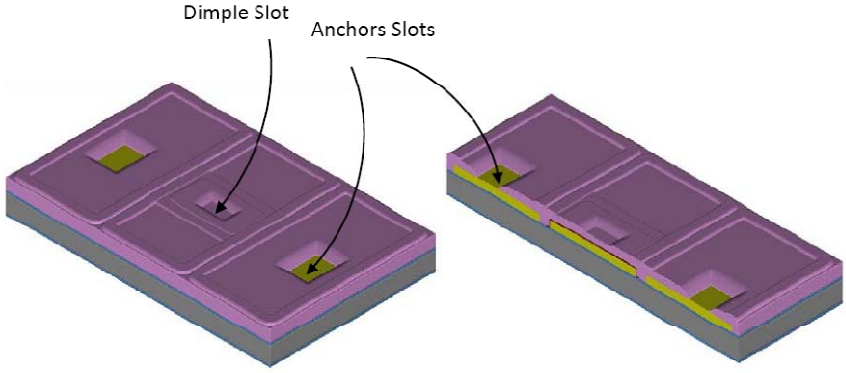

Fig A2.8. The sacrificial layer after patterning for the anchors and the dimples.

After the sacrificial layer is obtained, the anchors as well as the dimples will be patterned in this layer. First, the sacrificial layer is fully exposed, for 12 seconds, with the (**ANCHOR)** mask in order to completely remove the sacrificial layer from the anchor areas. Then, the sacrificial layer is partially exposed, for 5 seconds, with the (**DIMPLES)** mask in order to partially remove the photo-resist to define the dimples. Finally, the photo-resist is developed in order to obtain the anchors area with no photo-resist and the dimples points with small thickness of photo-resist, Fig. A2.8.

Step (6): Defining the bridge or the Cantilever

Following the sacrificial layer patterning, the bridge or the cantilever of the switch will be defined using electroplated gold. First, 100nm gold is evaporated on the sacrificial layer in order to be used as the seed layer for the gold electroplating. This is followed by the electroplating process in order to obtain a gold layer of 3 μm thickness. The last mask in the process (**BRIDGE**) is then used in order to define the bridge. Then, the electroplated gold layer is wet etched using KI+I2 bath and the photo resist layer is removed, Fig A2.9.

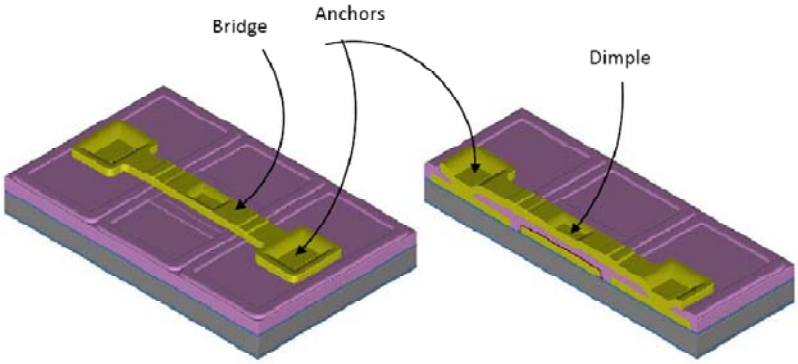

Fig A2.9. The switch after defining the bridge.

Step (7): Releasing the bridge

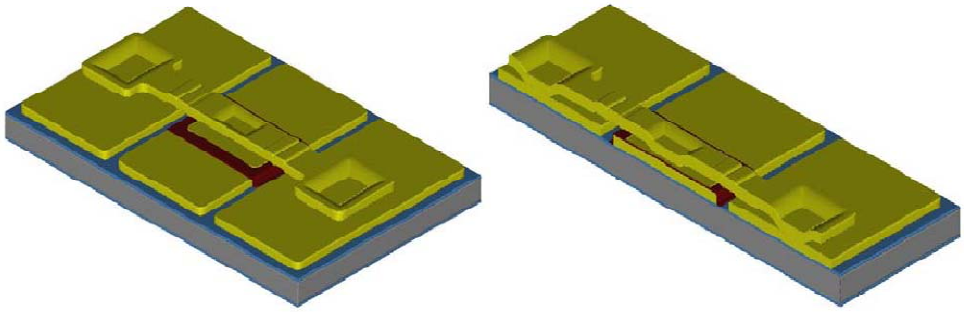

Fig A2.10: The switch after releasing the bridge

After defining the bridge, the wafers are diced and then the sacrificial layer is completely removed in order to release the movable structure, Fig A2.10. The releasing step is performed by immersing the chip in consecutive bathes of Acetone, AZ100 remover, DI water and Ethanol at room temperature. Finally, CO_2 critical point drying is utilized in order to overcome the stiction problem.

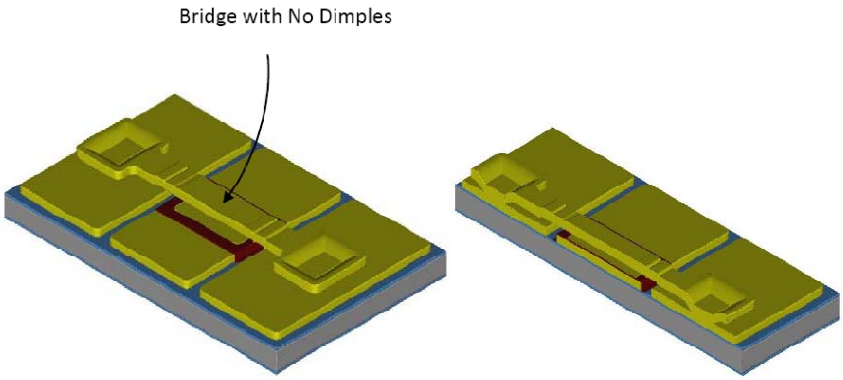

Fig. A2.11: RF MEMS switch with no dimples within the bridge (a) 3D model of the device (b) 3D Cross section.

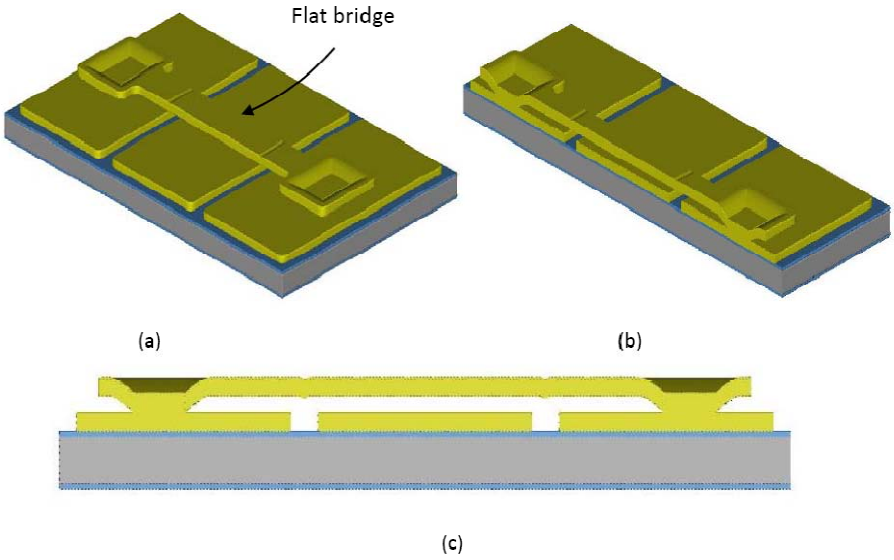

Fig. A2.12: RF MEMS switch without dielectric or floating metal layers (a) 3D model of the device (b) 3D Cross section (c) 2D Cross section.

Fig. A2.11 shows a 3D model of a capacitive MEMS switch with no dimples within the bridge. On the other side, Fig A2.12 introduces a 3D model of a switch with no dielectric and floating metal layers. It is clear from the figure that both of these layers affect the planarization of the bridge.

LIST OF PUBLICATIONS

Review Articles:

1. H. B. El-Shaarawy, F. Coccetti, R. Plana, Mostafa El-Said and Essam A. Hasish, "Novel reconfigurable defected ground structure resonator on coplanar waveguide," *IEEE Antenna and Propagation Transactions*, accepted for publication.

2. H. B. El-Shaarawy, F. Coccetti, R. Plana, Mostafa El-Said and Essam A. Hasish, "A novel reconfigurable DGS cell for multi-stopband filter on CPW technology," *Microwave Optical Technology Letters*, accepted for publication.

3. H. B. El-Shaarawy, F. Coccetti, R. Plana, Mostafa El-Said and Essam A. Hasish, "Compact bandpass ring resonator filter with enhanced wide-band rejection characteristics using defected ground structures," *IEEE Microwave and Wireless Components Letters.*, Vol.18, N°8, pp. 500-502, Aug. 2008.

4. H. B. El-Shaarawy, F. Coccetti, R. Plana, Mostafa El-Said and Essam A. Hasish, "Defected ground structures (DGS) and uniplanar compact-photonic band gap (UC-PBG) structures for reducing the size and enhancing the out-of-band rejection of microstrip bandpass ring resonator filters," *WSEAS Transactions on Communications*, Vol.11, No. 7, pp.1112-1121, Sep. 2008.

International Conferences:

5. H. B. El-Shaarawy, F. Coccetti, R. Plana, Mostafa El-Said and Essam A. Hasish, "Compact reconfigurable defected ground structure (DGS) based multi-band bandpass filters on coplanar waveguide technology," IEEE *Asia Pacific Microwave Conference (APMC 2009)*, Singapore, 7-10 Dec. 2009.

6. H. B. El-Shaarawy, F. Coccetti, R. Plana, Mostafa El-Said and Essam A. Hasish, "Novel compact defected ground structure based bandpass filters on coplanar waveguide," *Progress in Electromagnetic Research Symp. PIERS 2009*, Moscow, Russia, 18-22 August 2009.

7. H. B. El-Shaarawy, F. Coccetti, R. Plana, Mostafa El-Said and Essam A. Hasish, "Novel reconfigurable multi-band bandpass filter using defected ground structure on CPW technology," *IEEE International Symposium on Antenna and Propagation AP-S 2009*, Charleston, South Carolina, USA, 1-5 June 2009.

8. H. B. El-Shaarawy, F. Coccetti, R. Plana, Mostafa El-Said and Essam A. Hasish, "Analysis and design of a novel reconfigurable defected ground structure resonator on CPW technology," *Progress in Electromagnetic Research Symp. PIERS 2009*, Beijing, China, 23-27 March 2009.

9. H. B. El-Shaarawy, F. Coccetti, R. Plana, Mostafa El-Said and Essam A. Hasish, "A novel reconfigurable DGS cell for multi-stopband filter on CPW technology," *Asia Pacific Microwave Conference (APMC 2008)*, Hong Kong, Chine, 16-20 Dec. 2008.

10. H. B. El-Shaarawy, F. Coccetti, R. Plana, Mostafa El-Said and Essam A. Hasish, "Miniaturized extended-stopband microstrip ring resonator bandpass filter using uniplanar compact photonic bandgap (UC-PBG) structures," *8th Internat. Conf. Applied Inform. Comm. (AIC'08)*, Rhodes, Greece, 20-22 Aug. 2008.

National Conferences:

11. H. B. El-Shaarawy, Badreddine Ouagague, F. Coccetti, R. Plana, Mostafa El-Said and Essam A. Hasish, "Miniaturisation d'un filtre à résonateur en anneau en utilisant des stubs repliés et des « DGS » circulaires, " *16èmes Journées Nationales Microondes (JNM 2009)*, Grenoble, France, 27-29 May 2009.

12. H. B. El-Shaarawy, Badreddine Ouagague, F. Coccetti, R. Plana, Mostafa El-Said and Essam A. Hasish, " Filtre multi coupe-bande reconfigurable utilisant un nouveau résonateur à base de structure à plan de masse usiné en technologie CPW" *16èmes Journées Nationales Microondes (JNM 2009)*, Grenoble, France, 27-29 May 2009.

Structures Électromagnétiques à Bandes Interdites Pour les Applications de Filtre

Le développement croissant des applications sans fil nécessite de nouvelles conditions pour les architectures d'émetteur récepteur qui doivent avoir d'excellentes performances micro-onde (linéarités, réjection, niveau de bruit et largeur de bande) et une capacité d'intégration augmentée réalisée grâce à la miniaturisation des modules, cela sans oublier l'introduction de multiples fonctionnalités standards. Toutes ces conditions traduisent le besoin des circuits de filtrage comme la miniaturisation, les hautes performances au niveau des pertes d'insertion et du rejet.

De nos jours, des systèmes mobiles, ou en d'autres termes, le téléphone mobile « moderne » est exigés pour offrir beaucoup d'applications annexes suivant différentes normes utilisant différentes technologies, à partir du MP3, du NFC (la communication champ près), de la TV mobile, GPS,... Chaque application a sa propre technologie, par exemple le NFC est réalisé par RFID (identification par radiofréquence), la localisation est réalisée par le GPS et ainsi de suite. Cela signifie que nous avons un spectre de fréquence serré pour opérer commençant à 800 MHz pour le GSM en basse fréquence jusqu'à 6 GHz pour l'IEE802.11a pour le Wi-Fi.

Basé sur les applications nécessaires dans le téléphone mobile, on peut récapituler les conditions requises pour avoir ces applications comme suit:

- Le mobile devrait fonctionner dans un grand choix de fréquences à partir de 0.8 à 6 GHz; il devrait donc permettre l'opération multi-bande.
- Le téléphone mobile devrait permettre des multistandards (par exemple, Bluetooth + GSM +Wi-Fi) avec différents débits (10k-2Gpbs).
- Interférence minimale (la sélectivité est obligatoire) car plus d'une application est présente le long de la même bande de fréquence.
- Adaptation facile à de nouvelles normes qui permet un temps court pour la mise en commercialisation.

- Plus de fonctionnalité/services, car ce n'est pas simplement un téléphone, mais un système multimédia (vidéo, appareil-photo, commerce électronique, cartes postales électroniques, parc d'attractions sans fil).
- Une plus grande autonomie et une consommation de puissance réduite par fonction.
- Petite taille, légère et compacte.
- Faible coût.

Pour que toutes ces applications aient leur place, l'architecture du mobile moderne se compose d'un grand nombre de dispositifs passifs et actifs avec environ 5~10% d'entre eux activés à la fois. En même temps ces composants occupent environ 80% de la carte électronique et 70% du coût. Afin de réaliser ainsi la réduction de la taille et du coût, ces filtres et amplificateurs supplémentaires devraient être miniaturisés ou enlevés. Pour réduire la taille et le coût des composants, la miniaturisation et la reconfigurabilité devraient être employées. L'architecture réduite reconfigurable du mobile impose l'implémention des filtres passe-bande reconfigurable miniaturisés le long de la bande de fréquence de 0.8 à 6 GHz. Le but de cette thèse est d'avoir les filtres réglables miniaturisés et reconfigurable au-dessus du spectre précédemment mentionné avec de bonnes caractéristiques.

Depuis la fin des années 1980, les structures électromagnétiques à bandes interdites (Electromagnetic Bandgap Structures-EBG) et les structures à défauts de plan de masse (Defected Ground Structures-DGS) ont attiré l'intérêt de beaucoup de chercheurs grâce à leurs propriétés intéressantes en termes de miniaturisation de taille, suppression des ondes de surfaces et bandes interdites arbitraires. Depuis lors, elles ont été employées dans beaucoup d'applications comme les filtres passe-bas, les filtres passe-bande, les antennes, les guides d'ondes et d'autres. Basé sur des dispositifs intéressants proposés par EBG et DGSs, le but principal de cette thèse est de réaliser des filtres reconfigurables miniaturisés qui peuvent servir dans les systèmes de communication sans fil.

Les structures électromagnétiques à bandes interdites (EBG) sont des structures périodiques qui ont au commencement évolué dans le domaine optique par le nom des structures à bandes interdites photoniques (PBG) vers la fin des années 80. Des

structures d'EBG peuvent être implémentées par différentes manières : par gravure de motifs dans le métal du plan de masse, ou de la ligne de signal ou en réalisant des trous périodiques dans le diélectrique.

Ces structures périodiques sont très intéressantes ce qui en fait des candidats très prometteurs à un certain nombre d'applications. Les structures d'EBG permettent la propagation des ondes électromagnétiques dans certaines bandes de fréquence et les interdisent dans d'autres bandes connues sous le nom de bandes interdites. Cette première propriété est employée dans beaucoup d'applications pour la suppression des harmoniques d'ordre supérieur et des bandes passantes indésirables. Le deuxième intérêt de ces structures est qu'ils augmentent l'inductance effective et la capacité de la ligne supportant l'effet de propagation en onde lente. En conséquence, tous les composants passifs et actifs qui sont mis en application utilisant EBG ont une taille miniaturisée comparée aux composants conventionnels. Beaucoup d'articles ont rapporté la réduction de plus de 40% de la taille.

D'autre part, contrairement à toutes les technologies d'onde lentes, les structures d'EBG n'ont pas l'inconvénient des pertes excessives dans les bandes passantes ; au contraire, de telles structures pourraient donner de meilleures valeurs de perte d'insertion et de réflexion dues à leur capacité de supprimer les ondes de surface. Les ondes de surface sont provoquées par les réflexions multiples des ondes électromagnétiques entre le plan de masse et l'interface air-diélectrique.

Elles sont la source de deux problèmes de base dans beaucoup de systèmes. Le premier problème est la fuite de l'énergie par les ondes de fuite et le rayonnement à l'extrémité. Le deuxième problème est le faux couplage entre les composants de circuit et les éléments d'antenne. Ces problèmes causent une réduction globale de l'efficacité du système, limitent la largeur de bande, et limitent la gamme de fréquence d'utilisation des systèmes microrubans.

En conclusion, nous pouvons récapituler les avantages des structures d'EBG dans sept points principaux :

1. Fabrication facile.
2. Faible coût.
3. Compatibilité avec des technologies de circuit standard.

4. Capacité de ces structures de présenter des bandes interdites.

5. Effet de l'onde lente qui est très important pour la réduction de la taille.

6. Faible atténuation dans la bande passante.

7. Suppression des ondes de surface.

Les structures à base d'EBG ont été exploitées par beaucoup de chercheurs dans des applications divers dont on peut citer des filtres, des antennes, des amplificateurs, des guides d'ondes,…etc. Cependant, elles souffrent d'un inconvénient majeur qui est la difficulté de leur modélisation ainsi que les temps de calculs prohibitifs sur les simulateurs électromagnétiques. La difficulté de modélisation est liée au grand nombre de paramètres de conceptions qui doivent être considérés tel la période, la forme, la taille et l'emplacement de la cellule. En effet, cet inconvénient a aidé à l'évolution des structures à défauts de plans de masse (DGS). Une cellule unitaire de DGS est constitué d'un défaut (gravure d'une certaine forme) dans la plan de masse d'une ligne de transmission physique, soit en microruban, guide d'one coplanaire ou n'importe quelle structure où un plan de masse de référence existe. De tels défauts offrent les mêmes avantages des structures EBG avec la différence que l'utilisation d'une ou deux cellules seulement au lieu des structures périodiques est suffisante pour assurer les mêmes performances. Cet avantage des DGS par rapport aux EBG les rend faciles à modeler et par conséquent plus adéquats à être intégrer dans des structures plus compliquées.

De nos jours, de nouveaux motifs EBG et DGS sont exploités en vue d'atteindre le maximum de miniaturisation avec le minimum de pertes. D'autre part, depuis les années 2004/2005, la tendance vers des EBG et DGS reconfigurables a commencé et démontrait des résultats prometteurs. Pour toutes ces raisons, nous avons choisi les EBG et DGS pour accomplir nos objectifs.

Depuis son invention en 1987 dans le domaine optique, le progrès des structures EBG n'a pas suivi un parcours de développement en série. Au contraire, il a suivi des améliorations en parallèle par l'innovation de différents structures et modèles. Chaque structure s'est avérée avoir certains avantages qui la rendent appropriée pour des applications spécifiques. L'état de l'art présenté dans ce manuscrit est divisé en deux parties. La première partie traite les avancements dans les structures EBG, alors que la

deuxième partie concerne les structures à défauts de plan de masse tout en présentant une vue d'ensemble qui souligne les structures les plus marquantes et leurs applications spécifiques.

L'étude de la propagation des ondes dans les structures périodiques a une longue histoire qui remonte au moins à l'article classique du seigneur Rayleigh sur l'influence des obstacles disposés dans un ordre rectangulaire sur les propriétés d'un milieu. Ce travail a été bientôt suivi par celui de Kasterin, qui a étudié la réflexion et la réfraction d'une onde acoustique à basse fréquence par une grille orthorhombique de sphères dures (un cristal acoustique). Plus tard, la propagation des ondes dans les structures périodiques était un sujet d'un livre par Brillouin et Parodi. Le phénomène des structures à bandes interdites (EBG) est apparu vers la fin des années 1960 dans le domaine optique. Les premiers à donner une explication de ce phénomène étaient Kogelnik et Schank dans leur explication des caractéristiques de dispersion des lasers de rétroaction distribuée (DFB). À ce moment-là, ils n'ont pas évalué le phénomène des bandes interdites produit par les variations périodiques de l'indice de réfraction, mais ils se sont seulement concentrés sur l'explication du phénomène. Ils ont montré que les variations périodiques de l'indice de réfraction d'une structure génèrent des ondes se propageant vers avant et vers l'arrière dont l'interaction est gouvernée par des équations d'ondes couplées. Par la solution de celles-ci, ils ont trouvé en étudiant la relation de dispersion qu'il y avait une certaine bande de fréquence pour laquelle il n'y avait pas de propagation d'onde mais seulement des ondes évanescentes.

Dans les années 1980, Yoblonovitch a annoncé que ce phénomène de bande interdite photonique (PBG), produit par la variation périodique de l'indice de réfraction de la structure, peut être très utile pour supprimer l'émission spontanée des photons à certaines bandes de fréquence.

Par les années 1990, l'idée des structures à bandes interdites a commencé à trouver son chemin dans le domaine des ondes millimétriques et micro-onde. Deux approches sont généralement utilisées pour étudier le problème de la propagation des ondes électromagnétiques dans les milieux périodiques. La première est la théorie des modes couplés et l'autre est le formalisme de l'onde de Block. Dans cette thèse, la propagation de l'onde électromagnétique dans une structure périodique, où l'indice de

réfraction change périodiquement dans une direction et reste constant dans les deux autres directions, a été discutée. Cette structure périodique a été analysée en utilisant les deux approches précédemment mentionnées. Les deux approches ont validé que les structures périodiques ont une certaine bande interdite où aucune propagation n'est permise en raison de sa constante de propagation complexe dans cette bande de fréquence. À partir de cette conclusion importante, beaucoup de chercheurs ont commencé à étudier la possibilité d'employer ce phénomène de bandgap en structures plus complexes afin de contrôler le diagramme de dispersion de la structure et le travailler au besoin.

Vu le grand nombre des paramètres de conception des structures à bandes interdites électromagnétiques et la difficulté de leur modélisation électromagnétique un grand nombre de chercheurs exploitent les structures à défauts de plan de masse (DGSs), où deux ou trois défauts peuvent être utilisés pour obtenir la bande interdite souhaitée. Dans cette thèse, les différents modèles pour la représentation des ces DGSs ainsi que la méthodes d'extractions correspondantes sont considérés, précisant les avantages et les inconvénients de chaque circuit équivalent. La cellule unitaire de défaut de plan de masse sous forme d'haltère a été considérée pour explorer les différents circuits équivalents et modèles de DGSs. Tout défaut gravé dans le plan de masse perturbe la distribution du courant sur ce dernier. Cette perturbation peut changer des caractéristiques d'une ligne de transmission, telles que la capacité et l'inductance de la ligne. Les défauts dans les plans de masse des structures DGSs sous forme de gravure de secteurs étroits et larges provoquent l'augmentation la capacité et l'inductance effectives d'une ligne de transmission, respectivement. Ainsi, un circuit équivalent type LC parallèles peut représenter n'importe quel circuit unitaire de DGS. Les effets des dimensions physiques des DGS proposées sur les paramètres de ces circuits équivalents sont démontrés.

Un autre circuit équivalent de la structure à défauts de plan de masse est le circuit RLC parallèles. Dans ce circuit équivalent, l'inductance et la capacité parallèles représentent l'augmentation de la capacité et de l'inductance effectives de la ligne et la présence du pôle d'atténuation, alors que la résistance parallèle

supplémentaire représente les pertes dues au rayonnement et les ondes de surface. Ce modèle donne de meilleurs résultats une fois comparé à ceux donnés par le simulateur électromagnétique.

Un circuit équivalent plus compliqué sous forme de π est présenté. Dans ce circuit, la capacité et la résistance parallèles sont utilisées pour représenter les champs de fuite relativement importants au niveau de la discontinuité sur la surface métallique du plan de masse. Puisque la capacité parallèle pourrait changer le niveau d'impédance caractéristique et la longueur électrique de la section d'unité de DGS, elle devrait faire partie du circuit électrique équivalent pour une modélisation plus précise. Afin de dériver les éléments de circuit équivalent, les paramètres S de la cellule unitaire du DGS sont calculés au niveau du plan de référence à partir des simulations électromagnétiques. Une fois que les paramètres S sont calculés, les paramètres du circuit équivalent proposé peuvent être déduits en employant la relation entre les paramètres S et la matrice de chaîne.

Bien que le circuit équivalent π soit le plus précis, comme il tient compte de tous les effets, le circuit RLC parallèles est assez précis pour être utilisé pour représenter la section de DGS et plus simple pour calculer. D'autre part, si les pertes ne doivent pas être considérées dans la conception, le circuit LC parallèle pourrait être employé vue sa simplicité d'autant plus qu'il renferme les données principales requises dans la conception, comme sera montré dans la section suivante.

Utilisant ce circuit équivalent, les procédures de conception pour l'implémentation de filtres passe-bas d'ordres supérieurs sont démontrées sur des lignes de transmission microrubans et des lignes coplanaires. Les filtres passe-bas utilisant des circuits DGS ont un certain nombre de caractéristiques attrayants, tel que :

1) Structure simple ;

2) Bande de réjection plus large avec plus de réjection comparée à celle des filtres passe-bas conventionnels ;

3) Faible pertes d'insertion ;

4) Des valeurs extrêmement petites d'élément pour l'implémentation des filtres passe-bas peuvent être réalisées.

Une grande tendance vers les structures DGS reconfigurables où l'endroit des zéros de transmission peut être contrôlé et accordé peut être ressentie par quelques publications récentes. Cependant, la production scientifique dans ce domaine reste encore assez limitée. En outre, la partie majeure du travail publié à ce jour-à notre connaissance-considérait les structures à l'aide du circuit équivalent RLC parallèles pour représenter les zéros de transmission dans la réponse, ne fournissant aucune interprétation de cette dernière du point de vue de la propagation de l'onde électromagnétique et par conséquent ne fournissant aucune règle de conception. D'autre part, d'autres travaux ont employé des méthodes compliquées comme le théorème de Floquet, la méthode de Linpar, ou les réseaux neuronaux. L'inconvénient de ces méthodes est leur complexité mathématique et par conséquent leurs limitations à fournir des règles de conception initiales.

Dans cette thèse, une structure originale d'un résonateur à défauts de plan de masse reconfigurable est présentée en technologie de lignes coplanaires. Le résonateur est doté d'une conception originale qui permet la génération de zéros de transmission multiples à des fréquences arbitraires. La structure est en effet basée sur la présence de motifs de fentes gravées dans le plan de masse latérale d'une ligne coplanaire présentant ainsi le double avantage de permettre une reconfigurabilité simple, à l'aide de composants montés (ou fabriqués) à la surface, tout en proposant une solution compacte en exploitant la partie transversale de la ligne coplanaire.

La cellule est constituée de quatre motifs à fentes de formes carrées imprimées dans le plan de masse d'une ligne coplanaire d'une manière

symétrique par rapport à l'axe de celle-ci. Les deux résonateurs carrés sont de dimensions différentes et portent trois paires de diodes permettant ainsi huit configurations différentes. Parmi celles-ci, quatre configurations correspondantes à quatre différents états de diode sont présentées. Le circuit équivalent pour chaque état est obtenu à partir de la méthode conventionnelle d'extraction de paramètre de circuit. En plus du circuit équivalent RLC parallèles, l'explication électromagnétique de la structure, en utilisant les expressions de Janaswamy et de Schaubert relatives aux caractéristiques des lignes à fentes, est présentée fournissant des règles de conception simples et efficaces. Ces règles ont été appliquées à la conception des structures centrées à différentes fréquences arbitraires et validées par la visualisation du champ H, à partir du simulateur Ansoft HFSS, ifs à fentes aux fréquences de zéros. A ce stade, la reconfigurabilité est prouvée, dans un premier temps, à l'aide de courts circuits montés dans des endroits spécifiques des motifs à fentes. Ces courts circuits sont ensuite remplacés par des diodes réelles (Philips silicon PIN diodes BAP 63-02) pour assurer la reconfigurabilité. Des résultats simulés et mesurés sont présentés dans chaque cas, où les effets de la capacité et de la résistance de la diode PIN ont été également étudiés.

Cette structure est conçue et fabriquée sur un substrat diélectrique de Teflon de permittivité relative ε_r=9.5, d'épaisseur h=0.635mm, et tan δ de 0.0035. Le choix des diodes PIN utilisées ici était basé sur leur basse capacité de diode ($C_d \approx$ 0.36 pf), leur basse résistance (2 $\Omega \approx r_d$), leur inductance série très faible ($L_s \approx$ 0.6 nH) ainsi que de leur petite taille (1.1mm x 0.7 mm) qui les rend compatibles avec notre conception.

Un décalage de fréquence est observé en comparant les résultats de mesures des circuits réalisés avec les diodes et ceux réalisés par les courts-circuits représentant l'état « on » de ces derniers, les allures restent cependant conformes les unes aux autres. Ceci peut être expliqué comme les défauts des diodes (C_d, r_d et L_s) n'ont pas été pris en compte dans la phase de conception initiale. La

capacité et l’inductance des diodes ont effectivement l’effet de décaler (baisser) les fréquences des zéros. Ce décalage n'est pas pareil pour toutes les fréquences de zéros comme chaque état chaque zéro correspond à un différent de certaine(s) diodes ce qui est lié aussi à l’emplacement de cette (ces) dernier(es) dans le circuit. D’autre part, le facteur de qualité des zéros de transmission a baissé à cause de la résistance de diode introduite. Tous ces facteurs peuvent être négligés dans une première itération de conception, puis après l’obtention de l'endroit des zéros de transmission utilisant la théorie présentée des lignes à fentes, l'effet de la diode peut être considéré pour obtenir un accordement final dans la structure.

Ce résonateur reconfigurable à partir de défauts du plan de masse est un bon candidat pour un certain nombre d'applications où la suppression de bandes de fréquences arbitraires et la reconfigurabilité sont exigées. Par exemple, cette cellule de DGS peut être employée après une antenne multibande pour laisser ou supprimer une des bandes selon la nécessité, ou après une antenne large bande afin d'obtenir une largeur de bande reconfigurable, ou après un filtre passe-bande pour supprimer les harmoniques d’ordre supérieur.

Après avoir étudié le résonateur original à défaut de plan de masse, deux applications des structures DGS sont présentées. La première est basée sur la technologie des lignes coplanaires tandis que la seconde est basée sur celle des microrubans.

Dans la première application, une structure à défaut de plan de masse est introduite au sein d’un filtre à base d’un résonateur coplanaire à couplage inductif. Ce filtre se compose effectivement de deux parties, la première étant un résonateur conventionnel à couplage inductif assurant la fonction du filtre passe-bande. La seconde partie est le plan de masse à défauts qui est responsable de la miniaturisation ainsi que la reconfigurabilité. Le filtre avec le plan de masse à défauts a été conçu et optimisé afin d’assurer les même performances du filtre classique sans DGS en terme de fréquence de résonnance, bande passante, pertes

d’insertion et de réflexion tout en diminuant sa taille en passant d’une longueur physique de 12.9 mm à 5.5 mm pour une fréquence de résonance à 5 GHz.

Afin de valider notre théorie, un filtre d’ordre 2 est conçu sur la base de ce même résonateur et mesuré prouvant de meilleures caractéristiques en termes de réjection et bande passante. Les résultats de mesures sont en bon accord avec ceux des simulations électromagnétiques. En second lieu, la reconfigurabilité de ce résonateur est examinée en simulant expérimentalement l’élément d’accord de type MEMS à l’aide de courts-circuits et circuits-ouverts idéaux réalisés sur deux circuits test. Les résultats de mesures et de simulations sont encore une fois en bon accord.

La deuxième application présentée ici est consacrée aux résonateurs en anneaux. Cette fois-ci, la technologie est celle des lignes microrubans sur un substrat de Teflon. Un filtre passe-bande modifié à base de résonateur en anneau est présenté fournissant une taille compacte, de faible perte d’insertion, une bande passante large, une bonne réjection ainsi que la suppression des modes supérieurs.

Dans un premier temps, afin de réduire la taille du filtre, comme l’anneau est associé à deux stubs ouverts, ces derniers sont repliés à l’intérieur du corps de l’anneau pour. Les résultats de mesures et simulations sont en bon accord. La réduction de taille obtenue est de l’ordre de 70%, sans modification significative de la performance électrique.

Une seconde série de manipulation afin d’améliore les performances du filtre conçu par rapport à celles du filtre en anneau conventionnel consiste à associer aux structures précédentes des motifs DGS. Ces motifs sont conçus dans l’objectif de nettoyer la bande atténuée à droite de la bande passante de l’anneau. La réduction de taille réalisée en ajoutant ces motifs directement en dessous de l’anneau est de l’ordre de 25% avec un bon accord entre les résultats de mesures et ceux des simulations.

Nous avons également étudié l'utilisation des structures PBG (Photonique Band Gap) avec le filtre à résonateur en anneau. Bien que les structures EBG

soient difficile à employer dans la conception des composants microondes et millimétriques, elles offrent de plus grandes bandes atténuées dans la bande de fréquence supérieure à celle de la bande passante, supprimant ainsi les harmoniques avec réduction de taille dans l'ordre de 45 %. Tous les filtres sont fabriqués sur le substrat de téflon (CER 10-0250 CH/CH) de constante diélectrique ε_r de 9.5, d'épaisseur h de 0.635mm et de tangente δ de 0.0035. Les résultats de mesures et de simulations sont en bon accord.

Les futurs travaux s'inscrivant dans la suite de ce travail comportent deux lignes conductrices principales. D'une part, la réalisation des filtres à défauts de plan de masse et les filtres passe-bandes en technologie silicium en y associant des MEMS pour remplacer les diodes PIN et d'autre part d'étudier les potentiels des couches ferroélectriques du type BST en vue de la reconfigurabilité ou de l'accordabilité en considérant les pertes d'insertions liées à la technologie adoptée.